Tales of Intrusion and Eruption: bringing magmatic timescales to eruption monitoring

Fiona Kathleen Couperthwaite

Submitted in accordance with the requirements for the degree of Doctor of Philosophy.

The University of Leeds

School of Earth and Environment

July 2017

The candidate confirms that the work submitted is her own and that appropriate credit has been given where reference has been made to the work of others.

Acknowledgements

Firstly, I would like to thank my supervisors; Dan, Jason, Marge and Thor. Dan, thank you for your patience and guidance and the invaluable scientific discussions, without which I could not have completed this research. It was helpful to know that your door was always open. Thank you to Marge and Jason for your diligence in reading all the work I sent, often at very short notice. Finally, thank you to Thor for your fieldwork support and your feedback, which led to significant improvement of the thesis.

Carl, thank you for believing in me from the very beginning and whether intentionally, or unintentionally, helping steer my path to this point over the last 9 years. You have become a great advisor and friend since the start of this journey and you have my never ending gratitude.

Thank you to Richard Walshaw and Duncan Hedges in electron optics. We have had successes amongst the many battles and I am extremely grateful for your guidance, patience and attentiveness. Thank you also to Harri Wyn-Williams for the time spent preparing my samples and for always being there when something went wrong. Thank you to everyone in IT for always being on hand when help was needed and to Matt and Maren for lending an ear whenever I needed a chat.

Louise, you are a constant source of inspiration and your companionship on thesis boot camp parts one and two were crucial to starting the write up process. Thank you for keeping me sane and helping to keep me focused until the very, very end. To you no challenge is insurmountable and I look forward to seeing what we take on next.

Delia, Becky, Katie, Lucy, Amicia and of course Bobbie – a late, but much needed addition to office 8.152 – each of you have put up with a remarkable amount of wittering from me and without you this journey would have been much harder. Any situation that got too stressful could be resolved with a coffee, dinner or something stronger or with cuddles from our furry friend “the bobs”. Thank you for the constant distractions, they were always very welcome.

Thank you to Andy and Toby for helping to shape my time here in Leeds, always being available for beers and for facilitating the good times in the Pyrenees on fieldwork, a welcome interval each year. Laura, thank you for providing a constant

cheeriness and upbeat support. You always made any problem seem suddenly insignificant and provided much need positivity to counteract my pessimistic nature. And thank you to Luke for his Microsoft word capabilities and rock hammering skills in Hawaii.

Thank you to Alex, for basically looking after me. Hopefully I can return the favour one day. And finally, thank you to my mum and sister for your unwavering support and to my dad, although no longer with us, you always encouraged me to pursue and achieve my goals. You have all always told me that anything is possible and have given me the determination and drive to succeed in whatever it is that I am doing.

Abstract

Understanding sub-surface magmatic processes is key for assessing volcanic eruption timescales, eruption styles and their associated hazards. Geophysical and geochemical techniques are commonly used to monitor volcanoes to better understand the magmatic processes occurring at depth. However, although geophysical techniques can be implemented in near-real time, there is currently no geochemical or petrological technique that can be correlated with the geophysical datasets on this timescale.

Diffusion modelling is a petrological technique used to model timescales of magmatic processes using the composition of zoned minerals. However, in its current form, it is not suitable as an eruption monitoring tool due to the lengthy processing time required. In this thesis, I present new diffusion modelling methodology for Fe-Mg diffusion in olivine that can be implemented for use as an eruption monitoring tool in *near-real time*. To refine and streamline the processing methodologies I analysed olivine-rich samples from Piton de la Fournaise, La Réunion, Mauna Loa, Hawaii and Vatnaöldur, Iceland.

Using traditional processing methods, I applied suitable model parameters (e.g. temperature) and geometrical corrections (e.g. those for anisotropy) to a lava flow sample from Piton de la Fournaise and identified a simple, single crystal population. I used field, textural, compositional and timescale data (using the same traditional methods) to identify at least two crystal populations within two different samples from Mauna Loa (Hapaimamo and Moinui). Each of these populations, that vary in complexity, were considered to assess how each part of the processing workflow could be streamlined and I considered how to apply the necessary geometrical corrections at crystal population level rather than to individual crystal traverses. In doing so, I created a *rapid* processing workflow for Fe-Mg diffusion in olivine.

I stress tested this new streamlined methodology using tephra samples from Vatnaöldur. I processed the samples under simulated eruption conditions to quantify how rapid the new workflow could be. It took ~26 hours from initial sample preparation to timescale interpretation; this is significantly faster than traditional methods. I have discussed the potentials and pitfalls of diffusion modelling as a monitoring tool so the new rapid methods developed in this thesis can be implemented during volcanic eruptions.

Table of Contents

List of Figures

List of Tables

CHAPTER 1

Bringing magmatic timescales to eruption monitoring using diffusion chronometry and textural analyses on select case studies: an introduction

1.1. Overview and rationale

Volcanic eruptions are one of Earth's most impressive natural phenomena, but the processes controlling them and the timescales upon which they occur are little understood. It is important to consider what processes are occurring within the magma chamber pre-eruption (*Humler and Whitchurch, 1988, Nakamura, 1995)* and how and when magma is moving (*McNutt, 2005).* The eruption rate, magma rheology, composition and cooling rate ultimately dictates what form the eruption takes, from lava dome building (*Fink et al., 1998*), to the emplacement of extensive lava flows (*Self et al., 1997; Hon et al., 1994*), the occurrence of pyroclastic flows or surges (*Sparks et al., 1973; Fisher, 1979*) and/or the release of volcanic gases (*Giggenbach., 1996*). The study of these magmatic events and of eruption histories help us to understand the fundamental processes occurring in volcanoes at depth and are informative for eruption forecasting and monitoring (*Sparks,* 2003).

Monitoring before and during an eruption event is implemented by volcano observatories and research groups around the world using various geophysical methods. These include the use of seismics (*Bryan and Sherburn, 1999; Aki and Ferrazzini, 2000*), GPS (*Odbert et al., 2014*), magnetotellurics (*Ingham et al., 2009*), InSAR (*Gonzalez et al., 2015; Dzurisin, 2003*) and gravity studies (*Bagnardi et al., 2014; Rymer and Williams-Jones, 2000*). Seismic and GPS data networks provide robust monitoring datasets when set up to correctly target regions in the subsurface where magma migration can be detected. InSAR measurements may also provide an insight into magma movement, but can be affected by incoherence in particularly humid or vegetated locations. Data gaps are also prevalent where the satellite return time is low (though this is being improved by the launch of the Sentinel satellite system). Volcano seismology as a monitoring tool is not without controversy either when detecting the movement of magma – earthquakes or rock fracture networks

that are detected may be associated with movement of other fluids. Sufficient instrumentation also needs to be deployed; few volcanoes have a dense network coverage. The definition of a magma plumbing system has evolved in recent times from a single magma chamber to a complicated system of partially molten magma mush zones within a sill and dyke complex (*Hildreth and Wilson, 2007; Bachmann and Bergantz, 2008; Kahl et al., 2015*). If this interconnected system of sills and dykes is made up of magma bodies of various shapes and sizes, geophysical resolution of monitoring signals becomes much more difficult (*Kahl et al., 2015*).

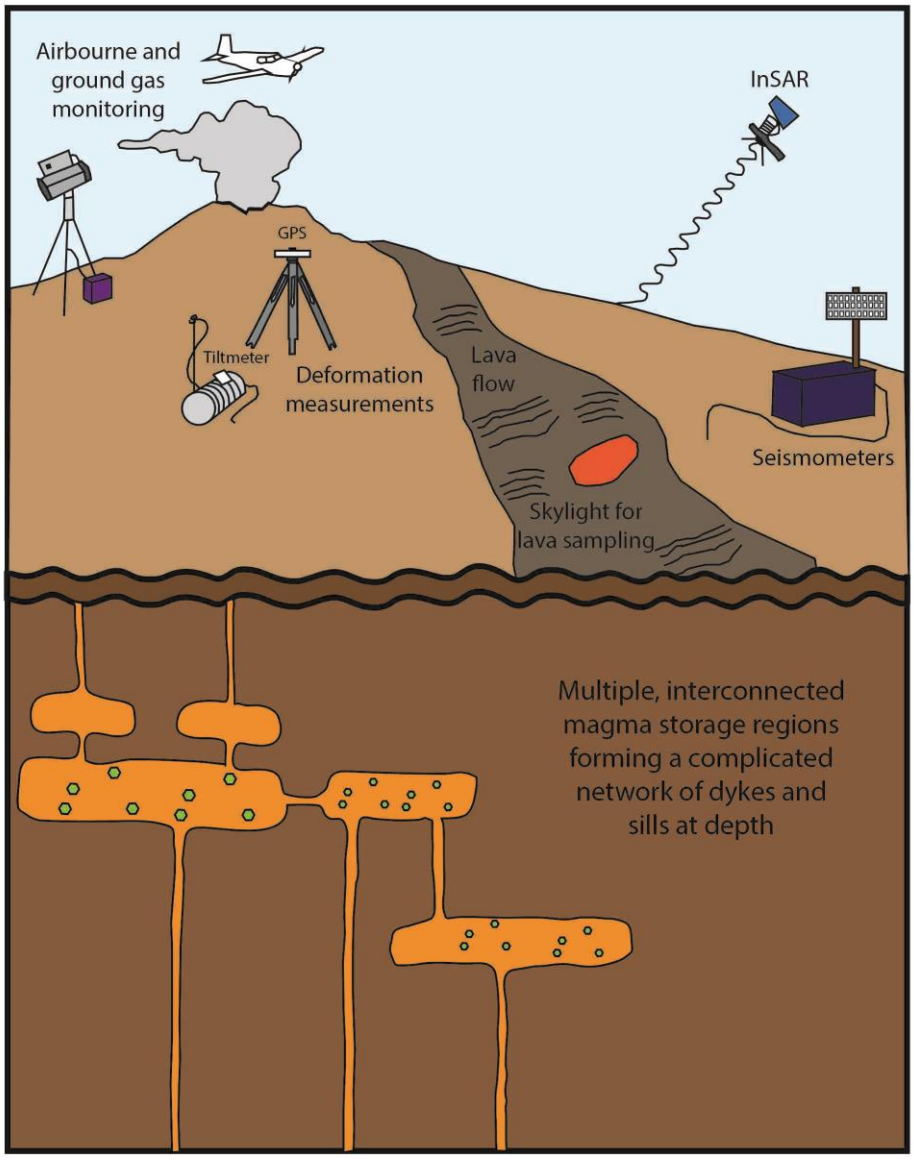

Figure 1.1: Schematic diagram of some of the current eruption monitoring methods and how they might be deployed (not to scale). At depth, the magma reservoirs with their crystal cargo are interpreted not to be simple geometries (not to scale), creating challenges for existing monitoring methodologies. Adapted from the Volcano Hazard Program.

Geochemical and petrological methods can be used to assess changes in bulk rock compositions, mineral petrography and volatile content, but these techniques are not predictive, nor can they be used for determination of magmatic timescales. Fumarole gases and eruption plumes are routinely sampled where possible once an eruption has commenced or during a period of outgassing that does not lead to an eruption (*Christopher et al., 2015*). These can give indications of ascending magma through changes in gas composition or CO_2/H_2O ratios (*Ilyinskaya et al., 2015*).

Tephra falls and lava flows are often fairly accessible eruption deposits and their textural properties are good indicators of processes occurring within the subsurface pre-eruption and syn-eruption and within lavas following emplacement. Petrological monitoring could be of great use during an on-going eruption, as it could provide researchers with a new magmatic perspective that can be used to complement and correlate with the existing geophysical monitoring datasets (e.g. *Morgan et al., 2006; Rae et al., 2016; Hartley et al., 2016*).

Diffusion chronometry datasets can provide the time stamp needed to usefully link petrological time series to existing eruption monitoring. They can provide high resolution magmatic time information of the longevity of a magma reservoir and can record the diverse storage conditions that the magmas experienced in the subsurface before eruption (*Kahl et al., 2015*). This type of dataset cannot be retrieved using geophysical methods. These data are obtained from compositional differences that produce zoning within a crystal. This zoning results from changes in temperature, pressure, volatile fugacity or changes in composition of the liquid in which the crystal resides (*Costa et al., 2008; Costa and Morgan, 2010*). If this zoning is modified due to a change in conditions driven by a magmatic process, a timescale can be extracted that can be correlated directly to the process recorded in the crystal.

Diffusion chronometry has been successful in deciphering the timing of magmatic events of volcanic eruptions but only long after an eruption has started (and often ended) (*Costa and Dungan, 2005; Morgan et al., 2006; Kahl et al., 2011, 2013, 2015; Pankhurst et al., 2017, in review*). The technique provides ways of inferring the dynamics of a volcano plumbing system (e.g. *Kahl et al., 2011)*, eruption triggering, (e.g. *Martin et al., 2008)*, magma recharge, (e.g. *Morgan et al., 2006)*, magma residence times (e.g. *Costa, Chakraborty and Dohmen*, *2003; Morgan et al., 2004),*

magmatic assimilation (e.g. *Costa and Dungan, 2005),* magma intrusion (e.g. *Costa & Chakraborty, 2004; Saunders et al., 2012)* and magma ascent (e.g. *Charlier et al., 2012)*. This is achieved by modelling major and trace element diffusion across zoned crystals. If the magmatic process responsible for diffusive exchange is known, robust and reliable timescales can be calculated provided enough data points are analysed and geometrical corrections are applied.

Existing processing methods are typically relatively complex and time-consuming, particularly when large datasets need to be derived. These processing methods are therefore not suited for real-time data acquisition during an event, particularly when the eruption evolves over a short time period with significant impact on society e.g. Eyjafjallajökull 2010, Iceland (*Pankhurst et al., 2017, in review,*). The purpose of this project is to take the current processing methods and streamline them. This will enable the technique to be utilised on an eruption time scale without compromising the reliability of the results – datasets will be processed days after an eruption has commenced rather than weeks, months or years later, as has been typical for traditional diffusion studies.

Fast processing methodologies for obtaining and processing mineral diffusion datasets from which timescales for magmatic processes can be extracted are required in order to use these types of petrological methods in volcano monitoring. Due to their reduced processing times and costs, streamlined petrological methods could also be used to recover larger quantities of data than traditional methods over the span of a dormant volcano's history. This property is unique to diffusive datasets as seismic, GPS and InSAR signals cannot be collected retrospectively. Armed with a dataset of such longevity, more information could be recovered from a particular volcanoes history than ever before, possibly identifying patterns in its historical behaviour and thereby better equipping the authorities and surrounding communities for a future eruption.

The success of these streamlined diffusion methods would allow petrological data to be combined with the geophysical data over the same, short time period to better inform authorities and local communities in the immediate aftermath of the start of an eruption. This thesis presents a new methodology that will provide a firmer understanding of what magmatic processes are occurring beneath a volcano during an eruption and over what timescales they have occurred.

1.2. Research outline and objectives

The aim of this project is to produce a user-friendly, easy-to-deploy petrological monitoring method that can easily be implemented (e.g. by non-expert observatory staff) in the event of an eruption and does not require extensive training. These methods will be composed of streamlined diffusion modelling techniques that produce results on the magmatic processes driving the eruption within days of sampling. Diffusion modelling will become more accessible for those who are not experienced users and cheaper to use for observatory staff working within strict budgets, limited analytical capability and tight time constraints. This new tool is also of scientific value to the wider science community, enabling a magmatic time perspective to be gained much faster than currently possible and will make the technique more widely used.

This study focuses only upon Mg-Fe inter-diffusion across zoned olivine crystals. The diffusion coefficient for Mg-Fe inter-diffusion in olivine is one of the most robust and best experimentally calibrated than all other diffusion coefficients in other magmatic minerals. This diffusion coefficient operates on timescales suitable for the modelling of magmatic processes (days to years). The focus of the project limits the use of the new streamlined methods as they can only be deployed to monitor mafic eruptions containing olivine but could reasonably be adapted to other systems. The global occurrence of mafic, olivine-bearing eruptives and therefore the applicability of this tool is discussed in chapter 7.

Various parameters are required for input into the model including temperature, pressure, oxygen fugacity (fO_2), an experimentally calibrated diffusivity, and the composition at the crystal rim (boundary condition) and composition at the crystal interior (initial condition). These crystal compositions and data points in between are extracted from a linear traverse perpendicular to the crystal face. The input of all parameters and their effects on the model are discussed in detail in chapter 2 together with analytical considerations, models and other methods used for this project. These parameters are required for both the current “traditional” methods and for the new “streamlined” methods.

Other geometrical corrections are applied to or need to be considered for each individual linear traverse (the composition measured from rim to core). Geometrical corrections are for anisotropy (the orientation of the linear traverse

with respect to the crystallographic axes must be known), shallow sectioning effects (when samples are prepared crystals are cut at random angles, some of these angles may lead to artificial lengthening of the diffusion profile) and for simultaneous crystal growth and diffusion effects, with or without changing boundary conditions during the diffusive history. Rarely have the latter two corrections (sectioning effects and crystal growth/changing boundary condition effects) been considered in current and past datasets. These geometrical corrections and their effects are described in more detail and applied to case studies in chapters 2, 3, 4 and 5.

Currently, each of these corrections are applied to individual crystal traverses to make the timescales as robust as possible and lower the uncertainties. It is this step of quantifying and then individually processing several different corrections to each data point that contributes significantly to the execution time of the diffusion modelling workflow. To create the streamlined methods, I will pick apart each of the processing steps from sample collection and composition retrieval to the application of the geometrical corrections to evaluate how they can be performed faster or more efficiently.

This thesis studies several different eruptions, rich in olivine crystals, to build a suite of case studies. These are used to construct, test, and refine the faster workflow and to understand how the new methods perform on crystal populations varying in complexity. A lava flow sample containing a "simple" crystal population has been selected from Piton de la Fournaise volcano (PdF) on La Reunion (chapter 3), to pull apart the processing steps and create new methodology to see how this simple population behaves. New correction methods are proposed based upon those results for application to entire populations in a single step rather than to individual crystal traverses to make processing more efficient (chapter 5).

Once the new methods have been established with a simple population they are applied to more complex case studies (chapter 4): a tephra fall and related lava flow "Hapaimamo" from Mauna Loa, Hawaii, and a second lava flow "Moinui" with striking textural characteristics. This will establish if the new methods generated using a "simple" population can withstand application to more complex crystal populations (chapter 5) formed as the result of processes such as magma or crystal mixing, which have been demonstrated to occur in natural systems.

Finally, the new methods are stress-tested on a tephra sample from the axial rift in Iceland (chapter 6) by simulating an eruption scenario and the rapid processing that would be necessary. The success and drawbacks of the new methodology and the use of petrological tools for monitoring purposes are outlined then discussed and further work is considered (chapter 7) before conclusions from this project are drawn (chapter 8).

CHAPTER 2

Methodology

2.1. Introduction

The main task of this project is to evaluate current diffusion modelling methods to determine how they can be adapted for monitoring use. Various techniques and analytical machines are typically required to retrieve accurate and precise compositional and crystal orientation measurements, to subsequently model the timescales that the changes in composition may represent. These methods and procedures are detailed in this chapter. Other techniques that have also been incorporated into this study include Crystal Size Distributions (CSD) and X-Ray Microtomography (XMT). Together, these methods provide a detailed context for the origin of the magmas, the processes they have been subjected to, the regions in which they have been stored and the timescales over which this has occurred. Methodologies and the associated uncertainties are described in detail in this chapter.

2.2. Diffusion Modelling

Diffusion modelling has been used over the last 30+ years to unravel pre- and syn-eruptive processes long after an eruption has finished (*Lasaga, 1983*; *Humler and Whitchurch, 1988; Chakraborty and Ganguly, 1990, 1991; Nakamura, 1995; Lasaga, 1998).*

The method uses compositional differences preserved as zoning within a crystal to determine timescales relating to the processes that gave rise to these heterogeneities (*Costa and Morgan, 2010)*. Zoning can be created if changes in temperature, pressure, volatile fugacities or changes in composition of the magma occur (*Chakraborty, 1997*). If diffusion is optimum, the zoning is modified and a timescale can be extracted that can be correlated directly to the process recorded in the crystal, as shown in figure 2.1 (*Costa, Chakraborty, and Dohmen, 2003; Costa and Chakraborty, 2004; Costa and Dungan, 2005; Costa and Morgan, 2010).*

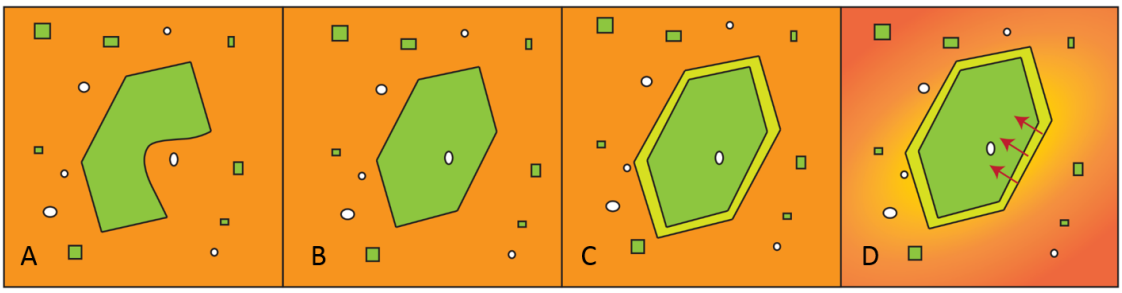

Figure 2.1: A schematic showing an olivine crystals growing in a melt containing volatiles (A). Melt and volatiles can get entrapped within the crystal (B). Changes in the pressure, temperature or composition of the magma leads to the formation of a rim around the crystal edge different in composition to its interior, giving a zoned crystal (C). If the temperature is optimal, diffusion of elements across the crystal can lead to modification of the zoning and a timescale can be retrieved for the magmatic process that brought about the modification (D)

Many factors and parameters need to be considered when using diffusion modelling methods, including values for the diffusion coefficient, the diffusion rates of certain elements, the initial and boundary conditions, anisotropy, zoning related to growth, and compositional dependence (*Costa and Dungan, 2005; Costa et al., 2008; Costa and Morgan, 2010*). The temperature and pressure conditions together with volatile fugacities and melt composition are important controls on the extent of compositional zoning and therefore the applicability of diffusion modelling (*Costa et al., 2008*). Different elements diffuse at different speeds. The element used for the modelling needs to diffuse fast enough to be able to pull useful timescale information out of the zoning in the crystal but also be slow enough so that the crystal does not fully re-equilibrate, erasing information we are trying to ascertain (*Costa et al., 2008*).

2.2.1. Fick's Law

The amount of material that moves in a given direction over a unit of time is called the flux (J). Fick's law relates the flux to the concentration gradient ($\partial C/\partial x$) and the diffusion coefficient (D) of the material as follows (*Crank, 1975; Lasaga, 1998; Costa et al., 2008; Costa and Morgan, 2010*);

$$\mathrm{J} = -D\,\frac{\partial C}{\partial x} \quad \text{(equation 2.1)}$$

To obtain Fick's second law and to introduce time into the equation (needed for diffusion modelling in a crystal over time) a mass balance is needed (*Costa and Morgan, 2010*). This can be defined as, "the difference between what goes in to a system over time and what comes out of the system is the net change in what is contained within that system" (*Costa et al., 2008*). Thus Fick's second law below (equation 2.2) (*Costa and Morgan, 2010*);

$$\frac{\partial C(x,t)}{\partial t} = \frac{\partial}{\partial x}\left(D \frac{\partial C(x,t)}{\partial x}\right) \quad \text{(equation 2.2)}$$

C(x,t) is the concentration as a function of time, (*t)*, at a point in distance, (*x)*. This equation describes how the concentration of an element of interest changes over a period of time at every position along the concentration profile (*Costa and Morgan, 2010*). This is further complicated in that for olivine, D is a function of composition (*Costa and Chakraborty, 2004; Dohmen and Chakraborty, 2007a and 2007b*). The flux in these equations is the net diffusive flux. A timescale can be extracted, for the process that initiated the flux, from the shape of the distribution of the curve C(x,t) assuming a set starting distribution at t=0 and assuming Fickian behaviour of the material of interest (e.g. elements within a mineral) (*Costa et al., 2008; Costa and Morgan, 2010*). Additional fluxes need to be carefully considered, such as those that enable net growth or dissolution of the crystal in the melt over the diffusion time period (*Costa et al., 2008*). Growth or dissolution of a crystal can be a major problem when trying to calculate a timescale using a diffusion model (if all of these processes are simultaneous) (*Costa et al., 2008*). A crystal that has been affected by either growth or dissolution and modelled with a fixed set of parameters will give an incorrect timescale (the timescales will appear longer as the profile is effectively stretched by the growth) so any crystal that is known to be affected is usually avoided (*Costa and Morgan, 2010*).

2.2.2. Diffusion Coefficient

The diffusion timescale is inherently dependent on the diffusivity (D) used (*Costa et al., 2008; Costa and Morgan, 2010*). Diffusion coefficients for different elements

within different igneous minerals have been determined and discussed in recent years (*Watson, 1994; Chakraborty, 2007a and 2007b; Chakraborty, 2008, 2010; Van Orman, 2010; Dohmen and Cherniak, 2010*) due to improvements in measurement technology and experimental procedures, as well as a greater understanding of the mechanisms of diffusion.

There are various ways to describe the types of diffusion coefficient depending on the diffusion mechanism. The simplest of these is the self-diffusion coefficient (*Costa et al., 2008; Costa and Morgan, 2010*). This refers to the random movements of atoms from one vacancy in a lattice to another vacancy, without the presence of a concentration gradient (*Flynn, 1972; Philibert, 1991; Costa et al., 2008; Costa and Morgan, 2010*). This method can be carried out experimentally with the use of an isotopic tracer (*Chakraborty, 1994*). This makes the diffusion process measurable, as an isotopic concentration gradient is artificially created and according to Fick's 2nd law (as above) the isotopic contrast evolves over time (*McCaig et al., 2007; Costa et al., 2008; Costa and Morgan, 2010*). More commonly used are chemical diffusion coefficients, where a chemical gradient is present (*Costa et al., 2008*; *Costa and Morgan, 2010)* as is present in zoned crystals. Depending on the system, an inter-diffusion coefficient (e.g. Mg-Fe in olivine), or a multicomponent diffusion coefficient (required when there are more than two elements diffusing e.g. Ca, Mn, Fe or Mg in Garnet), may need to be considered (*Costa and Morgan, 2010; Costa et al., 2008*). The diffusion of an element in a crystal involves at least two elements, vacancies or electrons, which is an inter-diffusion process (*Costa et al., 2008*).

The type and distribution of vacancies controls the type and rate of diffusion (*Putnis, 1992*). Diffusion coefficients are controlled by any variable that may affect the concentration of vacancies in the crystal. The generation and migration of vacancies are both thermally-activated processes and therefore diffusion too is thermally-activated (*Costa et al., 2008; Zhang, 2010*). At high temperatures, intrinsic vacancies dominate – the number of vacancies increases as the free energy of the system is lowered (*Putnis, 1992; Costa and Morgan, 2010*). At lower temperatures, vacancies can be created by charge difference e.g. a trace element with a difference charge substituting for a cation within the structure of a mineral with vacancies for charge balance (*Costa and Morgan, 2010*). Pressure and composition can also have an effect to different extents depending on the minerals and elements involved. For example,

any trace element coefficients in plagioclase depend on the major element composition (*Costa et al., 2003; Cherniak, 2010*). Major element diffusion in olivine e.g. Fe-Mg, Ni and Mn, has been found to be dependent on forsterite content (*Buening and Buseck, 1973; Misener, 1974; Costa and Dungan, 2005; Chakraborty, 2010*). The influence of water fugacity and oxygen fugacity (fO_2) on the diffusion coefficient varies. In olivines, the dependence on fO_2 decreases from Ca>Ni>Fe-Mg-Mn (*Petry et al., 2004; Costa and Dungan, 2005; Coogan et al., 2005; Chakraborty, 2010*).

The description of the diffusion coefficient is determined by the Gibbs phase rule due to the types and numbers of variables that affect the concentration of vacancies (temperature, pressure, water fugacity, oxygen fugacity, composition and crystallographic orientation) (*Costa et al., 2008*; *Costa and Morgan, 2010*). The transport properties of molecules in the system can be described by thermodynamic expressions (*Costa, et al., 2008*).

The temperature and pressure dependencies that are used to calculate diffusion coefficients can be written as an Arrhenius equation as follows (*Costa et al., 2008; Costa and Morgan, 2010*);

$$D = D_o \cdot exp\left(\frac{-Q-\Delta V\left(P-10^5\right)}{R \cdot T}\right) \quad \text{(equation 2.3)}$$

Q is the activation energy at 10^5 Pa, ΔV is the activation volume, P is the pressure in Pascals, R is the gas constant, T is temperature in Kelvin and D_o is the pre-exponential factor (*Costa et al., 2008; Costa and Morgan, 2010*). This parameterization depends on the favoured equation of state for the mineral. If over a range of temperatures diffusion is operated using the same mechanisms, linearity is expected of the diffusion coefficient on an Arrhenius diagram (figure 2.4) (*Lasaga, 1998; Brady and Cherniak, 2010*).

The pre-exponential factor relates to crystal structure, jump frequency, and distance (*Brady and Cherniak, 2010*). The effects of volatiles are often incorporated in to the pre-exponential factor D_o (*Dohmen and Chakraborty, 2007a and 2007b; Costa et al., 2008; Costa and Morgan, 2010*). Crystallographic orientation will also have an

influence depending on the mineral of interest (*Buening and Buseck, 1973; Costa et al., 2008; Costa and Morgan, 2010; Chakraborty, 2010,*).

The activation energy (Q) relates to the energy from defect formation and the energy needed to form an 'activation complex' (*Brady and Cherniak, 2010).* The size of Q and ΔV control the magnitude of the dependency of the diffusion coefficient on T and P (*Costa et al., 2008*). Most activation volumes (ΔV) in silicates are positive therefore diffusion is slower at higher pressures at a given temperature, due to reduced space in the crystal lattice (*Hozapfel et al., 2007; Costa et al., 2008*). If the activation energy is known, the effect of changing T at a given P can be resolved (*Costa et al., 2008*). Activation energies for diffusing elements are lowest for univalent cations and highest for tri or tetravalent cations, with activation energies for divalent cations somewhere in between (*Cherniak, 2003; Petry et al., 2004; Coogan et al., 2005; Dohmen and Chakraborty, 2007b; Costa et al., 2008*). The effect of activation volumes on P is less well constrained due to a lack of experimental data. The size of activation volume is usually relatively small and so experiments using large pressure ranges would be required which is challenging, therefore pressure dependence can be ignored for crustal processes (*Hozapfel et al., 2007; Costa et al., 2008; Costa and Morgan, 2010*). The effect of pressure and activation energies on diffusion rates is stronger at lower temperatures due to the reduced contribution of the T term in the denominator in equation 2.3 (*Costa et al., 2008*). In most cases, the pressure term can be left out as the effect of pressure on D is only significant for $P > 10^8$ Pa (*Costa et al., 2008; Costa and Morgan, 2010*).

2.2.3. Initial and boundary conditions

The choice of initial and boundary conditions is an important constraint when applying diffusion modelling. It is important to think about what magmatic process has been recorded in the crystal by the compositional zoning as it is this assumption that defines how the initial and boundary conditions are determined (*Costa and Morgan, 2010*). The initial conditions can be referred to as the shape of the zoning pattern before diffusive modification (*Kahl et al., 2011*). Three types of the most commonly used initial and boundary conditions can be defined as follows from Crank, (1975*)*;

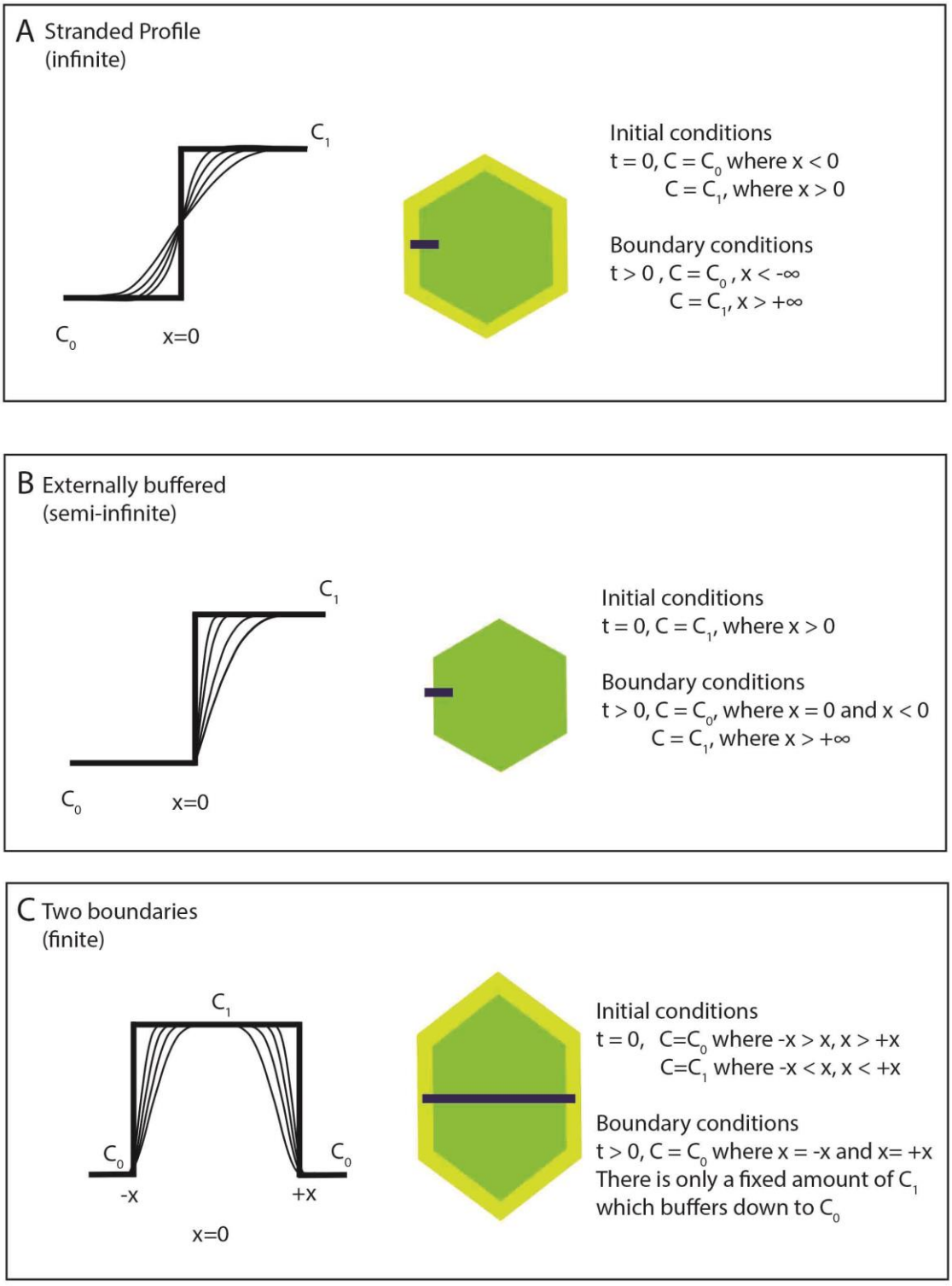

Figure 2.2: A schematic showing examples of three different types of initial and boundary conditions applied to diffusion profiles.. The green crystals are zoned and the yellow areas depict an overgrowth rim. A) a stranded profile (e.g. within the interior of a crystal) B) an externally buffered profile (e.g. by a melt) C) a profile with two grain boundaries (e.g. across the full width of a crystal). The purple lines shows the position in the crystal where the profiles would be measured. The thick black lines in the accompanying graphic shows the initial conditions in each case and the curved lines show the diffusion profile after some time.

Figure 2.2 shows examples of 3 types of initial and boundary conditions that are commonly used to model diffusion profiles – a stranded profile (within a crystal), an externally-buffered profile (at the edge of a normal or reverse zoned crystal) and a profile between two crystal faces across a crystal (*Crank, 1975; Costa and Morgan, 2010*). It is important to consider what magmatic process is being modelled and where the profile is being extracted from within the crystal, to apply the correct initial and boundary conditions. The conditions hold true if the concentration at the rims are constant and the crystals have volumetrically significant core plateaus of homogeneous composition (*Costa and Dungan, 2005*). The initial conditions effectively start the diffusion clock at time zero, as indicated above (*Costa and Morgan, 2010*). They refer to the distribution of the elements of interest in the crystal at the time (t=0) of the onset of diffusion (*Costa and Morgan, 2010*).

It can be difficult to estimate the initial conditions, as each case is unique with unique combinations of conditions (*Costa et al., 2008*). Figure 2.3 below shows some possible initial concentration distributions and their distribution after diffusive modification in compositionally heterogeneous crystals (*Costa et al., 2008*);

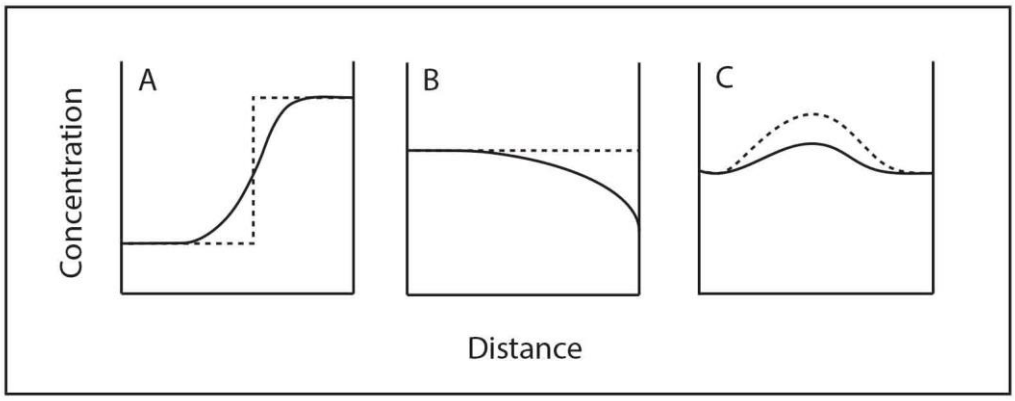

Figure 2.3: Adapted from Costa et al. (2008). Examples of initial zoning patterns (end member types) used for obtaining a time scale (dotted line) and distribution after a given diffusion time (solid line) for various magma processes – a) magma mixing b) a late change in boundary conditions or c) magma differentiation (Costa et al., 2008).

Using the zoning patterns in the crystals it is possible to obtain a time constraint to then directly relate to the process that is recorded as illustrated above. Within my samples the initial starting conditions are most similar to 2.3a and 2.3b. Setting the initial conditions takes careful consideration for each case. Analysing crystals of varying size is a method often employed, as the larger crystals are more likely to

preserve the original composition in the core region and be unaffected by diffusion due to their bigger size (*Kahl et al., 2011*). The distribution coefficient relating the partitioning of iron and magnesium between olivine and the liquid fixes the initial conditions and is reported as 0.3 +/- 0.03 and is independent of temperature (*Roeder and Emslie, 1970*). This was determined experimentally to understand the equilibria between olivine crystals and basaltic liquids and therefore the conditions under which the olivine crystallises. These experiments were carried out with a range of basaltic compositions at varying temperatures (1150-1300°C) and oxygen fugacities ($10^{-0.68}$ – 10^{-12}atm) (*Roeder and Emslie, 1970*).

There are several common methods currently undertaken to assess the initial conditions;

(1) Estimating the initial concentration distribution of faster diffusing elements by assessing the relatively unmodified profile shapes of a slower diffusing element in the same crystal. Therefore the profile-shape of these slower diffusing minerals may be used to infer the initial concentrations of a faster diffusing mineral (*Costa and Dungan, 2005; Morgan and Blake, 2006; Costa et al., 2008; Costa and Morgan, 2010; Allan et al., 2013*).

(2) Use a reasonable value for maximum concentration – a very sharp concentration profile such as a step profile (2.3a) –which would provide a maximum diffusion timescale (*Humler and Whitchurch, 1988*; *Lasaga, 1998*; *Costa et al., 2008; Costa and Morgan, 2010).*

(3) Assume an initially homogeneous concentration profile. This is particularly effective when modelling olivine crystals (*Costa and Chakraborty, 2004; Costa and Dungan, 2005*). Robust timescales have been produced by analysing the diffusion of multiple elements along various traverses in each direction of orientation. This proves that this is an effective and useful judgement to make (*Costa et al., 2008; Costa and Morgan, 2010*).

Costa et al. (2008) have shown that with all other factors remaining the same e.g. temperature, fO_2 etc. the difference in timescales retrieved from two extreme possibilities – flux at the boundary of a homogeneous crystal (2.3 b) and flux at the boundary of a crystal consisting of a core with rim overgrowth (2.3a) - produces timescales that only differed by a factor of 1.5. This could range as high as a factor

of 4, if the step is exactly half way in to the profile width relative to the external buffer solution.

There are broadly two end member cases when defining the boundary conditions, 'open' and 'closed'. They depend on how elements of interest interact with the surrounding matrix through exchange at the crystal boundary (*Costa et al., 2008*). The boundary may be closed to the exchange of matter or equilibration with the surrounding liquid/melt (*Costa et al., 2008; Costa and Morgan, 2010*). This can occur if the element of interest in the surrounding melt does not exchange at a quick enough rate as the element in the mineral phase or if the element in the crystal does not partition favourably in to the surrounding melt/liquid (*Costa et al., 2008*). Secondly, the boundary may be open. This is where exchange of elements may take place and re-equilibration of the crystal with the surrounding melt may occur (*Costa and Morgan, 2010*). Within an open system this may result in either the concentration at the rim being constant with time where the crystal is surrounded by a much larger volume of melt than the crystal itself. Alternatively, the concentration at the rim may be variable if there is a change in certain conditions such as temperature or oxygen fugacity (fO_2), if crystallisation occurs or there is a limited volume of melt in which the crystal is suspended e.g. in a mush layer (*Costa et al., 2008; Costa and Morgan. 2010).*

The boundary conditions for open systems can be used for groups of crystals – Costa and Chakraborty (2004) used a single boundary condition for all olivines with a low forsterite (Fo) content from the Volcan San Pedro in the Chilean Andes but used two further boundary conditions for olivines with high Fo, as two time estimates could be retrieved. Alternatively, the boundary conditions can be chosen for each individual crystal as in Kahl et al. (2011). For each olivine crystal from a suite of lava flow samples from the SE flank eruption of Mt Etna, 1991-1993, a boundary condition was chosen depending on the specific magma pathway that each crystal tracked. In essence boundary conditions must be chosen depending on what works with a specific sample set. It is important to decipher carefully whether the system is open or closed. Models defined with closed boundaries will produce much shorter timescales than those with open boundaries (*Costa et al., 2008*). In a natural system, it is much more likely that the boundary condition is changing, as the composition of the melt buffer changes due to changes in ambient conditions. This can be seen in

some profile shapes that do not fit with diffusion models when calculated with a fixed boundary condition, as described in detail in chapter 3.

2.2.4. Uncertainties of modelling parameters and geometric considerations

Geometrical corrections are one type of correctable uncertainty. The aim of classical modelling is to correct out as many as possible. Uncertainty and geometrical corrections affect the modelling and resulting timescales in one of two ways; they are either associated with the parameters that shape the modelling e.g. temperature and oxygen fugacity (fO_2) and therefore the diffusion coefficient. Or they are associated with the chosen inputs applied to the model such as the composition, spatial resolution and orientation (*Costa et al., 2008; Costa and Morgan, 2010*). Various factors and parameters affect the uncertainties by varying amounts. Those that are considered to have the largest effect thereby reducing the certainty of the timescales are discussed in more detail.

2.2.4.1. Diffusion coefficient, Thermobarometry and Oxygen fugacity (fO_2)

The diffusion coefficient is defined experimentally and is composed of many parameters, as described theoretically in the earlier section. The diffusion coefficient I will be using for all of my Mg-Fe modelling is that defined by Dohmen and Chakraborty (2007b);

$$log_{10}[D_{FeMg}(m^2/s)] = -9.21 - \frac{201000+(P-10^5)\times 7\times 10^{-6}}{2.303RT} + \frac{1}{6}log_{10}\ (fO_2/10^{-7}) + 3X_{Fe}$$

(equation 2.4)

This expression is to be used for modelling along the c-axis, (001), at oxygen fugacities greater than 10^{-10} Pa, where T is in kelvin, P and fO_2 is in Pascals, X_{Fe} is the mole fraction of the fayalite component and R is the gas constant in J/mol/K (*Dohmen and Chakraborty, 2007b*). This expression is adjusted when calculating diffusivities along the a- or b-axis. The diffusion coefficient along an arbritary direction can be calculated using equation 2.5 if the diffusion coefficient along the principle axes are known. The diffusivity along the a- or b-axis is equal to ($D_c^{Fe-Mg}/6$) (*Dohmen and Chakraborty, 2007b*). The effects of oxygen fugacities, the

composition and crystallographic orientation are typically incorporated into the pre-exponential factor of the diffusion coefficient, D_0 (which has a value of -9.21 at these fO_2 conditions (equation 2.4)) (*Dohmen and Chakraborty, 2007b*).

To arrive at this expression, Dohmen and Chakraborty (2007a and 2007b), used an experimental approach and the thermodynamic expressions of two studies that looked at the nature and concentration of point defects in olivine (natural and synthetic) (*Nakamura and Schmalzried, 1983; Tsai and Dieckmann, 2002*). They analysed the vacancy concentrations as a function of temperature and fO_2 to understand the difference in diffusion behaviour between the two studies and formulate an equation for the diffusion coefficient. It is the temperature dependence of defect concentrations that is vital to the understanding of diffusion related properties such as activation energies (*Dohmen and Chakraborty, 2007a and 2007b*). They found that there is a change in diffusion mechanism at lower temperatures and/or fO_2, whereby the diffusion coefficients become independent of fO_2 and the activation energy increases (*Chakraborty, 1997*). The change in the diffusion mechanism leads to a smeared Arrhenius diagram (1/T vs $\log_{10}D$) meaning the slopes of lines become curved and characterisation of the diffusion behaviour becomes difficult. Therefore the straight line relationship described in the equation above is only valid for temperatures higher than 900°C and fO_2 of 10^{-10} Pa (*Dohmen and Chakraborty, 2007a and 2007b*). Two further equations describe the diffusion behaviour for lower temperatures or fO_2s and for the entire range with larger uncertainties. For point defect based diffusion mechanisms, together the equations calculate Mg-Fe diffusion coefficients over the entire stability field of olivine as a function of P, T, X_{Fe} and fO_2 (*Dohmen and Chakraborty, 2007a and 2007b*).

Uncertainties in the diffusion coefficient are limited by using crystals often from the same locality and source with a well-defined homogeneous composition, free of inclusions, cracks and deformation textures in experiments where possible (*Dohmen and Chakraborty, 2007a*; *Chakraborty, 2010*; *Costa and Morgan, 2010*). Experiments are carried out at different temperatures allowing the pre-exponential factor D_0, and the activation energy to be obtained from the following plot (*Dohmen and Chakraborty, 2007a and 2007b; Chakraborty, 2010*; *Costa and Morgan, 2010; Brady and Cherniak, 2010*).

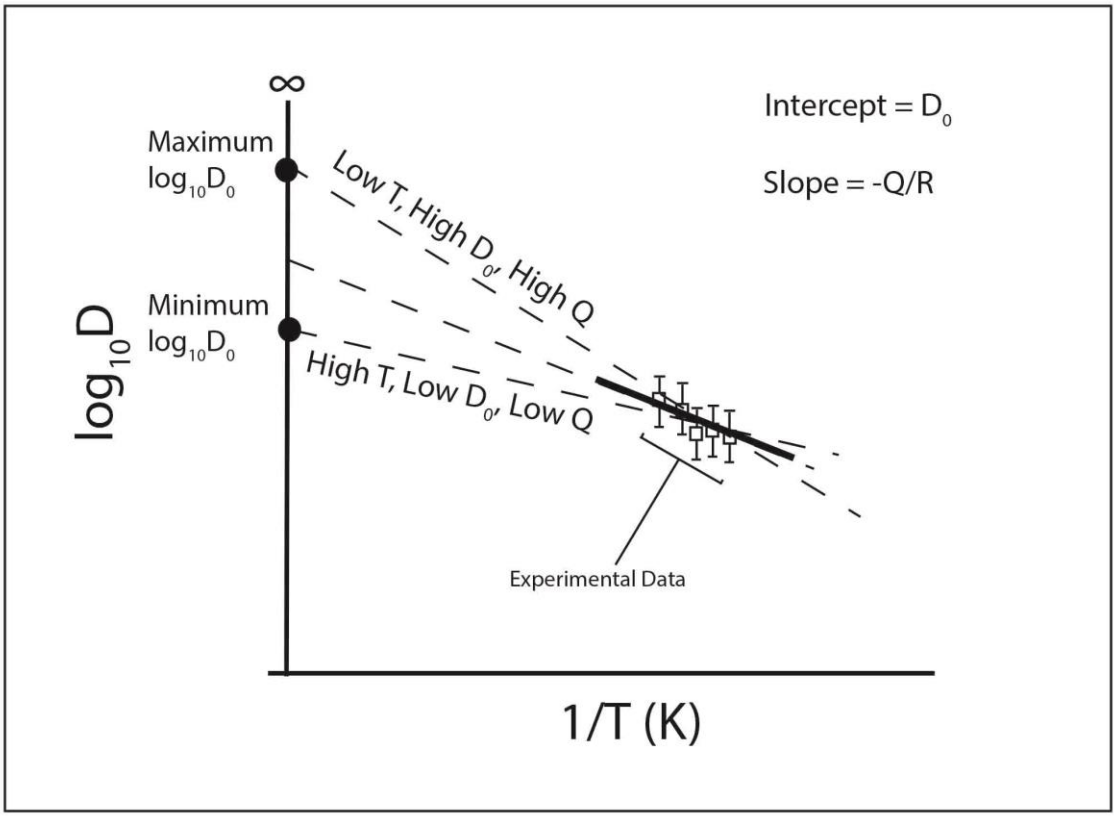

Figure 2.4: An Arrhenius-type plot used to determine the activation energy and D_0 from a series of experiments at changing temperatures to define the diffusion coefficient. Adapted from Costa and Morgan (2010), Putnis (1972) and Dohmen and Chakraborty (2007a and 2007b).

Temperature, D_0 and activation energy are all important sources of uncertainty (*Costa et al., 2008; Zhang, 2010*). It requires 6 orders of magnitude variation in fO_2 (fO_2 is incorporated into D_0) to produce 1 order of magnitude variation in D (*Dohmen and Chakraborty, 2007a and 2007b*). The uncertainty on the activation energy is dependent on the slope of the line fit through the experimental data. The effects on D_0 are similar – activation energy and D_0 are not independent of each other, and error needs to be propagated accordingly (*Costa and Morgan, 2010*). There is a positive linear correlation between activation energy and log D_0 (*Brady and Cherniak, 2010*). The fits provide a range in values for the diffusion coefficient. The range will be narrow if the calculated magmatic temperature lies within the temperature range of the experimental dataset and close to the rotation point on figure 2.4 (*Morgan et al., 2004*). Whilst changes in D_0 can result in changes to the activation energy, there will be little effect on the diffusivity at magmatic temperatures (*Morgan et al., 2004*). To calculate the timescale uncertainties, the extreme ranges in values of the diffusion coefficient (maximum and minimum) can

be combined with the maximum and minimum calculated 2σ errors on the temperature (*Morgan et al., 2004*).

Model error of thermometry results from problems with reproducing P or T during experiments, not attaining equilibrium, or errors in the compositional measurements (*Putirka, 2008*). "Error of treatment" may arise from the application of a model trending towards greater values as natural systems deviate from experimental conditions (*Putirka, 2008*) if equilibrium pairs (mineral-liquid) are not assigned correctly (*Putirka, 2008*).

Estimates for model error are derived from regression statistics such as "Standard Estimate of Error (SEE)" (*Putirka, 2008*) reported for T or P such that there is 68.26% (1σ) probability that the true value lies within the range calculated. Many thermometers give an uncertainty of +/- 30°C, probably representing the smallest magnitude for model error that we can expect for a silicate-based thermometer (*Costa et al., 2008, Putirka, 2008*). "Error of treatment" is difficult to define as it is difficult to pair equilibrium phases (*Putirka, 2008*) and so the method of Roeder and Emslie (1970) is used to calculate olivine-liquid equilibrium.

Compositional errors are dependent on the homogeneity of the standards used within the Electron Microprobe (EPMA) and the accuracy and precision of the instrument. The error on the spatial resolution is determined by the pixel size and beam convolution. The broader the diffusion curve (the less steep) the lesser the effect of convolution (*Costa and Morgan, 2010*). The error on distance, a crucial component of the diffusion equation is dependent on stage resolution and quality of the calibration. A 1% error in distance leads to a 2% error in time because 1.01^2 is equal to 1.0201, which relates back to the ($x\sqrt{Dt}$) scaling relation. Distance has a linear squared effect on time, whereas temperature has an exponential effect on time (*Chakraborty 1997; Costa et al., 2008; Costa and Morgan, 2010*). Incorporating each of these uncertainties and their effects on the diffusion timescales makes error propagating complicated and uncertainties are not reported consistently between various authors.

Costa et al. (2004) reported their error on timescales only for temperature and $f0_2$, as similarly reported by Costa and Dungan (2005). Costa et al. (2003) reported their uncertainties as a scale factor from the effects of temperature and uncertainties within the diffusion coefficient but did not specify which parameters. Kahl et al.

(2011) do not expressly state the effect of the uncertainties on the timescales, but they report the uncertainties on the thermometers used and calculate fO_2 using QUILF, similar to Martin et al. (2008). Ruprecht and Plank (2013) use a Monte Carlo simulation incorporating the location of the initial step, variation of compositions for the value of the initial step and variation of points in the extracted profile to report the uncertainties on their timescales. They kept pressure, temperature and fO_2 constant. This brief summary of uncertainty reporting on diffusion timescales from just a handful of papers demonstrates the inconsistency and variability in approach that is currently used.

The uncertainties reported in this thesis account for the effects of temperature, D_0 and activation energy on diffusion timescales and were stated as log units at 1σ standard deviation. Temperature, D_0 and activation energy have the largest effects on diffusion timescales as discussed above. The upper and lower limits on the uncertainty were calculated by combining the ideal, maximum and minimum D values using each of the three parameters (T, ΔQ and D_0). Internal and external uncertainty (uncertainty on the thermometer and quantitative mapping combined (for Piton de la Fournaise (PdF) timescales only) were both incorporated into the uncertainty for the thermometry. The differences between (D_{ideal}) and (D_{slow}) and (D_{ideal}) and (D_{fast}) were calculated and the base log ($\log_{10}$) was taken of the ideal, maximum and minimum D values. These provide the upper and lower bounds of uncertainty on the timescales within this project per sample set (chapters 3, 4 and 6).

2.2.4.2. Diffusion Anisotropy

Profiles that are not corrected for orientation can lead to highly inaccurate timescales. As presented in Dohmen and Chakraborty (2007a and 2007b), diffusion does not occur at equal speeds along each of the crystallographic axes within olivine – diffusion is anisotropic. Fe-Mg diffusion in olivine is ~6 times faster along the c-axis [001], than along [100] or [010], the a- or b-axis (*Nakamura and Schmalzried, 1983; Costa et al., 2004; Dohmen and Chakraborty, 2007a and 2007b*). The modelling software corrects for diffusion along the a- or b-axis using equation 2.5, by inputting crystallographic orientation information (as described in section 2.2.5.3). If $D_c^{Fe\text{-}Mg}$, $D_a^{Fe\text{-}Mg}$ and $D_b^{Fe\text{-}Mg}$ (diffusion of Fe-Mg along the c-, a-, and b-axes) are known, the

diffusion coefficient along any traverse can be found using the following equation (*Philibert, 1991; Costa et al., 2004; Costa et al., 2008*);

$$D_{trav}^{Fe-Mg} = D_a^{Fe-Mg}(cos \propto)^2 + D_b^{Fe-Mg}(cos\beta)^2 + D_c^{Fe-Mg}(cos\gamma)^2$$

(equation 2.5)

$\propto, \beta$ and γ are the angles between the traverse and the a-, b- and c-axes respectively (*Costa and Morgan, 2004*). The value of this angle will control how much of a contribution the diffusivity along each axis has on the measured traverse. This expression is commonly used however AUTODIFF (the software used for modelling in this project discussed later) projects the orientation correction slightly differently.

Electron backscatter diffraction (EBSD) is used to measure the orientation of a crystal within a thin section, which allows the diffusion coefficient in the appropriate crystallographic direction to be calculated, depending on which traverses are extracted (*Costa et al., 2004; Costa et al., 2008*). To apply this correction to crystal traverses, the orientation of the crystallographic axes within the crystal are measured relative to a defined sample reference frame. The EBSD detector is an attachment within the Scanning Electron Microscope (SEM). An electron beam scans a pre-defined area on the sample (through the surface of the crystal slice). The electrons interact with the atoms in the crystal lattice and some of these electrons rebound back from the sample (*Maitland and Sitzman, 2007; Oxford Instruments, 2017*). The direction of these rebounding electrons varies and produces a pattern of *kikuchi bands* on a fluorescent phosphor screen. The appearance and symmetry of the pattern is defined by the crystal structure when the beam hits the sample (*Maitland and Sitzman, 2007; Oxford Instruments, 2017*). The orientation of the strongest *kikuchi band* is output to determine the orientation with respect to the microscope axes (*Maitland and Sitzman, 2007; Oxford Instruments, 2017*). The uncertainty of these measurements is displayed as the *mean angular deviation* (MAD). For this study, any results with MAD larger than 1° deviation were rejected. The orientation of the crystallographic c-axis and the orientation of the compositional traverse extracted across the diffused zone in the crystal were input

into the diffusion model to complete the orientation correction and modify the applied diffusion coefficient accordingly. If these orientations are not calculated accurately, timescales can be incorrect by up to a factor of 6 as described in Dohmen and Chakraborty (2007a and 2007b).

2.2.4.3. Shallow sectioning effects

For more accurate timescale retrieval, the best sections to study are those that go through the centre of a crystal and are also perpendicular to at least one crystal face (*Pearce, 1984*). Sections that are not perpendicular to the diffusion front lead to artificially longer diffusion profiles and therefore artificially longer timescales for the traverses extracted (*Costa et al., 2004; Costa et al., 2008; Costa and Morgan, 2010*).

This artificial lengthening adds to the uncertainty on the timescale – it introduces a stretch factor on to the traverses as seen in figure 2.5 (*Costa and Morgan, 2010*).

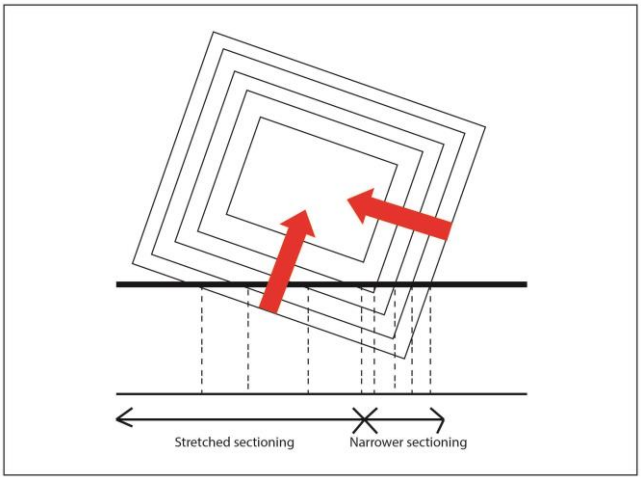

Figure 2.5: A schematic of a zoned crystal showing the effect of shallow sectioning on commonly measured diffusion profiles. The part of the crystal to the left is showing a stretch effect three times the true length ('stretched sectioning'). The part of the crystal to the right has also been stretched but to a lesser extent ('narrower sectioning'). The true diffusion direction is shown by the red arrows. Adapted from Costa and Morgan (2010).

If the crystal boundary is aligned perfectly vertical during sectioning, there is no artificial increase in the diffusion width, as the diffusion front is perpendicular to the crystal face, indicated by the red arrows on figure 2.5 (*Costa and Morgan, 2010*). The over-stretch can be corrected for using the following equation (*Costa and Morgan, 2010*);

$$\text{Measured traverse length} = \frac{\text{true traverse length}}{\cos\theta} \quad \text{(equation 2.6)}$$

Where the angle θ is the angle between the crystal boundary and vertical (*Costa and Morgan, 2010*), which can be measured using a Universal-Stage (further work on this is discussed in chapter 5). The shallower (larger) the angle between the crystal boundary and vertical, the longer stretch factor on the timescale. For a true corrected diffusion dataset, the angle between the crystal boundary and vertical needs to be measured and the stretch factor calculated for each profile. This shallow sectioning often affects one crystal edge within a section more than others. Correcting for shallow sectioning may reduce scatter amongst multiple timescales extracted from the same crystal section. AUTODIFF can correct for shallow sectioning effects if the angle from vertical is known. Methods to acquire this angle and a description of how this affects the timescales are discussed in the following sections. The correction AUTODIFF performs is described later in section 2.2.5.3.

What is a U-stage?

A U-stage is an optical microscope with a difference. It can be regarded as an elaborate crystal goniometer, meaning that optical and geometric features of crystals can be measured (*Kile, 2009*). It is a costly piece of apparatus, with very few in working condition in the research community.

Angular measurements in both horizontal and vertical planes are possible. The device consists of graduating concentric rings that can be tilted and rotated which in addition to folding, permit the quantification of the angular movement of multiple axes (*Kile, 2009*). U-stages have been developed with two, three, four or five axes. Kyle (2009) state that Berek (1924) named these axes sequentially from innermost to outermost i.e. A1 to A5 for a five-axis stage. Only three axes are essential; two inner axes A1 and A2 (the inner rotating graduated circle (vertical axis) and the inner horizontal tilting axis) and one outer tilting horizontal axis, A4, controlled by a large vertical drum on the right hand side (*Kile, 2009*). The angular movement of each axis can be quantified, by reading from the 360-degree scales on their rings or reading from the graduations on one of the Wright arcs (*Kile, 2009*).

Thin sections are mounted between glass hemispheres using hand sanitizer gel (in this case) as a mounting agent, as it does not leave a residue on the thin section. This

allows light to pass through the mineral unobstructed without deviation by reflection when the stage is tilted to high angles (*Kile, 2009*). U-stages can be difficult to operate and measurements tricky to take, from personal experience.

U-stage measurements

It is important to note what is actually being measured on the U-stage to extract the sectioning angle. Consider figure 2.6.

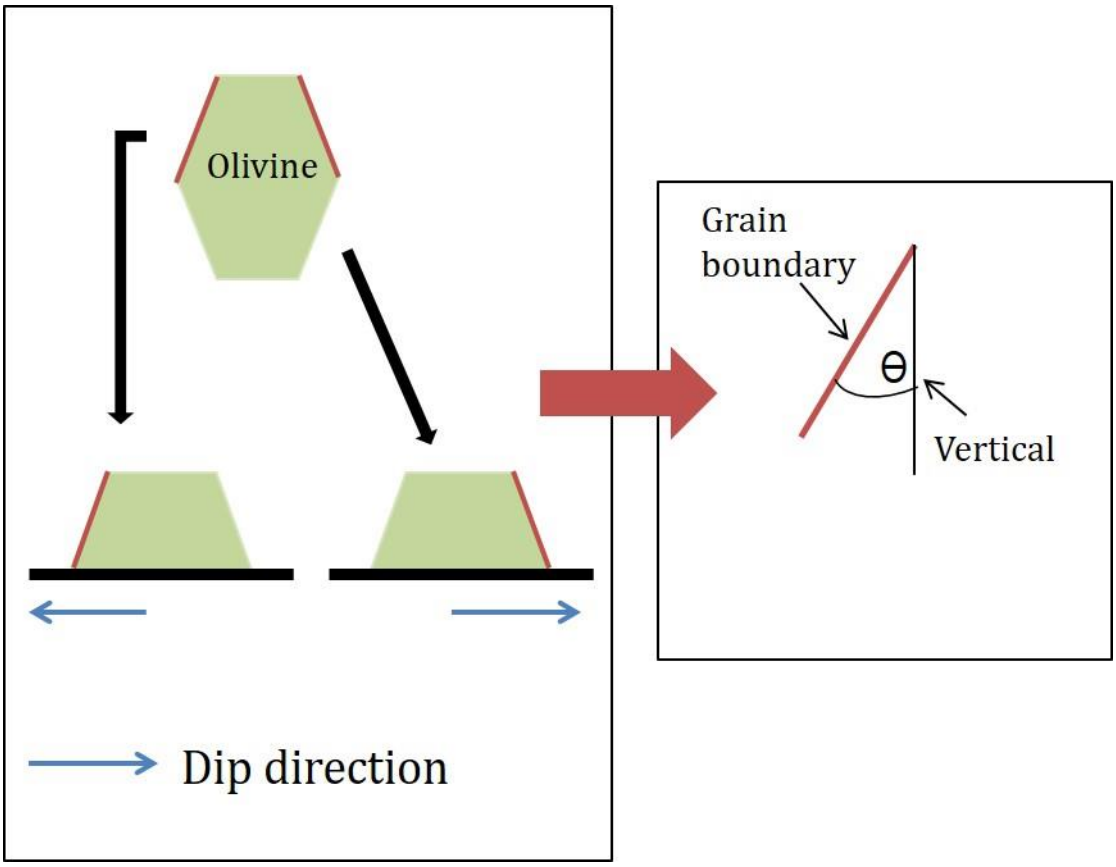

Figure 2.6: When an olivine is sliced at an oblique angle to the crystal boundary, the diffused zone appears 'stretched' (figure 2.5) and therefore wider than it actually is. The angle (θ) between the grain boundary and vertical (shown) can be measured with the U-stage to quantify the effects of shallow sectioning.

The U-stage is tilted until the crystal boundary is vertical and then the tilt (angle) is determined from the stage axes (*Costa and Morgan, 2010*). This measurement is called the hade (*as defined in the oxford english dictionary*). There are several basic optical rules to implement to decipher when the stage has been tilted so the crystal boundary is fully vertically inclined. They are as follows;

- The crystal boundary must be parallel to the rotation axis

- The cleavage can intersect the crystal boundary (where present) at 90°. These should appear as fine lines when vertically inclined.
- Birefringence should be constant from core to rim (apart from a slight difference at the iron rich rim) when the crystal boundary is vertically inclined (the birefringence is more constant where the olivine is of equal thickness).
- Use of the becke line. This is the bright band at the edge of the crystal that moves in to the material of highest refractive index when focusing. It is sharpest/most visible when looking straight down a vertically inclined crystal boundary. The becke line moves much faster, 'pulling' the colour of the olivine (in cross polars) in to the groundmass when the crystal boundary is perfectly aligned. Otherwise, its movement when focusing is quite slow.

The true distance of the diffused zone (not the stretched distance is) 'xcosΘ', where 'x' is the width of a stretched diffused zone and 'Θ' is the angle from vertical (*Costa and Morgan, 2010*). Once 'cosΘ' has been calculated, a stretch factor is retrieved. The stretch factor[2] is then applied to the timescale. The shift in timescale can be quantified as the section angle becomes larger (shallower). This correction assumes that the diffusivity doesn't change. However, as the sectioning angle gets bigger and bigger this becomes a problem as explained in chapter 2, figure 2.8.

2.2.4.4. Crystal Shape

Most diffusion work is done using 2D crystal sections within thin sections or grain mounts applying one-dimensional (1D) or two-dimensional (2D) models. These models do not account for the three-dimensional (3D) process of diffusion and give an over estimate of the true timescale (*Costa et al., 2008; Costa and Morgan, 2010,*). An analytical solution for 3D geometry can be used to model 1D or 2D profiles but the standard geometries used are typically cylinders or spheres (*Costa et al., 2008*). These do not match observed crystal morphologies. However, a 3D solution may not be required if the diffusion distance is short and across a planar face as this closely approximates a 1D system (figure 2.7) (*Costa et al., 2008*).

When considering real crystal morphologies, such as a polyhedral crystal shape, the diffusion problem becomes more complex. Polyhedral crystals typically have more faces that intersect at angles <180° (*Shea et al., 2015a*). Diffusion fronts advance

perpendicular to the crystal face, and so at these angles, the diffusion fronts will merge and can lead to the incorrect timescales being calculated if modelled in 1D (*Costa et al., 2008, Costa and Morgan, 2010, Shea et al., 2015a*). Ignoring diffusion fronts from more than one dimension can lead to 1D-modelled times being lengthened by a factor of 3-5 (depending on if the section is through the centre of the crystal, "on-centre") (*Costa et al., 2003; Costa and Chakraborty, 2004; Shea et al., 2015a*). Where the zones of interacting diffusion fronts will occur depends on morphology and aspect ratio of the crystal in question (*Shea et al., 2015a*).

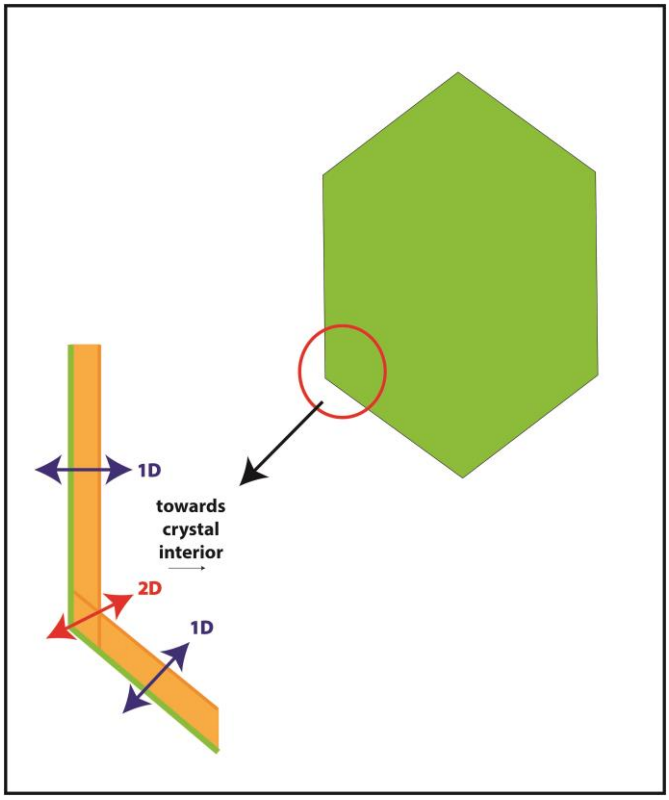

Figure 2.7: A schematic showing merging diffusion fronts at the corners of a zoned polyhedral olivine crystal (green). The blue arrows indicate where to take a profile and model in 1D. The red arrow indicates where two diffusion fronts merge, and 2D modelling is needed to get the correct timescale.

It is also important that traverses are extracted from sections that show a clear homogeneous plateau at the crystal core where possible, demonstrating that the initial condition is known (*Costa et al., 2008; Costa and Morgan, 2010; Shea et al., 2015a*). If a section is not taken through the middle of a crystal, "off-centre", and the traverse does not reach the core, there is potential for complex variability in timescale results from traverses taken within polyhedral shapes (*Shea et al., 2015a*). Aspect ratios will also affect how quickly the core plateau will be effected by diffusion e.g. the short axis of an elongate olivine will become more rapidly modified

potentially allowing the core composition to be effected more readily than if the crystal had the same volume, but was equant.

Out-of-plane diffusion can also considerably affect diffusion timescales. A diffusion front from a crystal face not preserved during sectioning may affect the profile being modelled (*Costa et al., 2008; Costa and Morgan, 2010*). This is difficult if not impossible to correct for. If scatter is prevalent amongst the timescales in a dataset it is worth considering if this is part of the cause.

2.2.5. Methodology

2.2.5.1. Sample preparation

Preparation of samples for this study varied depending on material type. Thin sections were made for lava flow samples from PdF and Mauna Loa. Rock samples were cut, ground to ~60 μm thickness and polished with a 3, 1 and ¼ μm diamond paste. Tephra from Mauna Loa was hand crushed. Olivine crystals were picked and mounted in grids within resin. These mounts were then ground and polished using the same methods as the thin sections. Both thin sections and grain mounts are carbon coated before analysis using a Quorum Q150TE 10V pulse rod carbon coating routine to generate a ~12 nm carbon coat, to eliminate the effects of charging.

2.2.5.2. Analytical techniques

Olivine locations within thin sections were mapped and high-resolution electron backscatter images were taken using the FEI Quanta 650 Field Emission Gun-Environmental Scanning Electron Microscope (SEM) at the University of Leeds. Compositional traverses from rim to core were measured on the JEOL JXA8230 Electron Microprobe (EPMA) also at the University of Leeds. The EPMA under normal conditions has precision and accuracy of ~1-2% (*Reed, 1997*). The length of the profile extracted is dependent on the width of the diffusion zone analysed – profiles were taken from the rim of the crystal through the diffused zone into the plateau within the core of the crystal. These profile lengths vary from tens to hundreds of micrometres, for PdF and Hawaiian olivines, respectively. Spot sizes of 5 μm were used at 5-10μm intervals (more widely spaced for profiles over 150 μm

in length) with the spot closest to the rim measured at least 5μm from the crystal edge. This distance was calculated as the optimum distance by calculating excitation volumes using a Monte Carlo simulation, to avoid problems from convolution and X-ray emission from the groundmass. Each profile contained at least 10-12 data points with 3-4 points within the curvature of the most diffused zone to ensure the best model fit.

The EPMA settings used for each sample set are reported in chapters 3, 4 and 6 before the compositional data is presented. Mineral standards obtained from the Smithsonian Institute, Washington D.C., were used to calibrate the EPMA (*Jarosewich, 2002*). San Carlos olivine was used as a primary and secondary standard for olivines. Repeat analyses of the San Carlos standard was used to estimate the precision of Fo measurements. Detection limits and assigned standards are reported throughout the appendices. Due to frequent intermittent EPMA breakdowns, faults, and spectrometer drift, the methodology was adapted for some of the Mauna Loa analyses, whereby the voltage was increased from 15kV to 20kV. The beam current was varied from 30-50nA. A focused beam was used to analyse minerals and a defocused beam was used to analyse volcanic glasses. Five wavelength dispersive spectrometers (WDS) were used for analysis with varying on peak count times. Due to problems with Si drift, Si was sometimes analysed by two spectrometers and so total on peak count times doubled for increased precision. Due to these EPMA problems, some analyses for PdF were carried out at the Open University on the CAMECA SX100 under standard probe conditions using similar standards. The Mg, Fe, Ni and Mn concentrations are used to calculate forsterite (Fo) values to enter in to the diffusion model as composition.

To retrieve high resolution pictures from the SEM, the spot size was set to 5 μm, with a 20 kV voltage, a 12 mm working distance was used and the aperture set to 1 in most cases. For good SEM image quality especially when using such images for quantitative analysis (discussed in chapter 5), it is important to consider the effects of many of these variables (aperture, spot size, brightness/contrast, magnification, working distance and voltage). The aperture limits the beam diameter which is essential to control spherical aberration (*Reed, 1996*). This is when the outer rays are focused more strongly (*Reed, 1996*). For high spatial resolution, a smaller aperture should be selected (smaller beam diameter). The spot size, is the size of the

beam on the surface of the sample. This can affect the resolution of the image and the number of electrons generated (*myscope*). The brightness and contrast of an image is a function of the mean atomic number of the material being analysed (Z) as the fraction of electrons in the beam that are backscattered strongly depends on Z (*Reed, 1996*). Magnification is equal to the ratio of the size of the image to that of the area scanned by the beam on the sample (*Reed, 1996*). The SEM has the ability to over zoom (*Reed, 1996*). The working distance is the distance from the point of focus on the sample to the end of the pole piece (*myscope*). A consistent working distance enables consistency between images taken. Finally, the voltage controls the acceleration of the electron beam to the sample. A higher accelerating voltage leads to greater penetration of the samples and larger interaction volume, which can reduce the spatial resolution (*myscope*).

2.2.5.3. Modelling

Two types of software have been used for this project. AUTODIFF has been used for the modelling of all timescales from PdF, Mauna Loa and Vatnaöldur datasets. AUTODIFF is built around shapes of diffusion curves calculated within FINDIF. FINDIF has been used to illustrate the textural relationship and timing between crystallization of the groundmass and the diffusion of the large olivine crystals within the PdF sample.

AUTODIFF is a 2-and-a-½-D diffusion modelling software (it does not correct for out-of-plane diffusion to give a full 3D model) coded in Microsoft Excel by D. Morgan, paper in prep. A high resolution SEM image is input into an image processing software *"Image J"* (*Schneider et al., 2012*) and a profile of greyscale values per pixel is extracted from the rim of the crystal to the core across the same region from which the EPMA data was extracted. Profiles are extracted parallel to the diffusion direction if extracted from an a- b or c- axis face and oblique to the diffusion direction if extracted from any other direction e.g. an [021] face. This gives a grey-scale value for each pixel along the traverse. There are far more pixels along these traverses (typically each pixel is less than 1μm in size) than there are EPMA spots giving a much higher spatial resolution if each pixel is converted to an individual compositional value.

Using the core and rim compositional values from the EPMA dataset as the minimum and maximum composition, each pixel grey-sale value can be converted to a composition. The grey-scale of the image is defined by the backscatter intensity of the material plus a constant. The zoning evident in the electron backscatter image indicated by the changing grey-scale values is demonstrably linked to the Mg/(Mg+Fe) by a strong linear correlation ($R^2 = 0.96$) within orthopyroxene (*Allan et al., 2013*). These methods were adapted and used for Mg/(Mg+Fe+Mn+Ni) calculation in olivines for this project, similar to Hartley et al. (2016). These profiles with converted grey-scale values of high spatial resolution are input into AUTODIFF to model a best-fit timescale.

The functionality of AUTODIFF is described in Allan et al. (2013) and Hartley et al. (2016), yet the software itself is unpublished. AUTODIFF is built around diffusion curves generated within FINDIF (described later in this section). Dohmen and Chakraborty (*2007a and 2007b*) found that diffusion in olivine is composition-dependent and anisotropic, and so using a finite difference method, FINDIF can generate profiles obeying compositional-dependence in 1D. The more a grain shows contrast in composition the more a diffused profile will display asymmetry resulting in a different shape to the typical diffusion sigmoid (*Hartley et al., 2016*).

For a given set of boundary conditions e.g. temperature, oxygen fugacity, anisotropy, composition, all diffusion profiles are self-similar in time for composition dependence i.e. diffusion after 4 time units will be twice as wide as at 1 time unit but in all other aspects the curves are identical (*Allan et al., 2013; Hartley et al., 2016*). To bring all the curves in to congruency a simple stretch factor is applied (*Allan et al., 2013, Hartley et al., 2016*). For the measured diffusion profile if the boundary conditions are known, the correct diffusion shape can be matched from these simulated diffusion curves. To fit measured profiles with the appropriately shaped curve generated in FINDIF, the distance between the 20^{th} and 80^{th} percentile is calculated in the measured profile. This is scaled to the pre-modelled curve using the correct stretch factor depending on the relation of the measured profile to the crystallographic c-axis direction before overlaying them, setting the 50^{th} percentile of both curves to zero (*Allan et al 2013; Hartley et al., 2016*). The profiles fit at the mid-point of the distribution, rather than at the crystal edge. This is because a point that can repeatedly found on any profile is needed. It is more difficult to repeatedly

define the edge because it moves between different profiles – the edge value is often a free variable. The profile is stretched symmetrically to the rest of the profile around that point. The stretch factor is used to relate the model time to the diffusion time that elapsed within the sample it was measured from. The anisotropy factor can be extracted from AUTODIFF, which is often a useful way of comparing diffusion timescales from various crystal faces within the same crystal. This method is a rapid and repeatable procedure identifying and evaluating modelling difficulties quickly.

Measurements from the Universal-Stage can be incorporated in to the modelling when they have been measured (the strike of the crystal face and its dip from vertical). Without these measurements, the correct diffusion direction will not be used in the modelling (figure 2.8).

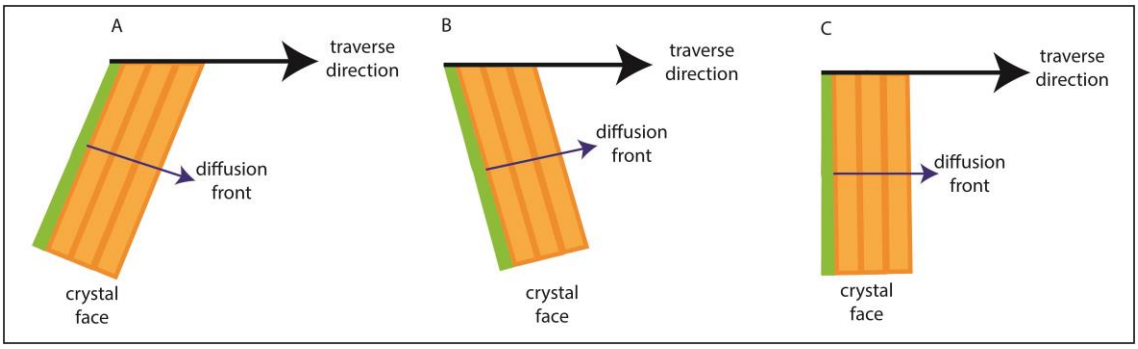

Figure 2.8: (a and b) schematic examples of shallowly sectioned crystal faces where the traverse direction is not parallel with the diffusion front leading to stretched diffusion widths and in correct timescale calculation (c) a non-dipping crystal face when sectioned where the traverse direction is parallel with the diffusion front.

AUTODIFF converts the c-axis direction, traverse direction, the dip of the crystal face and the strike of the crystal face into unit vectors. The fastest diffusion vector travels along the direction that meets the diffusion locus where the diffusion locus is parallel to the diffusion front. AUTODIFF uses a set of corrections (calculated from the EBSD and U-stage data) that calculates the true 3D fast diffusion vector (if there is a c-axis component in the direction of the extracted traverse) and projects the traverse onto that vector to solve for D. Examples of how to calculate a timescale using AUTODIFF is described in appendix D.

FINDIF is a 2D diffusion modelling software with the source code written in C++ programming language. The user interface consists of a terminal window to set up

a model run. Parameters are input within Microsoft Excel .csv files and image text files. This software was written by D. Morgan and is currently unpublished. The following describes how FINDIF can be used to model Mg-Fe inter-diffusion in olivine.

Maps are input as text files - areas of the crystal to be modelled defined by different grey scale values (0-255). Maps are created as overlays of small, cropped regions of SEM images along the edges of the diffused crystal boundary to be studied. The first input map defines the starting conditions, defining the area of olivine as black (0), the adjacent area of groundmass/melt as white (255), and any mineral inclusions/cracks/anything else that might block diffusion as grey (any value from 1-254). Only the melt (white) and the crystal (black) are open to diffusive exchange, all other boundaries are set as grey (thin regions around all edges but one of the olivine are defined as grey so diffusion occurs in one direction only). Different properties can be assigned to the grey-scale over time, one function of which can be used to simulate growth. This is described in detail in chapter 5. A 'mask' is the second map to be input. This is the same cropped SEM image from which the initial conditions map is built but the area around the edges of the olivine segment (the groundmass/melt/mineral inclusions) are masked as black. Put simply, once the model starts, the starting conditions map is 'diffused' until a best fit is produced to the 'mask'.

The parameters of the diffusion are controlled with a .csv file. There is an example .csv file on the enclosed CD. This contains all inputs and parameters. This includes information such as image width and height (for the starting conditions and mask), the grey-scale indices assigned (olivine = 0 etc.), crystallographic orientation, diffusion coefficients, composition and Mg number per pixel (calculated from the minimum and maximum greyscale values and composition values across the diffused zone). The .csv file also contains conditions files. More than one conditions file with different settings can be set per simulation to generate different conditions e.g. different temperatures as diffusion progresses. The conditions file contains information on temperature, the length scale of a pixel, the buffer grey-scale (in this case melt is white = 255), and run time of the model – time steps can also be defined so that progress files can be output as the diffusion progresses through the total model time.

Diffusion is simulated within FINDIF using a finite difference method. The number of elements, minerals, grains and number of conditions files are defined and then diffusion begins using the parameters and input files set by the .csv file. The diffusion space within FINDIF is defined as a square grid of equal spacing. The maximum grid size is 512 x512. Files are run at a much smaller size than this for efficiency. The c-axis direction is always north to keep a model convention. Across this grid, composition, the partition coefficient (K_d) for Fe (for olivine only), activity (composition/K_d), flux and diffusion coefficient are calculated for each time step and then applied across the diffusion space. 0.23 of the activity contrast is allowed to decay in the FINDIF 2D model due to numerical stability issues. Models are more accurate if a smaller amount of activity contrast is allowed to decay. The flux is controlled by the activity and by the local diffusivity. Upon completion of the simulation (when a best fit image has been modelled to match the original SEM image of the diffused area of the crystal (contained within the 'mask')), a score text file (score.txt) is output, as well as a difference image (diffimg.txt), and two new image files (dumpimg.txt and dumpcmp.txt). The score file compares the original SEM image to the new model image that FINDIF has produced, the better the match, the lower the score. The difference image shows the difference between the model image output and the original SEM image. The two new image files consist of a new model image that is the closest match to the original SEM image and a second that is a raw map of the composition with no conversions. A series of activity ("ares") and composition ("cres") maps for each time step are also output - the best fitting maps are defined in the score file.

An example of a FINDIF simulation is described in chapter 3, as applied to a portion of a PdF olivine crystal. An example of a FINDIF crystal growth and its changing boundary condition are described in chapter 5, also applied to PdF olivines.

2.3. X-Ray Microtomography (XMT)

2.3.1. Sample preparation and analytical techniques

A core through a piece of picritic lava flow from PdF was analysed using X-Ray Microtomography (XMT) as part of this project to analyse the 3D shape of the crystals (chapter 3). The rock was cored using a hollow drill-bit 6cm in length and 1cm in diameter in the University of Leeds workshop. The core was analysed using

helical scanning by Matthew Pankhurst and Sara Nonni at the Harwell campus of the University of Manchester using the Nikon XTH225 STX-ray Microtomography (XMT) system. Methods are described in Pankhurst et al. (2014), although this study uses rock core instead of tephra fragments. XMT methods applied to the geosciences are reviewed in more detail by Cnudde and Boone (2013).

Once the rock core was scanned, the resulting stacked images were processed with the aim of segmenting the large olivine crystals (up to 4 mm in size, used for diffusion studies in chapter 3) from the surrounding groundmass composed of smaller olivines, plagioclase, clinopyroxene, and oxides.

2.3.2. Segmentation of olivine crystals

The olivine crystals were segmented from the surrounding groundmass using a workflow put together with the advice and assistance of Matthew Pankhurst. The detailed workflow is described in Appendix E

Within this workflow, several segmentation methods were tested to see which arrived at the best result, retaining as much of the true shape and aspect ratio of the olivine as possible. The stacked images show density contrasts mapped in 3D between the mineral phases present. Different mineral phases can be identified by different greyscale values, depending on the mineral compositions. Due to the presence of groundmass olivines surrounding the larger olivine crystals to be segmented, preserving the true shape and volume of the segmented crystals was difficult. These large olivine crystals were isolated from the surrounding groundmass following the workflow established in "FIJI" image processing software (*Schindelin et al., 2012*). Once segmented, volume rendering was completed using "Avizo". The three segmentation methods that were tested to see which performed the best are "trainable weka", "watershed" and "K-means clustering".

K-means clustering (*MacQueen, 1967)* partitions a data set into k-groups (clusters) (*Wagstaff et al., 2001).* For this dataset, the plugin performs pixel-based segmentation based on clusters discovered within the image. Initial cluster centres are selected and iteratively refined so that each pixel is assigned to its closest cluster centre. Each cluster centre is the mean of its constituent pixels (*Wagstaff et al., 2001*). When there is no further change in assignment of pixels to a cluster the

algorithm converges (*Wagstaff et al., 2001*). A cluster centre tolerance can be set so that if the centre of the clusters move less than a tolerance value between iterations the algorithm is assumed to have finally converged.

The watershed segmentation considers the input image as a topographic surface, with the brightness of each point representing its height (*Soille and Vincent, 1990*). This entire relief is flooded from its' source with dams or barriers placed where different sources meet (*Soille and Vincent, 1990*). The first image points reached are the lowest grey scale values until all image points are progressively reached until the highest value (*Soille and Vincent, 1990*). At a given minimum, all similar points constitute the catchment basin associated with that minimum (*Soille and Vincent, 1990*). The zones dividing adjacent catchment basins are the watersheds.

The trainable weka plugin combines machine learning algorithms with image processing. I assigned areas of interest (in this case, 'olivine' and 'not olivine') to two different 'classes' forming the training dataset. When the image is trained the features in the image are extracted and converted in to a set of vectors of float values (*Arganda-Carreras et al., 2017*). The classifier performing this training uses the "random forest" algorithm. An ensemble of decision trees (a forest) is grown, using random vectors that are generated from the examples in the training dataset (*Breiman, 2001; Hastie, Tibshirani and Freidman, 2008*). Each tree is grown from a random vector independent of other random vectors but with the same distribution (*Breiman, 2001; Hastie, Tibshirani and Freidman, 2008*). The random vectors govern the growth of each tree in the ensemble (*Breiman, 2001; Hastie, Tibshirani and Friedman, 2008*). This ensemble of trees (forest) then votes for the most popular class ('olivine or 'not olivine') (*Breiman, 2001; Hastie, Tibshirani and Friedman, 2008*) i.e. how many trees classify that selection as 'olivine' and how many trees classify that selection as 'not olivine'. The trees with the most "votes", ultimately classifies the selection.

Each of these segmentation methods are quite different and it is important to choose the one most appropriate for my dataset. After testing each segmentation method, the trainable weka segmentation was chosen to be applied across the dataset. Whilst each of the methods performed well on individual images slices, the whole image stack contains over 7,000 slices, and the final segmentation process is automated. Due to inconsistencies in the brightness/darkness contrasts of some of the images

within the stack, the k-means and watershed segmentation methods would need to be adjusted manually throughout the segmentation process and this would be too time intensive. The trainable weka segmentation methods coped much better with these inconsistencies.

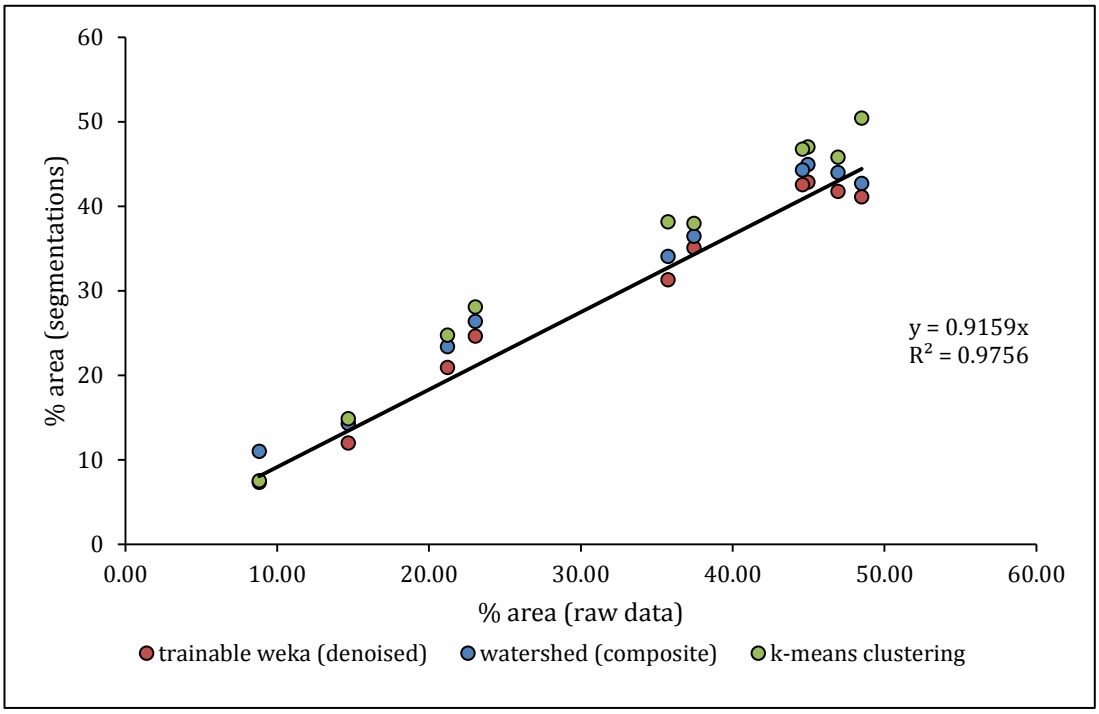

Figure 2.9: The percentage (%) area of an olivine calculated from raw, unsegmented XMT images compared against olivines segmented from these images using 'k-means cluster' segmentation methods (green), 'watershed' segmentation methods (blue) and 'trainable weka' segmentation methods (red). Each data point represents the % area of the olivine from one slice through the imaged olivine. There are ten data points each from one slice evenly spaced throughout the stack of images comprising the imaged olivine.

Thirty olivines to be segmented were cropped out of the 7,000+ image stack for processing. Figure 2.9 shows the segmentation results (% area of olivine within the image) for the three methods of segmentation as applied to one of the olivines (189 slices in height). These results are plotted against the % area of the raw, unsegmented slices of the same olivine. Ten slices at equal spacing through a 189 slice cropped-stack (containing this olivine) were extracted at the same position from each of the raw, trainable weka segmented, watershed segmented and k-means clustering segmented datasets. None of the methods give a perfect segmentation compared to the raw data however, the trainable weka and watershed segmentations perform better than the k-means clustering segmentation. The graph shows that there is a small systematic difference between the segmentation

methods (a much smaller difference exists between the watershed and trainable weka methods).

A difference of less than 10% between the raw, unsegmented data and the segmented images is considered workable for this study. Each of the segmentation methods show there is ~8-9% difference between the segmentations and the raw, unsegmented data, however, the trainable weka overall performs slight better (has a tighter fit to the 1: 1 line) and is more efficient in batch processing using FIJI image processing software (*Schindelin et al., 2012*). Considering the % difference of ~8-9% between the trainable weka segmented image and the raw, unsegmented image, if this olivine were artificially diffused to study how crystal shape and diffusion interact, a diffused profile length from that crystal edge towards the core may be ~100 μm. Therefore, ~8 μm of the profile would be gained or lost during extraction from the segmented crystal slice. Traverses taken from the EPMA are only resolvable to 5-10 μm so this difference of 8-9% between the segmented image and the raw, unsegmented image should not have an effect on the full profile length.

2.4. Crystal Size Distributions (CSDs)

Crystal size distributions (CSD) are the distribution of crystal sizes in three dimensions. Data from thin sections, slabs or outcrops are typically in two dimensions and converting this information into three dimensions is complex (*Higgins, 2000*). Whilst providing information on crystal shape, CSDs can also yield information about how rocks solidify (*Cashman and Marsh, 1988; Higgins, 2000*) and the conditions under which this occurs e.g. thermal history of a magma, its crystal growth rate and magma repose time (*Cashman, 1993*).

Cashman and Marsh adapted the 'CSD diagram' in 1988 for use in igneous systems which provided a method for recent CSD studies. The natural logarithm of the population density is plotted against crystal size (*Higgins, 2000*). An example of this is shown in figure 2.10.

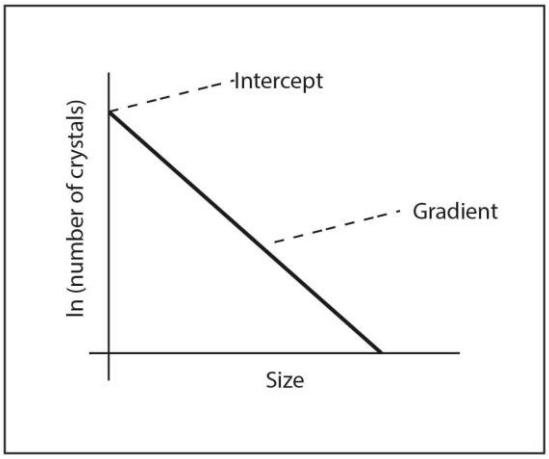

Figure 2.10: Adapted from Higgins (2000) and Cashman and Marsh (1988). Shown is a basic CSD diagram. Further points on the interpretation of this diagram are explained below.

This graph is described by equation 2.7 (*Cashman and Marsh, 1988*),

$$n = n^o \exp\left(-\frac{L}{Gt}\right) \qquad \text{(equation 2.7)}$$

The gradient is -1/Gt, which is a product of average crystal growth rate G (mm/s) and average crystal growth time, t (s) (*Cashman and Marsh, 1988*). Therefore Gt gives the mean crystal size (mm). The intercept on the y-axis is n^o, the nucleation density (J/G where J is the nucleation rate (mm^3/s^{-1})), (*Cashman and Marsh, 1988*). This represents how many nuclei there are per unit volume (*Cashman and Marsh, 1988; Vinet and Higgins, 2010*). n is the population density (mm^{-4}) and L is crystal size (mm) (*Cashman and Marsh, 1988; Vinet and Higgins, 2010*).

For igneous systems there are two end member possibilities, a steady-state open system and a closed batch model system (*Cashman and Marsh, 1988*). In the open system there is balance between the nucleation and growth of grains (input) and the loss or gain from other mechanisms e.g. mixing or fractionation (output) *(Marsh, 1998; Vinet and Higgins, 2010*). An idealised system may be a continuously tapped and refilled magma reservoir where these processes are occurring at the same rate (*Vinet and Higgins, 2010*). This would result in a straight CSD plot as shown above and as described by equation 2.7. A closed system, where there is no input or output of crystals, could also produce a straight CSD, with exponentially increasing nucleation rates and a constant growth rate. The volume proportion of magma crystallising would decrease over time (*Vinet and Higgins, 2010*). However, in nature typically a hybrid of these two end member types is often found, reflecting the

dynamic regime of the environment (*Vinet and Higgins, 2010*). The steady-state model can be relevantly applied to near-surface crystallisation and the closed system model to a deep seated cumulate body (*Vinet and Higgins, 2010*). The open, steady-state is most commonly assumed in natural case studies (*Marsh, 1998, summarised in Vinet and Higgins, 2010*).

Variations in pressure and temperature will change the driving force for crystallisation, the magnitude of which controls the rate of nucleation and growth (*Vinet and Higgins, 2010*). Any variation in the driving force will change the intercept and/or slope of the CSD diagram, allowing better interpretation of the environment of the nucleation and growth of crystals. Examples of the varied CSD diagrams that can be produced by these changes are illustrated below in figure 2.11.

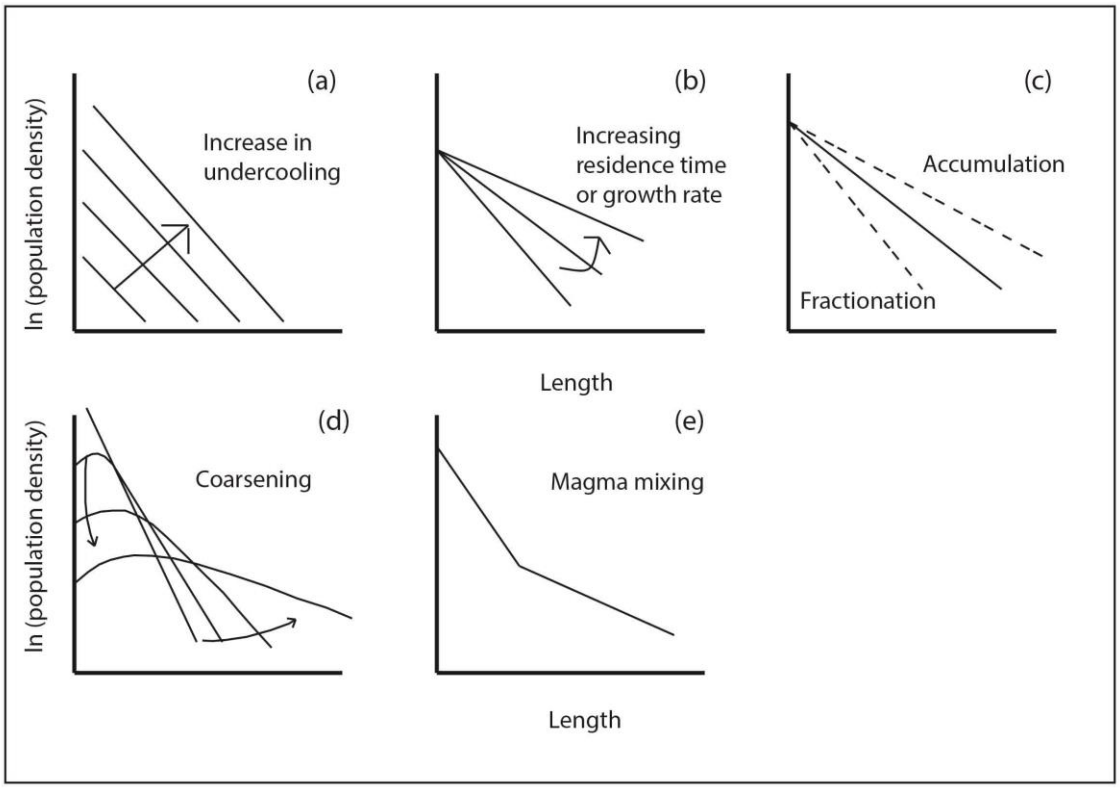

Figure 2.11: *Adapted from Vinet and Higgins (2010). A series of diagrams showing CSD results that can be used to infer various magmatic processes (a) indicates an increase in undercooling, of a single crystal population (b) indicates an increasing residence time or growth rate - an increase in residence time will favour an increase in larger crystals (c) indicates the accumulation or fractionation of crystals (d) indicates coarsening - due to crystal fractionation and settling event, the bigger crystals are missing. (e) magma mixing of two crystal populations or an 'excess' of large crystals due to a sudden change in growth behaviour.*

Figure 2.11 shows that a change in the intercept and/or slope of a CSD implies that different processes were occurring during solidification. These different plots infer

different textures e.g. a high intercept infers there are lots of smaller sized crystals in a rock, which can infer a magmatic process that brought about this rock texture.

2.4.1. Methods

Generally two parallel sections with a known spacing are taken through each crystal slice to be measured (*Higgins, 2000*). The lengths and widths can be defined in many ways e.g. maximum length or length normal to the minimum width. How they are defined is not as important as long as there is consistency (*Higgins, 2000*). Crystal slices from thin sections are commonly traced on to an overlay for measurement later (*Higgins, 2000; Vinet and Higgins, 2010*). This is often done using computer software such as "*Image J*". The minimum size that can be recognised and measured needs to be established (*Higgins, 2000*). Information on area, orientation and the length of major and minor axes of a best fit ellipse to crystal outlines are gathered (*Vinet and Higgins, 2010*). These major and minor axes measurements are input into *CSDslice*, an extensive database of crystal shapes based on crystal aspect ratios (short:long:intermediate) by Morgan and Jerram (2006) to determine the best fit 3D shape of the crystal from raw 2D measurements (*Vinet and Higgins, 2010*). The crystal aspect ratios are essential for the correct stereological conversion from 2D to true 3D size (*Morgan and Jerram, 2006*). This shape information, a defined 2D length measurement and the area of the thin section are then input into *CSDcorrections* (*Higgins, 2000*) and a crystal size distribution plot is calculated and 3D stereological correction are made retrieving a 3D data set (*Higgins, 2000*). This 3D population can then be used to determine the magmatic processes that shaped its own formation (*Morgan and Jerram, 2006*). Both of these programs currently use a reference cuboid for crystal shape and size distributions rather than a natural crystal shape.

An accurate estimate of the 3D crystal habit is key to the final stereological correction procedure (*Morgan and Jerram, 2006*). Investigations into 2D sections from 3D crystal habit showed that 'certain distributions of the short axis/long axis measurements can be recognised from random sectioning of a known 3D shape' (*Higgins, 1994*). This is shown in figure 2.12.

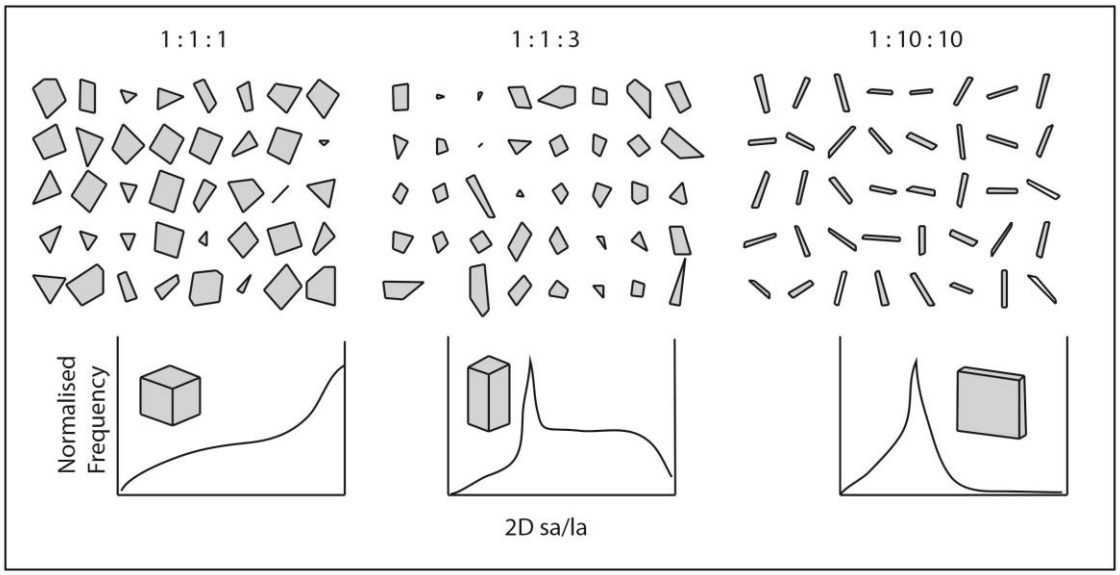

Figure 2.12: Adapted from Morgan and Jerram (2006). The schematics show random sectioning through known 3D shapes giving the resulting population curves. The normalized frequency is plotted against short axis: long axis ratios (sa/la). 2D data is used to estimate 3D shape of a crystal.

The frequency distribution of the area number density is calculated (*Higgins, 2000*). For this the data is binned based on various factors including the range in crystal sizes (*Higgins, 2000*). Higgins (2000) argues that more bins can introduce errors as there would be less crystals in each bin and a greater number of stereological correction cycles applied. However Morgan and Jerram (2006) argue that more bins are required in order to have enough points to define the CSD curve well, but have few enough bins to give a relatively smooth distribution, whilst not incurring any empty bins which will increase the uncertainty. The number of crystals in each bin is divided by the total area measured to give the number area density (*Higgins, 2000).* A CSD has been undertaken for each of the samples from PdF as discussed in chapter 3.

2.5. X-Ray Fluorescence Whole Rock Analysis (XRF)

The measurements for X-Ray Flourescence (XRF) whole rock analysis for the Mauna Loa samples (Hapaimamo and Moinui) were made by Origin Analytics in Welshpool. Approximately 10g of rock powders were crushed at the University of Leeds using an agate tema barrel.

At Origin Analytics samples were prepared as described below by Alex Finlay, one of their employees;

“Samples were prepared as fused disks using a Claisse M4 fusion instrument. 0.5000g ± 0.0005g of sample was combined with 7.5000g ± 0.0005g of flux (50:50 mix of LiT&LiB) and fused using the Claisse default program 3 before being poured into 32mm casting dishes. Analysis was undertaken using a 4KW Bruker S4 WD-XRF calibrated using 25 geological reference materials prepared in an identical manner to the samples. Drift was monitored using the Ausmon drift correction standard (XRF Scientific Ltd) and corrected within the instrument software. Loss on ignition was determined gravimetrically on a separate aliquot after heating to 1025°C”.

XRF analysis for the PdF sample was carried out by James Day of Scripps Institution of Oceanography as part of a different study. The results for the sample analysed are reported in chapter 3. The XRF analyses for the Mauna Loa samples are briefly discussed in chapter 4 and reported in Appendix G.

To summarise, a variety of methods have been discussed in this chapter. They have been used to analyse data in chapters 3, 4 and 5.

CHAPTER 3

Piton de la Fournaise, La Réunion

3.1. Introduction

Piton de la Fournaise (PdF) is located on the southeastern part of Reunion Island in the Indian Ocean 942km off the coast of Madagascar and is a highly active ocean island volcano (*Lenat et al., 2012*).

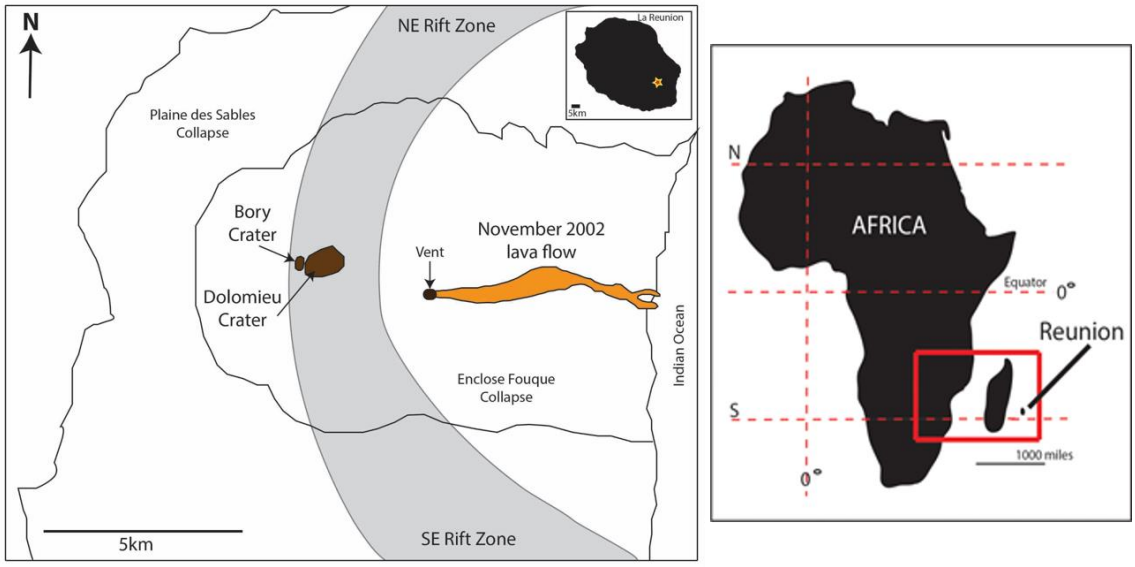

Figure 3.1: A *schematic map of PdF. This shows the central caldera and northeast and south east rift zones. The sample used for the diffusion studies came from the November 2002 lava flow (indicated). Adapted from Longpre et al. (2007) and Servadio et al. (2013).*

There have been multiple eruptions in nearly all decades since historical records began in 1640 (*Global Volcanism Program*). Recent eruptions have occurred in 1990, 1991, 1992, 1998-2010, and 2014-present. Activity is mainly confined to the central caldera – Enclos Fouque – containing summit craters Bory and Dolomieu – and from the northeast and southeast rift zones (*Lenat et al., 2012*).

For the purposes of this study, it is important to find a dataset with a simple magmatic history and apply the necessary geometrical corrections and diffusion parameters to retrieve a population of diffusion timescales. The population of timescales can be evaluated to determine how the geometries and crystal shapes interact with the diffused zone, so the current diffusion modelling methods can be

streamlined. Once refined using more complex datasets, it may become possible to apply the diffusion modelling technique to crystals rapidly, yielding results as soon as possible after the onset of eruption. An initial diffusion and CSD study has been carried out on lava flow samples to determine the nature of the crystal populations.

3.2. Sample Summary

Samples were collected in 2007 by James Day of Scripps Institution of Oceanography, California, mostly from road cuts or quarries within the Enclos Fouque caldera. The five samples collected for this study are shown on the location map and their field locations described in table 3.1.

Sample ID	Deg (S)	Deg (E)	Altitude (ft)	Place name	Age/ unit	Description
RU0701 (64217)	-21.13136	55.48424	223	Enclose	AD 2002 (PDLF4)	Oceanite
RU0705 (64219)	-21.16757	55.47719	402	Enclose	AD 2007 (PDLF4)	Oceanite
RU0706 (64220)	-21.16723	55.47092	707	Enclose	AD 2007 (PDLF 4)	Oceanite
RU0708 (64221)	-21.15303	55.42138	7374	Cratere Rivals	AD 1937 (PDLF 4)	Olivine-phyric basalt
RU0719 (64223)	-21.10078	55.48131	1263	Road D57	AD 1977 (PDLF 4)	Oceanite

Table 3.1: Summary of the field data for PdF

Other samples have been omitted from the study due to being heavily oxidised. This renders them unsuitable for diffusion studies, due to changes in the oxidation state of the iron and the effective destruction of the olivine. From here onwards I will refer to the samples as 64217, 64219, 64220, 64221 and 64223. All of the samples have been used for CSD study however only 64217 has been used for the detailed diffusion study.

3.3. Sample description

All of the samples are picrites or oceanites as defined below. The term oceanite – first introduced by Lacroix in 1923 (*Peltier et al., 2009; Lenat et al., 2012*), is defined in *Boivin and Bachelery,* (*2009*) as,

"*a melanocratic variety of picritic basalt made of numerous large crystals* (>20%) *of olivine and a lesser proportion of clinopyroxene, in a matrix enclosing microscopic crystals of augite, olivine, oxides and plagioclase*".

Only 64217 has been looked at in any detail for this study as preliminary work done by Peter Marshall, a MSc student, showed this sample containing large, zoned olivines probably represented a single crystal population. This type of sample is required to evaluate how the diffusion methods and parameters are applied to crystals. All petrological and textural descriptions will refer to this sample only. Further evidence for the single crystal population will be presented in this chapter.

3.3.1. Textural observations

Large 'euhedral' olivine crystals (figure 3.2 and 3.3A) (see section 3.4.2.5) up to 2-3 mm in size, are contained within a fine grained groundmass made up of clinopyroxene (19%), olivine (6%), plagioclase feldspar (35%) and spinel (3%). The groundmass crystals are up to 500 μm in size (figure 3.3 B and C) and are randomly orientated showing no apparent flow direction indicators, implying that the lava flow was stagnant when the groundmass started to crystallise. The lava flow is partly vesicular (13%). The modal abundance of the large, 'euhedral' olivines is ~25%. All modal abundances were calculated using the point counting function within the software '*JMicrovision*'.

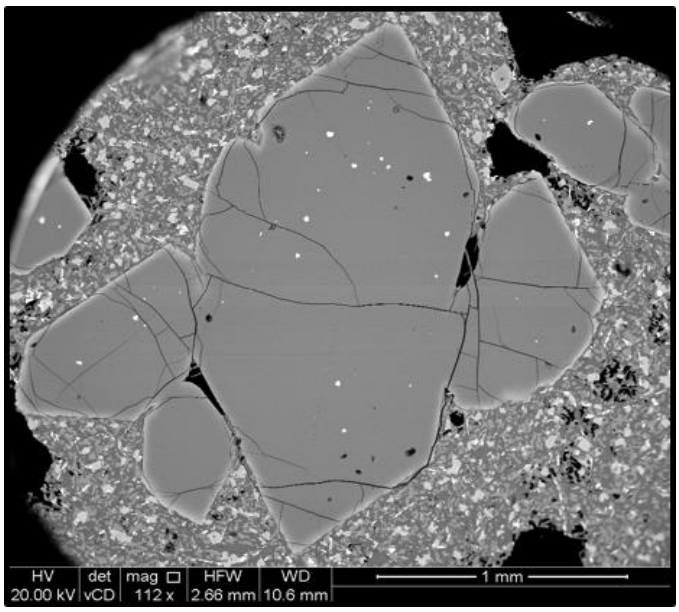

Figure 3.2: An SEM image showing the microlitic groundmass (containing plagioclase feldspar, clinopyroxene, olivine and oxides), vesicular texture and a cluster of large olivine crystals with distinctive edge zoning.

These large 'euhedral' crystals will be discussed in further detail in a later section. Note the term 'phenocryst' has not been assigned. This refers to a crystal that is significantly larger than its surrounding matrix and is in chemical equilibrium with its host magma. Nor has the term 'xenocryst' been used, which refers to a crystal which is not derived from the original/host magma (*Imperial College London, rock library*).

The origin of these large crystals has been subject to debate for many years. Villemant et al. (2009) and Albarede et al. (1997) argue that these crystals are xenocrystic, incorporated during magma ascent. By contrast, Welsch et al. (2012) state that they are not xenocrystic, with the olivines growing near the vicinity of the cold walls of the conduit or magma reservoir and being mobilised pre-eruption. Famin et al. (2009) also strongly argue that these crystals are cognate and are present due to crystal settling. These view-points are summarised by Lenat et al. (2012). They make no commitment to either argument. It is not clear what the glass/matrix MgO wt. % values are from the Albarede et al. (1997) study. Famin et al. (2009) report primary melt inclusion MgO wt. % values of 8.4-11.1 wt. %, which is considered high for a basaltic lava and correlates with his conclusions of non-xenocrystic origin for the large olivine grains but rather that they can be explained by fractional crystallization from the parent melt. Quantitative mapping (discussed

in section 3.4.2.2) of the groundmass in sample 64217 calculates MgO wt. % values of 4.94-6.47 MgO wt. % (+/-0.5 wt. %). This groundmass is low in MgO to crystallise the abundance and size of the large olivine crystals present in the lava (discussed in 3.3.3.).

In a study of olivine populations from the 1963-1965 eruption of Irazu volcano in Costa Rica, Ruprecht and Plank (2013) discuss that mantle xenocrysts typically show a narrow compositional range in major and trace elements due to their long residence times at high temperatures. The olivine cores are uniform in composition within the intermediate Fo range (Fo_{85-70}) and identify that mantle xenoliths are also typically coarse grained (>1000 μm) with anhedral crystals. Using these criteria, the Irazu olivines were judged to be phenocrysts. Ruprecht and Plank (2013) apply the same textural arguments to crustal xenocrysts that are derived from magmatic ultramafic cumulates. With this consideration, the criteria outlined above are consistent with what is seen in the PdF olivine population (olivine crystal are large, up to 3 mm, and have consistent core values of Fo_{84}) suggesting "xenocrystic" origin for the PdF population.

Some of the large grains exhibit embayments which may infer chemical disequilibrium (figure 3.3E and F). But olivine commonly grows with embayments and can be one of the mechanisms by which melt is trapped to form inclusions (*Faure and Schiano, 2005*). This is suggested by the presence of oxide grains at the tip of embayments (figure 3.3E) and may lead to the conclusion that these olivines are phenocrysts. However, the diffusion width around the embayments is inconsistent suggesting that although the embayment may have been pre-existing it was active with a combination of crystal growth and chemical disequilibrium occurring. Furthermore, the tip of the crystals shown are rounded not pointed which may be due to chemical or mechanical disequilibrium. The olivine rims are of similar composition to the groundmass olivine composition (~Fo_{65}) (figure 3.3c) and plotting of rim compositions on a simple Rhodes diagram (figure 4.9) shows compositions could be equilibrium but this may be expected if olivine loading has occurred. From this evidence I conclude these olivines are antecrystic, whereby they could have been derived from an earlier magma in the magma plumbing system and therefore have a common genetic heritage with the magma they have been found in

rather than having a completely different origin. It is a fair supposition that the crystals of olivine had to be accumulated.

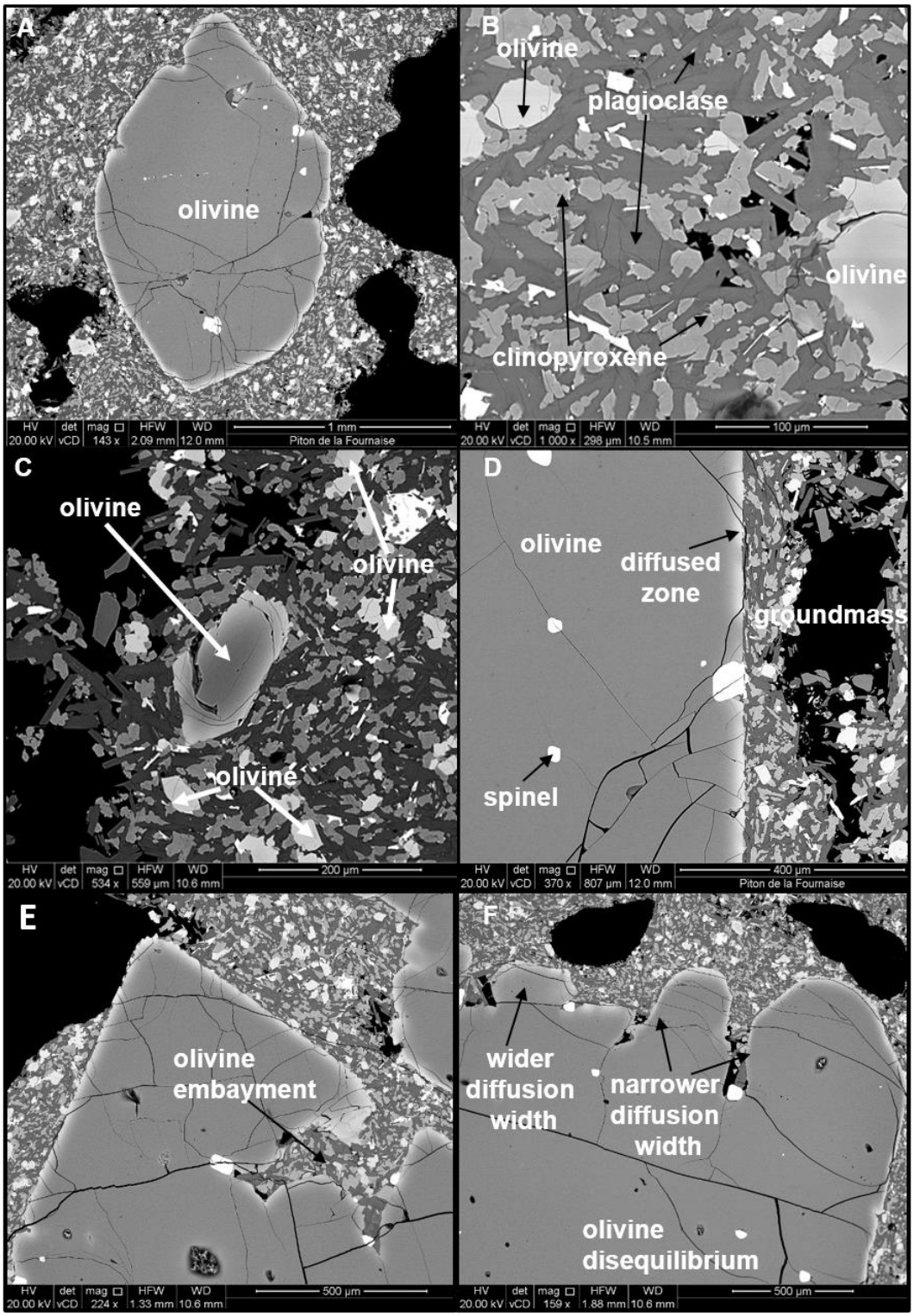

Figure 3.3: SEM backscatter images showing a range of textures within sample 64217 A) large, subhedral, antecrystic olivine surrounded by microlitic groundmass B) microlitic groundmass containing olivine, plagioclase, clinopyroxene and some oxides (Chromium-spinel or Titano-magnetite) C) smaller, phenocrystic olivine, also zoned, surrounded by the microlitic groundmass D) rim of a large antecrystic olivine crystal showing a diffused zone E) antecrystic olivine with large embayment F) antecrystic olivine displaying disequilibrium texture.

The antecrysts exhibit a thin diffusion rim around the edge of the grain, ~80 μm thick (figure 3.3D). The diffusion rim is due to Mg-Fe inter-diffusion, between the olivine and the surrounding melt. They often contain mineral inclusions of small microlitic plagioclase grains or clinopyroxene grains around the edge. Figure 3.3 shows a collection of SEM images showing the large antecrystic olivines, microlitic groundmass, diffused edges and evidence of chemical disequilibrium of the antecrystic olivine.

3.3.2. XRF whole rock geochemistry

The table below shows the bulk-rock composition for sample 64217 measured using X-Ray fluorescence (XRF), as published by Peters et al. (2016). This was performed at Franklin and Marshall University using a PW 2404 PANalytical XRF vacuum spectrometer, following procedures outlined in Boyd and Mertzman (1987).

Major elements	**Oxide wt. %**	**Oxide wt. % (normalised to 100%)**
SiO_2	43.34	43.83
TiO_2	1.56	1.58
Al_2O_3	8.15	8.24
Fe_2O_3T	14.46	13.75
MnO	0.19	0.19
MgO	23.50	23.77
CaO	6.55	6.62
Na_2O	1.45	1.47
K_2O	0.37	0.37
P_2O_5	0.18	0.18
Total	99.75	100
FeO	11.23	11.36
Fe_2O_3	1.98	2

Table 3.2: *Bulk-rock composition data for sample 64217 acquired using XRF. CIPW norm calculated using online excel spreadsheets coded by Kurt Hollocher, Union College, NY. Normative minerals have been calculated as follows: plagioclase 27.20 wt. %, orthoclase 2.24 wt. %, diopside 13.54 wt. %, hypersthene 1.40 wt %, olivine 48.92 wt. %, ilmenite 3 wt. %, magnetite 2.90 wt. %, apatite 0.42 wt. %, zircon 0.02 wt., and chromite 0.36 wt. %.*

The compositional data from the table falls in the range for an ultra-mafic/basaltic (SiO_2 wt. % <45%-55%) rock with a high MgO wt. % content (of 23.50 wt. %) consistent with its identification as an oceanite (8-28 wt. % MgO, *Lacroix, 1936*). This high value for MgO wt. % is further evidence of olivine accumulation.

3.3.3. Mineralogy

Olivine

The sample contains ~25% modal abundance of olivine as large antecrysts up to 2-3 mm in size as well as phenocrysts from 40 μm-200 μm in size. Most of the larger antecrysts exhibit edge zoning with core values of Fo_{84}, similar to the findings of Albarede et al. (1997) and rim values of Fo_{65-75}. All of these olivines are normally-zoned (Mg-rich core and Fe-rich rim). There is no evidence of reverse or complex zoning, implying that these crystals have had a relatively simple magmatic history or the original zoning has been erased due to prolonged residence at higher temperatures (*Costa et al., 2008*). Few olivines contain melt inclusions and where melt inclusions are present, they are fully crystalline containing plagioclase, clinopyroxene and olivine (i.e. the primary melt has not been preserved). This post eruptive texture is not suitable for thermometry measurements (*Gaetani and Watson, 2000*). Some olivines contain inclusions of chromium-spinel, often several crystals are present per grain. Olivine crystals do not appear to be deformed or kinked, consistent with observations from Welsch et al. (2012).

Plagioclase

Only small plagioclase phenocrysts are present in the groundmass at ~35% modal abundance. These brick- or lath- shaped grains can be up to 50 μm in size. Some occur as small inclusions around the edge of the antecrystic olivines however the majority occur with clinopyroxene in the groundmass (figure 3.3 B and C). Importantly, the inclusions have grown against the rim of the antecrysts before the onset of diffusion. Chemical zoning within the plagioclase is not immediately obvious, with core values of ~An_{52-67}.

Clinopyroxene

Clinopyroxene is found in the groundmass as small phenocrysts at ~18% modal abundance. Crystals can be up to ~40 μm in size, with the magnesium number of

crystal cores and rims ~Mg_{72-80}. Crystals often show textures of some resorption at the edges and are often complexly zoned. This may be due to local scale magma mixing.

Figure 3.4: Complex zoning within microlitic clinopyroxene in the groundmass of sample 64217. The edges of these crystals also show evidence of resorption.

Oxides

The oxides in the groundmass are chromium-spinel (Cr number ~Cr_{55}) and titanomagnetite (Ulvospinel component ~57). The oxides are present in ~3% modal abundance. They are frequently included within olivine, ~10-50 µm in size and are larger in size where they appear in the groundmass rather than as inclusions.

3.4. Crystal Size Distributions (CSD)

Crystal size distribution (CSD) analysis has been applied to olivine crystals from 25 thin sections (5 per sample, for samples 64217-64223). Data from multiple thin section was combined for each sample to make the CSDs more valid. Typically the minimum number of crystals included is ~200 (*Mock and Jerram, 2005*). For this study, each thin section contains ~100-150 olivine crystals therefore 450-600 crystals were analysed per sample. Methods are described in chapter 2, section 2.4.

CSDs are a quantitative textural technique (*Cashman and Marsh, 1988*). They quantify the distribution of crystal sizes in three dimensions which can give information on how rocks solidify and the magmatic conditions under which this occurs e.g. magma mixing, fractionation, accumulation, coarsening or an increase in undercooling (*Vinet and Higgins, 2010*). Figures for these scenarios and the equation which describes them can be found in chapter 2, section 2.4. A change in intercept or slope of the plot – log frequency vs crystal size histogram - can tell us a lot about crystal populations and the conditions under which they were formed (*Cashman and Marsh, 1988*). Below is a crystal size distribution plot of all the PdF samples. Half of

the data for all the PdF CSDs were collected by Peter Marshall during his MGeol project and Julia Hill, on a Nuffield Placement.

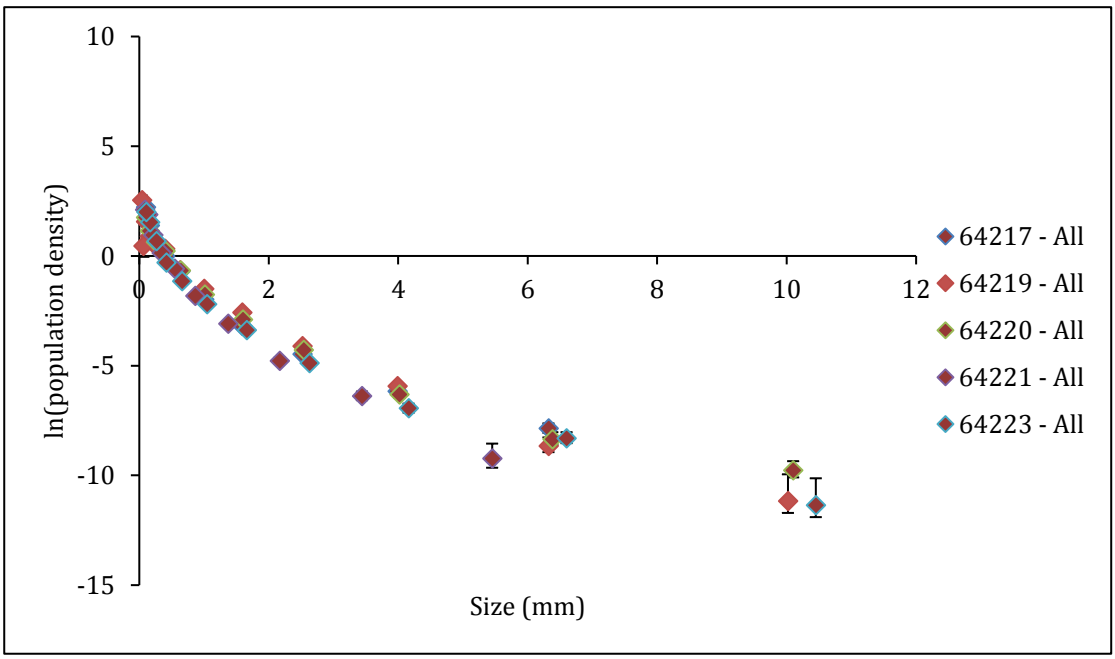

Figure 3.5: *CSD plot showing PdF CSD data for samples 64217, 64219, 64220, 64221, 64223. The CSD for each sample shows a curved distribution.*

The PdF dataset shows a broad curvature i.e. the profiles are not linear, showing that there was a continuous variation in the magmatic process that was occurring. The profile is slightly kinked which may be an indication of the presence of a variable amount of sub-0.5 mm crystals that are authigenic – they grew in-situ in the lava flow. Those over 0.5 mm are thought to be accumulated crystals. Each one of the PdF samples plot very closely to one another and there is little variation in terms of intercept on the y axis or shape of the curves. This suggests these populations are from the same source, potentially one nominal population. Alternatively, the kink could be an indication of some magma mixing occurring, such as the mixing of the antecrystic olivines into the residual magma. Magma mixing may give rise to compositional variability amongst the olivines. Only the larger olivines have been analysed for composition (showing consistent major element compositions) and examination of SEM images shows no difference in backscatter. There may be differences in trace element signatures however further analysis would be required.

3.5. Thermometry

A raster-matrix method was used to collect compositional data from the coarsely microcrystalline groundmass, known as '*Quantitative Mapping*' using the '*Probe for EPMA*' software, coded by Jonathan Donovan at *Probe Software. Inc. 2005-2016* and further processing carried out using '*Golden Software Surfer, LLC*'. This method scans a pre-defined grid /map over the groundmass that is user-defined, and applies a matrix correction on a pixel-by-pixel basis. This is more appropriate for each mineral phase and reduces the error on the elemental compositions. Four compositional maps of various elements (Mg, Fe, Ti, Si, K, Na, Ca, Cr, Mn, Ni, Al, P) have been taken from the groundmass of sample 64217. Examples are shown in figure 3.6. All MgO wt. % maps and totals maps can be found in Appendix A.

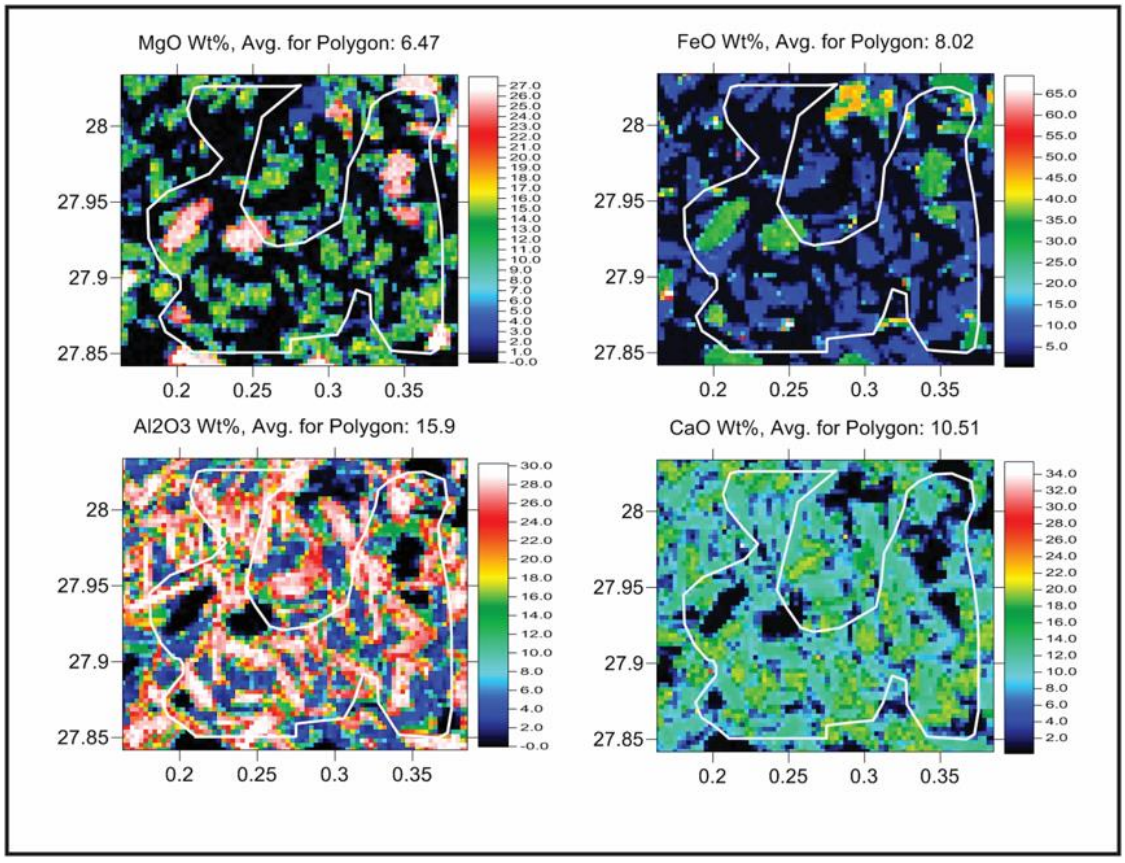

Figure 3.6: Example of 4 elemental quantitative maps, Mg, Fe, Al and Ca. The colour bar shows composition in elemental wt. %. Each pixel is defined by a colour depending on its composition for the measured element. The white line indicates the polygon used to calculate the compositions for each map. The x and y axes are arbitrary stage positions in mm's relative to a reference frame. The graphics are outputs from Golden Surfer software, LLC.

The Helz and Thornber (1987) liquid-only thermometer is used to calculate temperatures for input into the diffusion model (equation 3.1).

$$T(^{o}C) = 20.1\ (MgO\ wt\%) + 1014 \qquad (3.1)$$

This thermometer has been widely implemented to investigate the thermometry of Piton lavas in previous studies, e.g. *Famin et al.* (*2009*)*; Clague and Delinguer* (*1994*)*; Bureau et al.* (*1998*)*; Boivin and Bachelery* (*2009*). The internal uncertainty on the thermometer is ± 10°C (*Helz and Thornber, 1987*).

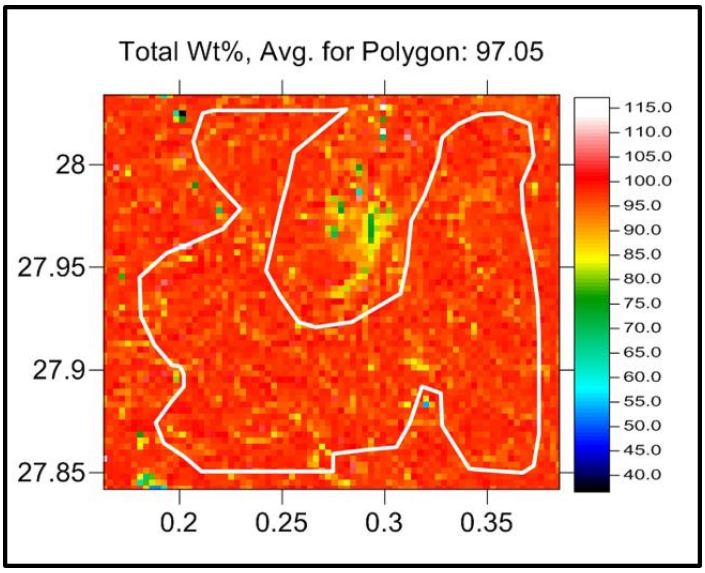

Figure 3.7: Quantitative map showing the totals for each measurement in wt. %. The white polygon shows the area quantified (as in figure 3.6). The polygon was defined so as to only include totals from 95-105 in the composition calculations for improved accuracy. The x and y axes are arbitrary stage positions in mm's relative to a reference frame.

Figure 3.7 shows the total wt. % per pixel and an average wt. % for the mapped area within the defined polygon (97%). Polygons were defined (figure 3.7) rather than using totals from pixels across the whole map in an effort to filter out bad analyses (green/blue pixels in figure 3.7). The average MgO wt. % for the groundmass from 4 maps with defined polygons is 4.94-6.47 (± 0.5 wt. %). This produces a temperature of ~1127 °C (± 10°C), which correlates with the thermometry from Boivin and Bachelery (2009). They calculated temperatures mostly within the range 1110-1150 °C (for various eruptions from 1977 to 1998) up to 1170 °C when directly measuring the flows with optical pyrometers and K-type thermocouples. Temperatures measured by the pyrometer are from the interior of the eruptive fissure, the outlet of the eruptive vent or directly on the active flow or through windows of a lava tube and are often slightly hotter (*Boivin and Bachelery, 2009*). Temperatures measured with a thermocouple come from accessible areas of the

flow often at a distance from a vent (*Boivin and Bachelery, 2009*). As the diffusion has been identified as late stage, the temperature of 1127 °C that has been calculated seems appropriate.

3.6. Oxygen fugacity (fO_2)

Due to the lack of Fe-Ti oxide couples, oxygen fugacity values were adjusted after consultation with various literatures. Work done by Rhodes and Vollinger (2005) states that the oxidation state of Hawaiian lavas generally lies at the QFM buffer (quartz-fayalite-magnetite). Hawaiian lavas are a similar composition to PdF lavas and are from a similar tectonic setting. They concluded that near-vent lavas and those that have been rapidly quenched are likely to be nearer the MW buffer (magnetite-wustite). Sample 64217 was sampled at 223ft (69m) (above sea level). A detailed study of the 2002 eruption by Longpre et al. (2007) observed that during the lava effusion phase, eruptive activity was rapidly focused at the main vent at 1540 m altitude. Therefore if my current sample was collected at 69m altitude (some distance from the vent) it may suffice to input oxygen fugacity into the modelling at the QFM buffer (Ni-NiO (NNO) +1) (*Huebner and Sato, 1970*). Olivine-plagioclase textures, as described in section 3.3.3 and 3.4.1 suggest the diffusion is post-eruptive, providing further supporting evidence for the use of this redox buffer in the diffusion model. This correlates well with the findings of Boivin and Bachelery (2009) who used direct measurement of intrinsic oxygen fugacity and olivine-liquid equilibrium on samples whose emission temperature is known. Values range from 3 log units below to 1 log unit above the NNO buffer.

3.7. Diffusion modelling

Back-scattered electron (BSE) images covering the traverse positions were retrieved using an FEI Quanta 650 FEG-ESEM Scanning Electron Microscope (SEM) to acquire compositional data with a better spatial resolution as described in chapter 2 section 2.2.5.2. Compositional traverses were retrieved using a JEOL JXA8230 Electron Microprobe (EPMA). Both facilities are at the University of Leeds Electron Optics facility. Some analyses were also done at the Open University, Milton Keynes using a CAMECA SX100 EPMA as outlined in chapter 2. The dataset was

collected over several different EPMA runs. Core and rim values were measured using a focused beam of 15- 20kV and a beam current of 30-50 nA. Peak counting times were as follows; 30-60s for Ni and Mn, 30-40s for Si, Fe, Al, and Mg and 20-30s for Cr. Most analyses returned totals of 98-101.1 wt. %. Repeat analysis of the San Carlos olivine standard were used to estimate the precision of Fo measurements. The Fo content of the San Carlos olivine was determined with a precision of 2σ = 0.07-0.14 mol. % (n=66). Primary standards and detection limits are reported in Appendix C.

A total of 105 traverses were modelled for Fe-Mg inter-diffusion using AUTODIFF (*Morgan, 2017, in prep*). This is a 2-dimensional diffusion modelling coded spreadsheet constructed in Microsoft Excel, described in chapter 2 section 2.2.5.3. The timescales produced are shown in table 1.2. These traverses were retrieved from across 30 olivine grains providing a statistically large dataset (in the context of published studies) with typically multiple profiles per crystal. Profiles were extracted on all available faces of a crystal or were taken along each diffusion 'direction' (relative to crystallographic orientations) within a crystal.

The uniform forsterite core compositions of the large antecrysts (Fo_{84-85}) together with the CSD dataset suggests they are only one olivine population. Once modelled, it might be expected that timescales should therefore converge to a single time. As these grains are thought to be antecrysts they do not represent processes in the deeper magma plumbing system but may tell us something about the shallow or surface transport system (consistent with formation of the relatively thin diffusion rim of 10s of microns) which may provide short magmatic timescales (days or weeks rather than years).

3.7.1. Timescales

Figure 3.8 shows an example diffusion profile from the PdF dataset. Whilst the profile in figure 3.8 is not a perfect fit, it is representative of the modelled profiles. The cause for the mismatch will be discussed later in this section.

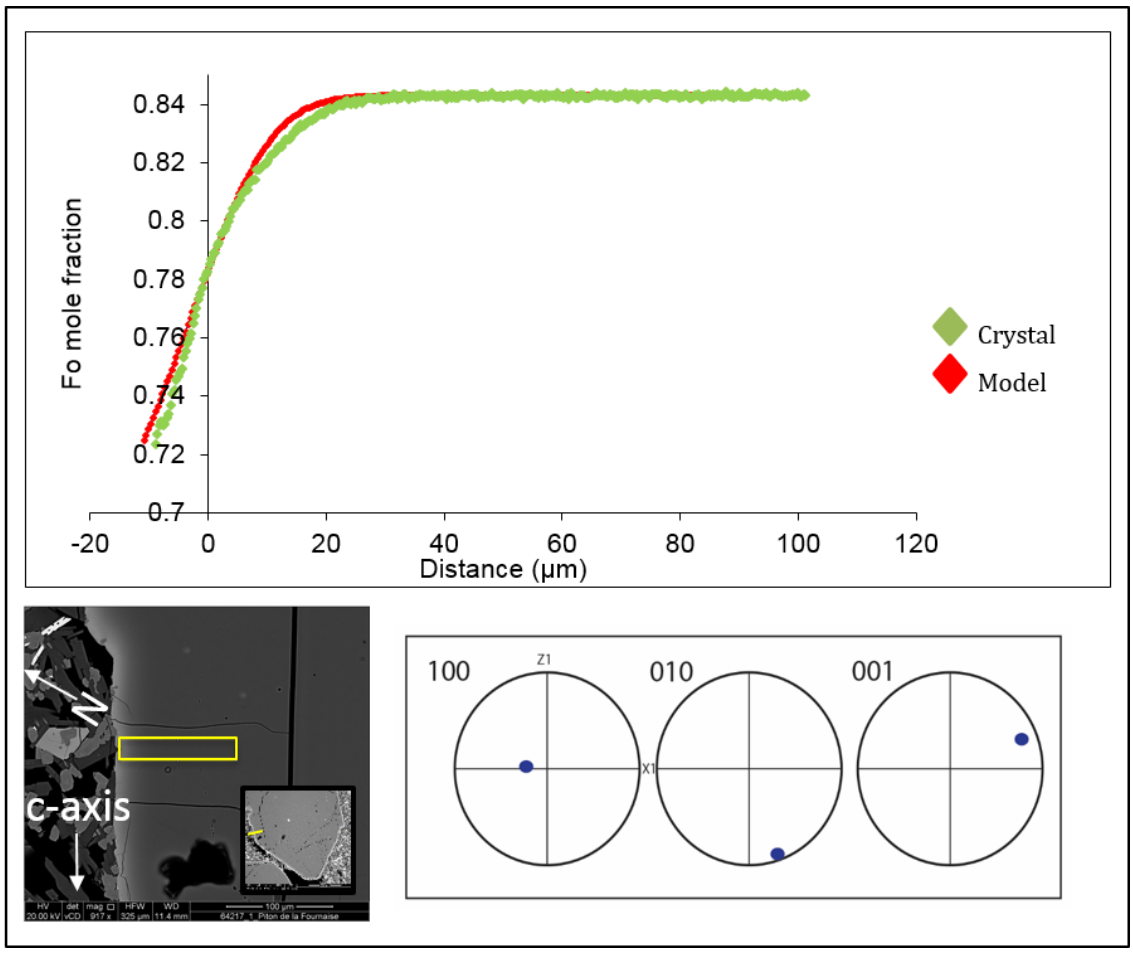

Figure 3.8: An *example of a model timescale from AUTODIFF (red) and a compositional profile (green) from crystal 64217-1_G_1. The SEM image (and inset image) shows where the profile was extracted. The pole figure displays the crystallographic orientation data processed in Aztec Channel 5 software by Oxford Instruments. The north arrow refers to the top of the EBSD reference frame. The c-axis arrow refers to the direction of the c-crystallographic axis.*

Crystal traverse	Timescale (days)
64217-1-A (1, 2, 3)	20, 24, 44
64217-1-B (1, 4)	11, 13
64217-1-D (2,3)	7, 35
64217-1-E (2)	18
64217-1-F (1, 2, 3)	19, 17, 45
64217-1-G (1, 2, 3, 4)	31, 15, 12, 20
64217-1-H (5, 6)	16, 12
64217-1-I (1, 2, 3)	7, 19, 12
64217-1-J (1)	18
64217-1-K (1, 2)	104 , 75
64217-2-A (1,2, 3, 4)	15, 20, 15, 14
64217-2-B (1, 2, 3, 4)	17, 14, 18, 12
64217-2-C (1, 2, 3, 4)	11, 13, 17, 15
64217-2-D (1, 2, 3, 4)	36, 21, 18, 18
64217-2-E (1, 2, 3, 4)	12, 18, 18, 21
64217-2-F (1, 2, 3)	25, 13, 12
64217-2-G (1, 2, 3, 4, 5, 6)	16, 27, 12, 17, 30, 14
64217-2-H (1, 2, 3, 4)	10, 28, 16, 38
64217-2-I (1, 2, 3, 4)	31, 17, 11, 15
64217-2-J (1, 2, 3, 4, 5)	22, 10, 8, 83, 22
64217-3-A (1, 2, 3, 4)	14, 23, 24, 18
64217-3-B (1, 2, 3, 4)	16, 13, 19, 12
64217-3-C (1, 2, 3, 4)	22, 14, 21, 17
64217-3-D (1, 2, 3, 4)	13, 18, 26, 39
64217-3-E (1, 2, 3, 4, 5)	14, 12, 10, 13, 11
64217-3-F (1, 2, 3, 5)	16, 16, 27, 13
64217-3-G (1, 2, 4)	14, 18, 11
64217-3-H (1, 2, 3)	62, 13, 19
64217-3-I (1, 2, 3, 4)	17, 17, 22, 11
64217-3-J (1, 2, 3, 4, 5)	14, 18, 10, 12, 14

Table 3.3: Timescales (days) extracted from each crystal traverse for sample 64217. These timescales are corrected for anisotropy. Red circles highlight crystals where anomalous timescales were calculated, likely due to simultaneous growth and changing boundary conditions whilst diffusion was ongoing, sectioning effects and/or out of plane diffusion. The average uncertainty on each calculated timescale is 0.38 log units (1σ).

The timescales range, in general, from 7 to 45 days across the whole dataset. There are one or two anomalies between 60-104 days. The average uncertainty on each calculated timescale is 0.38 log units (1σ). These longer timescales are not prevalent throughout the dataset, nor are they associated with a more varied forsterite composition at the core or rim of the crystals. They are not indicative of a second, older olivine population which is in agreement with the hypothesis (that this is a single olivine population). Timescales are corrected for anisotropy using electron

diffraction backscatter (EBSD) methods described in chapter 2, using "*Aztec Channel 5*" software by Oxford Instruments. These corrections were applied individually to each crystal traverse.

The timescales are indicative of late-stage diffusion and are interpreted to record initial cooling of the lava. The textural evidence for this very late-stage process is the relationship between the large olivine antecrysts and some of the surrounding plagioclase groundmass; some plagioclase grains have grown as mineral inclusions against the olivine grain. As the diffusion rim is narrow, the antecrysts may have been mobilised by the residual magma on transport through the conduit just prior to eruption. Post eruption, late-stage rim overgrowth and sustained high temperatures created the diffusive modification of the compositional zoning from the rim towards the core i.e. crystal boundary open to element exchange, from which the timescales have been retrieved. A simple lava flow cooling rate calculation for the PdF flow (at a thickness of 2-3 m) results in cooling rates of 9-19 days, which is in agreement with the diffusion timescales (7-45 days). Extensive modelling of late-stage growth of the PdF crystals is discussed in chapter 5 and it appears plausible from these results that late-stage overgrowth occurred.

Results from FINDIF (*Morgan, in prep*), as described in the chapter 2 section 2.2.5.3, confirm the textural evidence that plagioclase crystals have started to grow around the outside of the olivine grains before the olivine has started to diffuse.

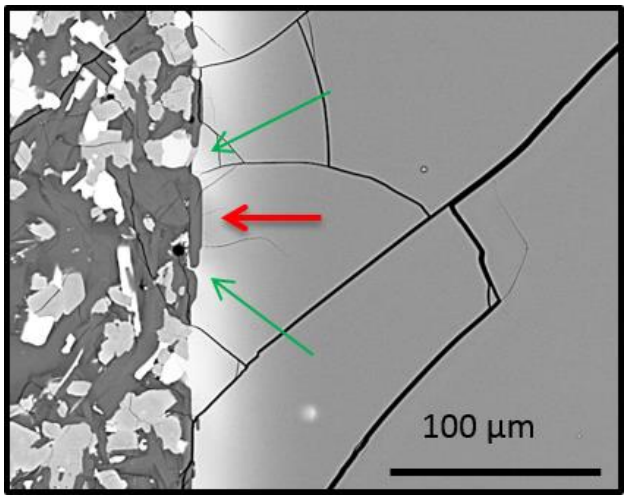

Figure 3.9: *an olivine-plagioclase boundary that appears to show some blockage to diffusion immediately along the long face of the plagioclase shown by the darker greyscale colour (red arrow). Diffusion proceeds around the ends of the plagioclase where the olivine is in direct contact with the 'melt' shown by the light greyscale colour (green arrows) A boundary closed to diffusive exchange between the plagioclase and the olivine appears to be present.*

Figure 3.9 shows that the presence of the plagioclase inclusions have partially blocked diffusion from rim to core. The results from FINDIF modelling simulating this condition are shown in figure 3.10.

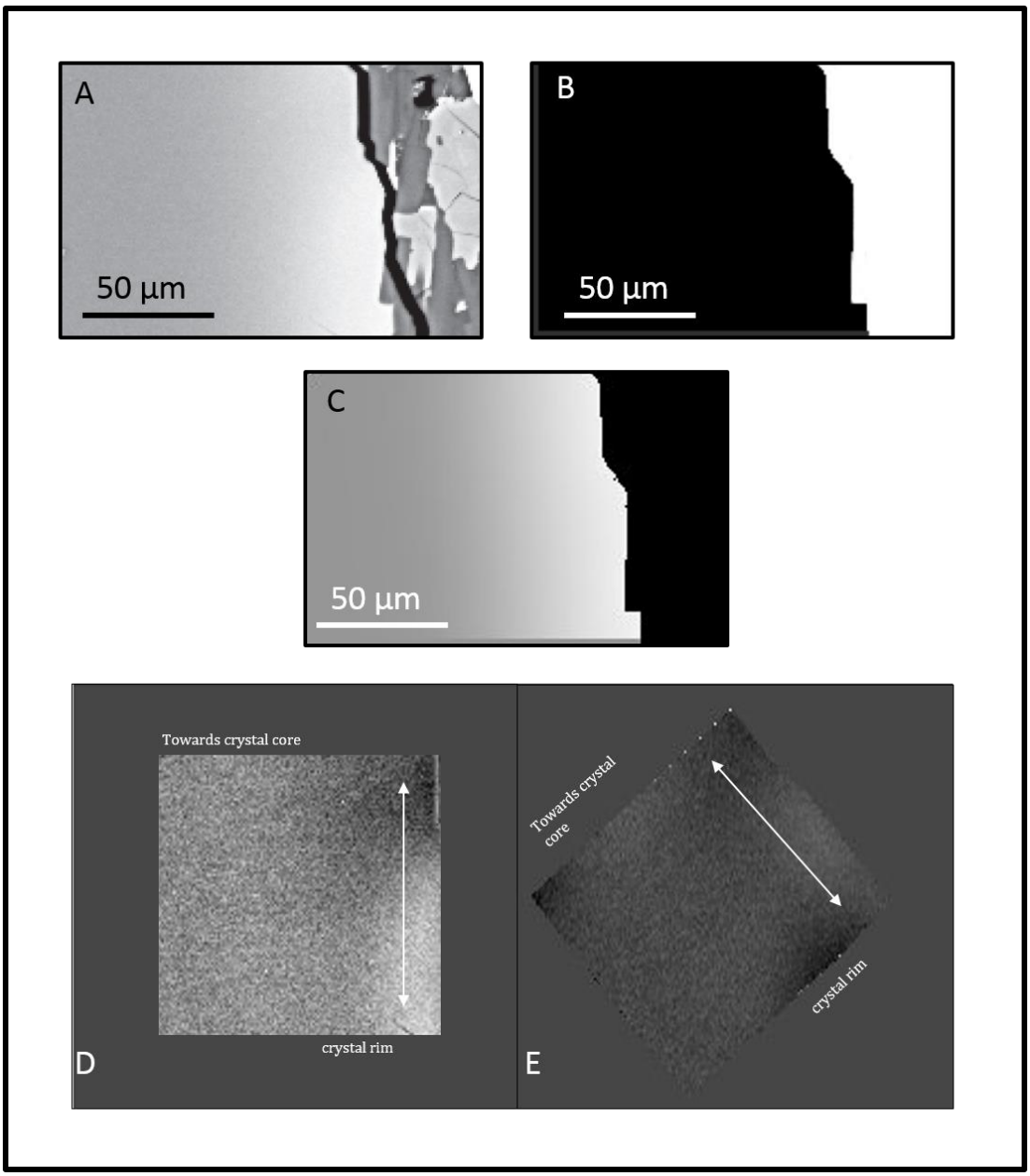

Figure 3.10: A) an original SEM image showing plagioclase along olivine rim B) initial conditions file for input into FINDIF. Black: olivine, white: groundmass/cracks, grey on the left and bottom edge: buffer C) FINDIF model output showing the closest match to the SEM image D) and E) 'difference images' comparing the grey scale values per pixel between the input SEM image (A) and the model output (C) along the boundary of the olivine segment. The white arrows indicates the position of the crystal rim. If there is a perfect match between the model output and the SEM image, the grey scale distribution in (D) and (E) would be uniform (D) is the result with the olivine crystal boundary modelled to be open to diffusion where plagioclase has grown against the rim of the olivine (E) is the result with the olivine crystal boundary modelled to be partly closed to diffusion where plagioclase has grown against the rim of the olivine. This simulation is also correctly orientated for crystallographic orientation of the olivine segment and the FINDIF diffusion grid.

Figure 3.10D shows the area of the olivine towards the core (less diffused) has a good match between the FINDIF output and the original SEM image – the pixel grey scale values are very uniform. The area at the rim of the olivine has a poor match

(indicated by the white arrow) with a stark contrast between pixel grey scale values at either end of the image almost from black to white. This simulation was run with a fully open boundary between the melt and the olivine, despite the presence of plagioclase crystals juxtaposed and partially included within the diffusion rim.

Figure 3.10E shows a much better fit between the original SEM image and the model output shown by the more uniform grey scale values within the core and vast improvement at the rim. This simulation was run with groundmass plagioclase crystals partially blocking diffusion towards the bottom section of the image but adjusted to simulate a slightly open boundary between the plagioclase inclusion and the olivine grain (figure 3.11).

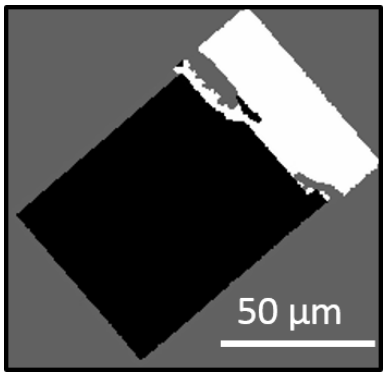

Figure 3.11: initial conditions file for diffusion within the olivine with a partially closed crystal boundary, due to the juxtaposition or inclusion of groundmass plagioclase crystals. Black: olivine, white: melt in open exchange with the olivine, grey: buffer – no diffusive exchange can take place. The grey sections within the melt are representative of the plagioclase barriers. Refer to figure 3.10 (A) for comparison to the original SEM image.

The FINDIF diffusion grid and c-axis direction of the crystal are also correctly aligned. Whilst the plagioclase inclusion is certainly acting as a block to diffusion, the vastly improved fit demonstrates that the grain boundary between the olivine and plagioclase block are indeed open for Mg-Fe exchange. The variation in grey scale still prevalent nearer the rim of the crystal (indicated by the white arrow) may also be due to other effects, e.g. diffusion front may be moving oblique to the crystal face, not normal to it, as is currently assumed.

3.7.2. Handling Uncertainties in Diffusion Models

There are many different potential sources of uncertainties as outlined in chapters 1 and 2, for example, sectioning angle, anisotropy, crystal shape uncertainty,

changing boundary conditions and crystal growth. If these uncertainties are not identified they can lead to large margins of error on the absolute timescales.

If each geometric correction and diffusion parameter has been applied correctly to the traverse extracted from the crystal, very little scatter between timescales from different faces of the same crystal (each with different crystallographic orientation, sectioning angle etc.) would be expected, and each traverse should correct to the same absolute timescale. There may be slight variation in timescale between olivine crystals of the same population but not a systematic difference, unless it was truly representative of magmatic processes.

3.7.2.1 Scatter amongst timescales

Figure 3.12 shows the range in timescales within each of the 30 crystals analysed, calculated with the 2D diffusion model and only an anisotropy correction applied.

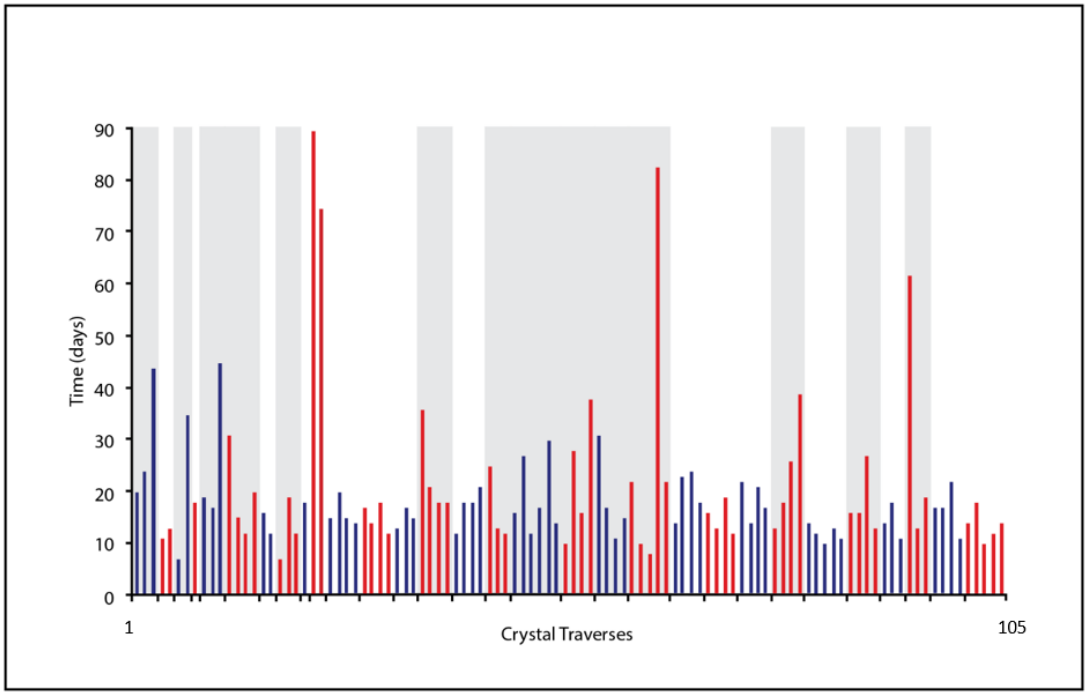

Figure 3.12: Scatter amongst timescales calculated with AUTODIFF (2D) within a single crystal. All timescales are corrected for anisotropy. The average uncertainty on each calculated timescale is 0.38 log units (1σ). The alternate colours mark the separation between crystals. There are 30 crystals in total. Crystals highlighted in grey show the largest amounts of scatter.

The diffusion timescales from all crystals measured appear broadly agreeable – they are on the scale of days-weeks rather than months-years. But there is some scatter

between timescales within the same crystal in many cases (highlighted in grey on figure 3.12) at most by up to a factor of 2 or 3, and between crystals themselves. This adds to the uncertainty and questions the reliability of the timescales and therefore the robustness of the interpretation of the magmatic process responsible.

Figure 3.13 shows examples of EBSD corrected timescales from two different crystals.

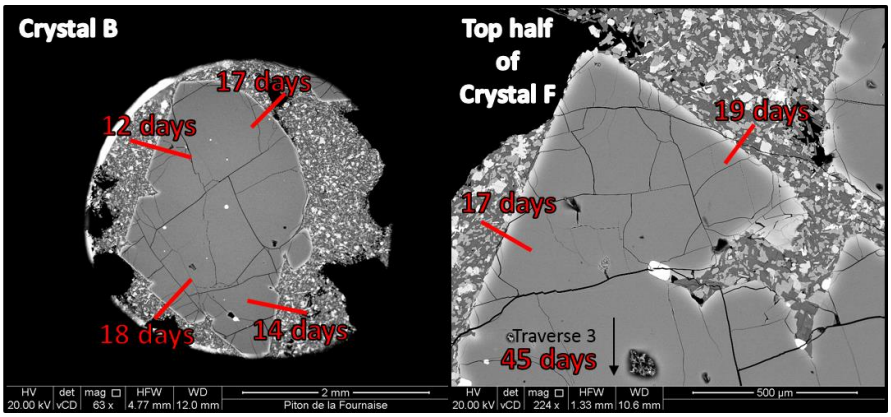

Figure 3.13: Two crystals from 64217. One showing very little scatter between timescales calculated (crystal B). The other shows much more scatter between timescales (crystal F) – two timescales are similar but a 3rd timescale is much longer than the previous two. Timescales are calculated using Autodiff (2D).

Whilst an anisotropy correction removes a large amount of scatter between timescales it is important to inspect the fit between the crystal traverse and model profile to understand what factors or processes could be responsible for the remaining scatter. Crystal B shows little scatter between the 4 timescales extracted, with a range from 12-18 days. Crystal F shows more scatter between the three timescales extracted, two are similar at 19 and 17 days, but the third is much longer at 45 days.

The population of timescales don't reduce to one single value between crystals as might be expected. This is due to the nature of the dataset. It is unlikely that the 'diffusion clock' in each crystal was set at the same time, and so they form a narrow continuum of timescales. As well as between crystals, there is also still scatter within crystals, as highlighted by those in figure 3.13. This is likely, due to sectioning effects (as described in section 3.4.2.1.b), crystal growth and changing boundary condition effects whilst diffusion was ongoing (as described in section 3.4.2.1.a) and out-of-plane diffusion. The latter is something that cannot be corrected for as the out-of-

plane diffusion can no longer be measured and so this scatter will prevail throughout the dataset between traverses of the same crystal. Shallow sectioning effects and crystal growth and changing boundary conditions are discussed below.

Crystal Growth and Changing Boundary Conditions

Below is a common example of such a fit within the PdF dataset. Figure 3.14 shows a poor model fit between the crystal traverse and the model profile near the rim of the crystal (A) and also nearer the core of the crystal before the flat plateau (B) – the main zone of diffusion. This portion of the curve contains the most information pertaining to the magmatic timescale and so any degree of misfit is therefore a potential cause of uncertainty.

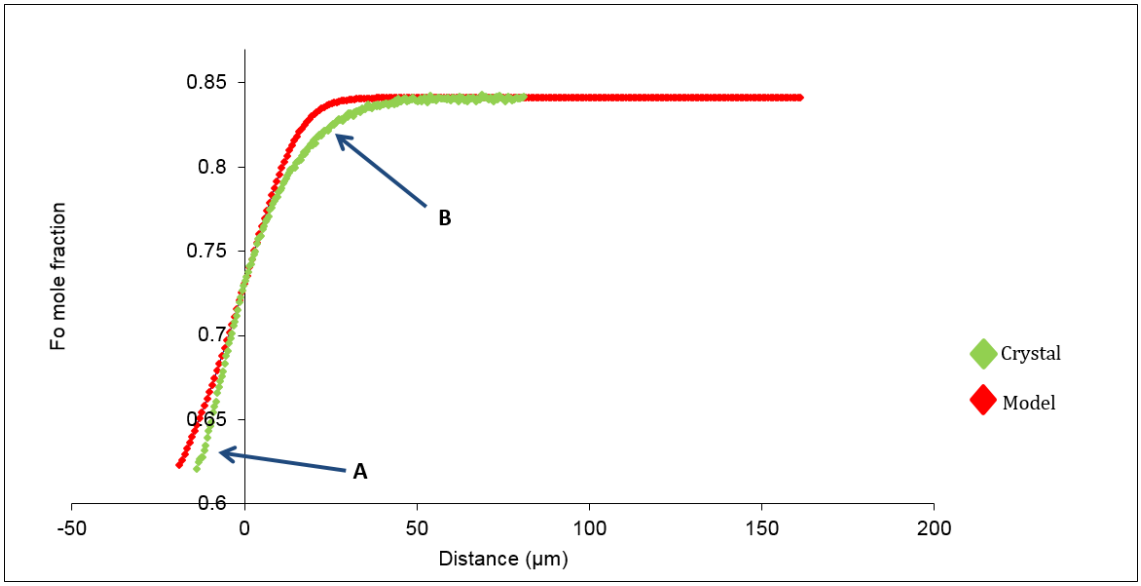

Figure 3.14: Example of a bad traverse to model fit for crystal traverse 64217_3_G4. The fit is poor at A and B, marked out by the arrows.

Interpreting the curve, shows that the data from the traverse is older than the model in the upper portion (B) and younger (steeper) than the model in the lower portion (A) (it is more 'diffused' than the model and from first glance 'should' have a longer timescale). Therefore the shape of the compositional data implies it is the result of a more complex history than diffusion alone – the profile is both older and younger than the model can calculate.

The lower portion (A) shows a slight kink at the rim edge. This occurs when "the growth rate is faster than diffusion" (*Costa et al., 2008*). Profiles affected by growth

will lead to an overestimate of the timescale retrieved (*Costa et al., 2008; Costa and Morgan, 2010*). If the crystal is growing as diffusion is occurring, extracting a profile through the growth and diffusion zone and modelling both zones as diffusion, artificially lengthens the length of the diffused zone and therefore artificially increases the diffusion timescale. The upper portion (B) shows different shaped curves between the traverse and the model. The data curve is much broader than the model curve. This is due to changing boundary conditions at the crystal edge as diffusion is progressing – the crystal boundary is open to chemical exchange with the liquid (*Costa and Morgan, 2010*).

The cause of changing boundary conditions in any particular case is unclear. Costa and Morgan (2010) state that fO_2, composition and temperature all play a role in changing boundary conditions. They outline two types of open boundary (i) concentration is constant with time e.g. the concentration and diffusion rate of the element of interest is significant within the volume of melt in which the crystal is sitting (*Costa et al., 2008*) or (ii) concentration at the boundary changes because of crystallization, mixing, the melt reservoir has limited volume or there are changes in temperature, fO_2 and the partition coefficients on the diffusive timescale (*Costa et al., 2008*).

In a study by Coogan et al. (2007), they attribute the partitioning of Ca between olivine and clinopyroxene as temperature dependent (*adapted from Dodson, 1986*). This partitioning behaviour of the element will create a changing boundary condition. Using the distribution of Ca between olivine and clinopyroxene, it was found that at higher temperatures more Ca is concentrated in the olivine than at lower temperatures.

Faak et al. (2013) also found temperature to be a key control on changing boundary conditions where the partitioning of Mg between plagioclase and clinopyroxene decreases with decreasing temperature. They also found that plagioclase composition plays some role with the partitioning of Mg between plagioclase and clinopyroxene, increasing with increasing X_{An} in the plagioclase. Although these studies focus on minor elements within their respective minerals concerning solid state diffusion, the processes may be analogous to the processes controlling the major element distribution in the PdF olivines.

Figure 3.15 shows examples of PdF profiles that have been affected by crystal growth and/or changing boundary conditions compared to a profile that is unaffected.

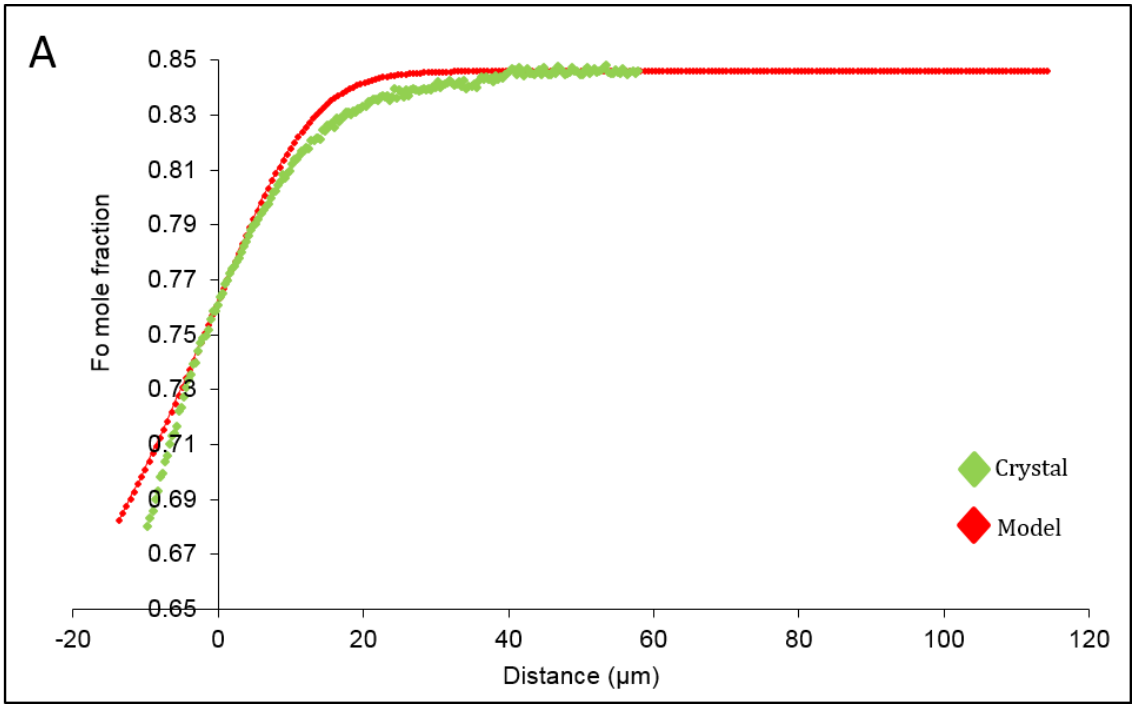

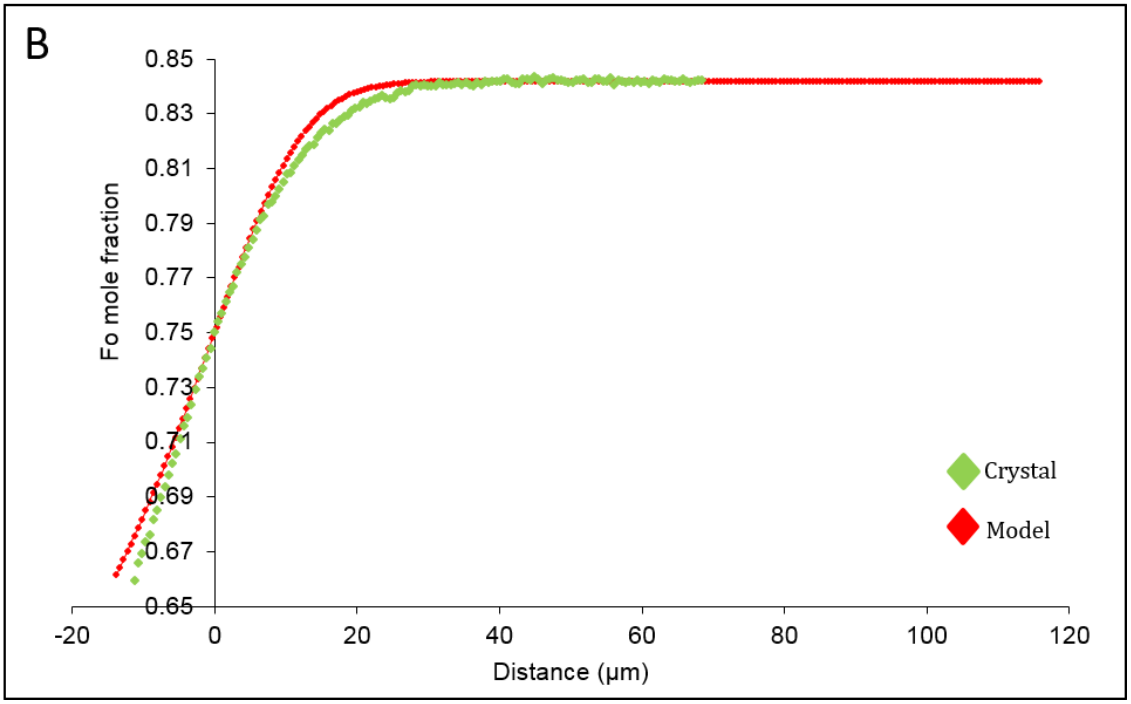

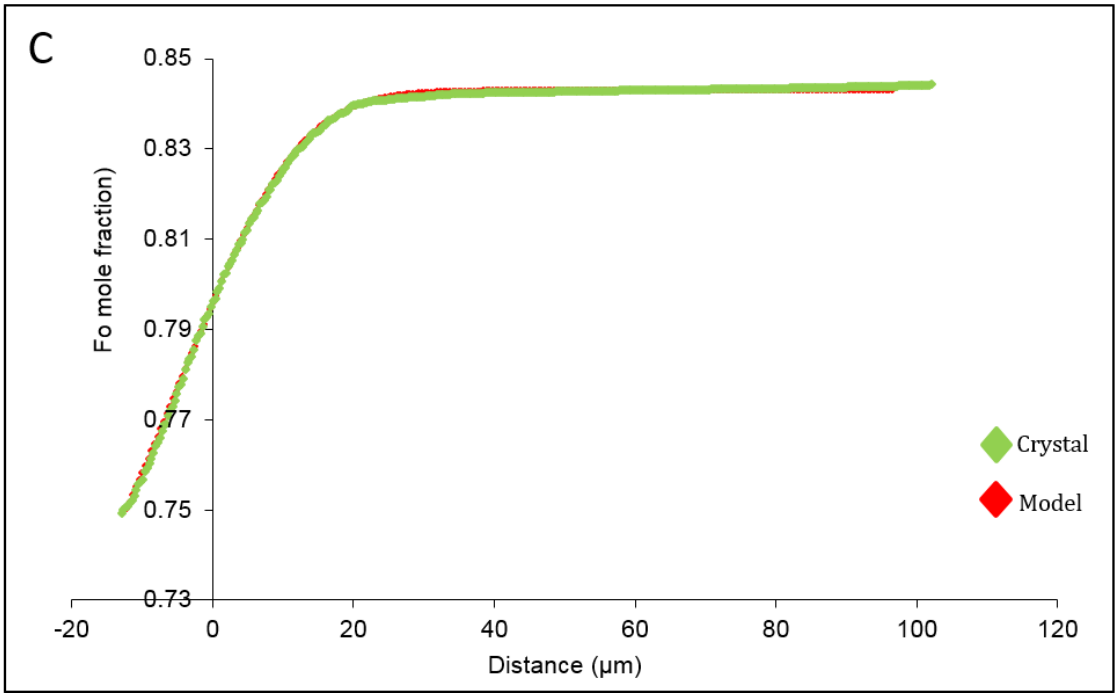

Figure 3.15: Compositional profiles and model fits from 3 crystals – 64217_3_D4, 64217_1_D3 and 64217_1_F3. (A) is an example of a profile substantially affected by simultaneous crystal growth and/or changing boundary conditions whilst diffusion was ongoing; there is significant mismatch both at the crystal rim and through the curved portion of the profile between the compositional profiles and the model fits. Fitting is also poor at the plateau (B) is an example of a profile that is affected to a lesser extent by simultaneous crystal growth and/or changing boundary conditions, showing less mismatch between the compositional profiles and the model fits both at the rim and through the curved portion of the profile (C) is an example of a profile that is not affected by simultaneous crystal growth and/or changing boundary conditions; the compositional profile is purely due to diffusion only showing a good fit between the compositional profile and model fit at the crystal rim and through the curved portion of the profile.

Referring to figure 3.15 showing examples of the grouping criteria, of the 105 crystal traverses collected from the PdF dataset, 32% (34 traverses) of traverses are substantially affected by the occurrence of growth and/or changing boundary conditions at the same time as diffusion (A). These had rim compositions with an average Fo of ~64 (~Fo 60-70). 39% (41 traverses) of traverses are affected to a lesser extent by growth and/or changing boundary conditions (B). These had rim compositions with an average Fo of ~68 (~Fo 63-73). 28% (29 traverses) of traverses represent purely diffusion (C). These had rim compositions with an average Fo of 72 (Fo~68-76). An initial, simple conclusion could be drawn from this that composition is playing a role in controlling the changing boundary conditions. The phenocrystic olivine in the groundmass have compositions ranging from Fo 58-66. These compositions are consistent with the rim compositions of olivines that have been affected in some way by growth and/or changing boundary conditions.

Olivines with compositions of ~Fo 75-85 would be expected to grow in equilibrium with the host liquid, calculated using a Rhodes diagram. It is hypothesised that the control on the changing composition is caused by changing temperature (as discussed earlier) perhaps as the lava flow cools. This is investigated further in chapter 5.

Further evidence for crystal growth within this dataset can be seen in figure 3.16.

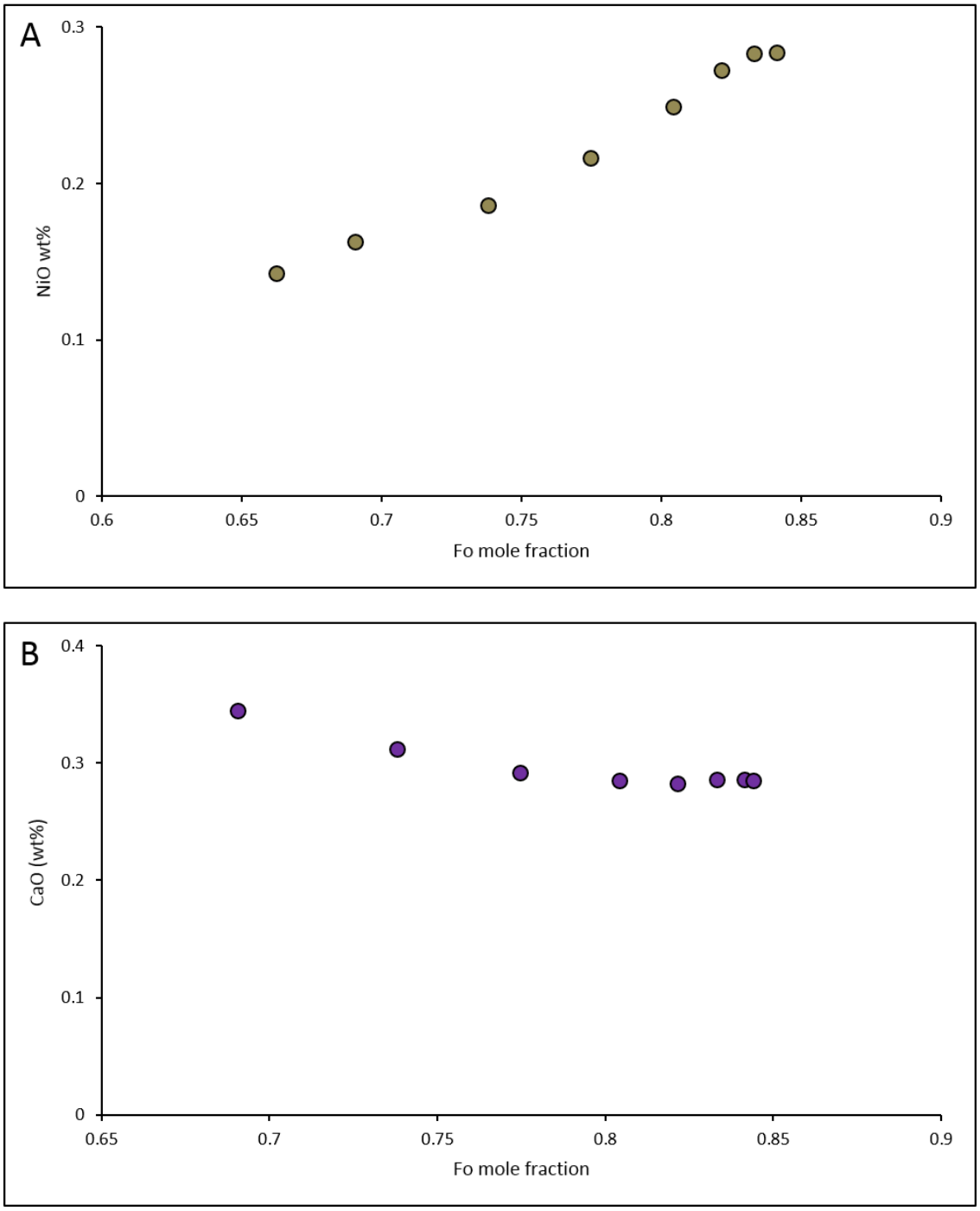

Figure 3.16: A) NiO wt. % v Fo mol. % and B) CaO wt. % v Fo mol. % to show effects of crystal growth (Traverse 64217_3_G2).

This minor element data was collected using the EPMA with similar settings to those described at the beginning of this chapter but on peak count times were higher for the minor elements (20s for Si, Mg and Fe and 120s for Cr, Mn, Ni, Na, Al, Ca). Most analyses returned totals of 97-100.4 wt. %. Repeat analysis of the San Carlos olivine standard were used to estimate the precision of Fo measurements. The Fo content of the San Carlos olivine was determined with a precision of $2\sigma = 0.08$ mol. % (n=24). This minor element data from an example traverse in figure 3.16 shows some crystal growth signatures. If the compositional profiles were controlled mainly by diffusion, Fo would have linear relationships with other elements (e.g. Ni) (*Costa et al., 2008*). However, these profiles show kinked relationships between the Fo and the Ni and the Ca. This is indicative that the diffusion has not erased the growth zoning and if these different profiles were modelled for diffusion, different times would be obtained for different elements which is indicative a significant component of growth zoning (*Costa et al., 2008*).

In total, 71% of the dataset shows some incorporation of crystal growth and/or changing boundary conditions while diffusion was ongoing. These crystal traverses are remodelled to incorporate these effects as diffusion occurs in chapter 5 using FINDIF – boundary conditions will be lowered towards the rim of the crystal for shorter time periods to simulate a lowering temperature to provide a better model match for the affected profiles. The implications of this will be quantified so that we know what effect these processes have on the diffusion timescales at a population level, as part of streamlining the diffusion modelling methods.

Sectioning angle

Another potential source of this scatter amongst diffusion timescales is the sectioning angle (*Costa and Morgan. 2010*). If a crystal face has been shallowly cut as part of the thin section making process, the diffused zone at the edge of the crystal will appear wider than it is or 'stretched' (*Costa and Morgan, 2010*). See chapter 2, figure 2.5.

If a traverse is taken from a shallowly sectioned crystal face and modelled, the timescale will be over-estimated producing a large anomaly compared to the true timescale, inducing scatter into the dataset. By measuring the angle of hade (between the crystal boundary and vertical) with a Universal-stage (U-Stage), the

timescales can be modelled with a correction for sectioning effects applied, as described in chapter 2, section 2.2.4.3.

Figure 3.13 shows two datasets - one relatively unaffected by shallow sectioning effects and a second affected by shallow sectioning effects. Both sets of timescales were corrected for sectioning effects by inputting the angles measured from the U-stage in to the diffusion model. With the correction for sectioning effects the new timescales for crystal B are 17, 14, 18 and 12 days to 16, 17, 16 and 11 days and the new timescales for crystal F, are from 10, 17 and 45 days to 18, 12 and 36 days. The sectioning effects for crystal F are larger than those for crystal B as measured from the U-stage.

It is noticeable that a couple of the timescales got slightly longer even though they were expected to get shorter. This is due to how the correction for sectioning effects is operated in AUTODIFF.

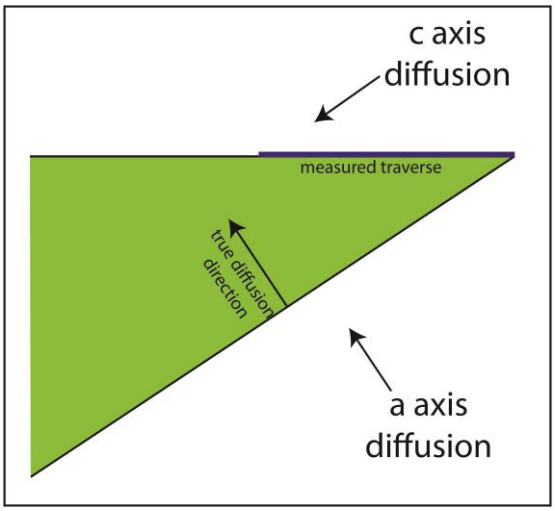

Figure 3.17: a schematic diagram illustrating how a profile would be measured with respect to the crystallographic axes of the olivine before the new sectioning effects correction is applied within AUTODIFF compared to the true profile that is calculated when the sectioning effects correction is applied within AUTODIFF.

Figure 3.17 indicates that the new timescales calculated with a correction for sectioning effects may increase slightly or decrease depending on how much the diffusivity shifts. The measured traverse with no correction for shallow sectioning appears to have a large c-axis component whereas the true diffusion direction (which is calculated with sectioning affects and re-orientated with respect to the true diffusion direction in 3D) has no c-axis component and so diffusivity will be lower resulting in longer timescales. A loss of c-axis component when the traverse is re-orientated can result in a slight increase in timescale.

3.7.2.2. Thermometry

The largest source of uncertainty on a population of timescales is temperature, discussed in chapter 2 (*Costa et al., 2008; Zhang 2010*). Diffusion is a temperature-controlled process. Together with the diffusion coefficient (of which temperature is a controlling parameter), they are the most important inputs into the diffusion model for accurate and reliable timescales (*Costa et al., 2004; Costa and Dungan, 2005; Costa et al., 2008; Costa and Morgan, 2010*). Primary melt inclusions (for olivine-liquid equilibrium thermometry) or matrix glass compositions are often used to estimate the temperature at the time of diffusion, depending on the position of the melt inclusion within the crystal and the extent of the diffusion width through the crystal. The traditional method to acquire EPMA data for thermometry from a melt inclusion is to defocus the beam over a wide area to hit a representative area of the glass. The compositional data is amalgamated to a single analysis through the EPMA software and a matrix correction is applied to produce an average composition (*Richard Walshaw, personal communications*). These values for the relevant elements that are used as inputs into the thermometer (these vary depending on which thermometer is being used) and a temperature (and its uncertainty) is calculated. A single temperature value is often input into diffusion models however, this is likely not a true representation of the thermal history when diffusion occurred, leading to large uncertainties.

Glass will not always be present in lava flows, unless there is the presence of a glassy rind at its edge or the flow has been rapidly quenched, unlike tephra or spatter (air-fall deposits) where glassy material is often prevalent. Due to the absence of glass in sample 64217 and the coarse microcrystalline nature of the groundmass, the quantitative mapping methodology was used to mimic beam defocusing for this study. Where possible, the beam defocusing method is preferable.

3.7.2.3. Crystallographic orientation

Electron backscatter diffraction (EBSD) is used to measure the crystallographic orientation of the traverse. Mg-Fe inter-diffusion in olivine is anisotropic, as discussed in chapter 2 section 2.2.4.2. EBSD errors are expressed as the “Mean Angular Deviation” (MAD) as calculated in Aztec Channel 5 software during analysis time. The MAD indicates the misfit between the measured and simulated *kikuchi*

bands (described in chapter 2 section 2.2.4.2). Maps with a MAD over 1° are rejected (the higher the MAD the larger the misfit).

Facilities with EBSD capabilities suitable for use with geological materials are scarce. The preparation, acquisition, and processing time of EBSD data has been identified as the most time-limiting correction to a streamlined workflow. A faster method is discussed in chapter 5.

3.7.2.4. Crystal shape

Shea et al. (2015a) performed a comparison between 1D, 2D and 3D modelling of timescales from slices based on a theoretical polyhedral olivine shape, a sphere, and a cuboid. They find that timescales can be wildly variable, due to merging element fluxes from multiple directions as discussed in chapter 2 section 2.2.4.4. The polyhedral shape typically has more faces meeting at <180°, promoting interaction of diffusion fronts, compared to a cuboid shape where faces meet at 90°. These findings were for along axis, on-centre slices. For on-centre slices taken at random orientations (most likely to be used for diffusion studies), time-frequency histograms displayed multimodal time distributions, that were dependent on the probability that transects are taken across a given set of faces. Cuboid-shaped crystals showed bimodal time distributions that correspond to the fast and slow diffusion directions when uncorrected for anisotropy. A well-defined third mode is present in the polyhedral crystal shape. This third peak may correspond to transects taken across prismatic faces e.g. [021], that are not present in the cuboid shape. Whilst this study by Shea et al. (2015a) is important, conclusions with respect to subtle differences between natural olivine morphologies and the absence/presence of various crystal faces and their effect on timescale need to be evaluated in more detail. Other factors and their effects on diffusion that need to be considered are euhedrality, arrangement (are grains of interest present as a single crystal or as an aggregate) and the size of the crystal.

Combining the morphological complexity of natural crystals with random sectioning during thin section preparation affects calculated timescales considerably (*Shea et al., 2015a*). The convergence of diffusion fronts from different crystal faces can result in a longer apparent concentration gradient and therefore an apparent longer timescale when modelled. These zones are typically found at crystal corners, shown

in figure 2.7, and are best avoided (*Shea et al., 2015a*). Recognizing a lack of euhedrality from the rounding of crystal faces is important to consider as rounding will enhance this effect. Rapid growth leads to complex e.g. skeletal or dendritic morphologies (*Faure et al., 2003; Welsch et al., 2012*) that will give rise to more of these regions of interacting diffusion fronts (*Shea et al., 2015a*).

In terms of crystal size effects, the polyhedral morphology often used for study (*Faure et al., 2007; Welsch et al., 2012; Shea et al., 2015a*) can have a variety of aspect ratios that will also influence the zones of interacting diffusion fronts (*Shea et al., 2015a*). The compositional plateau at the core (giving the initial condition) may not always be preserved in smaller crystals, which can lead to only partial retrieval of the correct timescale (*Costa et al., 2008; Costa and Morgan, 2010; Shea et al., 2015a*). Also, depending on whether a crystal aggregate grew as such, or came together by synneusis (the 'swimming together of crystals') (*Schwindinger and Anderson, 1989*), or paired nucleation, diffusion timescales may become affected by a change in boundary condition. Attachment of an olivine to another, may block the exchange of elements depending on whether diffusion occurred pre-, syn or post-attachment of a crystal/growth of an aggregate. These factors and processes can be assessed from the 3D PdF crystal dataset produced using X-Ray Microtomography (XMT).

Crystal Shape Evaluation

A core of picritic basalt from PdF sample 64217 containing more than 100 olivine grains was analysed using XMT. The large olivine crystals (antecrystic olivines) were digitally segmented from the microcrystalline groundmass (containing smaller olivines) using '*Image J (FIJI)*' and '*Aviso*' image processing software. The ~6cm long core was imaged using a Nikon XTH225 STX-ray Microtomography (XMT) system at the University of Manchester (Harwell Campus). A more detailed methodology of XMT settings and the segmentation workflow post-imaging can be found in chapter 2 and Appendix E. Thirty large olivine crystals were digitally segmented from the basaltic rock core. Figure 3.18 shows 4 examples of the resultant segmented crystals.

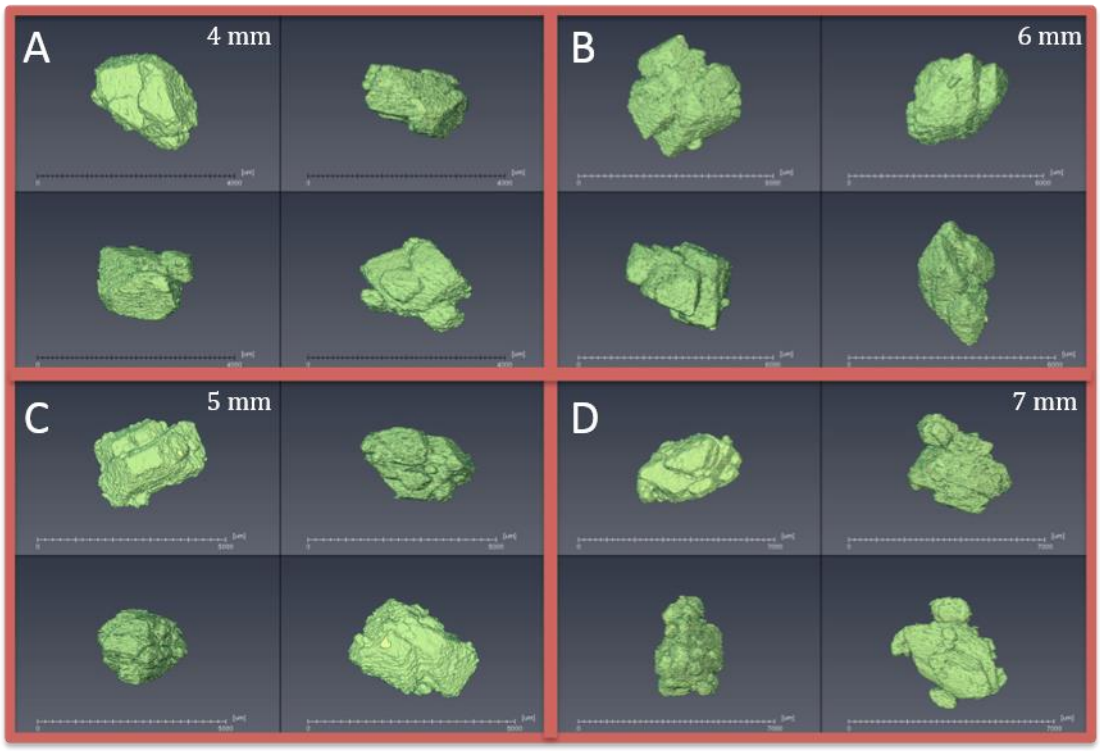

Figure 3.18: Composite image of 4 olivine clusters digitally segmented using 'image j' and 'aviso' (A-D). Each cluster is shown from 4 different orientations (images within each red box). The length of each scale bar below each cluster is noted at the top of each image. All of the olivine clusters/individual olivine crystals that were segmented are provided on the additional CD.

Shea et al. (2015a) assume an 'ideal' olivine for their respective studies as shown in figure 3.19A. This is compared to a crystal cluster segmented by XMT as shown in figure 3.19B.

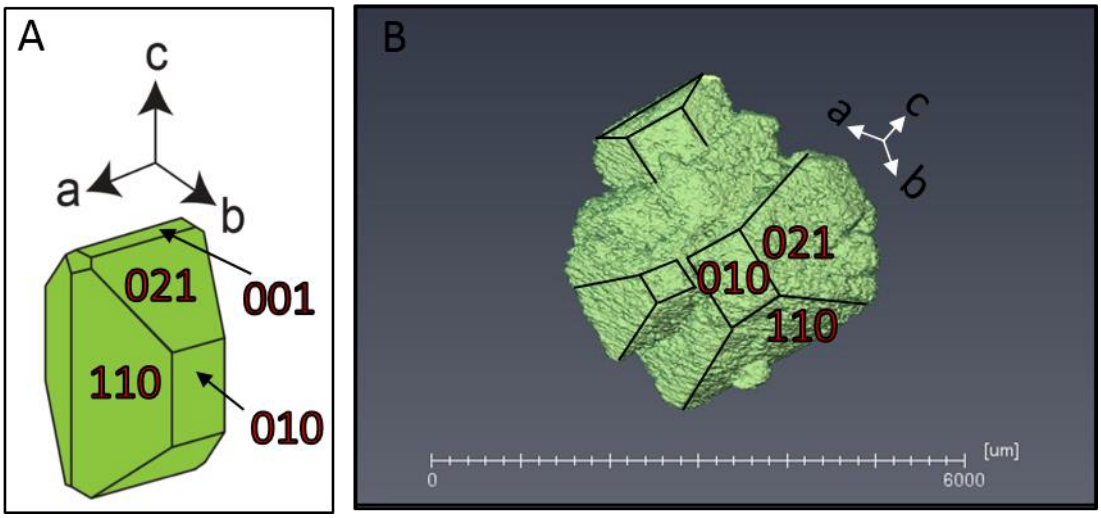

Figure 3.19: (A) an 'idealised' theoretical olivine crystal used in various studies e.g. Shea et al. (2015a) (B) a PdF olivine cluster imaged using XMT and segmented using 'image j' and 'aviso'. Miller indices denote matching faces. Black lines highlight crystal face edges.

An initial observation here is the absence of an [001] face on the segmented olivine crystals compared to the theoretical olivine grain (which does have a [001] face). Another point to notice from the segmented olivine crystals is that they do not conform to an ideal solitary crystal morphology.

Preliminary shape comparisons between a slice through the theoretical crystal and natural slice (taken at the same orientations using the EBSD data) are shown in figure 3.20.A-B.

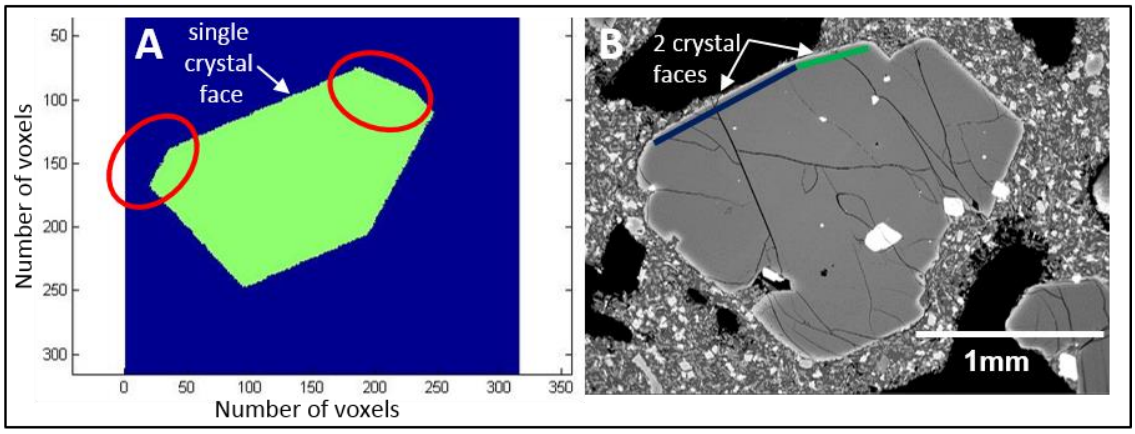

Figure 3.20: *(A) A Matlab image of a slice through a theoretical olivine shape (green) taken at the same orientation as the natural slice by inputting its EBSD orientations. Red circles highlight extra faces that are not present in the natural crystal (B) SEM image of a slice through a natural olivine crystal. This crystal has clear embayments.*

The comparison between the theoretical crystal slice and a natural crystal slice shows that the natural crystal is not perfectly euhedral and that other faces are present, within both crystals (highlighted with (A) red circles and (B) blue and green lines) . The theoretical crystal is, of course, perfectly euhedral.

Across the whole XMT dataset, 25% of the grains were euhedral, 7% were anhedral, and 68% were subhedral. It is not clear from the XMT dataset what has caused these imperfections, but they may be due to differing degrees of erosion at the crystal corners and faces, as is seen in some SEM images. They could be due to extra faces being present as shown in figure 3.20. Or they could be due to pitting or cracking. Some cracking is seen in the XMT data. Also, 25% are individual crystals, and 75% are found as an agglomerate of crystals. The agglomerates are generally crystallographically aligned as seen in figure 3.18 and 3.19. Nearly all the crystals are polyhedral apart from one or two tabular shaped ones, 19% are rounded nodules and 13% of the agglomerates show parallel organization/hierarchy as

described by Welsch et al. (2012). This is when large units have adjacent, smaller units occurring as reduced-size replicas.

The origin of the crystal agglomerates and what effect this has on the diffusion timescales is an important consideration. The study by Welsch et al. (2012) summarised the origin of these large PdF olivine crystal agglomerates. Welsch et al. (2012) have stated that the macrocrysts are organised and subdivided into parallel units and argue for crystallization by dendritic growth and ripening, rather than a combination of paired nucleation, crystal aggregation (*Schwindinger, 1999*) or synneusis (*Schwindinger and Anderson, 1989*). Further evidence of this is suggested by the occurrence of hollow faces, P-rich zones, melt and Cr-spinel inclusions formed from the accumulation of slow diffusing impurities in the liquid at the contact with rapid-growing olivine (*Welsch et al., 2012*).

The crystals agglomerates from the XMT data set from this study don't all appear to be subdivided into parallel units in a hierarchical way, as inferred by Welsch et al. (2012). Vance (1969) suggests that if two or more distinct crystals are involved and they were relatively large when coming into contact, oriented with prominent faces in common, then the crystals may be exhibiting synneusis structures. Some of these structures are exhibited in the XMT images in figure 3.18. Schwindinger and Anderson (1989) hypothesised that crystals from different environments formed attachments by this synneusis mechanism. What is important to consider is whether the PdF crystals came together prior to or after the onset of diffusion. The PdF rims vary somewhat in composition and form a simple, continuous population in time, due to the diffusion clocks not starting in all of the crystals at the same time. This observation may fit with the hypothesis that they came together from slightly different environments. SEM images shown earlier in the chapter show a lack of diffusion along crystal faces in contact with other crystals as part of a crystal cluster. This may indicate that the timing of synneusis was prior to the onset of diffusion.

The effects of varying degrees of euhedrality and arrangement of the crystal agglomerates and what affect this has on the diffusion timescales would need to be more fully evaluated to quantify the effects of crystal shape uncertainties.

3.8. Conclusions

Sample 64217 from the 2002 PdF lava flow exhibits a large modal abundance of antecrystic olivine and a picritic composition. These olivines are normally zoned, implying that there have been perturbations somewhere in the volcanic system from either magma storage or a transport related process. Textural evidence suggested that this zoning was late stage, recording some of the cooling of the lava flow.

These zoned olivine crystals were modelled to retrieve timescales for the magmatic process that modified this zoning. These timescales derived by diffusion modelling occupy a narrow continuous range; 7-45 days with a few anomalies between crystals and within crystals. This is strong evidence that there is a nominal monodisperse crystal population in this lava flow. Other evidence that points to this conclusion includes the consistent core values across all of the crystals (Fo_{84-85}) and CSD data that is in agreement across each of the samples (over 2500 crystals in total) showing a similar intercept and curve shape.

Analysis of 3D crystal shapes from the XMT dataset and the shapes of random slices taken through crystals were analysed. But understanding the interaction between crystal shape and their diffusion patterns needs to be further quantified.

This somewhat 'simple' (lack of other crystal populations or other more complex zoning patterns) crystal population has been identified as ideal to serve as the "best-case" baseline dataset to further analyse the diffusion parameters and geometrical corrections that are applied to diffusion data elsewhere in this study (chapter 5). Evidence of scattering between timescales of the same crystal highlighted some problems with this dataset, the causes of which point to growth, changing boundary conditions and shallow sectioning angles, but also indicates that natural populations simply do not correct to a single timescale. These corrections and sources of error will be further expanded upon in chapter 5 to better understand the affects these have on a population of diffusion timescales. They will be quantified and some corrections will be tweaked to make methods more efficient e.g. those for crystallographic orientation. This is a large dataset and so will provide information with regards to how many diffusion profiles are sufficient to identify the dominant timescale(s) and therefore the magmatic process.

Evaluation of this data will enable corrections to be applied to an entire crystal population rather than to individual traverses within individual crystals. This will not be the first study to do so. Kahl et al. (2011) and (2013) have been using crystal populations and systems analysis methods to track their journey through different magmatic environments before eruption. However my methods will be implemented differently. Studying crystal populations as a whole is crucial to being able to successfully streamline the diffusion modelling methods enough to be able to apply them in an eruption scenario much quicker than we can at present day.

This sample is simple enough to initially evaluate these corrections and uncertainty, but nature is often more complex. Added complexity will need to be tested for newly developed methods to be successful. I have looked at other samples from Mauna Loa, Hawaii, with a view to understanding the magmatic processes occurring here and identifying more complexity that can be tested within newly developed diffusion methods as part of this study. These samples are described next in chapter 4.

CHAPTER 4

Mauna Loa, Hawaii

4.1. Introduction

Eruptive activity at Mauna Loa has been regular throughout recent historical time, with frequent eruptions throughout the 19th and 20th centuries until activity ceased in 1984 (*Lockwood and Lipman, 1985; Barnard, 1995*). The average historical lava production rate (1843 to present) is higher than the average production rates from the preceding six centuries (1200-1843) (*Lockwood and Lipman, 1985*). During this period (pre-1843) the present Mokuaweoweo summit crater formed with increased eruption from the radial northwest flank vents to the summit and low levels of rift zone activity (*Lockwood and Lipman, 1985*). For nearly 1,000 years previous to this (pre-1200 AD) voluminous pahoehoe flows from a summit lava lake characterised the activity (*Lockwood and Lipman, 1985*).

Pahoehoe and a'a lavas are present in nearly equal amounts at the surface of Mauna Loa, but the rift zones typically produce more a'a than summit eruptions (*Lockwood and Lipman, 1985*). Lavas from the southwest-rift zone (SWRZ) will be the focus of this study (both a'a and pahoehoe). An abrupt change in chemistry of the lavas ~1877 has been related to the effects of a 7.5 magnitude earthquake which preceded a large picritic eruption in 1868 (*Lockwood and Lipman, 1985; Rhodes, 1995*). Picrites are relatively uncommon in the recent Hawaiian volcanic record, comprising only 7% by volume of the lavas erupted in historical times (1843 -1984) (*Rhodes, 1995*).

Two picritic lava flow fields that pre-date historical eruptions (pre-1843) are '*Hapaimamo*' and '*Moinui'.* These have largely been overlooked for detailed petrological, geochemical and certainly diffusion studies to date with very little literature available for either eruption (*Perring et al., 2004; Tsang et al., 2008*).

Timescales from the crystals in the deposits of these eruptions will form my Hawaii dataset, which builds upon the PdF dataset presented in chapter 3. Olivine crystals

from these two events may introduce an added element of complexity in the development of the new diffusion methods e.g. they may contain clearly distinct crystal populations. These complexities test the extent to which the new methodology (developed in chapter 5) is useful for both 'simple' and more complex crystal populations. This will make the streamlined methods more robust in an eruption scenario, by either defining the certainty on the techniques or by allowing an enhanced method to be developed.

Both the Hapaimamo and the Moinui lavas originated from the SWRZ as shown in figure 4.1.

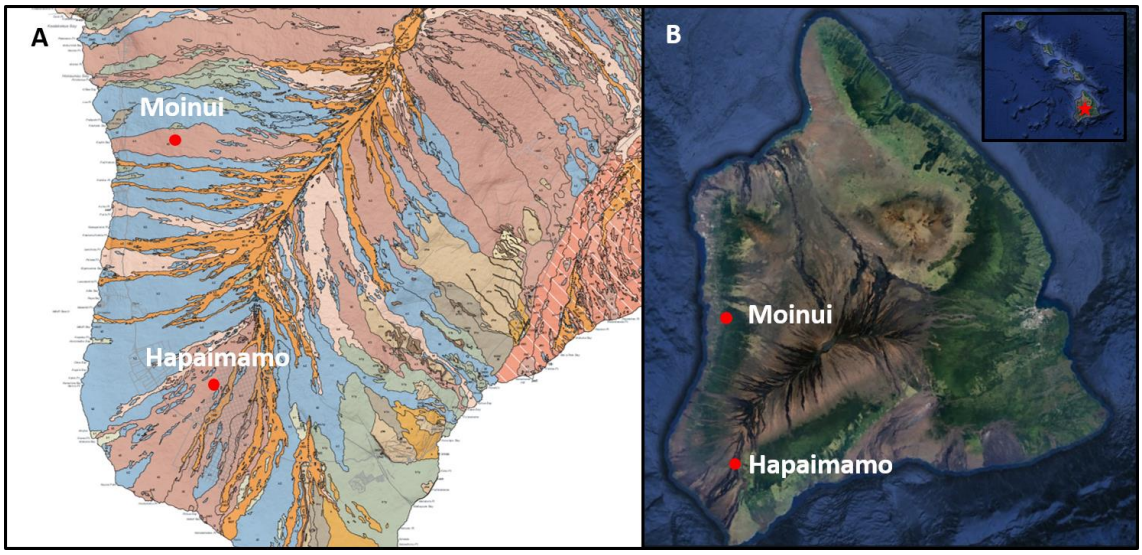

Figure 4.1: Maps showing the locations of both the Moinui and Hapaimamo lava flows A) A segment of the geological map of the Big Island by Wolfe and Morris (1996) identifying the Moinui and Hapaimamo lava flows (red circles) B) The position of each flow with respect to the rest of Mauna Loa from Google Earth (inset, the Hawaii volcanic chain).

Petrological, geochemical and diffusion modelling data and interpretations are discussed below for both eruptions.

4.2 Hapaimamo

4.2.1. Introduction

The Hapaimamo lava flow field is located on the SWRZ dated (from charcoal at the base of a flow) at ~240 years old (*Tsang et al., 2008*; *Garcia and Rhodes, 2012*). The flow is estimated to be ~468x10^6 m^3 in volume with a rapid effusion rate of 200-

100m^3/s suggested by flow modelling (*Mueller, 2005; Garcia and Rhodes, 2012*). The flow originated from spatter ramparts at an elevation of ~1880 m on the SWRZ (*Tsang et al., 2008*). A large scoria cone comprised of tephra is present at an elevation of ~1700 m (*Wolfe and Morris, 1996*). Three main flows are categorised by age and spatial distribution a) the Kaikia'ana flow b) the 'Akau flow and c) the Hema flow (figure 4.2). The 'Akau and Hema flows are younger and the Kaikia'ana flow is older, but it is unlikely that much time elapsed between them (*Mueller, 2004; Garcia and Rhodes, 2012*). The Kaikia'ana flow is found at upper elevations near the spatter ramparts, and the 'Akau flow and Hema flow are found towards lower elevations, both extending down the slopes of the volcano to the sea (*Tsang, 2008*). This categorisation is shown in figure 4.2.

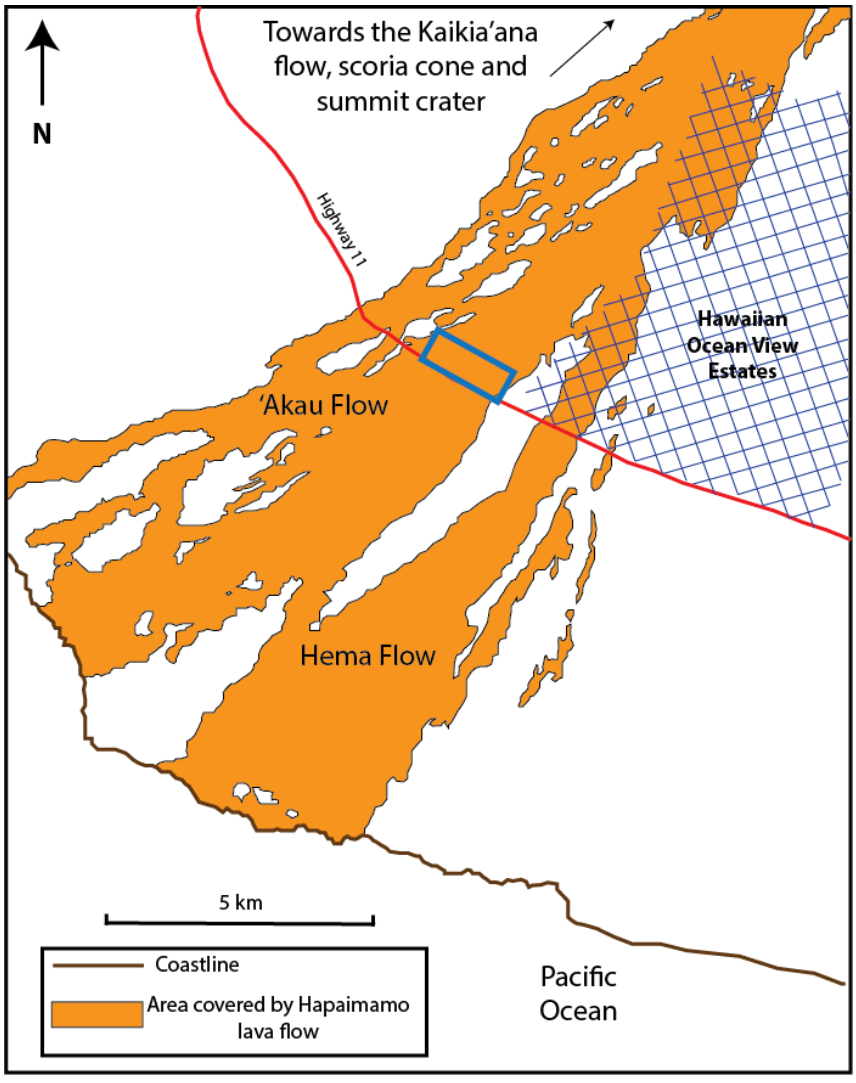

Figure 4.2: Schematic map showing part of the Hapaimamo flow field on Mauna Loa's lower slopes, adapted from Tsang (2008) and Garcia and Rhodes (2012). The blue square defines one of the sample areas on the 'Akau part of the lava flow.

4.2.2. Fieldwork Description and Sample Summary

Fieldwork was conducted in January 2015. I collected lava flow samples from the ‘Akau flow only along a road cut exposed on the Mamalahoa Highway (Highway 11) from GR 0203440E 2114919N to GR 0203482E 21154886N (UTM Zone 5Q). Tephra samples (reticulite) were sampled from the scoria cone deposits to the north of Hawaiian Ocean View Estates within Kahuku Ranch. Permits and permissions were sought through the Hawaii Volcano National Park Service with the help of Frank Trusdell from the United States Geological Survey (USGS) Hawaii Volcano Observatory (HVO). Frank Trusdell provided orientation and logistical support for the tephra sampling.

The Hapaimamo flow is an a’a flow. The sample sites are shown in figure 4.3.

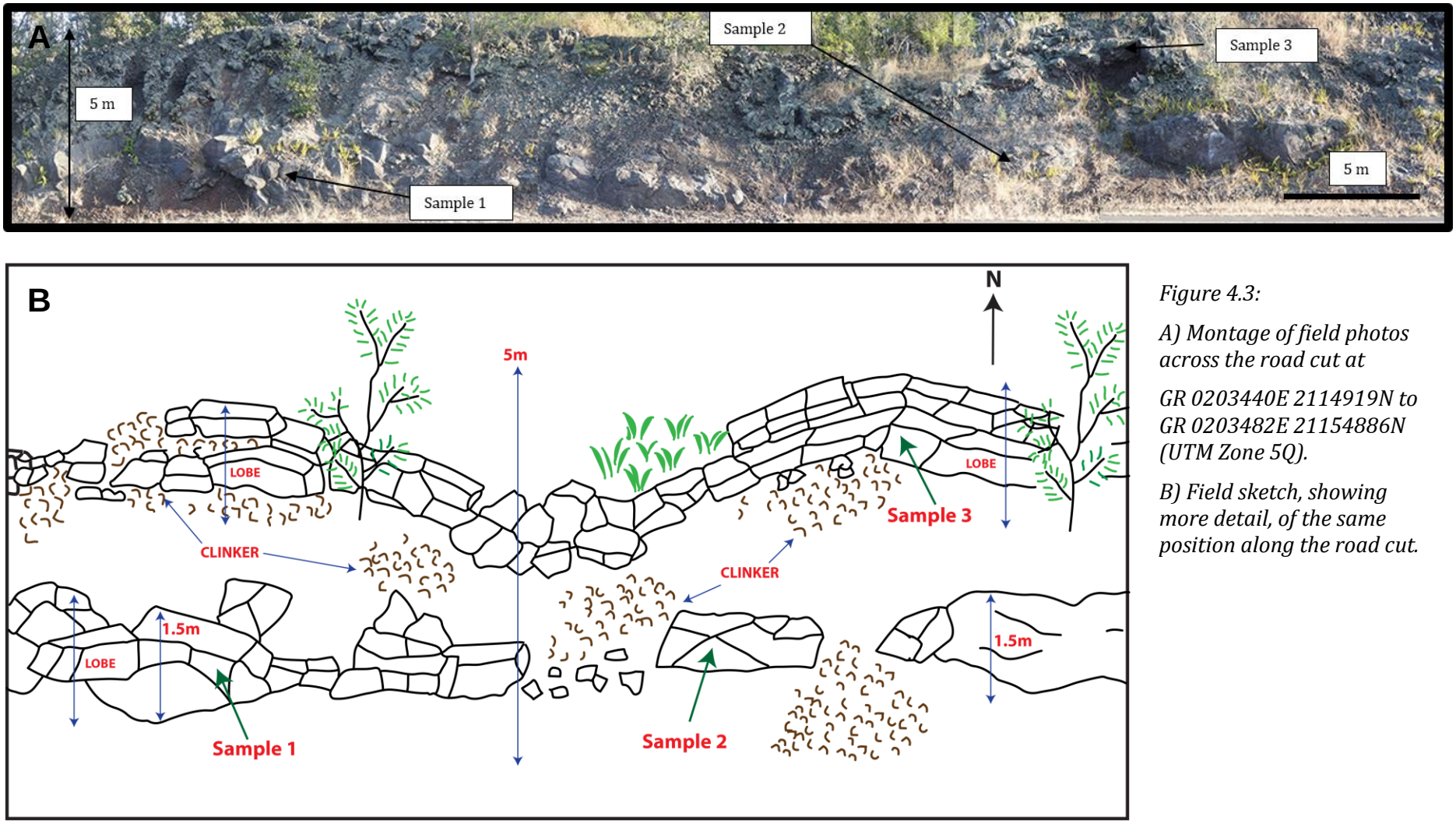

Figure 4.3:

A) Montage of field photos across the road cut at

GR 0203440E 2114919N to GR 0203482E 21154886N (UTM Zone 5Q).

B) Field sketch, showing more detail, of the same position along the road cut.

Figure 4.3 shows at least two thin sheets of lava. These can be interpreted as either different flows or different pulses from the same flow (different lobes) – the latter is the most likely as they are both part of the same flow field. Both sheets consist of a solid, blocky massive core forming the dense interior and an upper and lower crust of loose fragments called 'clinker' created by brecciation and viscous tearing of liquid lava as the flow is emplaced (*MacDonald, 1972; Rowland and Walker, 1987*). Collectively these form a single lobe shown in figure 4.3. A-B and 4.4A. As the flow moves, it carries the upper clinker horizon along with it and those that fall off the front are buried by the flow as it advances forming the bottom clinker layer (*MacDonald, 1972*). The part of the flow that was sampled has the features of proximal a'a flow, following the definition of Rowland and Walker (1987). Proximal-type a'a' flows tend to be 1-3 m thick, have thin layers of spiny clinker, fine material mixed in with the clinker and often have vesicular interiors (*Rowland and Walker, 1987*). Distal flows are much thicker (up to 10 m), have thick top layers that are much blockier intermixed with fine sand and dust with poorly-vesiculated interiors (*Rowland and Walker, 1987*).

As seen in figure 4.3 and 4.4A, each sheet is up to 3 m thick from the basal clinker through the flow core to the top of the upper clinker unit. The upper sheet follows the shape of the landscape with the same general structures as the lower sheet, however it has a thinner interior core ~0.5 m (figure 4.3A and B).

The interior core is vesiculated, ~4-16% with large olivines present (figure 4.4B), up to 3 mm in size. The olivine content in this part of the flow is ~5-15%. The clinkers range from 4cm-10cm, are vesiculated (~20%) and are rough and spiny to touch (figure 4.4C). The clinker contains far fewer olivines (< 5%). Xenoliths (dunite (olivine)) and (peridotite (olivine + orthopyroxene)) ~1cm in size are also present in the interior core (figure 4.4D). Troctolite (olivine + plagioclase) xenoliths have also been found within the Hapaimamo (*Tsang et al., 2008)* but they were not identified as part of this study.

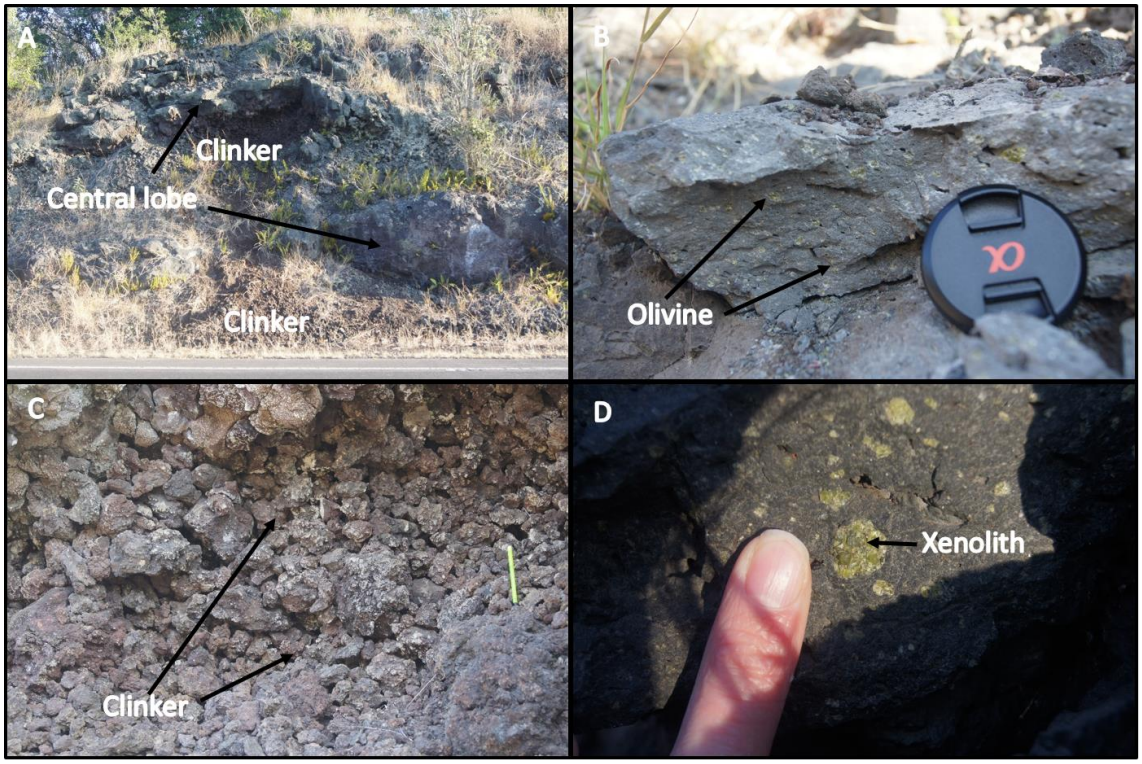

Figure 4.4: Field photos of the Hapaimamo flow A) clinker and central lobe from two lava sheets B) olivine within the central lobe C) varying size of the clinker D) an example of a dunite xenolith

Three sets of samples from different lobes were collected from the road cut as indicated on figure 4.3. Two sets of samples were taken from the lower sheet ~20 m apart (these are from different sections of the same lobe). The third sample set was taken from the upper sheet. Each sample set consists of bottom clinker, blocky core and upper clinker sampled through a vertical section of the sheet. Samples are denoted as follows; e.g. H1TC, H1CL, H1BC, for Hapaimamo sample 1 top clinker, centre lobe (blocky core) and bottom clinker. Sample locations were logged as shown in figure 4.5.

Thin sections were made for each part of the lava flow samples. Upon closer inspection of the thin sections, olivine crystals within the clinker were noted to have been oxidised and were therefore unsuitable for diffusion studies (as discussed in chapter 3). For each lava core sample, letters denote individual olivine crystals and the following number denotes individual traverses taken from a crystal face within an olivine e.g. H3CL_A_1.

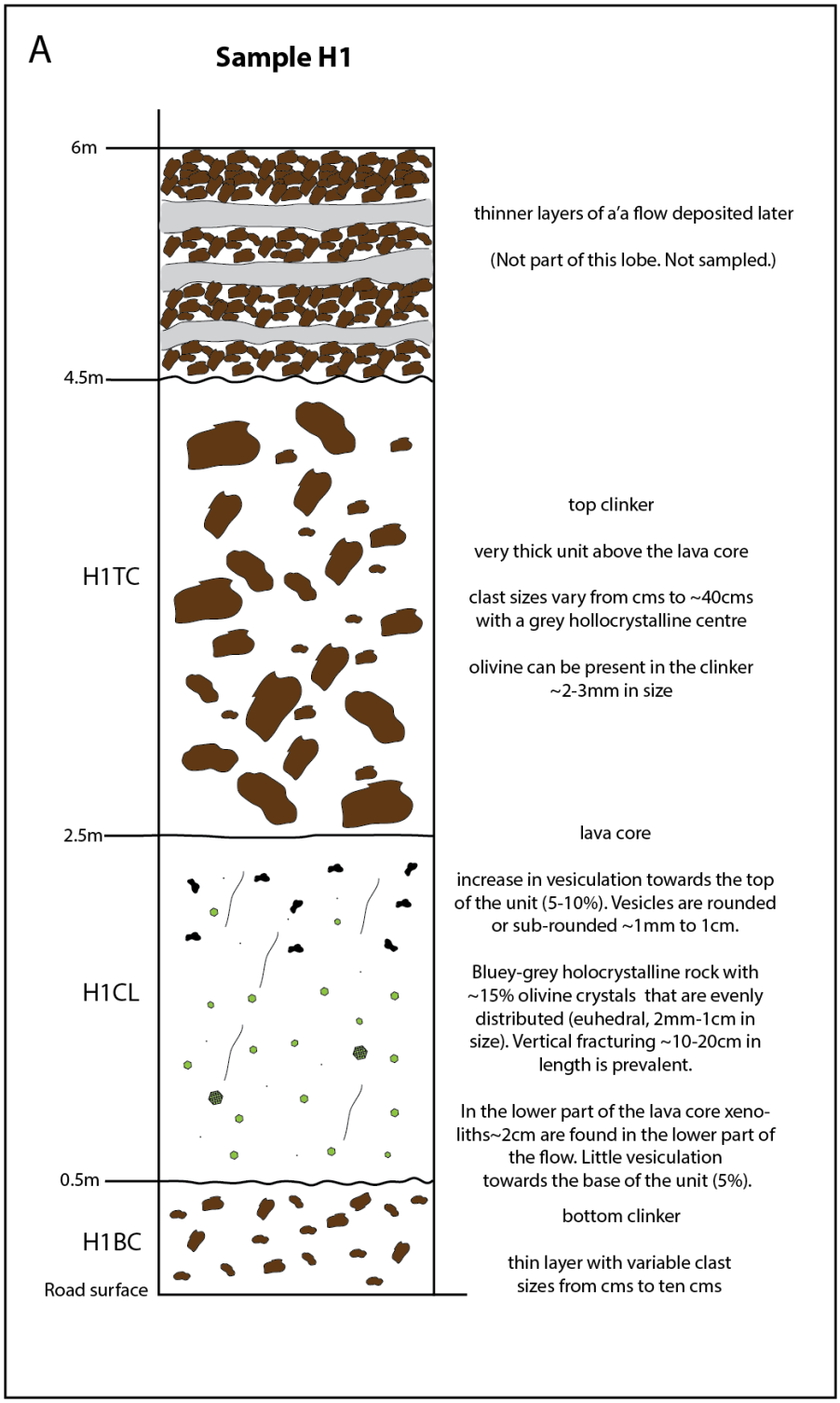

Figure 4.5.A: Field log for sample H1. A vertical section through a single lobe.

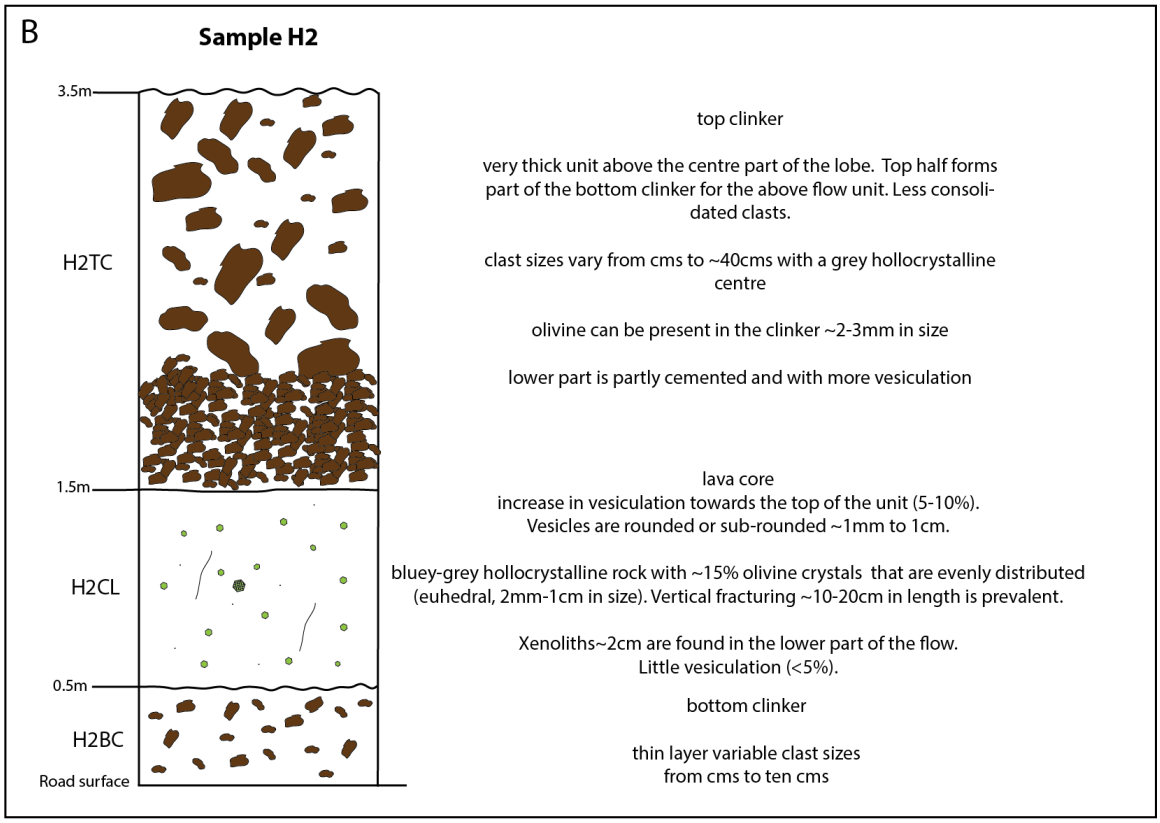

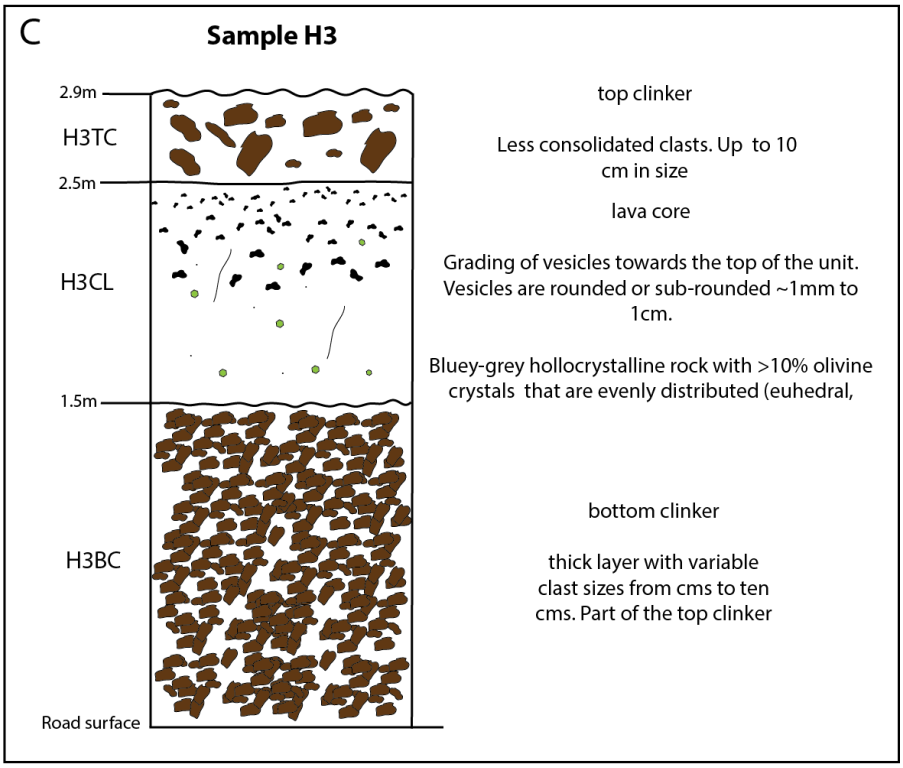

Figure 4.5.B and C: Field log for sample H2 and H3. Each log is a vertical section through a single lobe.

Hapaimamo tephra was sampled near the vent, < 1km away, near the road that runs roughly NW-SE through Kahuku Ranch at GR 0209477E 2122694N (UTM Zone 5Q).

Here the deposit is ~2 m thick, shown in figure 4.6, forming an extensive reticulite field. Each clast is several cms in size and can contain up to 2 or 3 olivine crystals easily visible with the naked eye encased within layers of volcanic glass. The reticulite was hand crushed, olivines picked then separated by size.

Figure 4.6: *Field photos of the Hapaimamo tephra (reticulite) deposit just north of Hawaiian Ocean View Estates.*

Olivine picked from the reticulite were mounted in resin creating 30 mm diameter grain mounts. Each grain mount contained a different size fraction of olivine. Five grain-mounts were made in total, named blocks 1-5 – block 1 containing the largest olivines (> 0.5 cm) and block 5 containing the smallest olivine (< 1 mm) ready for analysis. Tephra samples referred to as Block 1, Block 2, Block 3, Block 4 and Block 5 will be characterised and analysed as part of this chapter. Letters denote individual olivine crystals and the following number denotes individual traverses taken from a crystal face within an olivine e.g. Block 3_A_2.

The tephra olivines are the focus of this study. The aim was to find a Hawaiian air fall deposit rich in olivine crystals that have recorded subsurface processes. It was also hoped that these crystals may belong to more than one crystal population to provide additional complexity with which to test the streamlined methods (to be discussed in chapter 5). Olivine from the lava flow cores will be described and modelled for Fe-Mg inter-diffusion later in this chapter to evaluate any differences in timescale from the tephra. Variations in the magmatic processes and the source between sample types will be considered.

4.2.3. Tephra Sample description

As with the PdF samples, the Hapaimamo samples are picrites (as defined in Boivin and Bachelery, 2009). 127 olivine crystals were picked from less than 100 reticulite clasts.

4.2.3.1. Textural observations

Olivine crystals are found as both single crystals and as sintered clusters of 2-5 crystals (figure 4.7A and B) with well-defined planar faces. Most, if not all of the olivine crystals, are encased in a thin coating of volcanic glass from 10 – 150 µm thick.

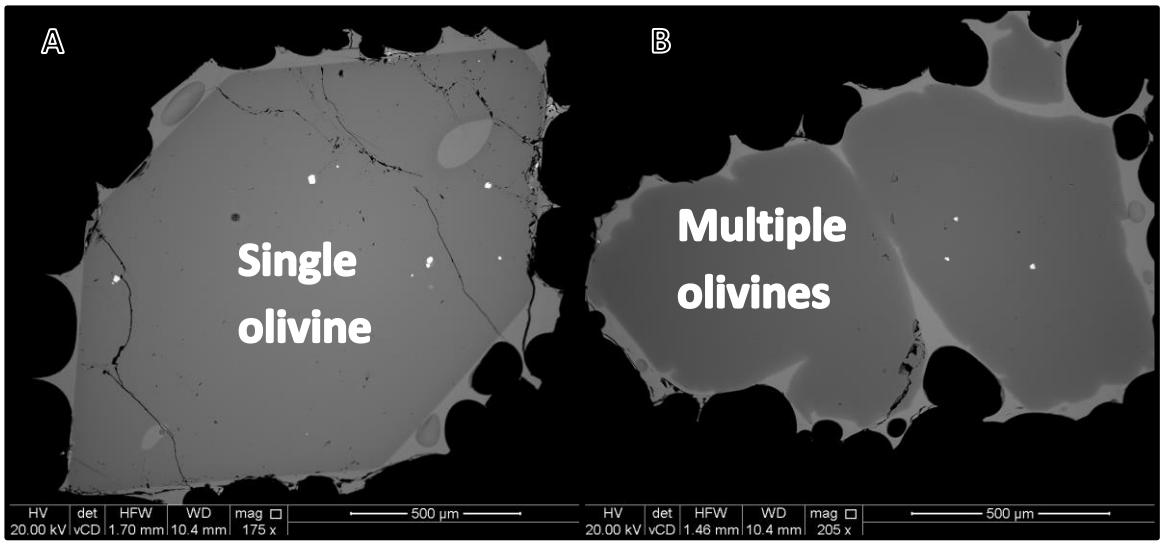

Figure 4.7: A) a single euhedral olivine crystal with melt inclusions and spinel inclusions (white) encased in volcanic glass (light grey exterior) B) multiple subhedral olivine crystals encased together in volcanic glass

Olivine was the most abundant mineral phase found within the tephra followed by clinopyroxene (~30% of crystals picked) then plagioclase (<5% of crystals picked). Opx was not saturated at the time of eruption. The timing of the formations of these clusters is important as it helps to understand the history of these crystals. Where the planar faces of a crystal are close to or touching an adjacent crystal (figure 4.7B), this may be evidence of crystal clusters being plucked from a mushy layer. This would hold true if there is no diffusion rim on these aggregated faces meaning the crystals came together before the onset of diffusion. However, the olivines do show

full diffusion rims even when found as part of a crystal cluster indicating diffusion took place before the crystals were aggregated. Therefore it is more likely these crystals existed as free-floating single crystals that came together after the onset of diffusion.

4.2.3.2. Mineralogy

Olivine

Large crystals of olivine are present in the tephra and range in size from 300 µm– 3 mm. Most tephra olivines are euhedral in shape.

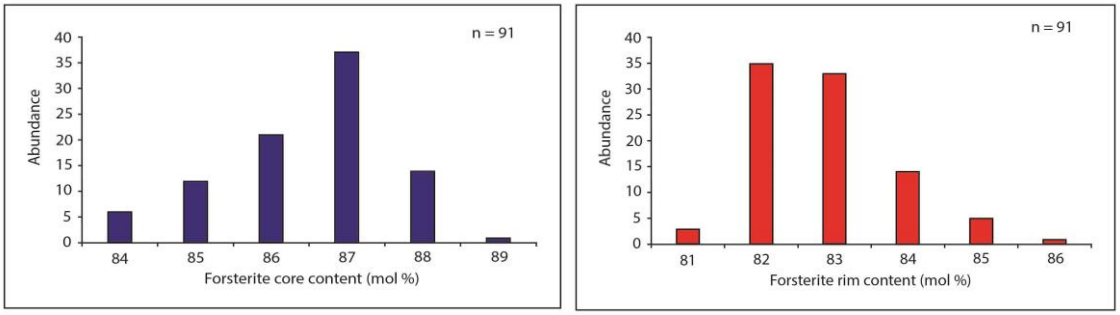

Figure 4.8: Core and rim values plotted by abundance of the Hapaimamo olivines within the tephra. Rim compositions are the compositions measured with the EPMA ~5 microns of the edge of the crystal.

Figure 4.8 shows the core values range from $Fo_{84\text{-}89}$ and the rim values range from $Fo_{82\text{-}86}$. All olivines are normally zoned, no reverse or complex zoning is observed. They are host to an abundance of glassy melt inclusions that range in size from 10 µm to tens of microns in diameter. These can be found with or without small inclusions of spinel crystals.

Plagioclase feldspar

No plagioclase within the tephra was mounted and analysed. Of the few found within the deposit they were no bigger than 1mm in size.

Clinopyroxene

A handful of bottle green clinopyroxene grains were picked from the reticulite. They are euhedral in shape and display complex zoning. No compositional data was retrieved for these crystals.

Oxides

Spinel is frequently found as an inclusion within the tephra olivine or within the matrix glass. They are up to 150 μm in size and occur as small as 5 or 10 μm.

Orthopyroxene

No orthopyroxene was identified in the tephra.

4.2.4. Tephra Thermometry and Oxygen Fugacity (fO_2)

All thermometry calculations were performed using matrix glass and glass within inclusions associated with the tephra olivines. Volcanic glass is a proxy for liquid composition. Both the glass incorporated as melt inclusions and the matrix glass were analysed to detect any change in temperature (and/or pressure) from initial crystal growth to quenching upon eruption. The oxygen fugacity is also carefully considered. Whilst it has an effect on the certainty of the timescale (discussed in chapter 2), it does not have as large an effect as the temperature.

Compositional data from the glasses to be used for input in to the thermometry was retrieved using a JEOL JXA8230 Electron Microprobe (EPMA) at the University of Leeds Electron Optics facility. To collect this data the beam current was lowered to 10nA with a beam size of 10 μm at 20kV. Spot analyses within the melt inclusions and matrix glass were measured. Most analyses returned totals of 97-101.2 wt%. The beam is defocused to increase the efficiency of the measurement of mobile elements such as Na (*Morgan and London, 1996*). The following elements were measured: Si, Ti, Al, Mg, Fe, P, K, Ni, Mn, Cr, Ca and Na. On peak count times were as follows; 24s for Mg and Ti, 30s for P, 20s for Mn, Fe, Ni, and Cr and 10s for Ca, Al, Na, K, and Si. Selected compositional data, primary standards and detection limits are reported in Appendix A.

4.2.4.1. Thermometry and barometry

The temperature at which diffusion takes place is of major concern due to the associated uncertainties and effects on model parameters such as boundary conditions. It is important to define whether to use data from melt inclusions (if

viable) or matrix glass for the equilibrium melt composition, for use in diffusion modelling.

Diffusion models (such as AUTODIFF) often only employ a single temperature estimate as input rather than a temperature range. A temperature range may be a more realistic assumption of the magmatic conditions when diffusion was occurring. When a crystal moves from depth through the plumbing system or whilst it is in residence in a magma chamber e.g. a crystal mush, it may be affected by changing temperature when new magma packages move through (*Passmore et al., 2012).* This induces another source of error into the temperature estimate so it is key to recognise whether the temperature being applied to the model is a maximum or a minimum temperature and the affect this will have on interpreting any timescales calculated.

It is likely that melt inclusions will provide hotter temperatures, as this melt was captured in the crystal as it grew at some depth within the lower crust whereas it is likely matrix glasses will provide lower closure temperatures as the sample is erupted and quenched. This may not always be the case depending on where the crystal has resided prior to eruption and which melts it has been in contact with.

Thirty melt inclusions were analysed across 25 olivines. Two or three analyses were taken per melt inclusion, resulting in a total of 61 melt inclusion analyses. Olivine compositions adjacent to each melt inclusion analysis were also retrieved. This compositional data can be input into olivine-liquid equilibrium thermometers. Melt inclusions were analysed if they were not close to the crystal edge or bounded by or intruded by cracks or fracture to ensure (as much is possible in 2D) that there was no connection to the matrix glass. This could affect the true composition of the melt inclusion and the data would need to be rejected. Melt inclusions were also selected to be large enough to enable more than 1 analysis (>30 μm in diameter) to ensure reliability of the data.

74 analyses of the matrix glass were taken with the same EPMA settings as described above. These analyses were taken from matrix glass surrounding 4 tephra olivines. Neither the matrix glass nor the melt inclusions appear zoned from initial observations.

There are many olivine-liquid thermometers and liquid-only thermometers to choose from, each with different dependencies e.g. consideration of pressure, mineral assemblages and water content, as described and reviewed by Putirka (2008).

For the Hapaimamo dataset, the Beattie (1993) olivine-liquid thermometer (equation 1) and the Montierth et al. (1995) (a variation on the Helz and Thornber (1987) thermometer) liquid-only thermometer were chosen (equation 4.2 a and b).

$$T(°C) = \frac{13603+4.943x10^{-7}(P(GPa)x10^{9}-10^{-5})}{6.26+2lnD_{Mg}^{ol/liq}+2\ln[1.5(C_{NM}^{L})]+2\ln[3(C_{SiO_2}^{L})]-NF} - 273.15 \qquad \text{(Equation 4.1)}$$

$$NF = \frac{7}{2}\ln(1 - X_{AlO_{1.5}}^{liq}) + 7\ln(1 - X_{TiO_2}^{liq})$$

$$C_{NM}^{L} = X_{MgO}^{liq} + X_{MnO}^{liq} + X_{FeO}^{liq} + X_{CaO}^{liq} + X_{CoO}^{liq} + X_{NiO}^{liq}$$

$$C_{SiO_2}^{liq} = X_{SiO_2}^{liq}$$

$$D_{Mg}^{ol/liq} = \frac{0.666 - (-0.049X_{MnO}^{liq} + 0.027X_{FeO}^{liq})}{X_{MgO}^{liq} + 0.259X_{MnO}^{liq} + 0.299X_{FeO}^{liq}}$$

NF = "network formers" – chemical constituents that comprise a silicate network with tetrahedral coordination in the liquid

C_{NM}^{L} = "network modifying cations" - charge balancing cations in higher coordination than tetrahedra

$C_{SiO_2}^{liq}$ = concentration of Si

(Subscripts refer to the components and superscripts refer to phases)

$$T(°C) = 20.1\ MgO^{liq} + 1014 \qquad \text{(Equation 4.2a)}$$

$$T(°C) = 23.0\ MgO^{liq} + 1012 \qquad \text{(Equation 4.2b)}$$

The Helz and Thornber (1987) liquid-only thermometer (equation 4.2a) is widely regarded as a simple yet effective way of retrieving temperature requiring only 1

compositional term, MgO wt. % (*Putirka, 2008*). The Montierth et al. (1995) correction (equation 4.2b) to the Helz and Thornber (1987) thermometer was chosen as it was calibrated specifically for Mauna Loa lavas and has an uncertainty of $\pm$10°C (*Montierth et al., 1995*).

The Beattie (1993) thermometer has an uncertainty of $\pm$44°C for an anhydrous system. The water contents of Hawaiian lavas are typically low 0.05%-0.5% (*Wright, 1971*, *Maaloe, 1985*) justifying the use of the Beattie (1993) thermometer. The thermometer is described as by far the superior thermometer based on Mg partitioning by Putirka et al. (2007) and as reviewed by Putirka (2008).

The Beattie (1993) thermometer was chosen to calculate temperatures associated with melt inclusions using their liquid composition and adjacent olivines. The Montierth et al. (1995) thermometer was chosen to calculate temperatures associated with the matrix glass. To employ the Beattie (1993) thermometer the melt inclusion liquid composition and adjacent olivine composition must be in equilibrium. This can be calculated using the following equation from Roeder and Emslie 1970 (equation 4.3);

$$K_D = \frac{(X_{FeO}^{Ol})}{(X_{FeO}^{Liq})} \frac{(X_{MgO}^{Liq})}{(X_{MgO}^{Ol})} \qquad \text{(Equation 4.3)}$$

The $K_D(Fe\text{-}Mg)^{ol\text{-}liq}$ must be equal to 0.3 ± 0.03 for the Beattie thermometer to be used appropriately. The $K_D(Fe\text{-}Mg)^{ol\text{-}liq}$ for the Hapaimamo melt inclusion liquid and olivine compositions were calculated and plot as follows;

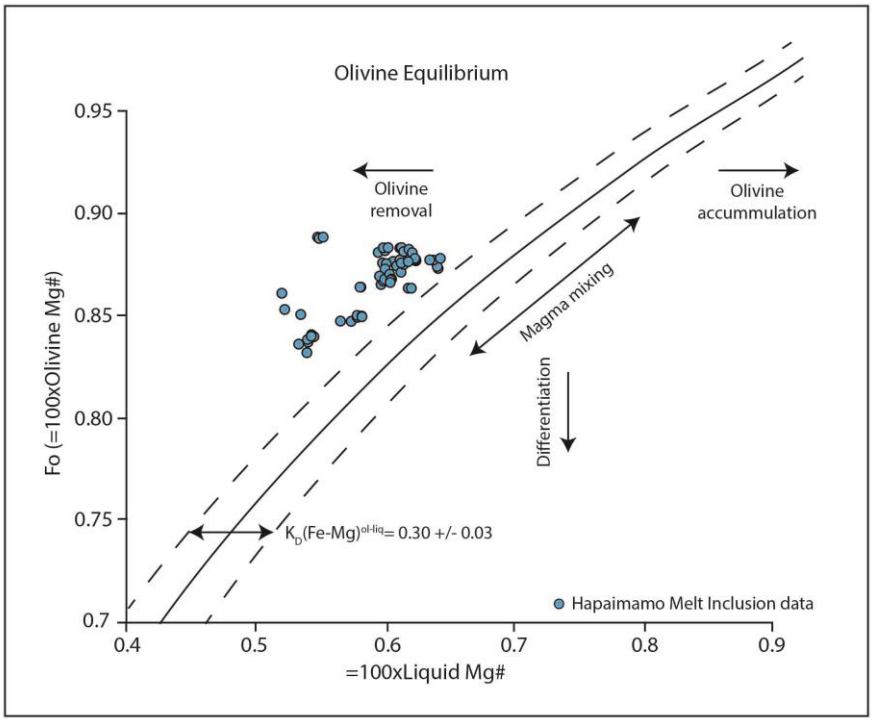

Figure 4.9: The Rhodes diagram adapted from Putirka, (2008). Hapaimamo melt inclusion Mg# olivine vs Mg# Liquid are plotted in blue. The melt in this instance is not in equilibrium with the olivine due to olivine removal from post entrapment crystallisation.

Figure 4.9 shows that the melt inclusion and adjacent olivine compositions are not in equilibrium, due to olivine removal. This occurs due to post entrapment olivine crystallisation around the melt inclusion walls (*Sisson and Layne, 1993; Kress and Ghiorso, 2004; Humphreys et al., 2008*).

The liquid composition was corrected by adding back a fraction of the olivine composition to the liquid until the liquid and adjacent olivine composition are back in equilibrium. This was achieved using the following equation;

$$\text{Olivine fraction in Melt Inclusions Corrected} = \frac{(Fe/Mg)_{ol} \times Mg_{melt} - 0.3 \times Fe_{melt}}{(Fe/Mg)_{ol} \times Mg_{melt} - 0.3 \times Fe_{melt} - 0.7 \times Fe_{ol}}$$

(Equation 4.4)

The corrected liquid and adjacent olivine compositions were then input in to the Beattie (1993) thermometer. A selection of the original liquid and adjacent olivine

compositions can be found below in tables 4.1 and 4.2. Further glass and olivine compositions can be found in Appendix A.

	Oxide wt. %						
SAMPLE	SiO_2	TiO_2	Al_2O_3	Cr_2O_3	FeO	NiO	MnO
Block 3_B_MI14	51.79	1.99	13.76	0.04	10.78	-0.01	0.16
Block 3_B_MI14	51.22	1.99	13.78	0.04	10.53	0.00	0.17
Block 3_Cb_MI15	54.42	1.87	14.69	0.04	6.73	0.03	0.12
Block 3_F_MI16	52.32	1.83	13.67	0.05	9.83	0.03	0.16
Block 3_J_MI17	53.35	2.01	13.99	0.04	7.79	0.02	0.15
Block 3_J_MI17	52.94	2.02	13.82	0.05	7.73	-0.01	0.10
Block 3_J_MI18	53.64	2.01	13.91	0.02	7.65	0.05	0.12
Block 3_J_MI18	53.56	2.04	13.90	0.04	7.66	0.03	0.13
Block 3_M_MI19	54.44	1.90	13.94	0.03	7.65	0.05	0.12
Block 3_M_MI19	54.24	1.87	13.90	0.03	7.71	0.03	0.12
Block 3_P_MI20	53.87	1.81	13.69	0.06	8.23	0.05	0.12
Block 3_P_MI20	54.30	1.84	13.57	0.05	8.23	0.03	0.14
Block 3_P_MI20	54.12	1.82	13.39	0.06	8.22	0.01	0.13
	Oxide wt. %						
SAMPLE	MgO	CaO	Na_2O	K_2O	P_2O_5	O	Total
Block 3_B_MI14	51.79	1.99	13.76	0.04	10.78	-0.01	0.16
Block 3_B_MI14	51.22	1.99	13.78	0.04	10.53	0.00	0.17
Block 3_Cb_MI15	54.42	1.87	14.69	0.04	6.73	0.03	0.12
Block 3_F_MI16	52.32	1.83	13.67	0.05	9.83	0.03	0.16
Block 3_J_MI17	53.35	2.01	13.99	0.04	7.79	0.02	0.15
Block 3_J_MI17	52.94	2.02	13.82	0.05	7.73	-0.01	0.10
Block 3_J_MI18	53.64	2.01	13.91	0.02	7.65	0.05	0.12
Block 3_J_MI18	53.56	2.04	13.90	0.04	7.66	0.03	0.13
Block 3_M_MI19	54.44	1.90	13.94	0.03	7.65	0.05	0.12
Block 3_M_MI19	54.24	1.87	13.90	0.03	7.71	0.03	0.12
Block 3_P_MI20	53.87	1.81	13.69	0.06	8.23	0.05	0.12
Block 3_P_MI20	54.30	1.84	13.57	0.05	8.23	0.03	0.14
Block 3_P_MI20	54.12	1.82	13.39	0.06	8.22	0.01	0.13

Table 4.1: Selection of values of the glass composition (not corrected for post entrapment crytstallisation)

	Oxide wt. %						
SAMPLE	SiO_2	TiO_2	Al_2O_3	Cr_2O_3	FeO	NiO	MnO
Block 2_MI14_Ol1	39.89	0.02	0.03	0.08	13.93	0.30	0.18
Block 2_MI15_Ol1	40.25	0.01	0.05	0.09	11.72	0.40	0.15
Block 2_MI16_Ol1	39.82	0.01	0.04	0.07	14.27	0.27	0.20
Block 2_MI17_Ol1	40.55	0.01	0.02	0.07	11.88	0.36	0.18
Block 2_MI18_Ol1	40.40	0.01	0.02	0.06	11.82	0.35	0.15
Block 2_MI19_Ol1	40.40	-0.01	0.03	0.09	12.02	0.36	0.18
Block 2_MI20_Ol1	40.38	0.01	0.00	0.10	11.97	0.33	0.16

	Oxide wt. %						
SAMPLE	MgO	CaO	Na_2O	K_2O	P_2O_5	O	Total
Block 2_MI14_Ol1	45.27	0.20	-0.03	0.00	0.01	0.00	100.49
Block 2_MI15_Ol1	47.18	0.18	0.00	-0.01	0.01	0.00	100.02
Block 2_MI16_Ol1	45.48	0.23	0.00	0.00	0.00	0.00	100.39
Block 2_MI17_Ol1	47.38	0.20	-0.02	0.01	0.01	0.00	100.65
Block 2_MI18_Ol1	47.15	0.20	0.03	0.01	0.00	0.00	100.20
Block 2_MI19_Ol1	47.08	0.21	0.00	0.00	-0.01	0.00	100.38
Block 2_MI20_Ol1	47.21	0.20	0.03	-0.01	0.00	0.00	100.39

Table 4.2: Selection of values of the adjacent olivine composition

The Beattie (1993) thermometer gives an average melt inclusion liquid temperature (temperature of the liquid when it was entrapped in the olivine crystal) of 1269°C ($\pm$ 44°C). The spread of temperatures from the melt inclusions is quite large ranging from 1363°C to 1213°C. Removing the 5 hottest and 5 lowest temperatures (assumed to be anomalous) and then recalculating the average temperature lowers the average temp to 1257°C ($\pm$44°C) for the melt inclusions. The Beattie, (1993) thermometer could not be applied to matrix glass and adjacent olivine compositions due to probe breakdowns and therefore time constraints.

The Montierth et al. (1995) thermometer gives an average matrix glass liquid temperature (the temperature post eruption before quenching) of 1168°C ($\pm$ 10°C). These temperatures were much more consistent ranging from 1173 to 1164°C so no 'anomalous' data points were removed to recalculate average temperature.

There is a significant change in temperature between the liquid entrapped within the olivine at some depth and the final liquid that was erupted and then quenched – a difference of nearly 100°C. Accounting for error it could be a difference of as little as 47°C or as large as 155°C. The choice of temperature to be input in to the diffusion model needs to be clearly justified.

The locations of the melt inclusions within the olivines were observed to determine if they were located within the diffused zone of the olivine or within the homogeneous part of the olivine in/towards its core. Over 90% of the melt inclusions analysed were located within the homogenous part of the olivine towards its core. Therefore this melt was trapped before the onset of diffusion and provides a maximum temperature. The temperature input in to the diffusion model is 1168°C. This marks the closure or minimum temperature. Therefore the timescales will either be correct or slightly faster (therefore producing shorter timescales).

The melt inclusion compositions can also be used to estimate pressure at the time of liquid entrapment. To do this I used methods developed by Lee et al. (2009).

They presented new thermobarometry methods based on magma Si and Mg contents to estimate the pressures and temperatures of basaltic magma generation. Mantle melting and magma generation producing the lavas we see at the surface occurs via different mechanisms at different pressures and temperatures depending on the plate tectonic settings (*Lee et al., 2009*). These mechanisms and conditions have been explored by Lee et al. (2009) using whole-rock compositions. I have used this thermo-barometry method to calculate entrapment pressures and temperatures of the melt inclusions using melt inclusions compositions.

The methods from Lee et al. (2009) can only be applied to samples if they are saturated in orthopyroxene and olivine at the source region as this assemblage buffers the silica content in the magma (*Lee et al., 2009*) and only magmas with higher than 8.5 wt. % MgO (higher than 9 wt. % MgO for Hawaiian magmas) are used. Although these lavas are not saturated in orthopyroxene at the surface, it is clearly not of dunite origin – the crystal assemblage contains olivine + clinopyroxene + plagioclase. At the time the melt was extracted from the mantle it would have been saturated in orthopyroxene, but orthopyroxene solubility increases as the melt moves shallower and it becomes unstable, therefore it is not present in the lavas at the surface. The barometer is based on SiO_2 activity which is buffered at a given temperature and pressure by the mineralogy of the system (*Lee et al., 2009*). When the melt is extracted from the mantle in equilibrium with orthopyroxene the bulk Si activity is fixed at that point. As the melt ascends the Si activity will change slightly as the composition changes (loses orthopyroxene) and so the pressures calculated

with the barometer will be inaccurate, but still give some idea of melt entrapment pressures.

A Visual Basic Excel Macro was used for the calculations provided in the supplementary materials of Lee et al. (2009). Figure 4.10 shows the pressures and temperatures calculated for melt inclusion entrapment for the Hapaimamo olivines crystals.

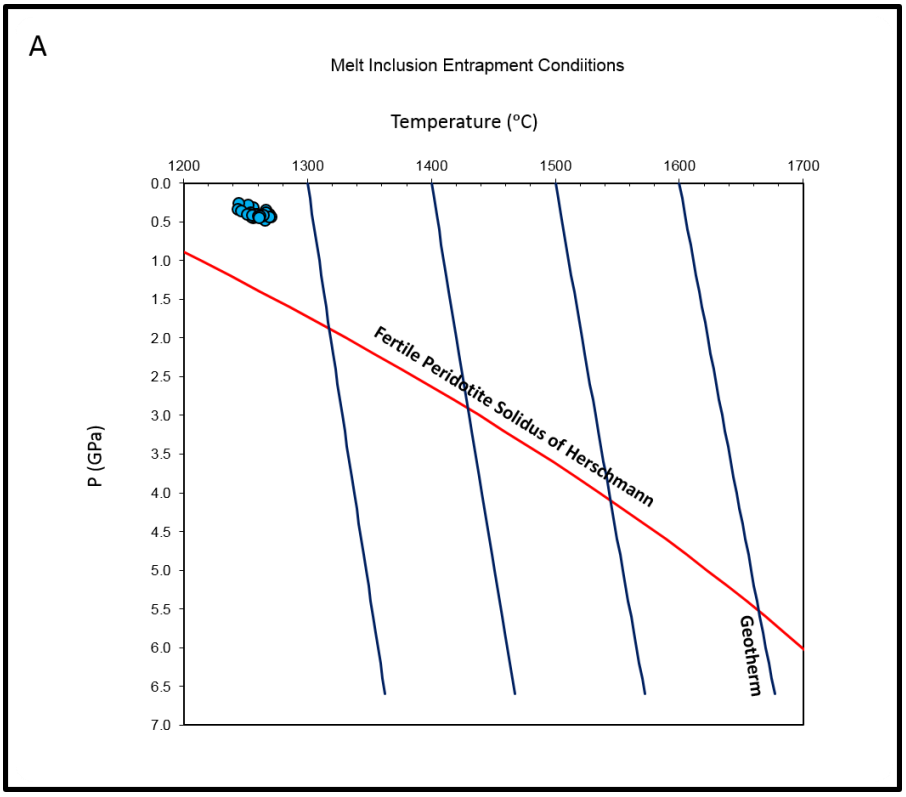

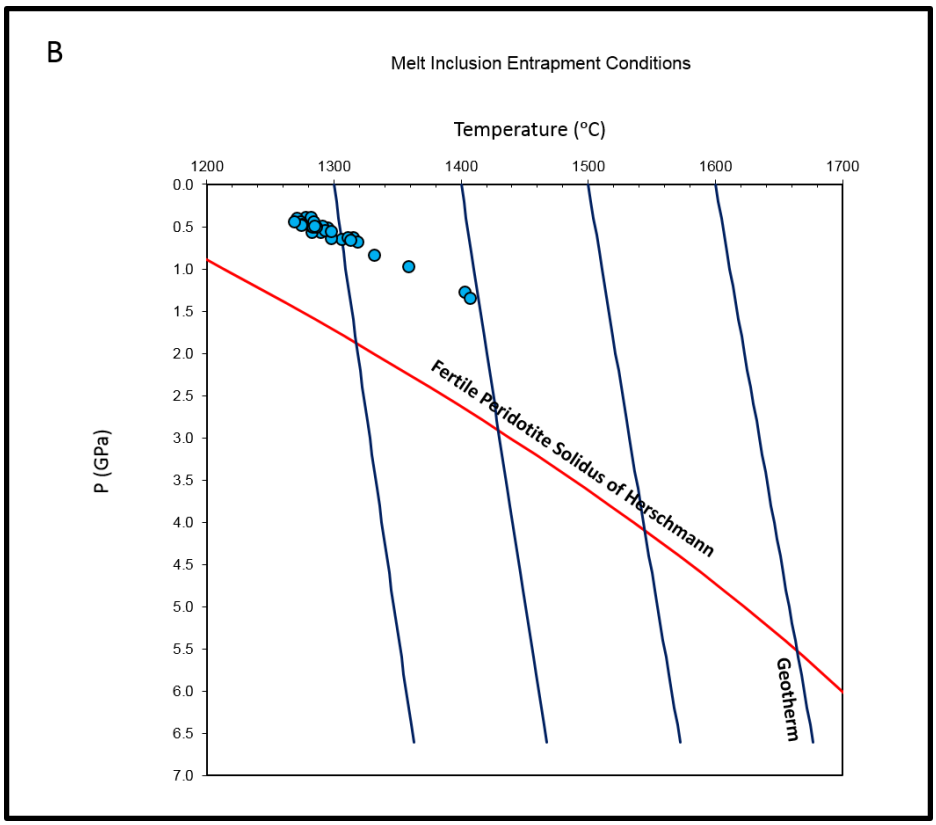

Figure 4.10: Melt inclusion entrapment pressures and temperatures calculated using methods from Lee et al. (2009) A) temperature and pressure conditions calculated for each melt inclusion containing 9 wt. % MgO (blue dots) B) temperature and pressure conditions calculated for each melt inclusion containing 10 wt. % MgO (blue dots).

The composition of the melt inclusions vary slightly across those that have been measured - most contain 9-11 wt. % MgO. Melt inclusions with a higher MgO compositions are generally associated with olivines with a more forsterite rich core. Fourty four melt inclusion analyses contain more than 9 wt. % MgO for input into the Lee et al. (2009) thermobarometer. For melt inclusions with 9 wt. % MgO content, temperatures range from 1242°C -1269°C (±38°C) with most temperatures falling within the range 1252°C-1268°C (±38°C), this is in agreement with the temperatures calculated using the Beattie (1993) thermometer. For melt inclusions with 10 wt. % MgO content, temperatures were slightly higher mostly ranging from 1274°C-1315°C, still in agreement with the Beattie (1993) thermometer within error. All compositions used for the calculations are the corrected compositions due to post-entrapment crystallisation.

Pressures calculated range from ~0.37-0.43 GPa (± 0.2 GPa at 2σ uncertainty) for the lower temperatures (lower MgO content) and ~0.38-0.62 GPa (± 0.2 GPa at 2σ

uncertainty) for the higher temperatures (higher MgO content). This difference in pressure and temperature calculations may be indicative of two or more different olivine populations, one crystallising from a hotter magma at a greater depth, before mixing or settling and becoming entrained in magma from another source. Major and minor element data are analysed later in the chapter for further discussion of the olivine sources.

The pressure and temperature conditions as calculated from Lee et al. (2009) at which the melt inclusions were entrapped are ~1250-1300°C and ~0.4-0.5 GPa at ~12-15km depth. The position of the melt inclusions within the more homogeneous interior of the olivines is evidence that diffusion occurred at some time after the melt inclusions were entrapped and so the melt inclusion temperatures will be too hot to be appropriate for the diffusion modelling. Instead the matrix glass temperatures are more appropriate and will be used for the diffusion modelling providing a temperature minimum (1168°C). The average pressure calculated from melt inclusion compositions using the barometer from Lee et al. (2009) is ~0.4 GPa. A pressure of 0.2 GPa has been inferred as appropriate for the diffusion model as diffusion occurred closer to the surface. This value will not have a large effect on the timescales calculated, as diffusion does not have high pressure dependence (as discussed in chapter 2).

4.2.4.2. Oxygen fugacity (fO_2)

Oxygen fugacity is applied differently to the tephra olivines than the lava flow olivines. This parameter has been applied with the same rationale as the PdF samples. According to Rhodes and Vollinger (2005) the oxidation state of rapidly-quenched vent lava is less oxidised than lava flows at some distance from the vent. The vent lavas are closer to the MW (Magnetite-Wustite) buffer. At the temperatures calculated, the MW buffer is ~NNO -0.5 log units. This value has been applied to the tephra olivines.

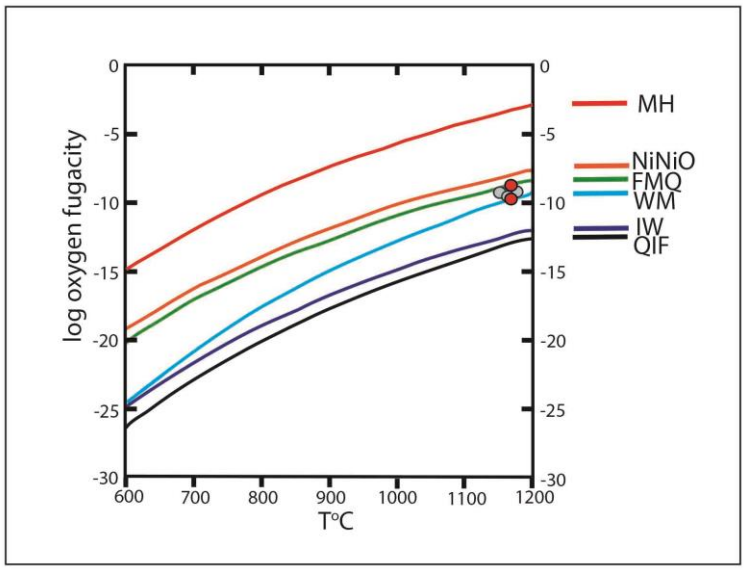

Figure 4.11: A selection of oxygen fugacity values that were used for recent Mg-Fe diffusion studies (grey circles) by Shea et al. (2015a), Rae et al. (2016), and Hartley et al. (2016). Studies are either Hawaiian or similar studies. The oxygen fugacity values I have used for the tephra olivine and later the lava flow olivines, are plotted in red.

It is clear from figure 4.11 that the values I have used for oxygen fugacity and temperature are in good agreement with those used by other authors studying similar samples.

4.2.5. Diffusion modelling of tephra olivines

Compositional traverses were retrieved from the olivines for input into AUTODIFF using similar methodology as the PdF traverses in chapter 3. Core and rim values were measured using the EPMA with a focused beam of 15-20kV and a beam current of 40-50nA. Peak counting times were as follows; 60s for Ni and Mn, 40s for Si, Fe, and Mg, 30s for Al and 20s for Cr. Most analyses returned totals of 98.5-101.2 wt. %. Repeat analysis of the San Carlos olivine standard were used to estimate the precision of Fo measurements. The Fo content of the San Carlos olivine was determined with a precision of 2σ = 0.05-0.14 mol. % (n=66). Primary standards and detection limits are reported in Appendix C.

Several handfuls of tephra yielded 127 olivine grains. From these crystals, 77 were zoned (55%) and suitable for modelling. It is likely that the unzoned olivines are of zero age, stirred in to the magma just prior to eruption. They are of similar size to those that are zoned showing no distinct differences in the backscatter images however they were not analysed for composition.

Of the zoned crystals, 91 traverses were retrieved for modelling. Two or three traverses were taken from the same crystal slice (at different orientations) where

possible and any crystal was targeted – no particular crystal slice shape was prioritised.

The olivines exhibit much longer diffusion profiles (figure 4.12) than those from the PdF olivines (by a factor of up to 3).

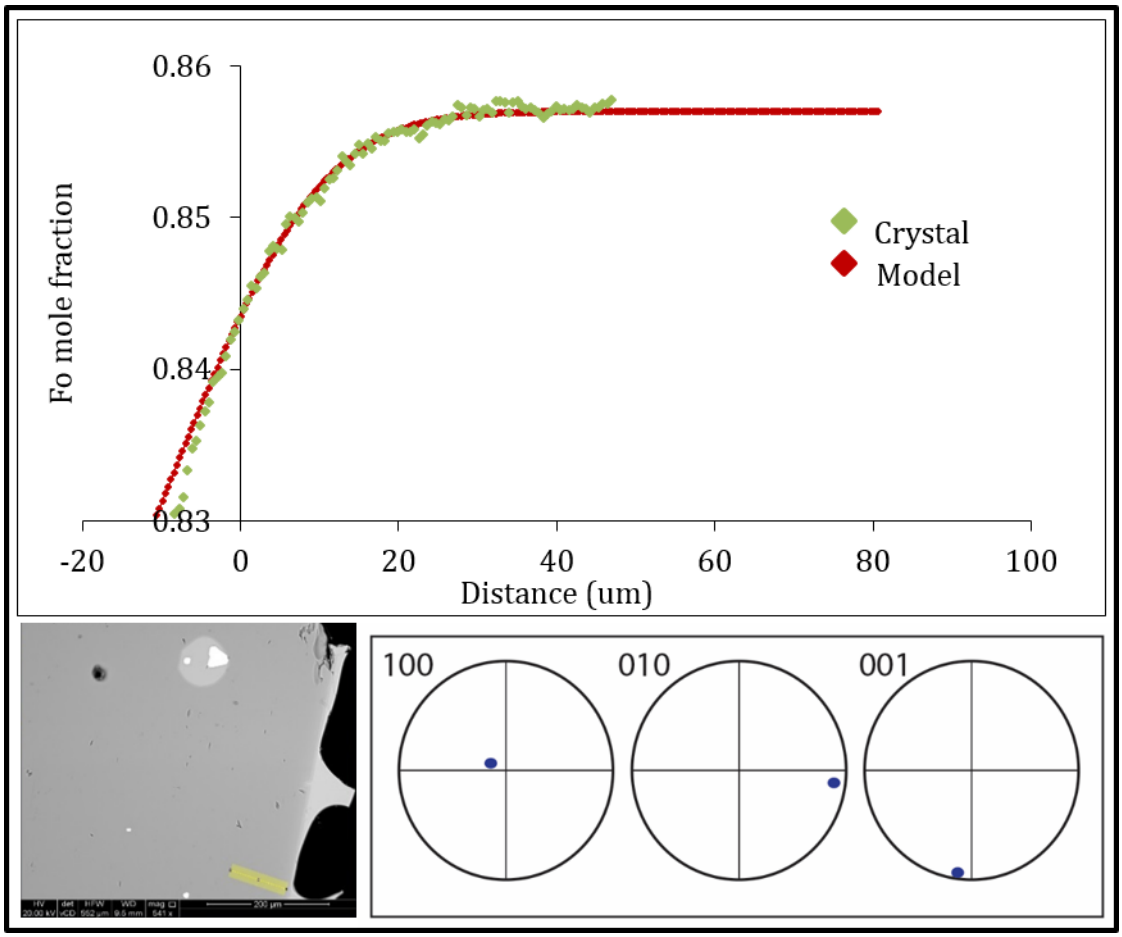

Figure 4.12: Example of the compositional profile (green) and model fit calculated using AUTODIFF (red) for an olivine crystal (Block 4_Q_2). The SEM image shows the position where the profile was extracted (yellow). The pole figure displays the crystallographic orientation data processed in Aztec Channel 5.

The compositions of the Hapaimamo olivines are also significantly more forsteritic (core compositions > Fo_{84}) and they lack the more evolved compositions at the crystal rim (> Fo_{75}). The more primitive compositions of the Hapaimamo olivines and the longer length of the diffusion profiles indicate that this diffusion is not a purely late-stage phenomenon; diffusion must have occurred within the magma plumbing system due to changes in magmatic conditions.

4.2.5.1. Timescales

The timescales were calculated using a temperature of 1168°C (calculated from *Montierth et al., 1995*), an fO_2 of NNO -0.5 log units (after *Rhodes and Volinger, 2005*) and a pressure of 0.2 GPa (calculated from *Lee et al., 2009*). The timescales range from 9-1112 days – (days to years) (figure 4.13). The average uncertainty on each calculated timescale is 0.35 log units (1σ). This is a much wider range of timescales than that seen within the PdF dataset and even at this point implies that this crystal population is not a simple, monodispersive population such as that observed at PdF.

Across the population, few crystals are demonstrably affected by growth/changing boundary conditions during diffusion (8 traverses out of 91). No corrections for shallow sectioning angle have been applied. These crystals are of similar size to those found in the PdF lava flows. Using the PdF crystals as an example (discussed in chapter 5) it is detailed that for crystals of this size, traverses affected by 'stretched' diffusion fronts (due to shallow sectioning) will be overestimated in time by only ~5%. On the scale of days this is negligible (less than half a day difference), but on the timescale of years, this overestimate is proportionally more significant (timescale would be overestimated by ~6 weeks). However, overestimates will be within the error on the timescale uncertainty for most datasets.

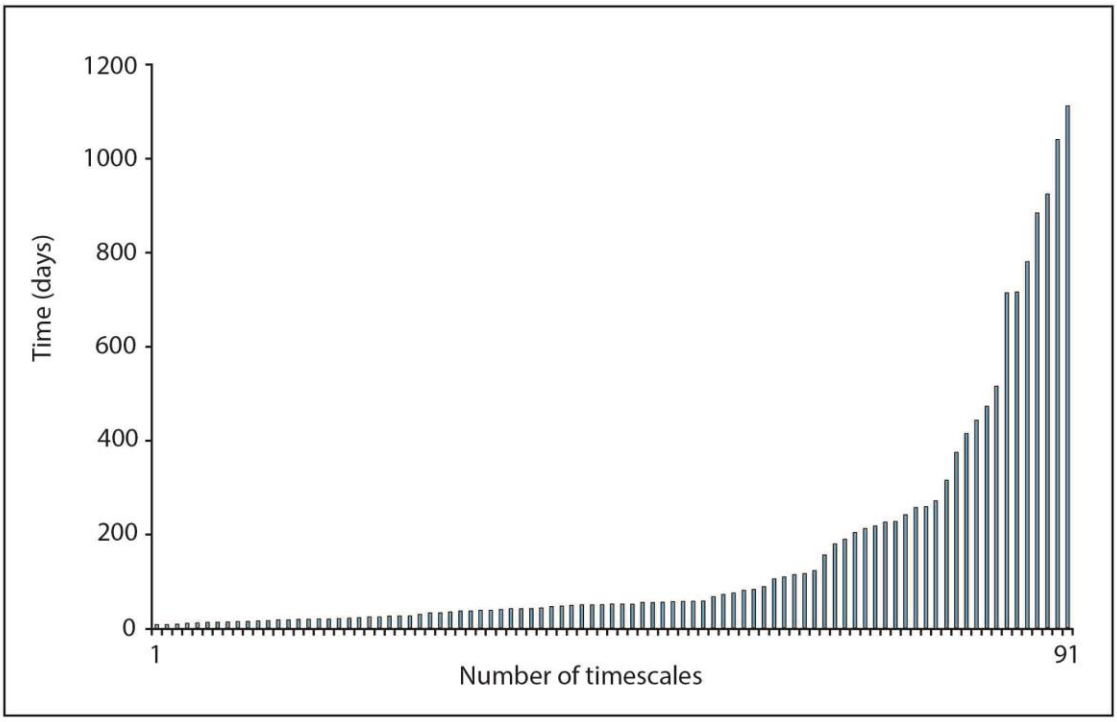

Figure 4.13: The distribution of timescales extracted from olivines within the Hapaimamo tephra deposit (n=91).

It is important to clarify whether the wide range in timescales is due to anomalous data points or the presence of one or more crystal populations. If it is due to the latter, further interpretation of the origin and transport of the crystals and the timescale over which this occurred is important. This information will reveal more detail of magma movement from the magma's source through the plumbing system. A quick and simple method to classify different crystal populations will be necessary as part of the streamlined processing methods. This will enable the dominant population and related timescale information to be retrieved and more complex or older populations to be flagged for a more detailed diffusion study using the more traditional methods.

Timescales were grouped according to which crystal slice they were retrieved from. It was found that many of the longest timescales were retrieved from the same crystal, leading to the initial conclusion that some of these crystals do indeed belong to an older (possibly smaller) population of olivines, an example of which is shown in figure 4.14.

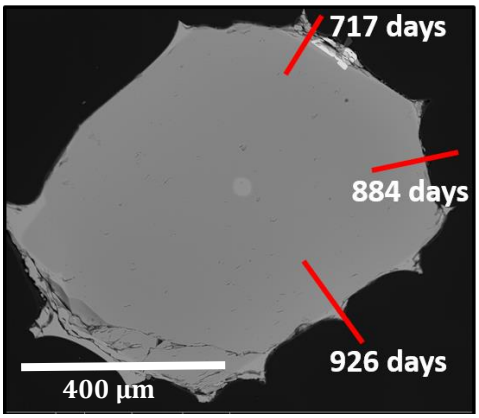

Figure 4.14: An SEM image of an olivine identified within the Hapaimamo tephra deposit. The timescales calculated from three crystal faces are labelled (they are EBSD corrected). These timescales are consistently long in duration compared to the majority of other timescales from the Hapaimamo leading to the initial conclusion that this may be part of a smaller, older crystal population.

These timescales within the same crystal do not correct to a single timescale. This may be due to some shallow sectioning, a small amount of changing boundary conditions and/or growth effects or out-of-plane diffusion. Nonetheless, they are all within the same longer range. To further conclude whether all of these olivines are one continuous olivine population or at least two separate populations requires further study of their chemistry (major and minor element compositions) and crystal textures. There are no obvious textural differences (i.e. disequilibrium textures) between the crystals of the two populations nor is there evidence of any mixing within the 2nd crystal population with a more primitive or heterogeneous melt (i.e. Mg-rich rim from a more primitive magma (*Kohn et al., 1989*).

The olivines are considered as two populations based on the bimodal timescales extracted. There is no significant difference in forsterite core values between the two 'populations' that would lead to two distinct clusters. This suggests that all of the olivine cores may have come from a similar source. There is more variation in the forsterite rim values (olivine rims were measured ~5 µm from the crystal edge) – those for the 2nd population lie consistently at ~Fo_{83-81} but mostly Fo_{82}. Rim values for the 1st population show a much wider compositional range ~$Fo_{86-81.}$ This is indicative that although the cores may have come from a similar origin, the rims are consistently lower in Fo for the 2nd population implying that these crystals have been diffusing for longer (these produce much longer diffusion timescales) and may

have undergone different magmatic processes in a slightly more evolved magma. Both the olivine rims and cores are out of equilibrium with the carrier melt. To be in equilibrium with the rim compositions, the melt Mg# would be expected to be between Mg_{60-65} (using the Rhodes diagram) however it is ~ Mg_{53}. To be in equilibrium with the olivine core compositions the liquid Mg# is expected to be even higher (~Mg_{70-75}).

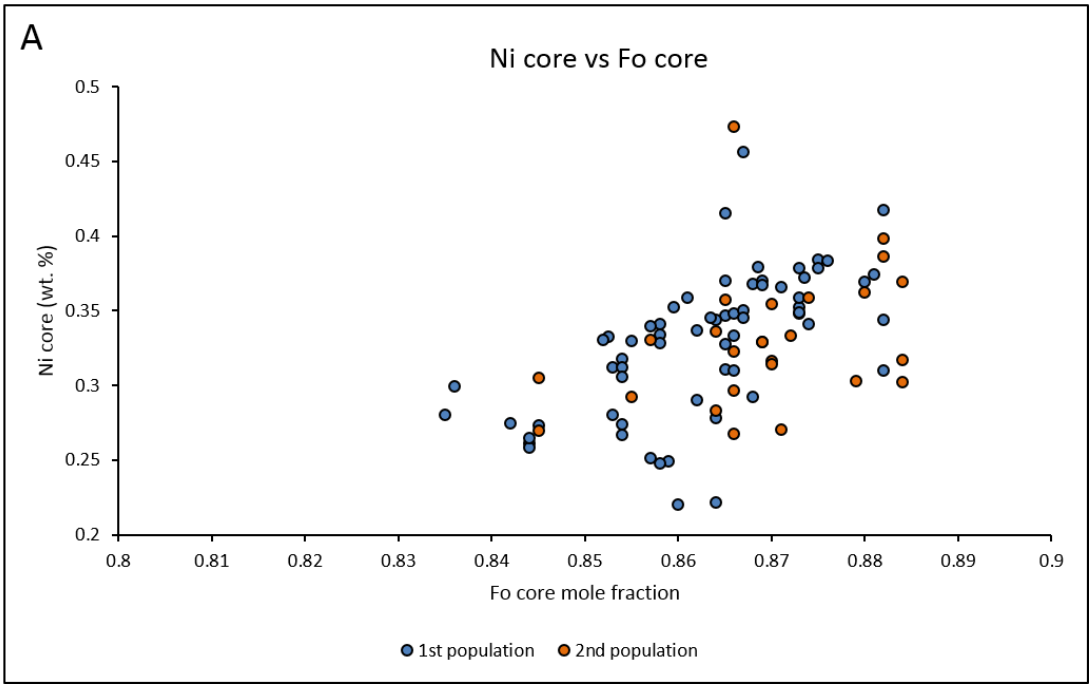

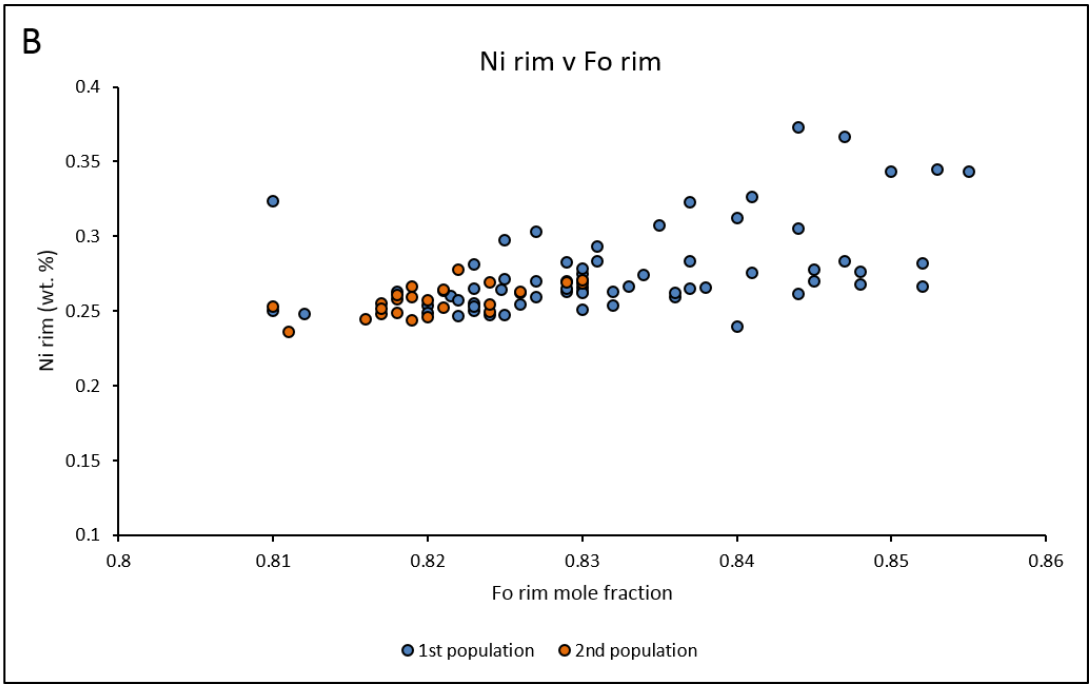

Figure 4.15: Nickel (Ni) core (A) and rim (B) compositions plotted against their forsterite equivalent for the two crystal populations.

There appears to be no distinct trend between the nickel and forsterite content of the olivine cores, consistent with the assumption that these cores have come from a similar source. However, there is a much tighter range of Ni concentrations at the rims of the crystals, giving two distinct trends. A more restricted Ni range shown by the 2nd population indicates that these crystals have undergone magmatic processes within a more fractionated magma (*Herzberg et al., 2013*) whereas the wider variation and higher concentration of Ni within the 1st population is indicative of residence in a more primitive, mantle-like source (*Herzberg et al., 2013*).

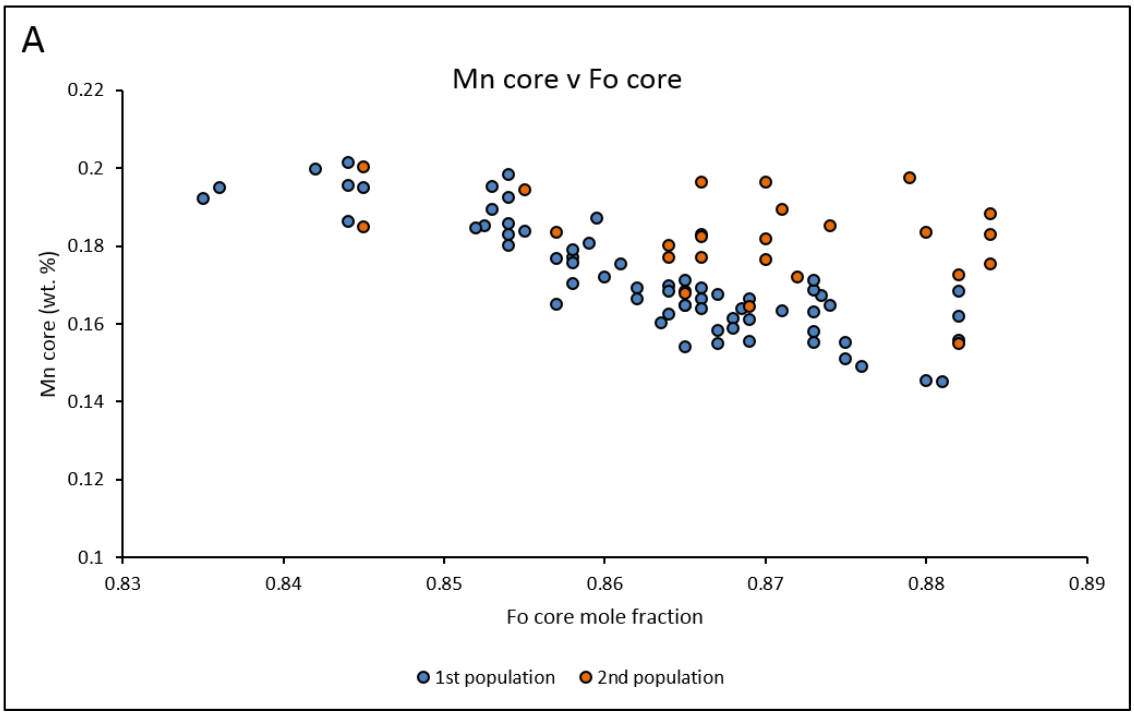

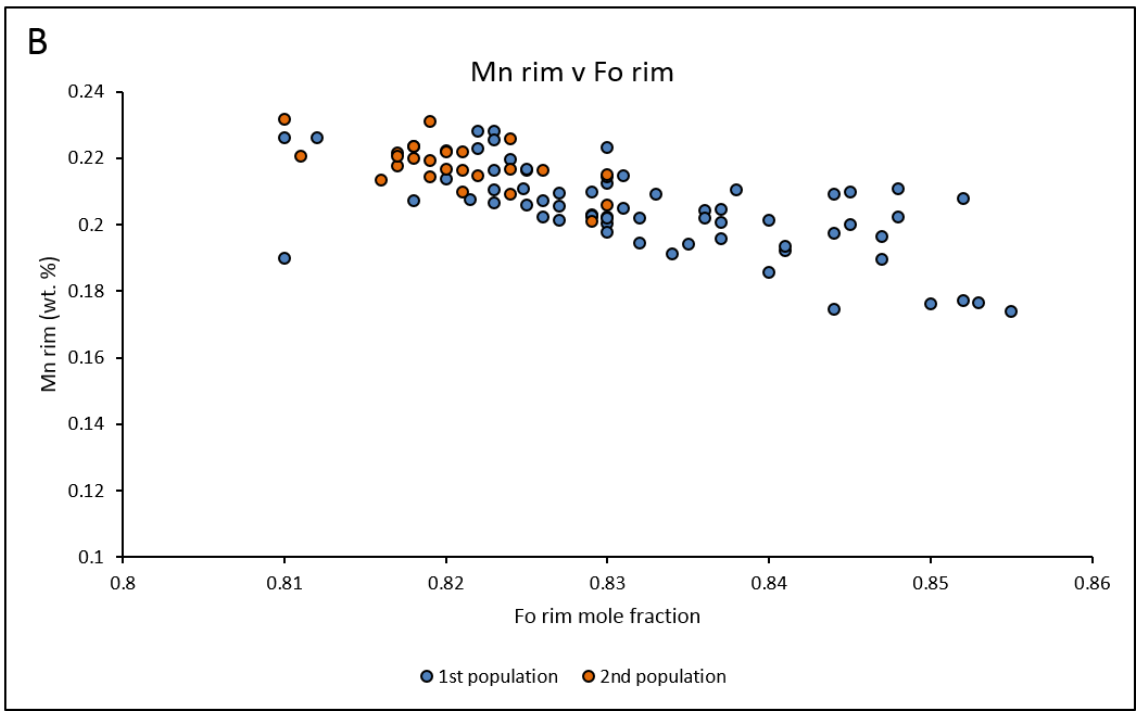

Figure 4.16: Manganese (Mn) core (A) and rim (B) plotted against their forsterite equivalent for two crystal populations

The cores and rims within the 2nd population mostly have higher Mn contents than those within the 1st population, evidence again for each set of populations having experienced slightly different magmatic environments. The higher Mn contents are consistent with the assumption that the 2nd crystal population fractionated in a more evolved magma.

This minor element data has helped to highlight subtle differences between two populations of olivines and their journeys through the magma plumbing system. All of the olivines show normal zoning (Fe-rich rim, Mg-rich core) which is consistent with decompression effects i.e. melt moving from depth to a shallower reservoir. Picrites are generated from melting at higher pressures (and depths) (*Herzberg and O'Hara, 1998*). When a high pressure partial melt decompresses at shallower depths, olivine precipitates to maintain equilibrium as the melt ternary changes (*Best, 2002*).

The consistent variation in high forsterite core compositions of both populations and variable Ni contents is indicative of a deep storage reservoir that is not uniform in composition (*Garcia et al., 1995; Gaffney 2002*). This may be due to input of magma

with local variations in composition due to heterogeneity in mantle melting and/or melting temperatures (*Norman and Garcia, 1999; Garrett and Mahoney, 2005*) or differentiates from deeper storage areas (*Chen, 1993)*. The 2nd (older) population have potentially been transported within a slightly more evolved magma from depth, supported by consistent Fe-rich rim compositions and low Ni and high Mn rim compositions to be stored as part of a mush (*Gaffney, 2002; Passmore et al., 2012; Neave et al., 2014*). Here they have diffusively re-equilibrated for some time (months to years). Transport of the 1st population in a less evolved carrier liquid from depth to the rift zone occurred much closer to the time of eruption than the 2nd population of crystals.

The range in pressures calculated from the melt inclusions (0.4-0.2 GPa) implies crystallisation and melt entrapment at various depths as the magma ascended. This is consistent with the Gaffney (2002) study on Mauna Loa xenoliths, which formed from crystalline remnants of Hawaiian magma. The diffused zone of the Hapaimamo crystals does not engulf the melt inclusions positioned nearer to the crystal cores which reaffirms the assumption that diffusive timescale represents the effects of pressure change after magma ascent.

Gaffney (2002) summarised that a large steady-state magma chamber, with homogeneity maintained through continuous replenishment of more primitive magma (*Rhodes, 1988*) is not consistent with an environment that could produce diverse compositions observed (consistent with my dataset). Gaffney (2002) states that small, isolated magma storage areas under Mauna Loa's SW rift zone and within the lower crust provide environments where crystallisation likely occurs. These isolated regions are free from frequent magma replenishment which would give rise to disequilibrium textures and hinder magma differentiation (*Gaffney, 2002*). Within these storage areas the magma crystallises undisturbed during episodes of low magma flux. Episodes of higher magma flux are associated with eruption of picritic magmas (*Rhodes, 1995*). During these high flux eruptions, magmas and crystals within these storage regions (the 2nd population) may then become entrained into the carrier liquid within the primary conduit. As the eruption rate decreases these picritic magmas may be abandoned back into these storage areas to crystallise the

next generation of magmas (*Gaffney, 2002*). This process may be cyclical leading to differences in the olivine compositions observed.

The short duration of many of the olivine timescales (8+ days) within the 1st population is indicative that magma ascent was rapid prior to eruption. The ascent rate has been calculated at ~0.01 m/s which is consistent with literature values for dyke propagation (*Rubin, 1995*). Short timescales also indicate that the shallow storage system was replenished shortly before eruption and may have remained an open system during the explosive eruption of the reticulite tephra layer. The 2nd population of crystals were likely mobilised into the carrier melt, from storage regions within the rift zone shortly before eruption. These processes are summarised in figure 4.22, on page 124.

4.2.6. Lava flow sample description

Each lava flow sample is described collectively as they are assumed to be part of the same event. Differences in texture are outlined if present. H1 and H2 were sampled from the same lobe taken from laterally different sections. The sample from the upper lobe, H3, is hypothesised to be a later flow, but part of the same eruption event.

4.2.6.1. Textural description

Large olivine crystals (500 μm – 4 mm in size) are contained within a completely crystalline fine grained groundmass (~50-200 μm in size) made up of clinopyroxene, plagioclase feldspar, and oxides, mineralogically similar to sample 64217 from PdF, although olivine is missing from the groundmass. There are also distinct textural differences. The large olivines are commonly subhedral or rounded. More curiously, many of these large olivines exhibit a corona of pigeonite (low Ca clinopyroxene) ~50 μm wide, as shown in figure 4.17.

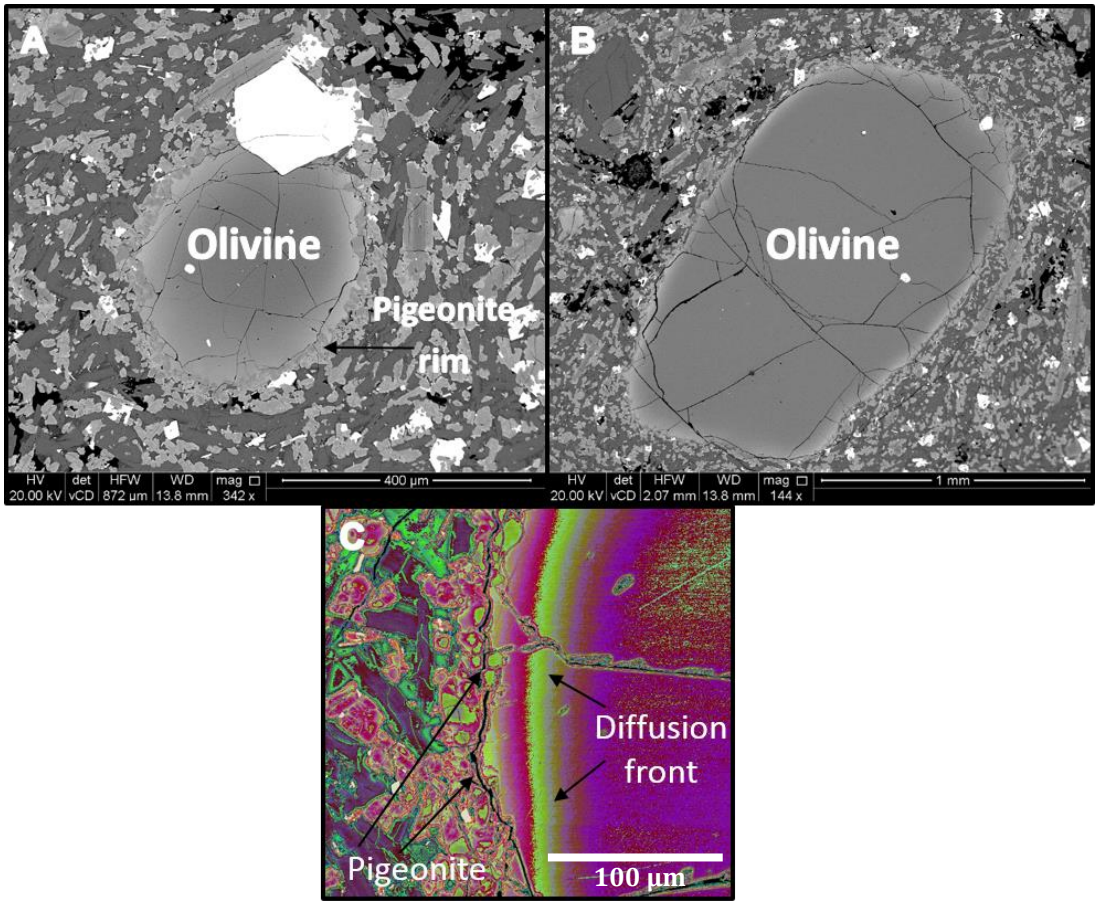

Figure 4.17: A) A large olivine with a rim of pigeonite from H1LC B) A large olivine without the rim of pigeonite from the same sample C) False colour SEM image showing the pigeonite rim cross cutting the diffusion front in places

This texture may be due to co-growth of pigeonite with olivine along the cotectic, evidenced by partial inclusion of the pigeonite crystals within the olivine as it has grown. Alternatively, it could be a result of disequilibrium reaction between the olivine crystal and a more silica-rich magma than the olivine parent magma (*Coombs and Garner, 2004; Erdmann et al., 2012*) or it may be due to peritectic crystallisation (*Zellmer et al., 2015,*).

Zellmer et al. (2015) suggest that dissolution of Mg-rich olivine results in an enrichment of Fe at the crystal rim and enrichment of Mg in the melt boundary layer surrounding the crystal. Orthopyroxenes will then nucleate and grow in this melt boundary layer. Once these orthopyroxenes touch the rim of the dissolving olivine they shield the crystal from further dissolution by the silica rich melt, hence the lack of complete replacement of the olivine. Then Fe-Mg inter-diffusion begins to destroy the Fe-enrichment at the olivine rim. A lack of a strong Fe-enrichment at the rim

(<Fo_{82}) of the large olivine within Hapaimamo is evident. Zellmer et al. (2015) postulated that this reaction was completed when the dissolving olivine crystal is completely mantled by orthopyroxene microlites. The pigeonite rim and lack of olivine in the groundmass suggests that these larger olivine crystals are out of chemical equilibrium with the carrier liquid and are xenocrysts.

The pigeonite rim resulting from the reaction between olivine and liquid could be a product of magma mixing (*Gerlach and Grove, 1982; Erdmann et al., 2012*). A diffusion profile from the rim may give information of the time elapsed since the mixing event – olivine crystals up taken into the more silica rich melt and erupted at the surface (*Coombs and Gardner, 2004*). However, the pigeonites can be seen to cross cut the diffusion front (figure 4.17C), meaning that diffusion occurred prior to the 'mixing' or the crystallisation of pigeonite and dissolution of the olivines. It is more likely that this mantle is due to a combination of both reaction and intergrowth. This pigeonite mantle is present on olivine crystals in all three samples, H1CL, H2CL, and H3CL, however there are olivines that also do not exhibit this texture. These olivines are round and have a thinner diffusion rim (figure 4.17B).

There is evidence of flow alignment of plagioclase around olivine xenocrysts, as seen in figure 4.17B and 4.18D. Crystals are not of equal size, with some plagioclase crystals are up to 1mm in size (figure 4.18A). There are large (~600 μm) crystals of pyroxene and plagioclase found within the clinker and the lava core, either as individual crystals or intergrowths (figure 4.18B). Most olivine display an Mg-Fe inter-diffusion rim up to 200 μm wide. Olivine display shapes from perfectly euhedral to strongly subhedral. These differences are clear between adjacent grains (figure 4.18C). Within H3CL there appears to be a stronger flow alignment fabric (figure 4.18D). The orthopyroxene rim encasing some olivine doesn't seem to be as prevalent (or even to be in existence) within sample H3CL (figure 4.18D). This may suggest that the magma is slightly more mafic within the lower flow.

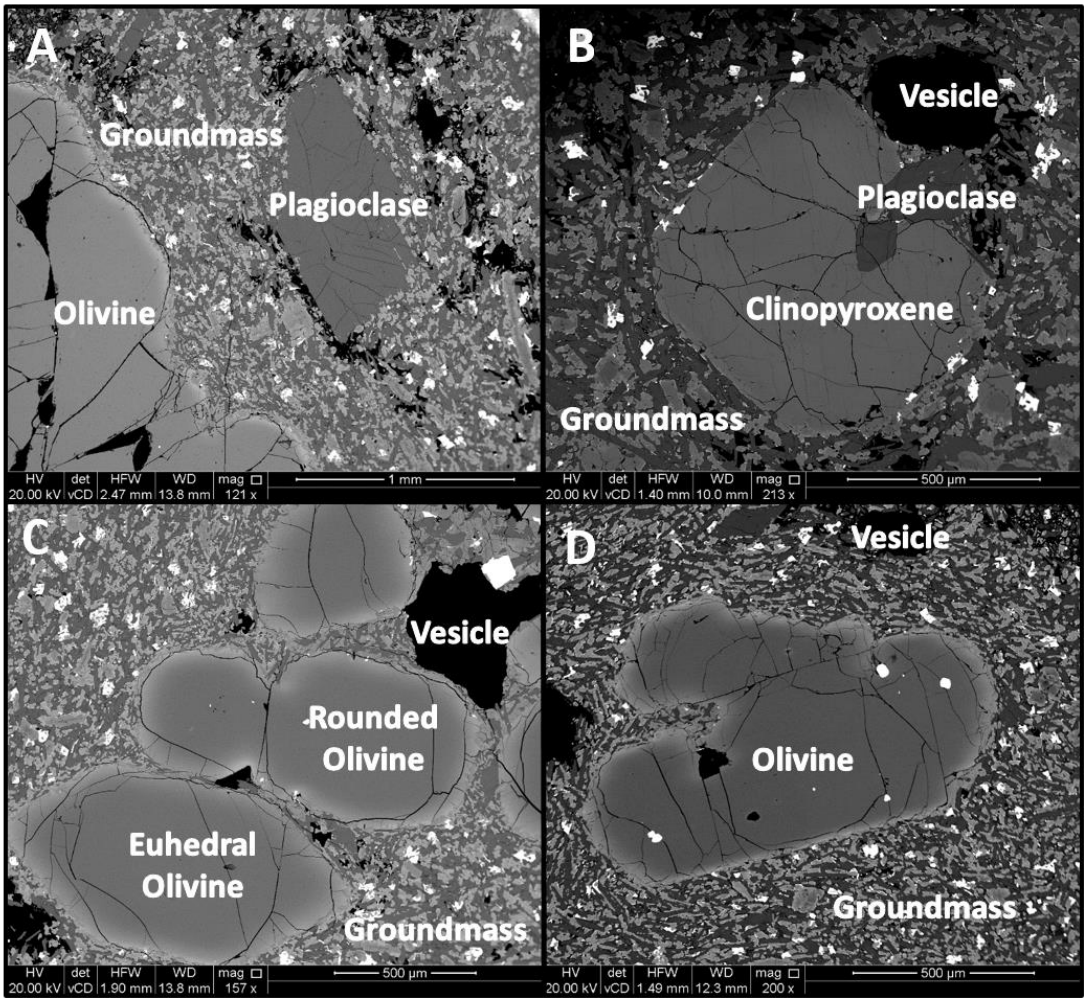

Figure 4.18: A) A large plagioclase crystal adjacent to an olivine crystal B) An intergrowth of plagioclase and clinopyroxene within the clinker C) euhedral and subhedral olivine crystals exhibiting compositional zoning D) some alignment of groundmass crystals possibly linked to a predominant flow direction.

4.2.6.2. Mineralogy

Olivine

Olivine crystals are present as xenocrysts from 1-4 mm in size. These crystals often display a reaction rim of orthopyroxene, as described in the previous section. All samples contain 5-8% modal abundance of this xenocrystic olivine within the lava core. Modal abundances within this mineralogy section have been determined using point counting software, '*JMicrovision'*. Due to their chemical disequilibrium and high abundance I have termed these olivines xenocrysts.

Olivine is not present in the groundmass. The xenocrystic olivine exhibit (for the most part) wide edge zoning from ~100-200 µm for samples H1CL and H2CL and

narrower edge zoning for sample H3CL from ~40-60 µm. H1 and H2 are from the same lava sheet, whereas H3 is from the one above.

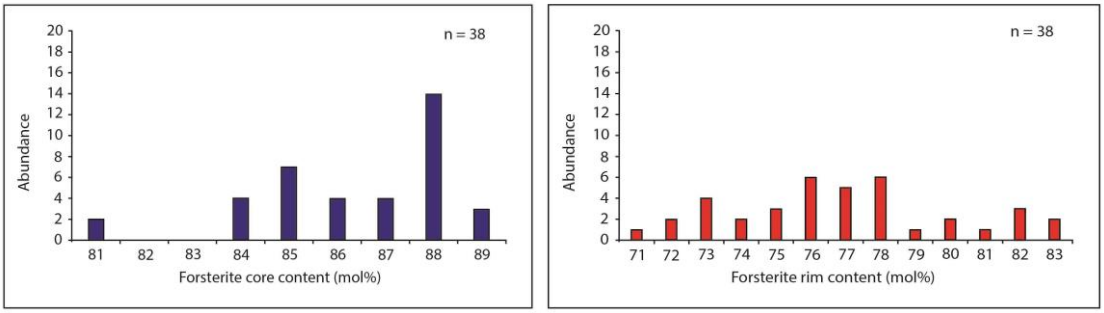

Figure 4.19: Core and rim values plotted by abundance of the Hapaimamo olivines within the lava flow.

Figure 4.19 shows core values range from Fo_{81-89}, but mostly range from Fo_{84-89}. Rim values range from Fo_{71-83}. These differences between rim and core values of various xenocrystic olivine may point to the presence of more than one crystal population. All of the olivine analysed displayed normal zoning patterns (Mg-rich core, Fe-rich rim). Olivine can be euhedral in shape but most display rounded or subhedral shapes which are consistent with disequilibrium processes. Olivines rarely contain melt inclusions, but where they do, they have undergone post-entrapment crystallisation (*Gaetani and Watson, 2000*). Some olivine contain inclusions of chromium-spinel, often several crystals can be present per olivine and the spinels can vary in size up to 80 µm.

Plagioclase

Plagioclase is present in the groundmass with a modal abundance of ~55-57%, often ~50 µm in size. Larger crystals up to 1 mm in size can be found (figure 4.18A) sparsely throughout the samples. These occur in isolation, or as intergrowths or glomerocrysts with clinopyroxene crystals. All crystals are lath or brick shaped and don't appear zoned, with core values of An_{60-69}. Only one rim was analysed due to time constraints with a value of An_{63}.

Clinopyroxene

Clinopyroxene crystals are present in the groundmass with a modal abundance of ~30-50%. They also occur as intergrowths or glomerocrysts with plagioclase or as larger isolated crystals, often up to 1mm in size. Clinopyroxenes frequently exhibit

a uniform rim ~20-40 μm in width. Both the smaller and larger clinopyroxene crystals show complex zoning often showing resorption textures. Magnesium number ranges from Mg_{76-81} in the core to Mg_{71-80} at the rim. Low Ca -pyroxene known as pigeonite is present around some rims of the large olivine crystals. They are often rounded or sub-hedral with some edge zoning, ~30 μm wide. They have a composition of Mg_{73-75}.

Oxides

The oxides in the groundmass are composed mostly of chromium-spinel (with an average Cr number of 0.50) and titanomagnetite (with an average ulvospinel component of 0.61). The oxides are present in < 5% modal abundance. They are frequently included within olivine and can be found as larger crystals up to 80 μm in size.

4.2.6.3. Whole rock geochemistry (XRF)

Major element analyses were determined by X-ray Fluorescence (XRF) at Origin Analytics, Welshpool using a 4KW Bruker S4 WD-XRF machine. Around 10g of homogenised powders were analysed from the bottom crust, centre lobe and top crust of sample H2. Procedures were followed as outlined in chapter 2, section 2.5. Calibrations were based on 25 geological reference materials and drift was monitored.

To have an idea of accuracy and reproducibility of the data, the published values of Harvey et al. (2012) for KH03-2 peridotite and KH03-10L basalt from Kilbourne Hole were compared to re-analysed values from these samples by Origin Analytics and percentage differences were calculated. As my samples are picritic, their compositions fall within this range of compositions. For the basalt, all major oxides (SiO_2, TiO_2, Al_2O_3, Fe_2O_3, MnO, MgO, CaO, Na_2O, K_2O and P_2O_5) were reproducible to within 3%. For the peridotite, SiO_2, TiO_2, Al_2O_3, Fe_2O_3, MnO, MgO and CaO were reproducible to ~10%. Na_2O, K_2O and P_2O_5 were much more variable. The full XRF dataset can be found in Appendix G.

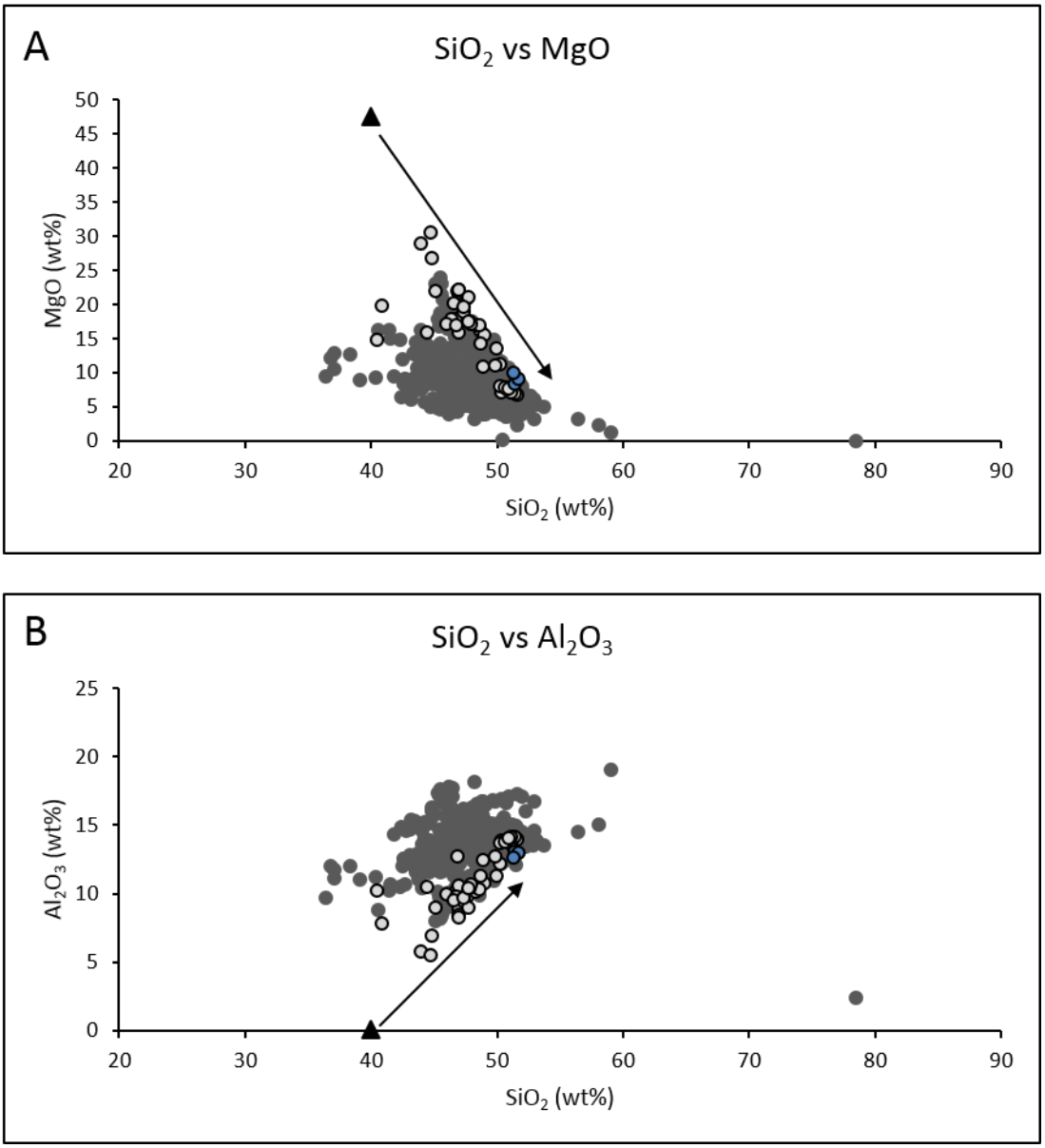

Figure 4.20: Bulk rock SiO_2 plotted against A) MgO and B) Al_2O_3. The dark grey points are a collection of published data from the GeoRock database for basalts and basalt-tholeiites, light grey points are a collection of published data from the GeoRock database for picrites, blue points are data from Hapaimamo. The black triangle in both plots is oxide weight percent of an olivine (Fo_{88}) from the Hapaimamo as measured with the EPMA.

Figures 4.20A and 4.20B show that the Hapaimamo bulk rock data is consistent with data from other studies conforming to the trend of a typical Hawaiian basalt and plotting to the higher MgO, lower SiO_2 range of Hawaiian basalts in keeping with their picritic nature. The olivine control line (black arrow) shows the compositional fractionation is controlled by the addition of olivine.

4.2.6.4. Diffusion timescales of lava flow olivines

Fourteen crystals (6 from H1LC, 4 from H2CL, and 4 from H3CL) were analysed from the Hapaimamo lava flows. From these 38 traverses were extracted, with the aim of extracting at least 2 or 3 profiles from each crystal slice. It is important to remember the relative sizes of each dataset as we gather interpretations– the tephra dataset is much larger than the lava flow dataset (91 timescales versus 38 timescales).

The timescales were calculated using a temperature of 1168°C (calculated from *Montierth et al., 1995*), an fO_2 of NNO +1 log units (after *Rhodes and Vollinger, 2005)* and a pressure of 0.2 GPa, (calculated from *Lee et al., 2009).* The matrix glass from the tephra was used as a proxy for the matrix glass temperature in the lava flow before the groundmass crystallised. If these olivines do not show evidence of significant sub-surface residence, this temperature would serve as a maximum temperature.

The timescales range from 9-535 days. The average uncertainty on each calculated timescale is 0.35 log units (1σ). Longer timescales might be expected for the profiles extracted from the lava flow olivine, if these are the same population as the tephra olivines. If the zoning in the lava flow olivines has been modified by transport processes rather than these crystals being quenched and the zoning patterns frozen akin to the olivines during the tephra eruption, diffusive relaxation would continue whilst being carried in the lava flow until cooling. These olivines may have therefore stayed hotter for longer, at optimal diffusion temperatures.

The lava flow olivines have almost identical core compositions to the tephra olivines ranging from Fo_{84-89} with one crystal with a core of Fo_{81}. The rim compositions however are much lower than those found in the tephra ranging from Fo_{71-83}. These lower values are due to continued diffusive relaxation as the crystal tries to re-equilibrate. These rim values are very similar to the lava flow olivines from PdF, discussed in chapter 3.

The similarity between olivine core compositions in the tephra and lava flow indicates that the lava flow olivines are likely from the same source as the tephra and hence have therefore undergone the same sub-surface processes. A comparison of the timescales retrieved from each dataset may further establish this. The

timescales were ordered from shortest to longest and normalised to a position in the population for this comparison.

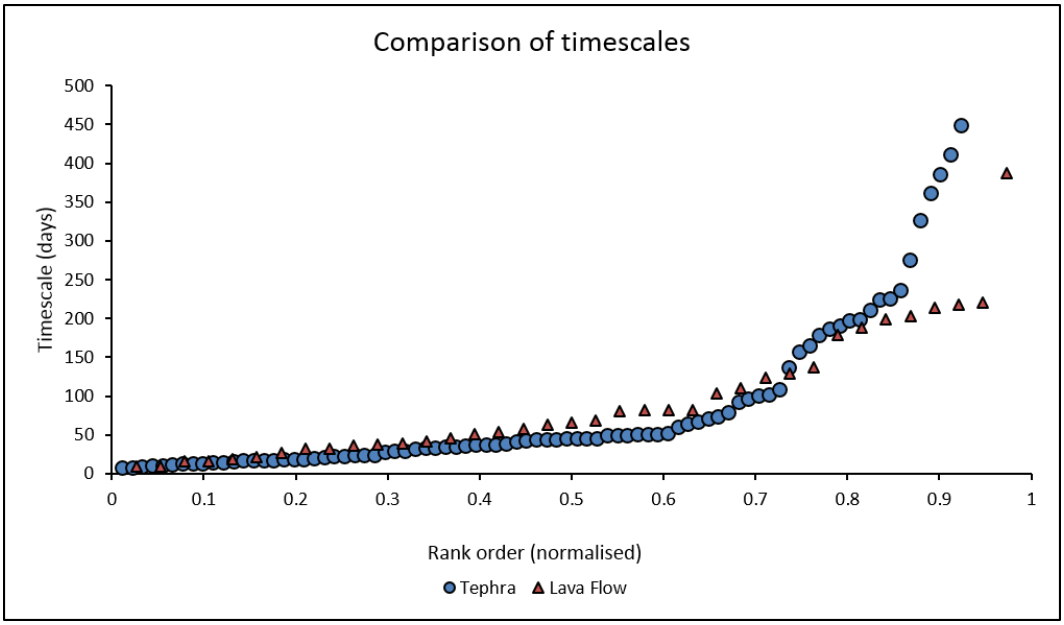

Figure 4.21: A comparison of timescales from olivines in the tephra deposit and the lava flow deposit of Hapaimamo.

Figure 4.21 shows that the lava flow timescales are comparable or slightly older than the tephra timescales. Cooling timescales calculated for a lava flow 3-5 m in thickness are ~10-30 days. This seems to account for the difference in timescales between some of the older olivines in the lava flow compared to the tephra– the lava flow olivines stayed hotter for at least a few weeks longer and continued to diffusively re-equilibrate. This is also clear from the more evolved rim compositions. Analysis of the timescale range of the lava flow olivines (9-535 days) shows that it is possible that the lava flow has also sampled at least two olivine populations that are also present in the tephra however the 1st, shorter population is more widely represented. It however needs to be considered that the lava flow dataset is much smaller than the tephra dataset (38 timescales versus 91 timescales) and may not be viable for comparison, as the 2nd crystal population may be under sampled. It should be noted that the older timescales within the lava flow dataset are considerably shorter than the older olivines in the tephra dataset, although, again, this may be an artefact of the difference in sample sizes.

If the tephra was erupted first, there is no necessity that these olivine populations need be the same. If the interval between the eruption of the tephra and the lava flow was lengthy, it is more likely that different olivine populations may have been tapped between the two events and that they have undergone similar, but not necessarily identical subsurface processes than if the eruption interval were short.

Figure 4.22 summarises the magmatic processes prior to and during the Hapaimamo eruption. A reminder that the tephra fall and the lava flow may not have occurred simultaneously, but the olivines in both deposits have similar chemistry and diffusion timescales so likely tapped similar sources.

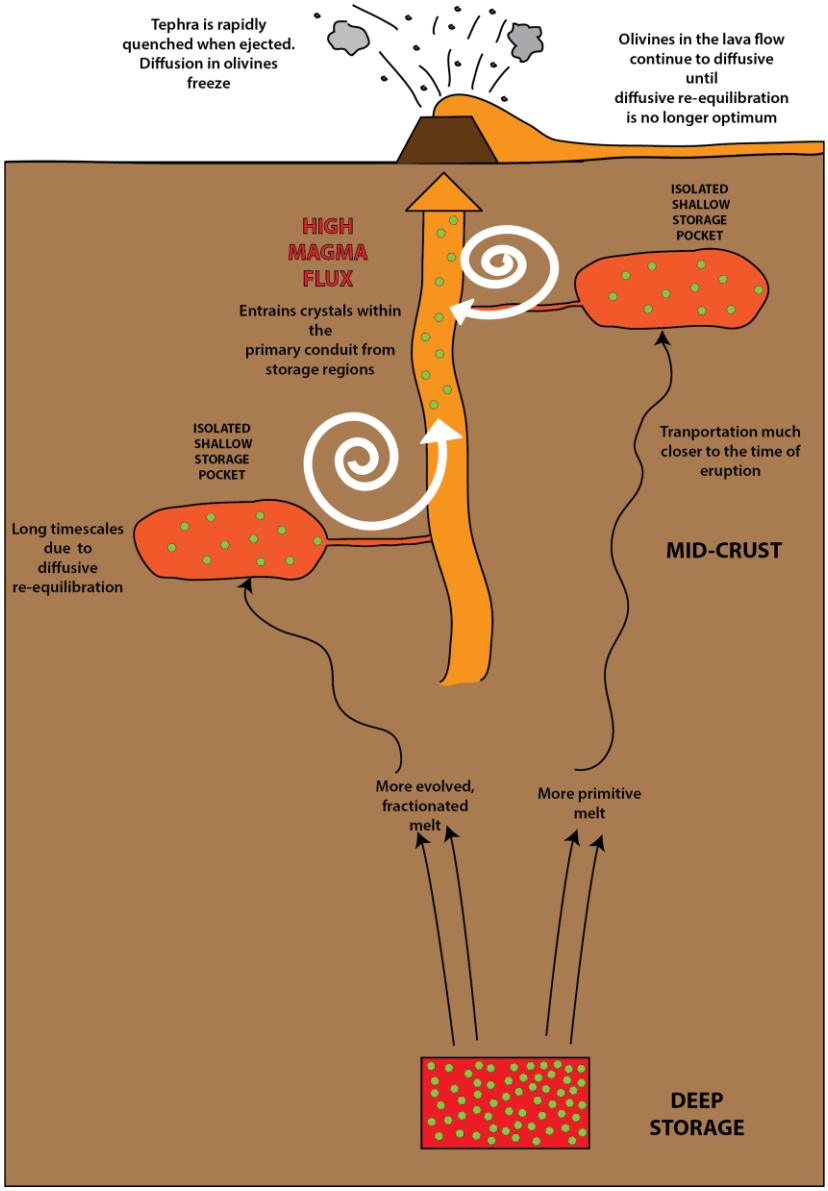

Figure 4.22: A schematic summary of the magmatic processes occurring prior to and during the Hapaimamo eruption. NOT TO SCALE.

4.3 Moinui

4.3.1. Introduction

The Moinui lava flow erupted from the SWRZ ~2100 years ago (*Perring et al., 2004*). The flow is picritic, with a very distinctive crystal assemblage of equant olivines and platy, 'bladed' olivines. The Moinui flow extends ~32 km westwards from the SWRZ to the sea. Only lava flow samples were collected, as the original issuing vent has been buried below more recent lava flow activity (*Trusdell, personal communications, 2015)*. There is at this time no other literature for this lava flow.

The flow is very well exposed in road cuts along Highway 160 near the entrance to Pu-uhonua O Honunau State Park and along Highway 11 just north of Keokea, as shown in figure 4.23.

4.3.2. Fieldwork Description and Sample Summary

Fieldwork was undertaken over several days in January 2015. Samples were taken along the road cut on Highway 160 from GR 0194285E 2150750N to GR 0194322E 2150721N (UTM Zone 5Q).

In contrast to the Hapaimamo A'a lava flow, the Moinui is a pahoehoe lava flow shown in figure 4.23.

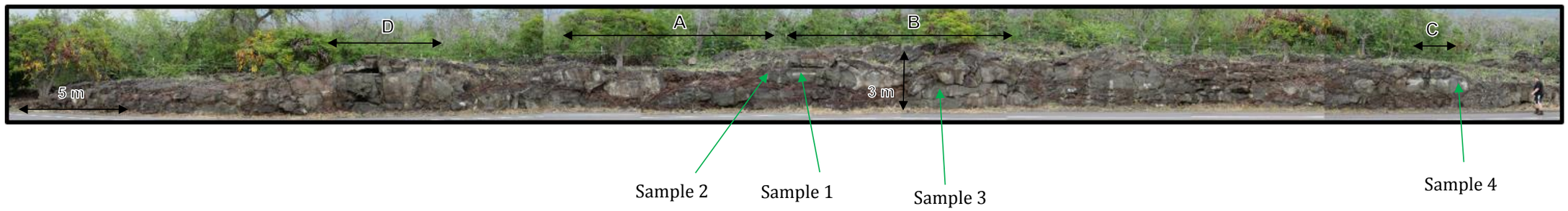

Figure 4.23: Montage of field photos across the road cut from GR 0194285E 2150759N to GR 0194322E 2150721N (UTM Zone 5Q). Field sketches across the road cut denoted A-D can be found below. Samples were taken from 4 locations. Each sample location 1-4 is consistent with the sample naming convention M1 (TC, CL, BC) to M4 (TC, CL, BC).

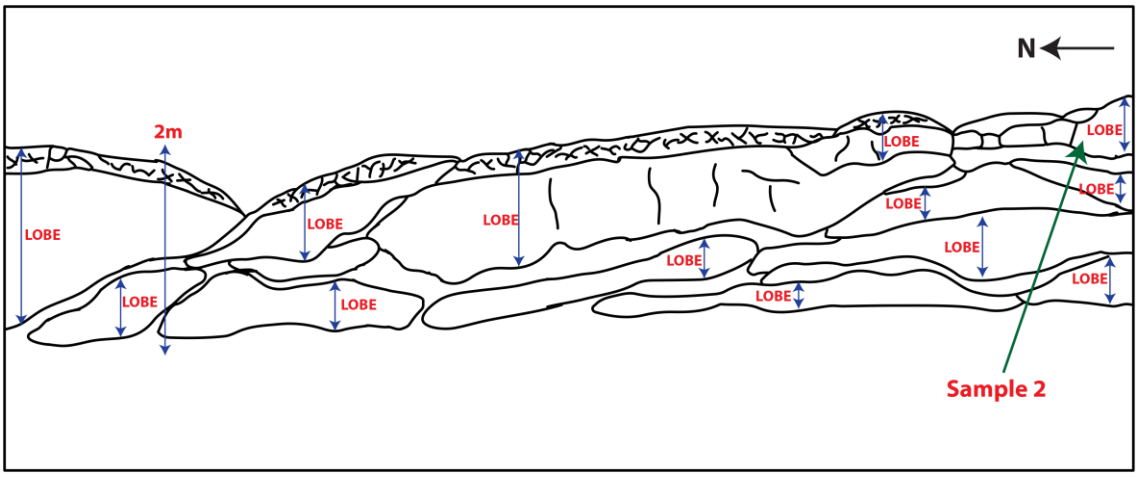

Location A on figure 4.23. Field sketch of the outcrop from GR 0194292E 2150754N to GR 0194302E 2150745N (UTM Zone 5Q) showing the distribution of the lobes and location of sample 2.

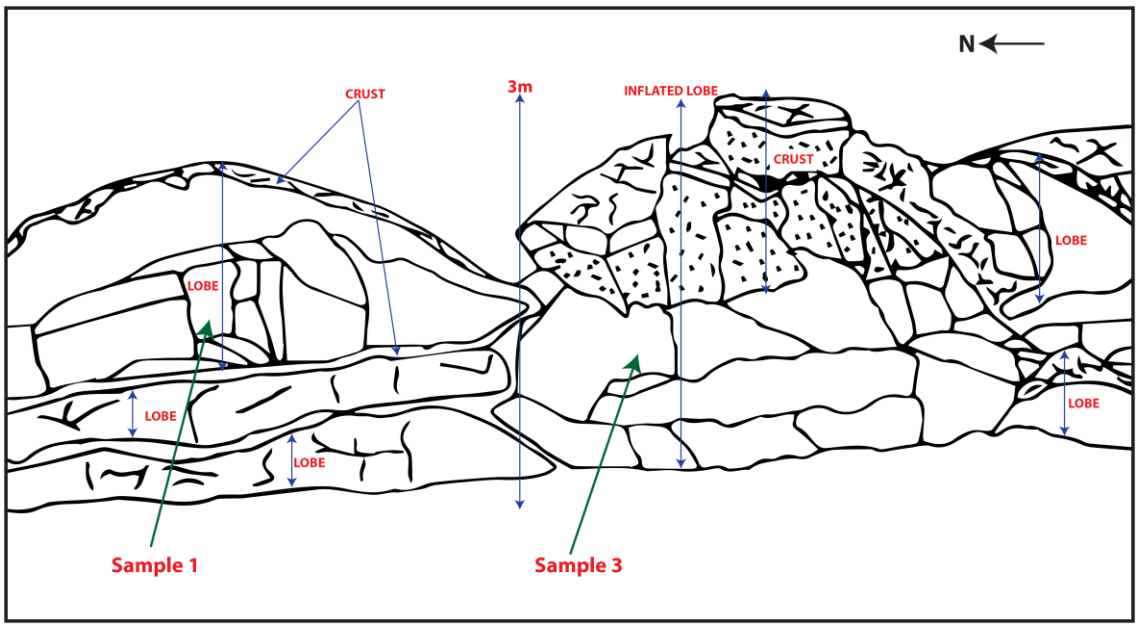

Location B on figure 4.23. Field sketch of the outcrop from GR 0194302E 2150745N (UTM Zone 5Q) showing stacked and inflated lobes and the location of samples 1 and 3.

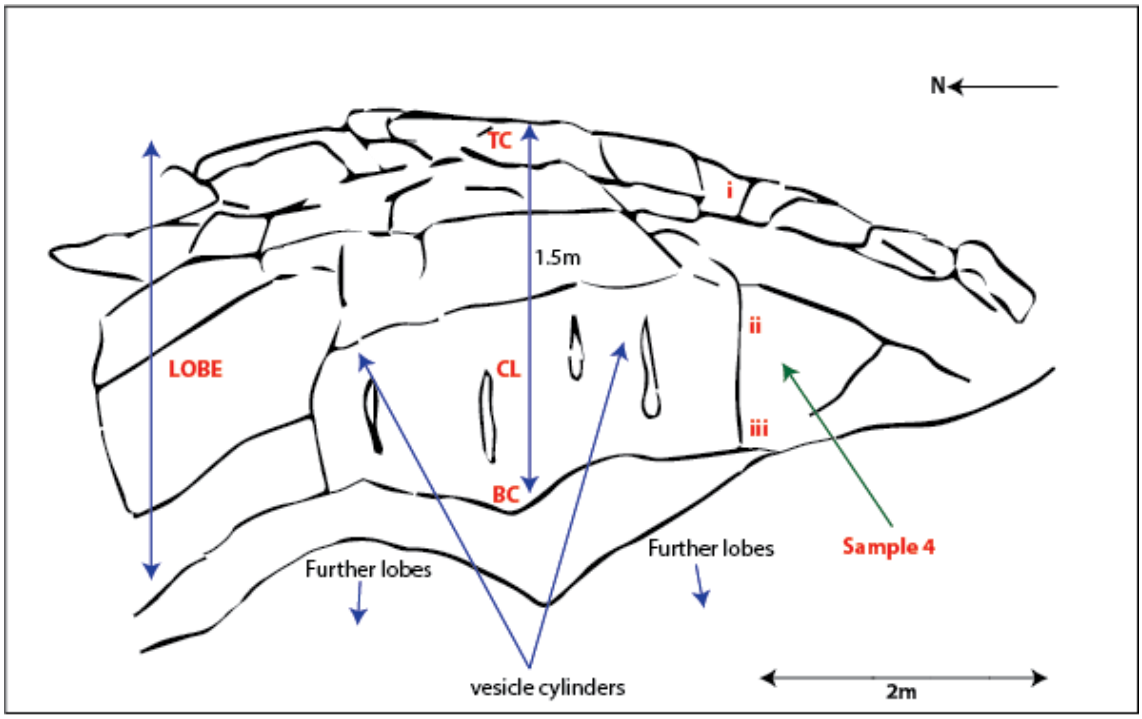

Location C on figure 4.23. Field sketch of the outcrop from GR 0194322E 2150721N (UTM Zone 5Q) showing a single lobe and the location of sample 4.

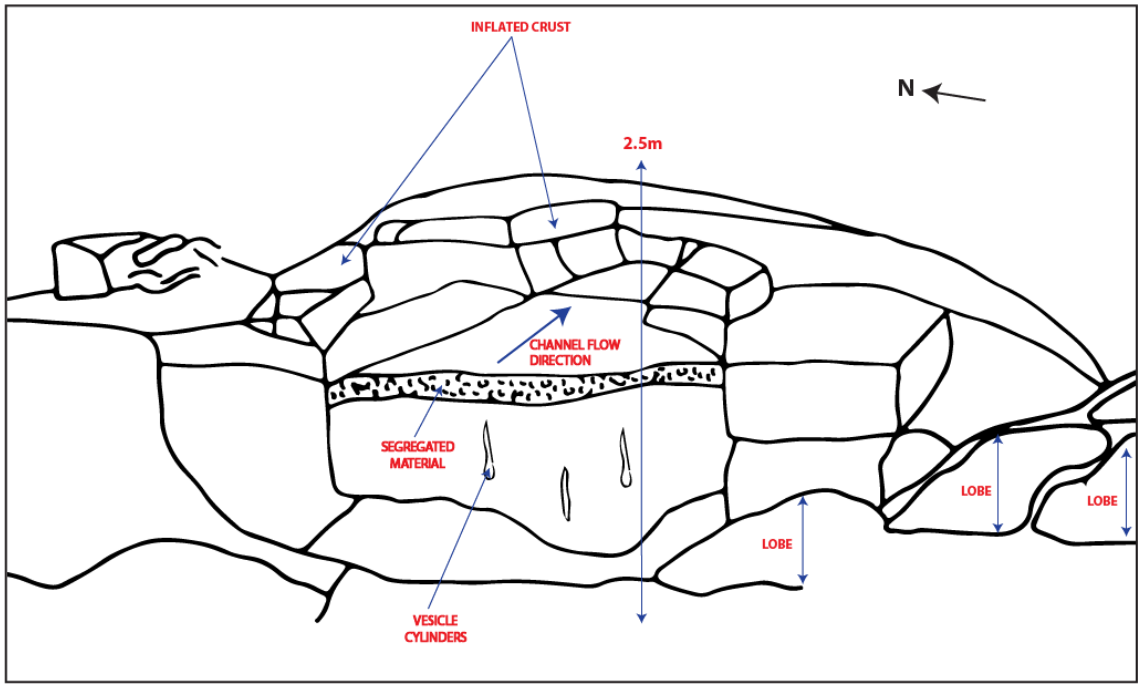

Field sketch of the outcrop from GR 0194285E 2150759N to GR 0194292E 2150754N (UTM Zone 5Q) showing a single lobe with gas cylinders through and segregated material atop the main channel flow. Location D on figure 4.23.

The Moinui is a pahoehoe lava flow field in contrast to the Hapaimamo lava flow field, which is an a'a flow. Differences in eruption and emplacement mechanisms

control the changing properties of lava flows between a'a and pahoehoe (*Rowland and Walker, 1990*). Lava flows can often transition between the two physical states (*Cashman et al., 1999*). Flow rate and flow front velocity are very different for the two types of flow; a'a often exhibits large flow rates that lead to high flow front velocity, whereas pahoehoe often exhibits low flow rates that lead to low flow front velocities (*Rowland and Walker, 1990*). Pahoehoe is characterised by insulated transport from vent to active flow front in a tube system so is thermally efficient, a'a is not (*Peterson and Tilling, 1980*; *Rowland and Walker, 1990*).

Pahoehoe flow fields are comprised of one or more lava flows, each made up of multitudes of small flow units called 'toes' (*Nichols, 1936; Walker, 1971*; *Rowland and Walker, 1990; Self et al., 1998*). These numerous small packages are evident in figure 4.23A-D. The low velocity of a pahoehoe flow allows a skin to form on the top of the 'toe' package, cooled by the air maintaining a smooth, unbroken, well-insulating surface (*Nichols, 1936; Walker, 1971; Rowland and Walker, 1990*). Therefore the temperature and viscosity of the lava do not change dramatically even at some distance from the vent (*Swanson, 1973; Rowland and Walker, 1990; Helz et al., 1991; Thordarson and Self, 1998*). This may have significant implications for the diffusion timescales extracted from Moinui in comparison to the Hapaimamo timescales – Moinui olivines will be kept hotter for longer, insulated by the transport system as the flow progresses downslope (*Thordarson and Self, 1998*; *Guilbaud et al., 2007*). The longer the lava flow stays hot for, the longer time available for diffusive re-equilibration to be reached. Diffusion timescales and crystal and flow textures from the Hapaimamo a'a flow and the pahoehoe Moinui flow will be considered to identify which type of flow may give more useful information in an eruption scenario. A flow that still retains the signature of the pre-eruptive magma processes rather than lava cooling and emplacement processes will provide more useful information for hazard mitigation. The lack of tephra available at Moinui to compare to the lava flow timescales may make this challenging.

The small flow packages referred to thus far as 'toes', will be referred to as 'lobes' for the rest of this chapter.

The road cut sampled is ~50 m long. Towards the centre of the road cut (the more central part of the flow field), the outcrop is ~3 m thick. At its periphery it is much

thinner, 1.5 to 1.8 m thick. It is composed of tens if not hundreds of lobes on this part of the exposure alone (figure 4.23). Each lobe appears to have a 'chilled margin' (skin) forming part of the crust (cms thick) around each lobe, helping to insulate its interior, although the contacts between the lobes remain distinct (*Thordarson and Self, 1998*). Each lobe consists of a top crust, lava core (central lobe) and bottom crust (*Thordarson and Self, 1998*). As seen in figure 4.23, the lobes are variable in size, up to nearly 2 m thick at their thickest point (vertically through its centre) to a few cms thick for the smaller lobes. A lobe inflates when lava flows through the centre to maintain the equilibrium thickness of the core of the flow (whereby flow in=flow out) (*Thordarson and Self, 1998*). When this is not maintained, voids are created in the space between the main tube flow and the base of the upper crust due to depressurisation (*Thordarson and Self, 1998*).

The thinner lobes are more uniform in size, seemingly flattened as a later lobe flows over. The latest lobes in the sequence (the last to be deposited on top of the previous lobes) are the thickest. Inflation of these latest lobes is not obstructed by a subsequent lobe flowing downslope (*Thordarson and Self, 1998*). If the surface the lava is flowing over is flat, a sheet-like lobe will form, if it is hummocky, then bulbous lobes result sitting in the lows between the hummocks (*Thordarson and Self, 1998*). Each lobe varies in composition, crystal content, shape, size, vesicularity and fracture style implying complex processes occurred through the magma plumbing system and during emplacement.

The top crust and bottom crust are more vesiculated than the dense interior (*Aubele et al., 1988; Thordarson and Self, 1998*). The top crust is rich in large bladed olivine crystals up to 1 cm in size and randomly orientated within a dark black hypocrystalline glass (figure 4.24.A.). These olivines have grown and cooled quickly (*Evans and Trommsdorff, 1974*).

Figure 4.24A: Bladed olivines within the Moinui lava flow.

This is in contrast to the lava core. Here, mostly large equant olivines up to 1 cm in size are packed together (~30 %) surrounded by a vesiculated (~20%), fine-grained basaltic matrix (~50%) (figure 4.24B). These olivines have been held at hotter temperatures for a longer period of time.

Figure 4.24B: Equant (cumulate) olivines within the Moinui lava flow

Vesicularity varies between lobes. Some parts of the upper lobes show a large proportion of vesiculation (~40%) (figure 4.24C) and lower amounts of

crystallinity, whereas some of the lower lobes show much lower proportions of vesiculation (30%) and higher or equal amounts of crystallinity. Vesicle cylinders (*Thordarson and Self, 1998)* are evident throughout the centre of some of the thicker lobes – these are vertical features (~20 cm long), somewhat cylindrical in shape (~ 1-2cm diameter) (figure 4.24D).

Segregated material is aphyric and vesicular (30%). This material sits atop of or cross cuts the lava core in several places across the road cut, as shown in figure 4.23D and figure 4.24E. This material was carried from the bottom of the lava core, through its interior through the vesicle cylinders (figure 4.24D) and flows laterally at the top of the lava core accumulating at the base of the top crust (*Thordarson and Self, 1998*). Gas blisters can form at the boundary of the liquid lava and viscous lava, causing the crust to bulge up due to expanding gases (figure 4.24F) (*Thordarson and Self, 1998).* Faulting and jointing varies across the lobes from columnar jointing to crustal jointing (*Thordarson and Self, 1998*).

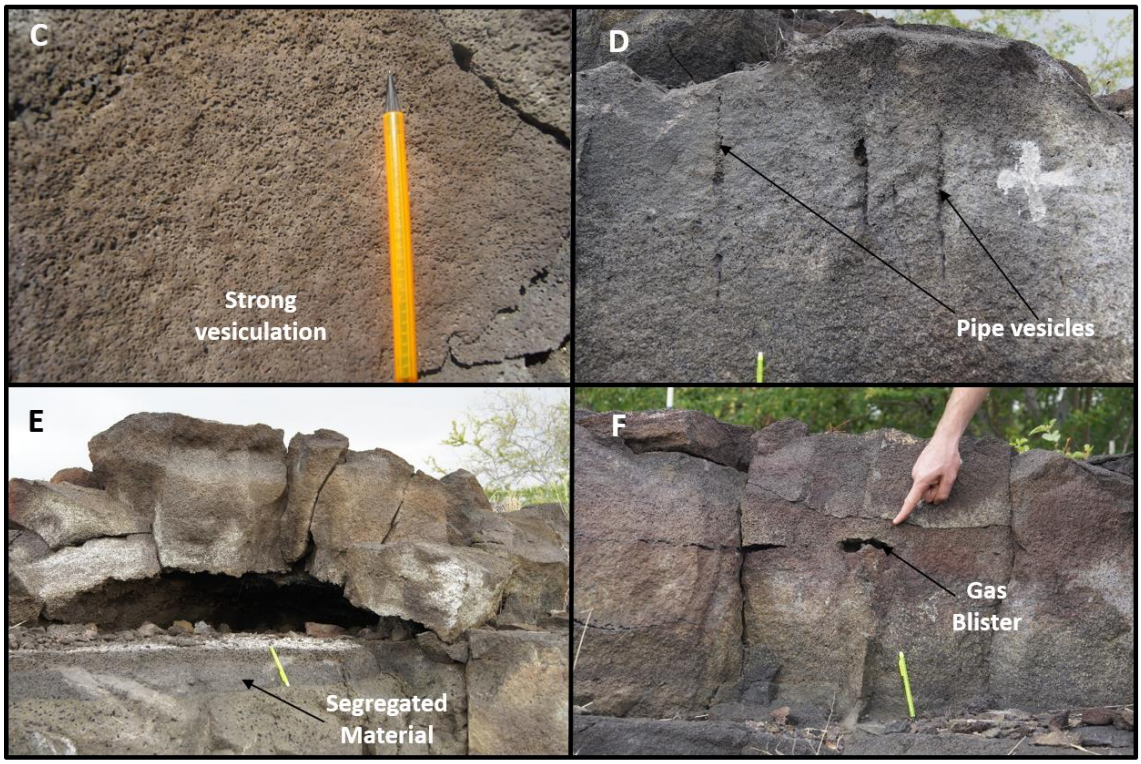

Figure 4.24: C) vesiculated upper lobe D) vesicle cylinders through the central lobe E) crystal poor segregated material atop of the lava core green with olivine F) small gas blister.

Samples were collected from this road cut less than 1km from the sea; 4 sets of samples were collected in total (M1, M2, M3, M4).

They were collected similarly to the Hapaimamo samples e.g. sample 1 was denoted M1TC, M1CL, M1BC for Moinui sample 1 top crust, central lobe and bottom crust. Each sample was collected from different lobes that vary in thickness and crystal content and from different parts of the same lobe to evaluate how timescales may change throughout. This information together with the sample locations are summarised in table 4.2.

Sample Name	Grid Reference	Lobe thickness(m)	Field sketch	Log
M1	0194394E 2150744N	0.7	Figure 4.23B	Figure 4.25A
M2	0194394E 2150744N	0.4 (Taken from the tapered edge of M1)	Figure 4.23A	-
M3	0194302E 2150743N	1.6	Figure 4.23B	Figure 4.25B
M4	0194322E 2150721N	0.6	Figure 4.23C	Figure 4.25C

Table 4.3: Summary of sample positions. All grid references are UTM Zone 5Q.

From field observations, the lava core of sample M1 (26%) contains the largest proportion of large, equant olivines and the lava core of sample M4 contains the largest proportion of bladed olivines (~20%), although some equant olivines are also suspended within the lava. The lava cores of samples M2 and M3 also contain large amounts of equant olivine (24-25%). The top crust of sample M3 was the only one to display a glassy rind.

Figure 4.25A-C shows field logs through the sampled (and sometimes adjacent) lobes.

Figure 4.25. Field logs A) Sample M1 B) Sample M3

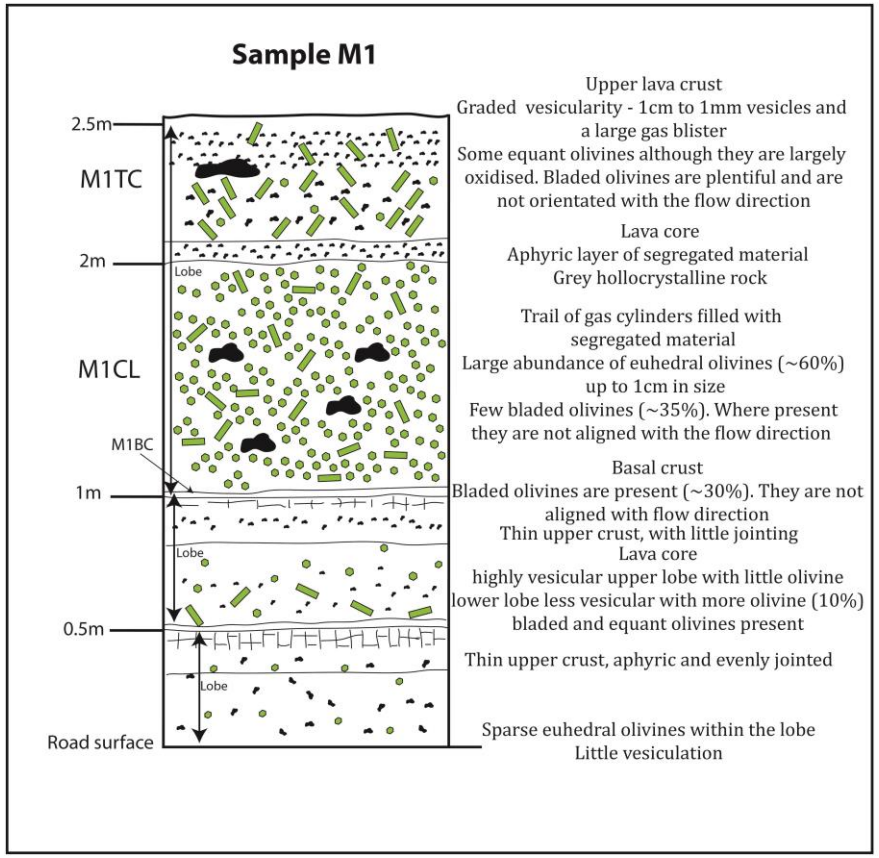

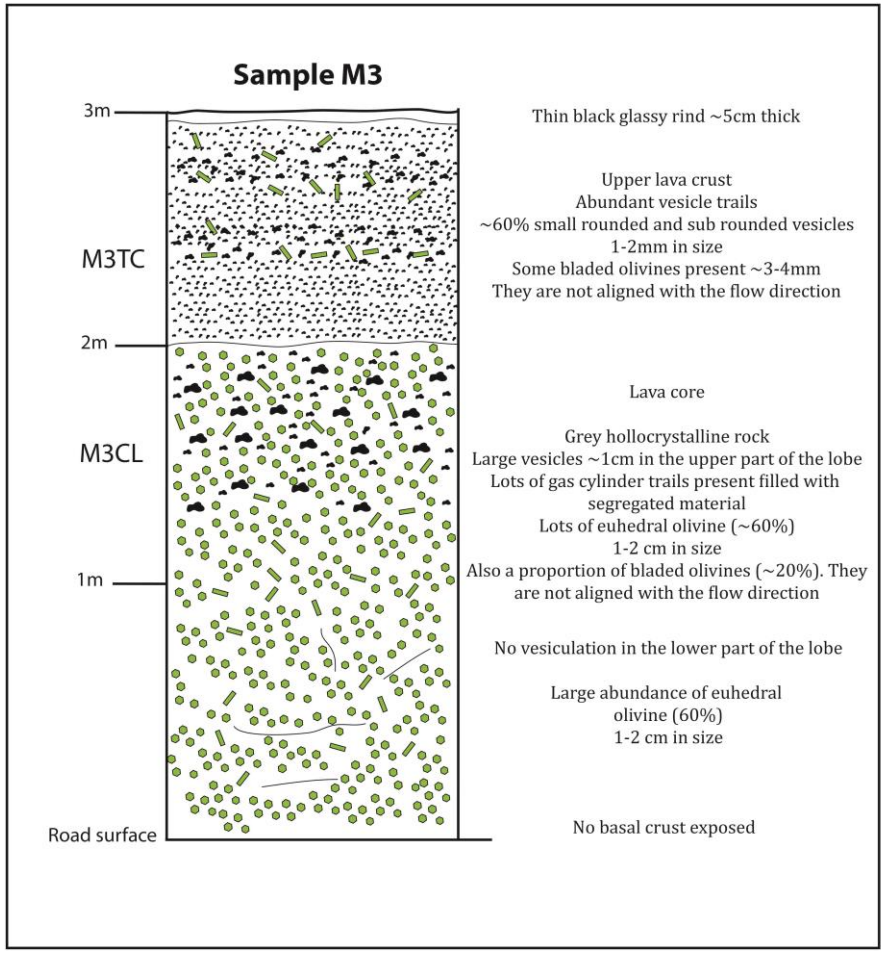

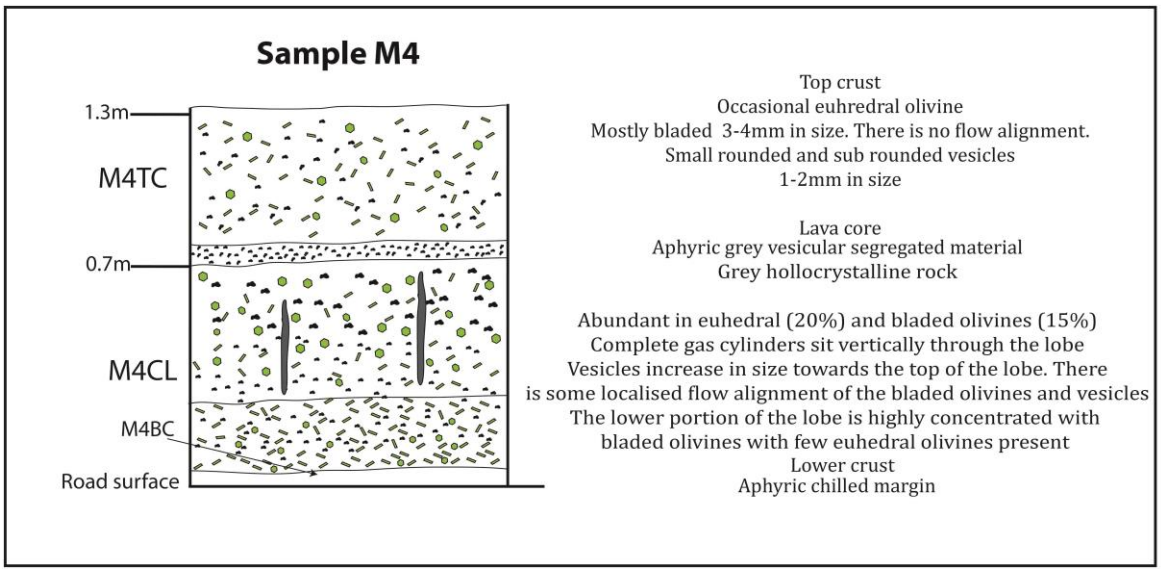

Figure 4.25. Field logs C) Sample M4

Thin sections were made for each part of each sample. The bottom crust samples were deemed to be too oxidised for Fe-Mg diffusion modelling and were excluded from further study, as was the case for the Hapaimamo samples. Olivines from the lava cores and the top crust were modelled and analysed further. Letters denote individual olivines and numbers will denote individual traverses taken within each olivine e.g. M1CL_A_1, similar to the Hapaimamo notation system. In some cases, bladed olivines are noted as e.g. M1C_1_A, where the number denotes the crystal and the letter denotes the traverse taken within the crystal.

4.3.3. Sample Description

As with the samples from PdF and Hapaimamo, these samples are picritic (as defined in Boivin and Bachelery, 2009). There are large textural differences between lobes and within lobes.

4.3.3.1. Textural Observations

Equant olivine crystals are present as large crystals (over 1-3 mm in size) ranging from euhedral to subhedral or rounded. Olivine is also present as elongate blades (figure 4.26.A-D). Varying crystal habits of olivine can be attributed to the inferred rate of cooling of the melt during crystallisation (*Donaldson, 1976; Walker et al.,*

1976; Lofgren, 1980; *Deer et al., 1997*). Equant crystals usually develop under equilibrium or near-equilibrium conditions. It is thought at higher cooling rates or with super-cooling the crystal habits can become more skeletal or elongate (*Donaldson, 1976, Walker et al., 1976; Bianco and Taylor, 1977; Lofgren, 1980*; *Deer et al., 1997*). Donaldson (1976) argued these shapes are due to rapid growth caused by a high normative olivine content of the magma in picrites or olivine-rich basalts rather than due to rapid cooling. This may be the case with the Moinui.

The equant olivines are most numerous throughout the lava cores but are also present within both the top and bottom crust (figure 4.26F). The equant crystals are solitary or found in groups with other equant olivines. The bladed olivines are also found throughout a lava lobe, both in the crust and in the core – they are evenly, randomly distributed. They can be solitary crystals or found in groups with other bladed olivines or with the equant olivines (figure 4.26A-C). The bladed olivines can show signs of skeletal growth (figure 4.26D). Both olivines types often exhibit diffused edge zoning. Diffused zones are wider in the equant olivines (100-300 μm) and narrower in the bladed olivines (30-50 μm). Olivines adjacent to each other in SEM backscatter images sometimes show variation in grey scale implying the crystals have differing Mg numbers (figure 4.26E).

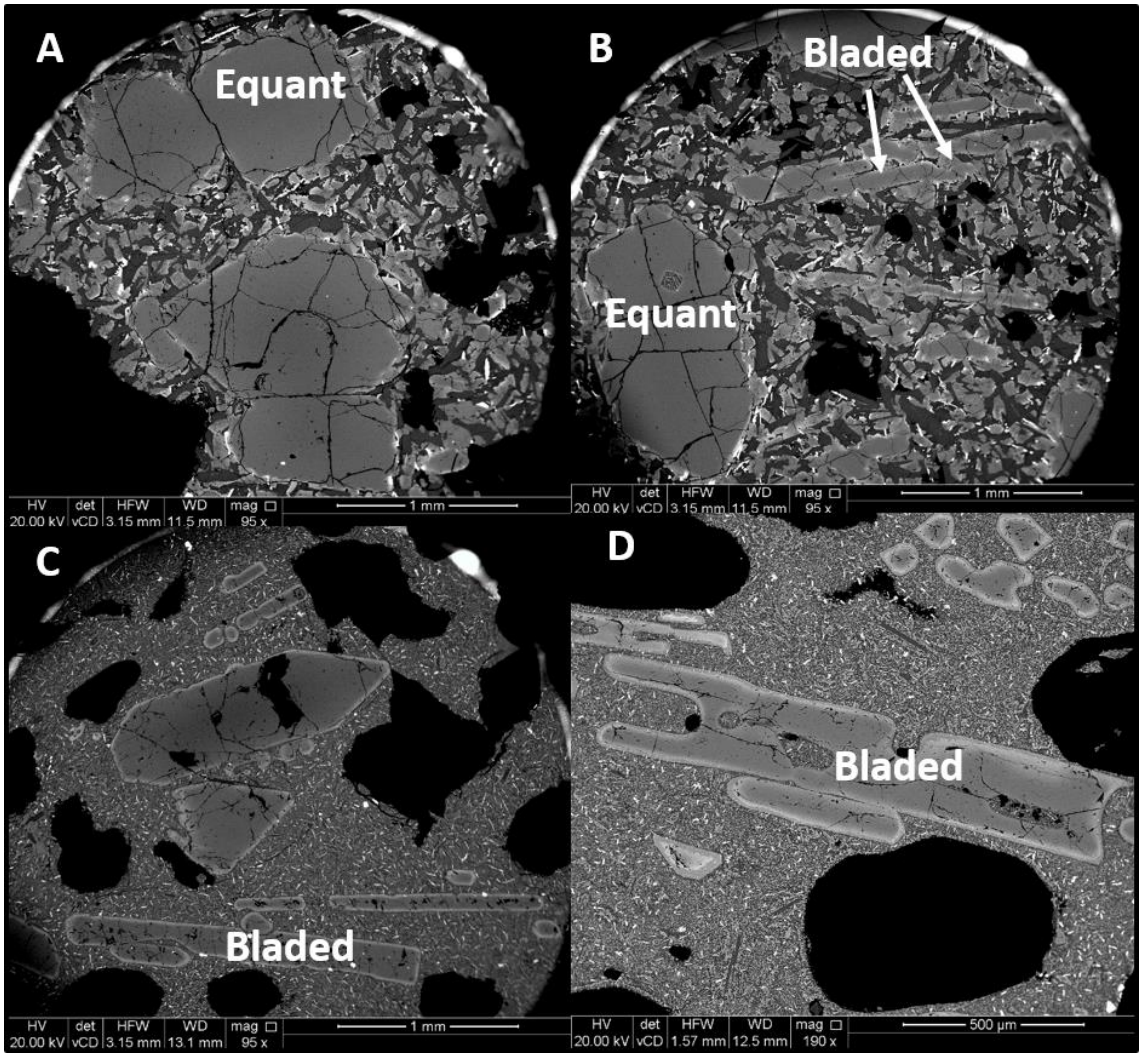

Figure 4.26: A collection of SEM images showing A) equant olivines surrounded by microcrystalline groundmass B) equant and bladed olivines surrounded by microcrystalline groundmass C) bladed olivines surrounded by a finer grained groundmass D) bladed olivines that have possibly undergone skeletal growth

Both olivines types (equant and bladed) can be found within the top crust. The bladed olivines here are unzoned but the euhedral olivines can be strongly zoned or not zoned at all (figure 4.26 F and G). The crystals here are often slightly smaller than those found in the central part of the lobe (< 1 mm). The glassy selvages may show the original distribution of the crystalline assemblage as the equant olivines have had no time to sink before the quench (*Guilbaud et al. 2007*).

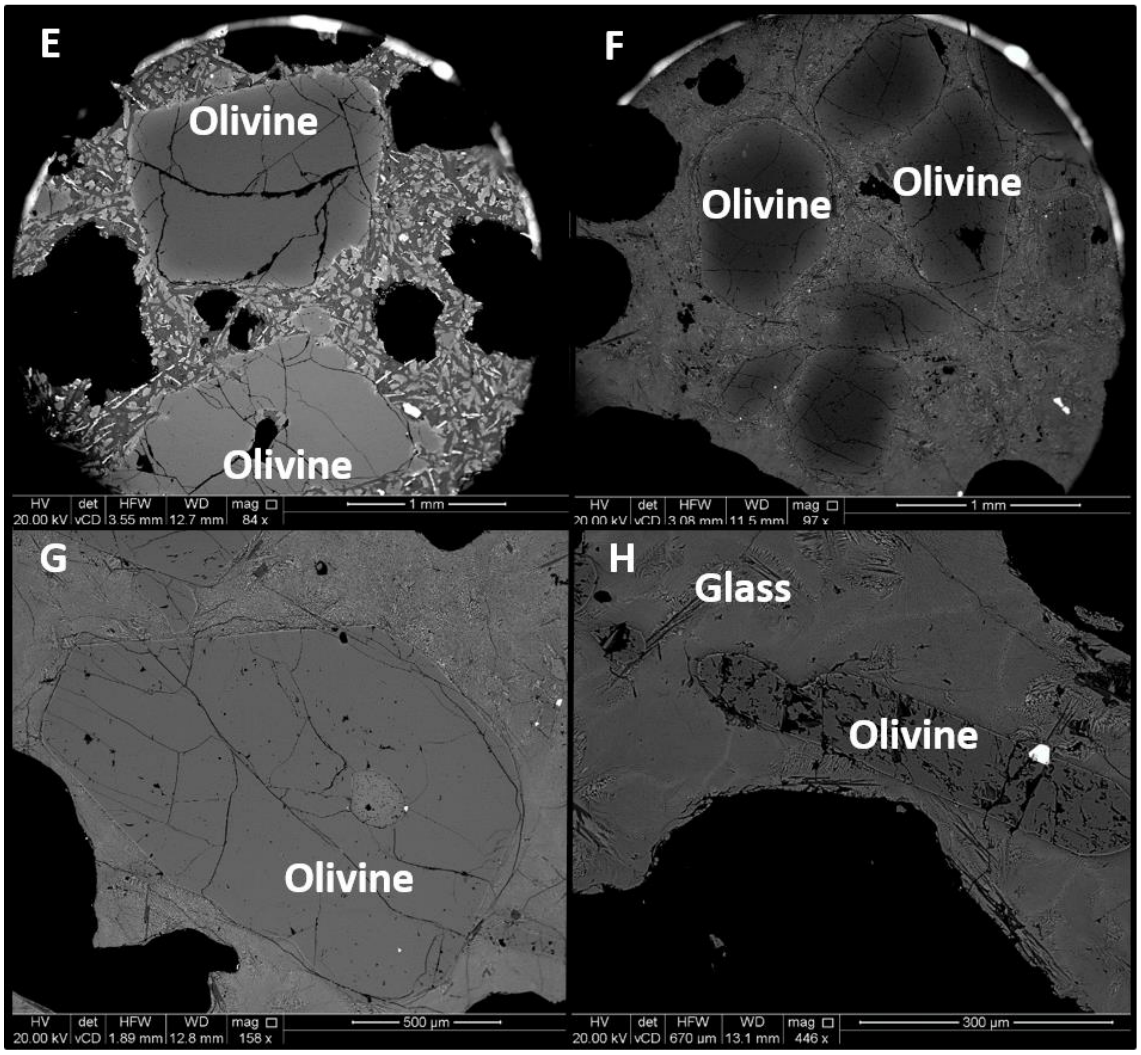

Figure 4.26 continued: E) two olivines with contrasting greyscale values indicating differences in composition F) zoned olivines within the top crust of a lava lobe G) unzoned olivines within the top crust of a lava lobe H) olivine within devitrified glassy crust of the upper part of a lobe.

There does not appear to be any flow orientation indicators within the groundmass of any part of the lobe (nor is there any flow alignment of the larger crystals), which suggests cooling occurred when the magma in the lobe was not moving. There is a much larger proportion of vesiculation within the groundmass of the Moinui samples (30%) compared to the Hapaimamo likely due to a higher gas content. This is also evident from the pipe vesicles and segregated material at outcrop scale that is not found at Hapaimamo.

The groundmass varies considerably between samples and different parts of the lobes. The groundmass in the top crust can show a variety of glass textures (figure 4.26 F, G and H and figure 4.27B). This could be due to a reduction in cooling rate as

the crust gets thicker (*Thordarson and Self, 1998*). The top surface of the 'top crust' from M3T is exposed laterally and is very glassy and dark in colour. Various crystal phases are suspended within it (plagioclase, olivine (zoned and unzoned, bladed and euhedral), clinopyroxene) (figure 4.27).

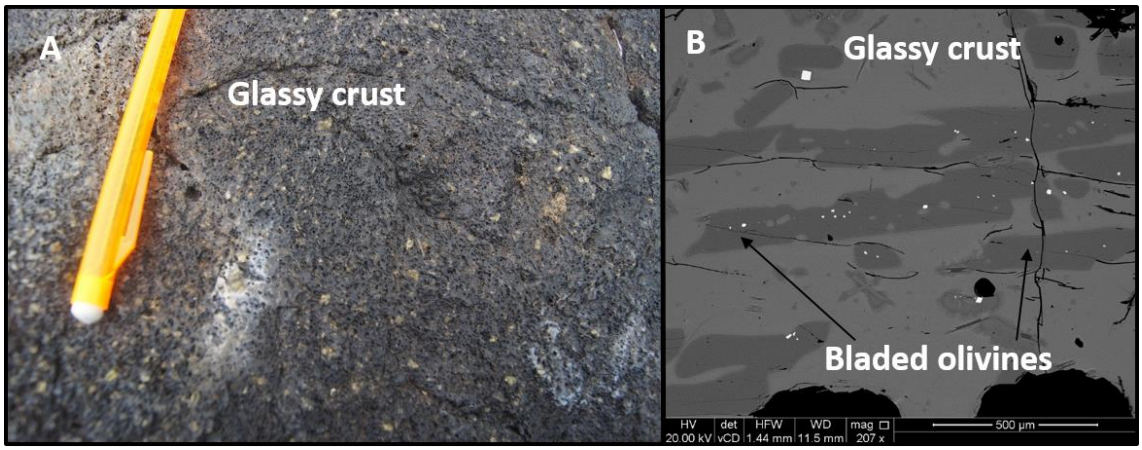

Figure 4.27: A) Field photo of the glassy crust at the top of an upper lava lobe (M3T) B) SEM image of the same part of the crust showing an abundance of unzoned bladed olivine in the glass

This is the only top crust with a completely glassy groundmass. In other parts of the top crust from this road section, the glass appears patchy (figure 4.26H) rather than smooth (figure 4.27B). A closer look at the plagioclase within the glass in these samples shows that these crystals are being used as a nucleation site leading to partial devitrification of the surrounding glass (*Friedman and Long, 1984*). The low viscosity of basaltic glass favours devitrification, whereby the glass cools and the release of water by crystallising glass increases the crystal growth rate (*Friedman and Long, 1984*). Anhydrous phases form (e.g. feldspar), concentrating water around the growing crystal. This speeds up crystallisation adjacent to the crystal by lowering the activation energy of viscosity of the glass (*Friedman and Long, 1984*). Crystallisation is spherulitic due to the sphere of high water content around the growing crystal (*Friedman and Long, 1984*).

Within the lava core, the groundmass varies greatly between samples. Whilst the components are similar (olivine+ plagioclase + pyroxene + oxides) the grain size is distinctly different. A more detailed image of one of the groundmass texture from the lava core of M4 is shown below in figure 4.28.

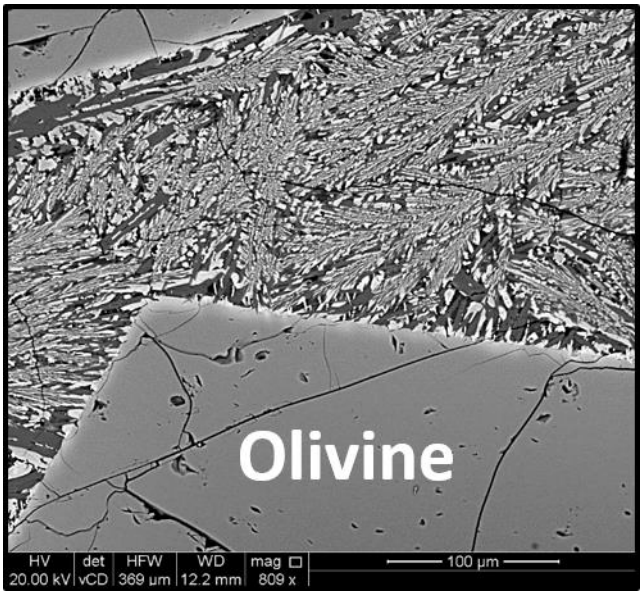

Figure 4.28: Branching groundmass texture found in sample M4C.

The texture looks 'plant like' branching in various directions. This texture is the result of rapid cooling rates producing fine-grained skeletal or acicular intergrowths of plagioclase and clinopyroxene (*Lofgren, 1980*). A range of cooling rates will produce a unique texture for a specific basalt. The difference between groundmass textures of lobes M1/M3 and M4 may be due to varying cooling rates, slightly different bulk rock compositions (or crystal contents), changes to the nucleation kinetics or fO_2 between the lobes (*Lofgren, 1980*). Within the lava core of M4 the crystals are ~50 µm in length, whereas the crystals within the lava cores of M1 and M3 are ~80 – 400 µm. M4C is the thinnest lava core of those sampled on the periphery of the flow field. No further lobe were deposited on top providing extra insulation. M1C and M3C are the thicker central lobes providing extra insulation and slower growth of the crystals in the groundmass.

Many of the olivines from the lava core of M4 exhibit a bright distinct diffusion rim around their edge (in contrast to the gradational diffusion zone seen in many of the other large olivine crystals from other samples).

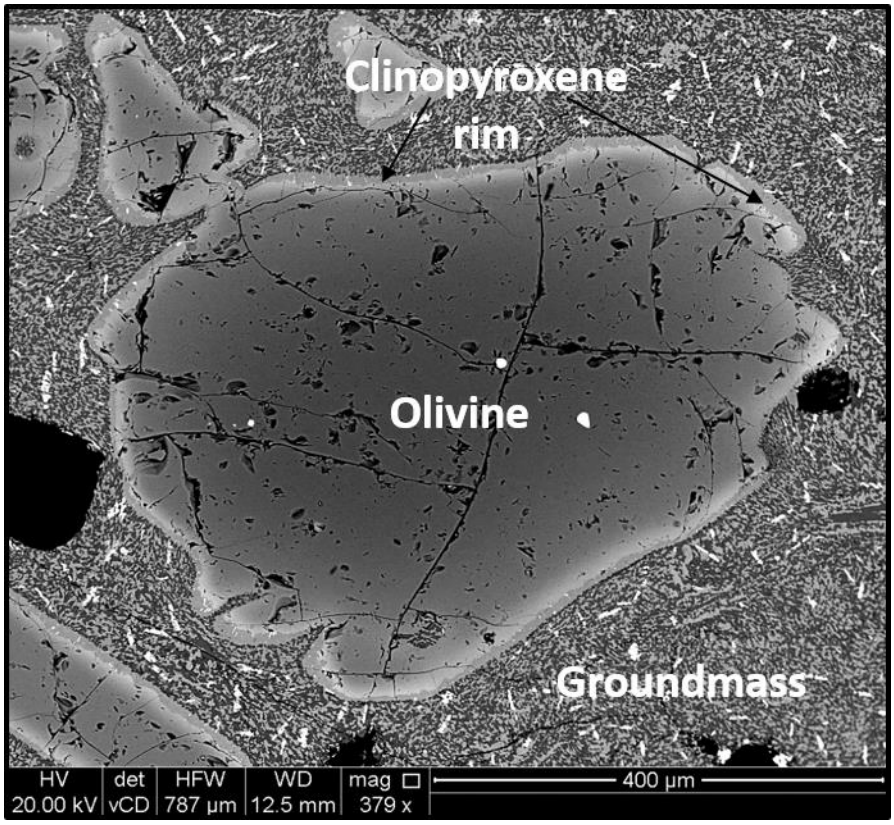

Figure 4.29: Olivine from sample M4C showing a pigeonite rim as seen in some of the Hapaimamo samples

These olivines from M4C also often have a corona of pigeonite similar to that found around the Hapaimamo olivines (figure 4.29). Where this rim is present, it is much thinner than those found on the Hapaimamo olivines (perhaps only 10 µm wide) and is monocrystalline. This rim is not present on olivine crystals found in any of the other lobes and is therefore likely due to local variations in the magma in this lobe (e.g. the presence of a slightly more SiO_2 rich magma in lobe M4 than the magma in the other lobes). As mentioned above the groundmass in this lobe is also very different to the groundmass elsewhere further supporting the idea that this pyroxene rim is due to local variations affecting crystallisation in the lobe e.g. due to a high pressurised breakout. The equant crystals are subhedral-anhedral and are not in equilibrium with the melt hence they are not phenocrystic.

4.3.3.2. Whole rock geochemistry

Major element analyses were determined as described in section 4.2.6.3. Around 10g of homogenised powders were analysed from the bottom crust, centre lobe and top crust of lobe M1. The full XRF dataset can be found in Appendix G.

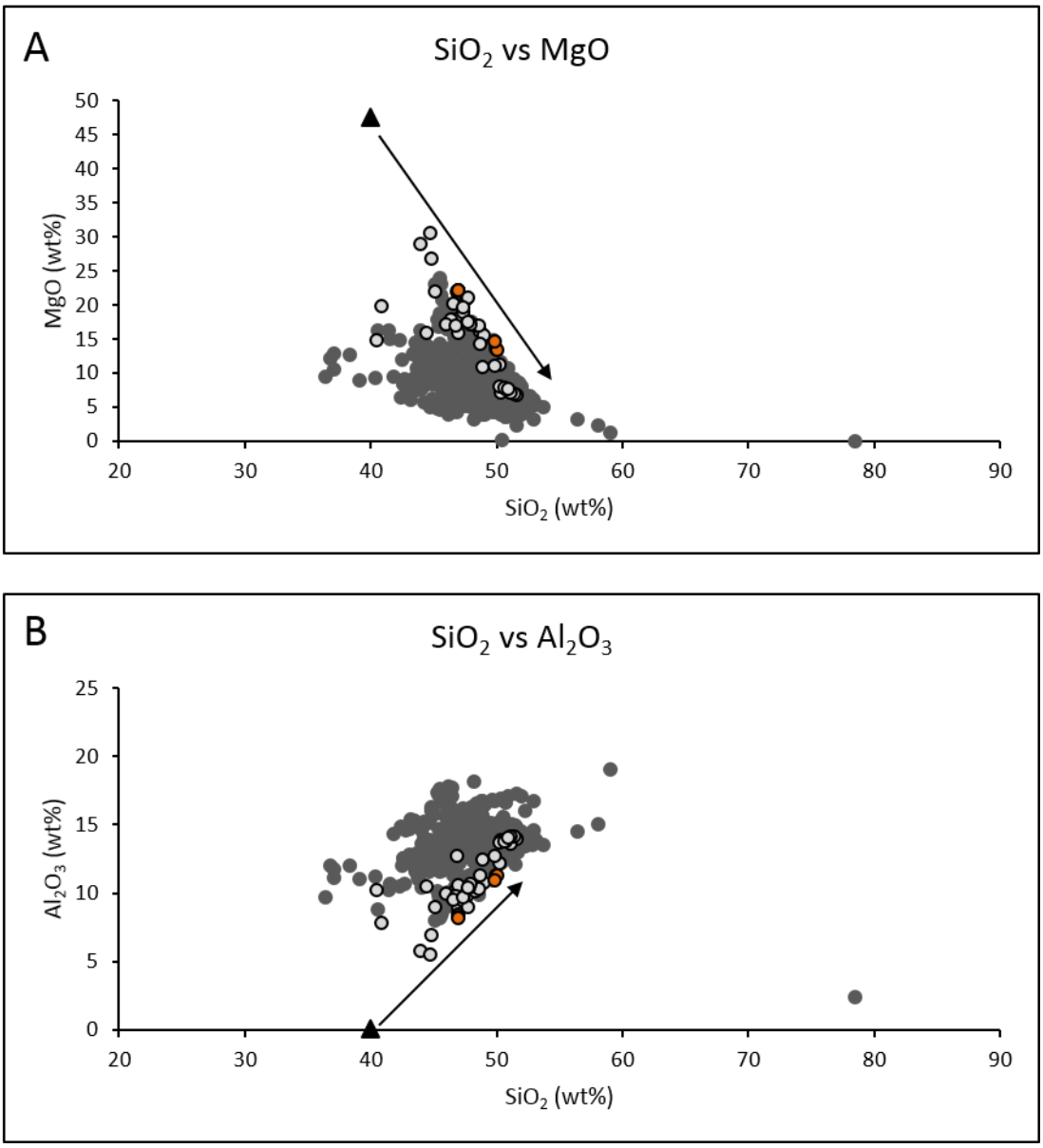

Figure 4.30: Bulk rock SiO_2 plotted against A) MgO and B) Al_2O_3. Dark grey points are a collection of published data from the GeoRock database for basalts and basalt-tholeiites, light grey points are a collection of published data from the GeoRock database for picrites, orange points are data from Hapaimamo. The black triangle in both plots is oxide weight percent of an olivine (Fo_{88}) from the Hapaimamo as measured with the EPMA.

Figures 4.30A and 4.30B show that the Hapaimamo bulk rock data correlates with data from other studies, conforming to the trend of a typical Hawaiian basalt. The

olivine control line (black arrow) shows the compositional fractionation is controlled by the addition of olivine.

4.3.3.3 Mineralogy

Olivine

There is a large proportion (15-25%) of coarse olivines within many of the lobes. Modal abundances have been determined using point counting software, '*JMicrovision'*. Their modal abundance is too large and their cores too primitive (Fo_{88-89}) at normal oxidation for these to be in equilibrium with the carrier melt (MgO 6.72 wt. %) and so they likely crystallised at depth from a more mafic magma (*Guilbaud et al., 2007; Passmore et al., 2012*). The large bladed crystals may be phenocrysts due to their less primitive compositions and more euhedral shapes. The equant olivines are 1-3 mm in size and exhibit euhedral or subhedral shapes and rounding where dissolution has started to occur. The large rounded crystals found in the central parts of the thickest lobes have diffused zones up to 300 μm in width, and the bladed crystals have the shortest diffusion widths at ~50 μm. Diffusion contours around the subhedral olivine rims are continuous, implying dissolution occurred prior to the onset of diffusion. Olivines from M4C have retained their euhedrality much better than those found within M1C or particularly M3C. In M1C and M3C the olivines are very round, further evidence that they are not in equilibrium with this melt (figure 4.31).

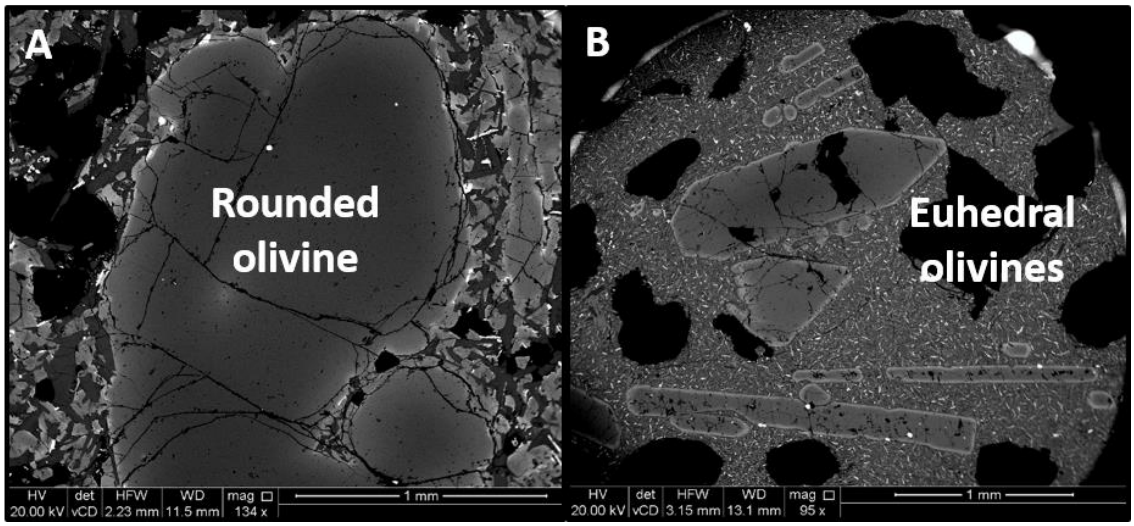

Figure 4.31: A) Subhedral olivine from sample M3C B) more euhedral olivine crystal from M4C

Olivine core values are bimodal (figure 4.32). Core values of the equant euhedral and subhedral olivines mostly range from Fo_{88-90}. The core values of the long, thin bladed olivine crystals range from Fo_{82-83}. Rim compositions are much more variable. M1T olivines collectively have consistent rim compositions of Fo_{82} whereas within M1C, olivine rim compositions vary from $Fo_{78-86.}$ M2C olivines have rim compositions from Fo_{81-86} and M3C and M4C olivines have rim compositions of Fo_{74-86} and Fo_{72-86} respectively. The rim compositions of equant olivines range from Fo_{78-86} and the rim compositions of the bladed olivines range from Fo_{64-78}. The varying rim and core compositions may reflect different crystal populations or time spent in different magmatic environments.

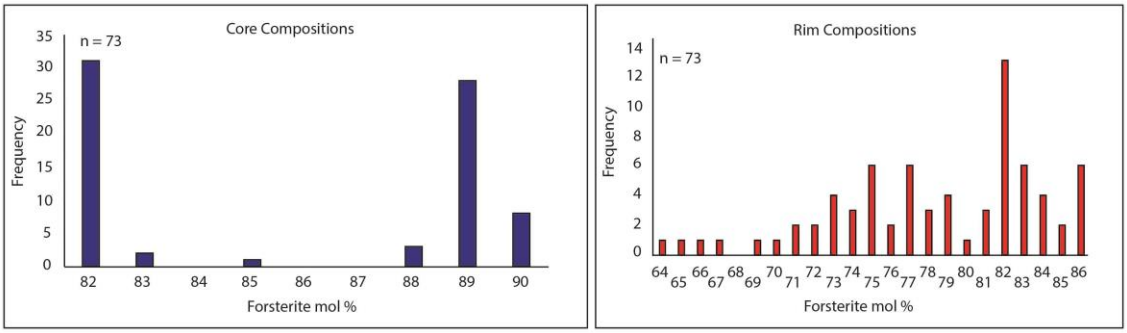

Figure 4.32: Distributions of olivine core and rim forsterite compositions within the Moinui lava flow. The bimodal split of the core compositions corresponds to the bimodality of the olivine shapes – equant vs. bladed.

Most of the olivine (equant and bladed) analysed displayed normal zoning patterns (Mg-rich core) although 1 or 2 displayed possible relict reverse zoning patterns. Some equant olivines displayed strongly kinked zoning patterns towards the rim that can be seen on core-rim traverse data (figure 4.33).

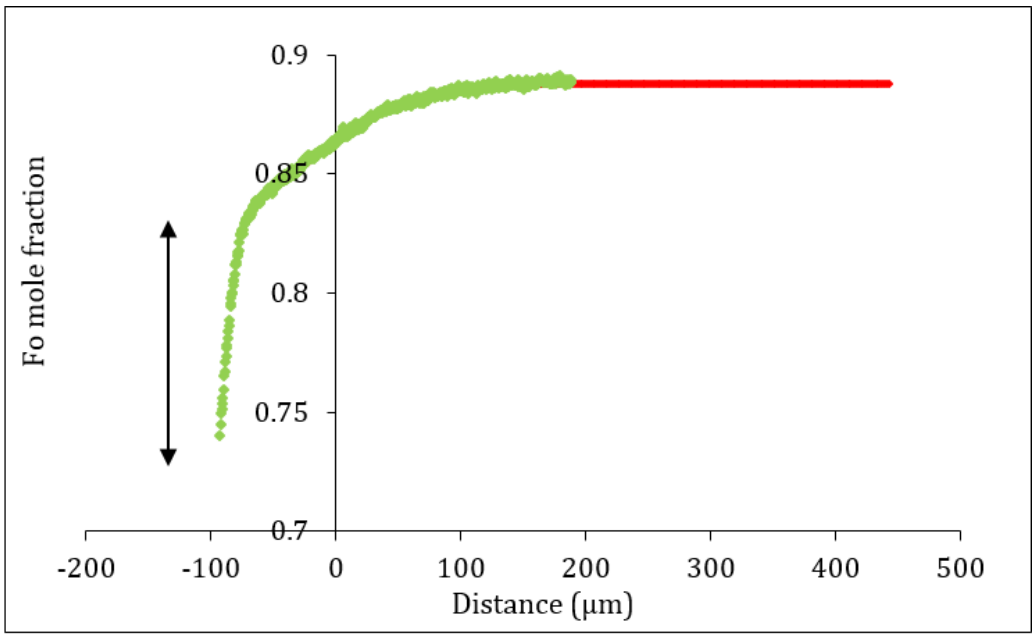

Figure 4.33: A compositional traverse (green) and model fit (red) calculated using AUTODIFF from crystal M3C_A1. The majority of the profile shows a classic diffusion curve until composition Fo_{84} near the rim. The composition rapidly changes from Fo_{84} to Fo_{74} (shown by the arrow) indicative of a later stage overgrowth rim.

This is due to rim overgrowth of a more evolved composition, similar to if not the same as that which crystallised the bladed olivines. These overgrowth rims have been rapidly quenched as shown on figure 4.33 and so formed close to or at the surface. The magma from which the overgrowth rim and bladed olivines formed is more evolved than that which formed the cores of the equant olivines. Half of the equant olivine inner rims (before the crystallisation of the overgrowth/quenched rim) are composed of Fo_{84} giving evidence the inner rim is composed from the same liquid from which the $Fo_{82\text{-}83}$ cores grew. For this reason, all timescales from equant olivines have been modelled from a rim composition of Fo_{84} or higher so as not to accidentally model the quench.

All olivines within the central part of the lobes have completely crystallised melt inclusions where they are present. Olivines within the glassy top crust often contain melt inclusions that have not undergone any obvious post-entrapment crystallisation (*Gaetani and Watson, 2000*) and are suitable for thermometry calculations. Some olivines contain inclusions of oxide, often several crystals can be present per crystal.

Plagioclase Feldspar

There are very few phenocrysts of plagioclase within the Moinui sample sets other than those of the microcrystalline groundmass. They are hundreds of microns in size. Crystals occur in the glassier top crust samples but they are not plentiful (< 10%). Where present they are up to 1 mm in length. Plagioclase feldspar is much finer-grained within some of the groundmass in the crustal samples (tens of microns in length) e.g. M1B and M4B, due to more rapid cooling. Plagioclase is present in ~50% modal abundance in the groundmass. The plagioclase do not appear zoned with core compositions of An_{60-71} and rim compositions of An_{63-69}.

Clinopyroxene

Clinopyroxene crystals occur in the groundmass of the lava core and the bottom crust. They are between 5 – 70 μm in size. Within the top crust they can be found as solitary phenocrysts ~50 μm in size. There are rare glomerocrysts where clinopyroxene has nucleated around plagioclase crystals. These are strongly resorbed and show evidence of complex zoning. Magnesium numbers range from Mg_{75-82} at the core and Mg_{59-82} in the rim. The modal of abundance of clinopyroxene found within the lava core is ~50%.

Oxides

The oxides in the groundmass are composed mostly of chromium-spinel with instances of titanomagnetite. The chromium-spinel has an average Cr number of 0.56 and titanomagnetite has an average ulvospinel component of 0.56. The oxides are present in < 5% modal abundance. They are frequently included within olivine and can be included within the other mineral phases. They are found as larger crystals up to 150 μm in size. They occur as elongate brick shapes (similar to the shape of plagioclase) and are much more abundant ~15%, in the lava core of M4.

4.3.4 Thermometry and oxygen fugacity

The matrix glass composition from the top crust of M3T was used to calculate the inputs for the thermometry. No other matrix glass was found in any other part of the samples and so the glass composition from M3T was used as a proxy composition for all of the lobes, as they are all part of the same flow. Melt inclusions were not

investigated for this sample due to the extent of their crystallinity. As with the Hapaimamo dataset, thermometry using matrix glass compositions will provide minimum temperatures for diffusive timescale processes.

Compositional data was retrieved from the matrix glass using spot analyses (10 μm) on the EPMA as described in section 4.2.4. Measurements were made using the EPMA with a defocused beam of 20kV and a beam current of 15 nA. Peak counting times were as follows; 20s for Si, Fe, and Mg, 16s for Al, Ni, Cr, Na, and K, 10s for Ca, Mn, Ti and P. Most analyses returned totals of 97.9-99.9 wt. %. Primary standards and detection limits are reported in Appendix A.

The Montierth et al. (1995) liquid-only thermometer was used to calculate temperatures for the diffusion models as described in equation 4.2b. The Moinui matrix glass MgO composition is 6.72 wt. % (calculated from 40 analyses (1σ = 0.06)). With this magnesium composition, temperatures of 1166°C ($\pm$ 10°C) were calculated. This temperature is in agreement with that calculated for the Hapaimamo matrix glass with the same thermometer (1168°C).

Oxygen fugacity has been applied with the same rationale as that for the Hapaimamo lava flow samples. As these Moinui samples were taken at some distance from the vent they are thought to be more oxidised (*Rhodes and Vollinger, 2005*), and so diffusion has been modelled at NNO -1 log units.

4.3.5. Diffusion modelling

Compositional traverses were retrieved to input into AUTODIFF using the same methodology as the samples from PdF and the Hapaimamo lava flow, as described in chapter 2 and the earlier parts of this chapter. Core and rim values were measured using the EPMA with a focused beam of 20kV and a beam current of 30-40nA. Peak counting times were as follows; 90-100s for Ca, 30-60s for Al, Ni, and Mn, 20-40s for Si, Mg and Fe and 15-30s for Cr. Most analyses returned totals of 98.4-101.1 wt. %. Repeat analysis of the San Carlos olivine standard were used to estimate the precision of Fo measurements. The Fo content of the San Carlos olivine was determined with a precision of 2σ = 0.1-0.21 mol. % (n=84). Primary standards and detection limits are reported in appendix C.

Zoned olivines suitable for modelling were difficult to find among samples M1C – M3C. Olivines were heavily cracked around the edges (it is unclear whether this was pre-existing or due to sample preparation) and heavily pitted despite many rounds of polishing. Lots of pitting within a crystal renders diffusion modelling difficult due to induced noise along the extracted profile.

Across samples M1C-M4C and M1T, 83 profiles were measured. Bottom crust samples were excluded from analysis due to oxidation effects. From these 73 profiles were suitable for modelling. The remaining profiles were rejected due to problems with analytical equipment or the profiles were affected by a large amount of crystal growth and/or changing boundary conditions.

4.3.5.1. Timescales

There are clear differences between the equant and bladed crystals – both chemically and texturally and between the calculated diffusion timescales. Figure 4.32 shows clear bimodal forsterite cores implying the presence of at least two distinct crystal populations within this flow – one with a dominant core population of Fo_{89} and another with a dominant core composition of Fo_{82}. These core compositions are directly linked to crystal shape – the more primitive olivines are equant in shape with a very high modal abundance as detailed earlier in the chapter, and the more evolved olivine cores are strongly bladed or elongate in shape. These more evolved cores (Fo_{82-83}) correlate well with some of the rims (Fo_{84}) of the more primitive equant olivines. These bladed olivines have a wider range of more evolved rim compositions (Fo_{64-78}) than the equant olivines (Fo_{78-86}).

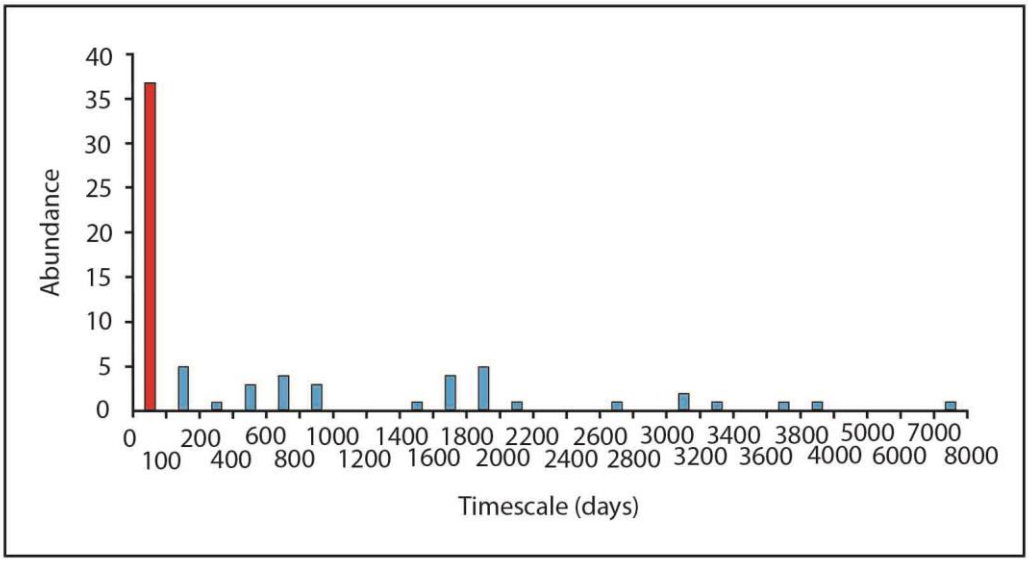

Figure 4.34: Timescale distribution for the Moinui olivines. All timescales associated with the bladed olivines are less than 100 days (red) whilst most of the equant olivines (blue) are more than 100 days - although a few are less than 100 days. The timescale range for the euhedral population is highly variable from hundreds to thousands of days. All timescales are EBSD corrected.

The timescales of the two populations of olivine (equant and bladed) are also mostly bimodal. From the bladed crystals, 32 traverses were modelled for timescale, all falling within a tight cluster from ~2-39 days with 4 anomalously longer timescales at 55-62 days. This is consistent with the possible cooling time for the lava flow, calculated at ~ 1 week. The more evolved forsterite compositions of the bladed olivines and short timescales represent late stage, shallow crystallisation. From the equant crystals, 39 traverses were modelled for timescales, 34 of which span a wide timescale range from ~52 days to nearly 8000 days at their most extreme (~22 years), but most timescales fall within the range 4 months to 7 years. The average uncertainty on each calculated timescale is 0.34 log units (1σ). These compositions and variable and significantly longer timescales imply the equant olivines have undergone processes in a deeper environment different to the bladed olivines.

The zoned bladed olivines with short diffusion timescales are found within the lava core. Within the crusts of the lobes, bladed olivines are not zoned and therefore have a timescale of zero. The cores of the bladed olivine are also in equilibrium with the the matrix glass. This is evidence that the bladed olivines grew in situ within the lava flow or very close to the surface upon ascent pre eruption in the transport system

(*Faure et al., 2014*). Experiments by Lofgren et al. (1974) showed that massive crystallisation of a second phase can lead to supersaturation of olivine in the liquid which could give rise to a morphological change i.e. the crystallisation of bladed olivines (*Lofgren et al., 1974*). However, the lack of evidence of this second phase and the short diffusion timescales supports the hypothesis that the bladed olivines appeared close to the surface or during rapid cooling upon extrusion. Alternatively, degassing of the melt during ascent or at the surface e.g. in a lava lake could have played a major role in rapidly undercooling the melt leading to supersaturation and a rich burst of nucleation and crystal growth (*Guilbaud et al. 2007*). The magma has a high proportion of vesiculation indicating a substantial volatile content. Gas escape structures observed in the field are also indicative of this. Re-equilibration of the melt to degassed conditions may have affected crystallisation conditions (*Guilbaud et al., 2007*). Figure 35 shows evidence that these bladed olivines may originally be chain olivines (*Donaldson, 1976, Lofgren, 1980*).

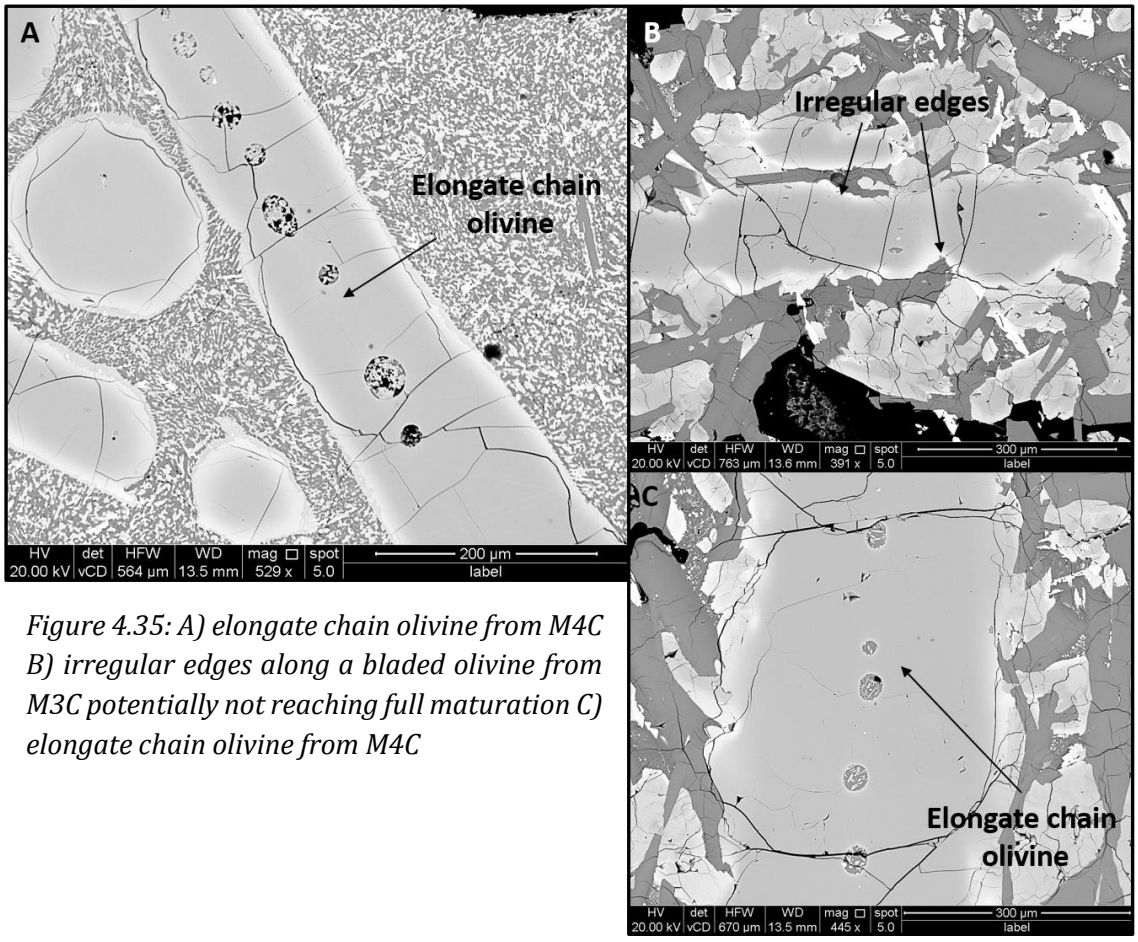

Figure 4.35: A) elongate chain olivine from M4C B) irregular edges along a bladed olivine from M3C potentially not reaching full maturation C) elongate chain olivine from M4C

Chain olivines are elongate composed of link units. They can be bladed or thinly tabular (*Donaldson, 1976, Lofgren, 1980*). It is possible these bladed olivines grew as chains at some distance from the equant olivines with maturation of the crystallisation within the tube system, where some did not reach full maturation and exhibit irregular edges. The total growth thickness is only a ¼ of the thickness of the full blade i.e. growth thickness was limited and may explain the lack of dendritic growth on the equant olivines. Also, the larger the nucleation density the slower the crystal growth (*Donaldson, 1976*). The large abundance of evolved crystal cores me have impeded nucleation and dendritic growth on the equant olivines. The fuller bladed crystals that have the longer timescales have undergone slower crystallisation allowing elements to migrate through the melt to form the crystal rim before the onset of diffusion.

The equant olivines are cumulates due to their size and modal abundance within the lobes compared to the MgO content of the liquid in which they are found (MgO 6.7 wt. %) and the long and variable timescales that have been preserved. These are accumulated in the lava pathways and breakouts at the surface. They have cooled slowly, producing the equant shapes although some show evidence of dissolution or round shapes (figure 4.31A). Their diffused zones are not cross cut by the dissolution and so this dissolution likely occurred in transfer (*Donaldson, 1985*), from a hot primitive environment in the lower crust, evidenced by their very primitive core compositions, to shallower storage regions in the mid-crust by entrainment in a melt (*Passmore et al., 2012; Neave et al., 2013; Hartley, et al., 2016*). The Moinui is 'slurry-like', reaching olivine saturation through olivine loading. The melt that entrained olivine from the lower crust may have been under-saturated, whereby olivine will dissolve until olivine saturation is reached giving rise to the rounded olivines. Upon decompression the melt will supersaturate and the cores may re-equilibrate with the melt.

The timescales, diffusion widths and variations in rim compositions are indicative that these olivines spent a considerable amount of time in shallow storage probably within a crystal mush zone (*Gaffney, 2002; Burgisser and Bergantz, 2011; Passmore et al., 2012; Neave et al, 2013; Bergantz et al., 2015; Hartley et al., 2016*). The large modal abundance of these cumulate olivines within the lobes of this lava flow field,

as detailed earlier in the chapter, is evidence that a substantial amount of mush was mobilised during this eruption. It is within the mush zone that the primitive cores may have acquired more evolved rims and if conditions remain hot, the olivines will equilibrate and diffuse. Some localised convection within the mush may also have been the driver of diffusion. Diffusive relaxation continued over many years. The long residence time within the mush pile may have contributed to the dissolution of the crystals. The inconsistent rim compositions may be due to localised heterogeneities in melt composition within the mush (*Passmore et al., 2012; Hartley et al., 2016*) or the tapping of a compositionally stratified sill (*McBirney, 1995; Gaffney, 2002*) or the tapping of a sequence of compositionally distinct sills (*Pankhurst et al., 2017*). The age of this lava flow precludes any historical accounts of seismic disturbances before the Moinui eruption. Therefore it is not evident whether this lava flow was pulsatory or one continuous flow. However, the consistency of the range in the short timescales of the bladed olivines are indicative of a consistent amount of time from eruption to emplacement of all lobes. These consistent timescales and the consistency of compositions between lobes from different parts of the flow field indicates tapping of a similar source.

The cumulate olivines are not only found within the hot lava core, but are also found within the top crust of a lava lobe. The top crust (M1T) contains olivines with some of the oldest timescales found within this deposit (~10 years). Rough calculations for both Stoke's Settling Velocity and the Reynolds number using a mixture of literature values and fieldwork observations are low. Values for the density of the lava (2600 kg/m^3), the density of the crystal (3300 kg/m^3) and viscosity of the lava (600-1500 PaS) were taken from Rowland and Walker (1988). The velocity of the lava was taken from Griffiths (2000) and the crystal diameter and channel thickness was taken from field measurements. The Reynolds number is < 50 which is consistent with other authors for Hawaiian lavas (*Griffiths, 2000*) and the Stokes Settling velocity is 1.92 x 10^{-5}. This suggests the flow was laminar with a slow settling velocity. The horizontal velocity (velocity of magma) was likely faster than the vertical velocity (crystal settling velocity) and so horizontal velocity will dominate. A laminar flow is likely maintained within the lava core but it is possible that cumulate olivines may be entrained nearer the crust and will not settle into the core before cooling hence their position in the crust of the lobes.

These processes have been summarised in figure 4.36.

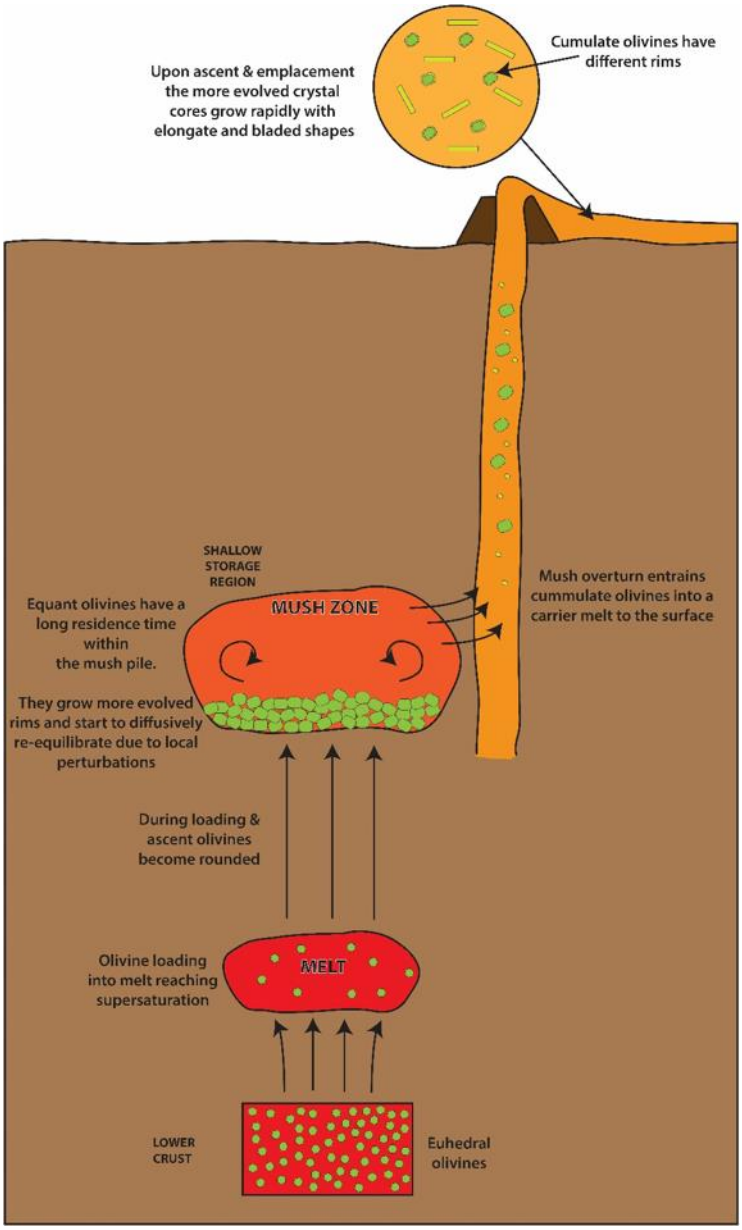

Figure 4.36: A schematic summarising the magmatic processes prior to and during the Moinui eruption.

To summarise, there is strong evidence that primitive olivine cores that crystallised in a hot, mafic magma at depth in the lower crust were mobilised to a shallow storage reservoir beneath the rift zone forming a localised mush zone. Olivines were dissolved and rounded before these olivines cores grew more evolved rims and diffusive relaxation occurred across the crystal over a long period of time whilst residing in the mush zone. Localised differences in melt composition within this mush led to varying rim compositions. Mush overturn leads to the rapid

entrainment of cumulate olivines into a carrier melt to the surface. These cumulate olivines are not in equilibrium with the melt. Upon ascent and emplacement the more evolved crystal cores in equilibrium with the melt grow rapidly due to supersaturation of the melt and rapid cooling due to degassing, possibly initially as chains and then mature to elongate and bladed shapes. Those in the crust are rapidly quenched and are unzoned. Those in the lava core and the cumulate olivines grow a rim of more evolved composition and diffusively re-equilibrate in the hot transport system before cooling.

Similar processes have been seen beneath rift zones in similar tectonic settings whereby crystals with ranging compositions and timescales are erupted within the same magma at the surface e.g. Laki 1783-1784 eruption (*Passmore et al., 2012; Neave et al., 2013, 2014; Hartley et al., 2016*). However, the bimodal nature of the crystal morphologies and timescales is unusual. This may be linked to different cooling processes, ascent rates or olivine saturations, or a combination of all three and will be looked in to in more detail before publication.

4.3.6. Lava flow cooling rate

The Moinui lava flow at this location is a sheet flow, noted by its' smooth upper surface and lack of meter-scale relief (*Hon et al., 1994*). There is textural evidence of varying rates of cooling within this lava flow from the bimodal olivine crystal shapes to the varying textures and grain size of the groundmass. It can be difficult to model complex cooling rates within lava flows, however considerable work has been done to try to constrain cooling rates in various parts of a lava flow (*Carslaw and Jaeger, 1959; Hon et al., 1994*). The rate that the solidification temperature penetrates the flow due to conductive cooling as the crust grows can be described by equation 4.5 (*Hon et al., 1994, Carslaw and Jaeger, 1959*):

$$C = \lambda\sqrt{4\mathrm{K}t} \qquad \text{(equation 4.5)}$$

C is the thickness of the crust (metres), λ is calculated as 0.879 for the upper crust and 0.611 for the lower crust as calculated by Hon et al., 1994, K is the average thermal diffusivity of solidified basalt as calculated by Hon et al., 1994 as $5.454\text{x}10^{-}$

^{7} m^2/s and t is time (hours). This can be rearranged for *t* to calculate the average cooling time.

$$t = \frac{(C/\lambda)^2}{4K} \quad \text{(equation 4.6)}$$

For the upper crust of lobe M1, the cooling time is calculated as 1.7 days (the upper crust is 0.5m thick). For the lower crust of lobe M1, the cooling time is calculated as ~1 hour. This is significantly faster due to the lower crust being much thinner than the upper crust (0.05m compared to 0.5m). For the upper crust of lobe M4, the cooling time is calculated as 4 hours (the upper crust is 0.15m thick). This cooling time is faster than the cooling time for upper crust of M1 which is consistent with the branching texture within the groundmass. For the lower crust of lobe M4, the cooling time is calculated as ~1 hour. This is consistent with the thickness of the lower crust relative to the upper crust but also consistent with the thinner lower crust from lobe M1C. Whilst the upper crust is in contact with air and should cool more slowly than the lower crust this does not seem to be the case from the thermal cooling calculations. This is because the lower crust is now thinner than it used to be due to emplacement processes. When a lava lobe is emplaced the upper surface is consistently cooler as the air keeps the top surface at ambient conditions. The lower surface has initial rapid growth and as the rock heats up below, the thermal contrast is lost and heat conducts. When magma travels through the lobe heat is efficiently extracted from the top surface, but the bottom surface is less efficient. The flowing lava reheats the base of the lava flow resulting in gas escape structures and the loss of segregated material to the upper part of the lobe resulting in loss of the volume of the lower crust (*Thordarson and Self, 1998*) – this can be seen in the field (figure 4.24D and E).

4.4. Conclusions

Both the Hapaimamo and the Moinui show a range in diffusion timescales together with a range in textures and compositions indicating a detailed and complex history through the magma plumbing system.

The Hapaimamo eruption deposits, from reticulite to lava flow, imply a spectrum of eruptions styles during this eruption (from explosive to effusive) likely due to a gas-

rich early eruption phase. However, a volatile study is beyond the scope of this project. The Hapaimamo olivines within the reticulite deposit show strong evidence of two crystal populations, identified by their minor element chemistry and distinctive diffusion timescales. It is likely that they have crystallised from a similar source but have undergone different magmatic processes and been subjected to localised variations in magma composition upon their ascent to a shallow storage region in the upper crust. The Moinui was likely solely an effusive eruption due to lack of evidence of air fall deposit. The vent is buried by younger flows (*Frank Trusdell, personal communications*). The Moinui olivines show at least two very distinct crystal populations characterised by their drastically different crystal shapes (bladed versus equant), bimodal core compositions and variable rim compositions and distinctive timescales. Both the Hapaimamo and the Moinui contain cumulate olivine. The diffusion timescales for these cumulates within Moinui can be much longer than those for the Hapaimamo (7 or 8 years compared to 2 or 3 years), likely due to longer residence time in the shallow storage pre-eruption and their presence in a better insulated flow.

It is clear from figure 4.21, comparing tephra timescales with lava flow timescales, that olivines sourced from tephra best preserve the pre-eruptive timescales due to their rapid quench. It may still be possible to retrieve the pre-eruptive timescale signatures from lava flows (even though they remain hotter for longer, enabling diffusive re-equilibration to continue), if there is a second crystal population recording later stage processes (e.g. the bladed crystals) enabling magmatic processes to be unpicked. Together these provide a more complete eruption history.

This petrological and geochemical study of two olivine-rich lavas from Mauna Loa clearly shows they have complex magmatic histories. The evidence for this is in the textures, crystal shapes, compositional range and diffusion timescales. The presence of at least two olivine populations within both sample locations has also been confirmed. The streamlined processing methods are formulated in the next chapter using the PdF olivines as a simple case study. Both the Hapaimamo and the Moinui have been identified as suitable samples to test new processing methods for robustness and to establish how complexities can be identified.

CHAPTER 5

Method development for near-real time magmatic timescale retrieval

5.1. Introduction

I have outlined the current methodologies and uncertainties of diffusion modelling in chapter 2 that are widely accepted within the wider research community (*Humler and Whitchurch, 1988; Costa and Dungan, 2005; Costa et al., 2008; Costa and Morgan, 2010*). There are slight differences in methodology and interpretation between various studies due to the use of different modelling software (e.g. DIPRA, AUTODIFF, (both diffusion specific packages), Mathematica or Matlab), variation in the retrieval of compositional data using either the EPMA or LA-ICPMS, and due to the integration and adaptation of different techniques from other scientific areas within different studies e.g. systems analysis (*Kahl et al., 2011, 2013; Girona and Costa, 2013; Ruprecht and Plank, 2013; Shea et al., 2015a*). However, no current workflow allows the retrieval of diffusion timescales and their magmatic interpretation in 'near-real time' – as soon as possible after a volcanic eruption has commenced – due to the lengthy processing times. Having this information would complement geophysical datasets (e.g. GPS, InSAR, seismics) where the geophysical signals and magmatic timescales can be correlated or there is a gap in the geophysical dataset as outlined in chapter 1.

A key part of achieving this goal of 'near-real' time timescale retrieval is to evaluate each part of the established diffusion modelling workflow and conclude which segments can be removed, adapted or streamlined. This enables the processing from sample preparation to timescale calculation and interpretation to occur in as short a time as possible, without compromising the reliability of those timescales. The key aspects of current workflows to be considered in this chapter are outlined in the flow chart below.

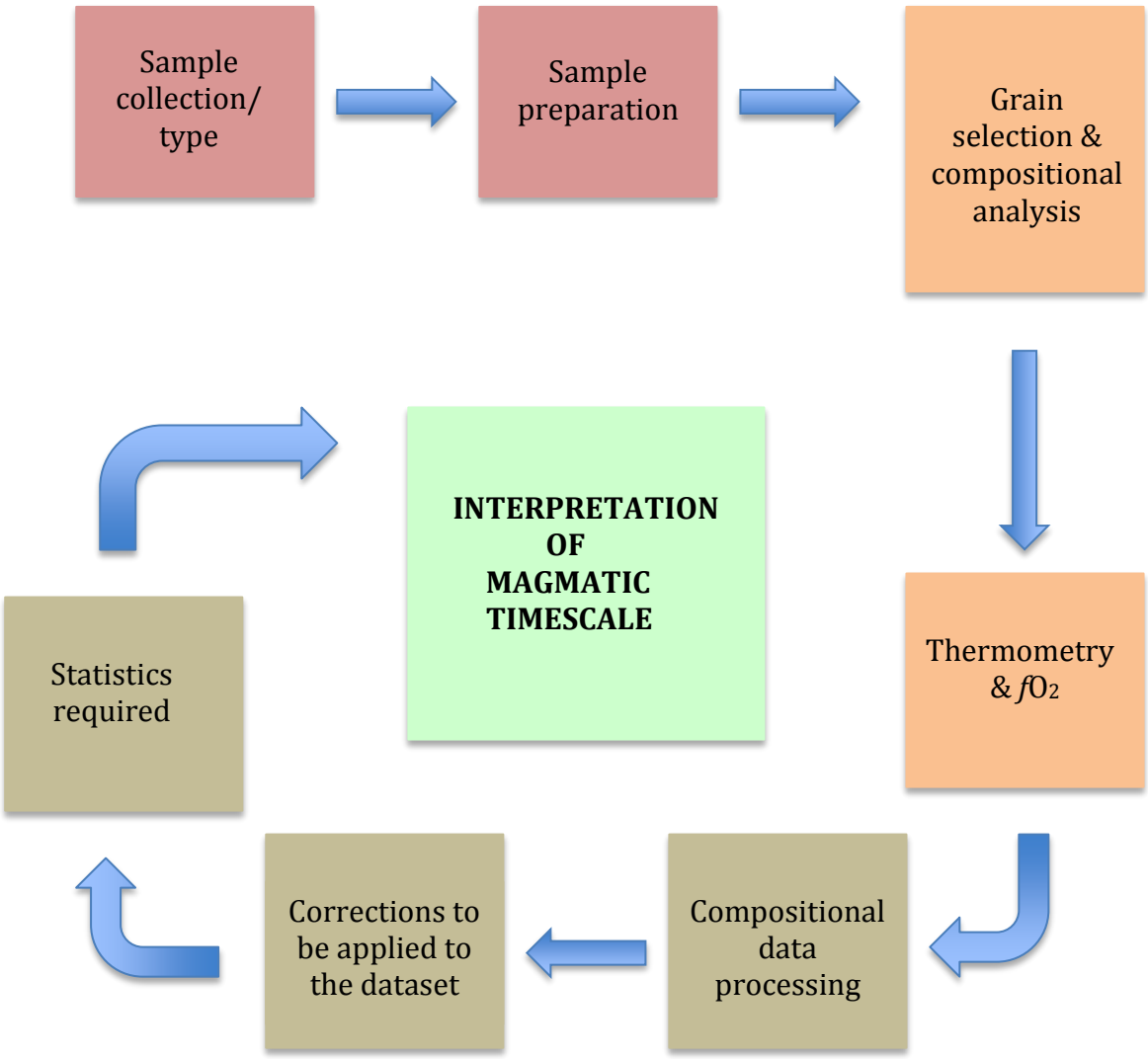

Figure 5.1: *A flow chart outlining the components of current diffusion modelling workflows to be considered in order to produce a streamlined methodology. The corrections to be applied to the dataset and their effects on the timescale quantified include growth, changing boundary conditions, shallow sectioning, crystal shape uncertainty and anisotropy (crystallographic orientation). The statistics that are required will also need to be considered – how large does our dataset need to be to pull out the meaningful timescale for the crystal population(s), how many crystals and traverses per crystal will give meaningful data*.

An optimised streamlined workflow also needs to be user-friendly and easy to deploy in an eruption scenario in order for it to be a useful tool for an observatory to implement. Whilst it would be ideal for a petrologist to carry out this workflow it need not be necessary and so must be simple enough for any field geologist to successfully apply with little training.

I will be using the results from the three datasets I have previously discussed in chapters 3 and 4 together with a synthetic dataset from Shea et al. (2015a) to underpin and evaluate the tests and adaptations I will make to the established workflow described in figure 5.1. These datasets are the 2002 lava flow, Piton de la Fournaise (PdF), Reunion Island; the Hapaimamo tephra deposit, Mauna Loa, Hawaii; and the Moinui lava flow, Mauna Loa, Hawaii.

The 2002 lava flow from PdF (sample 64217) provided a dataset with a hypothesised monodisperse olivine population that can be used as the baseline dataset to evaluate each correction and parameter applied to the data. The effects of these corrections and parameters will be considered at population level. It is assumed that this will reduce some scatter within the timescale dataset as calculated in chapter 3, however a narrow continuum of timescales within the population was identified. Samples from Hapaimamo and Moinui, Hawaii provide added complexity. Various textures, crystal shapes, differing crystal compositions and a wider range of diffusion timescales have been identified within these samples. Evaluating the effect of these complications on the new methods will be key to defining a successful streamlined work flow.

This chapter sets out to provide a diffusion modelling workflow that can be implemented in 'near-real' time. Once established, is stress-tested in chapter 6 to identify any problems or tweaks that may be necessary and to evaluate its performance under simulated eruption conditions.

5.2. Volcanic material

Ultimately sample type is one of the biggest limitations of any diffusion modelling methodology. The starting material is what will determine how much information (dominant timescale, number of timescales, number of crystal populations) and the type of information that can be retrieved e.g. information on magma remobilisation (*Hartley et al., 2016*), magma residence time deeper within the magma plumbing system (*Costa, Chakraborty and Dohmen, 2003),* recharge events (*Morgan et al., 2006*) or magma transfer (*Kahl et al., 2011, 2013*).

A wide variety of material can be, ejected from a volcano as air fall deposit (e.g. tephra (lapilli, ash or bombs)), spatter, reticulite, pele's hair, scoria, cinders), slowly extruded as dome rock or spines, extruded as a lava flow, or deposited as primary material that is reworked as part of a pyroclastic flow. This study has focuses on tephra, lava flow and spatter shown in figure 5.2.

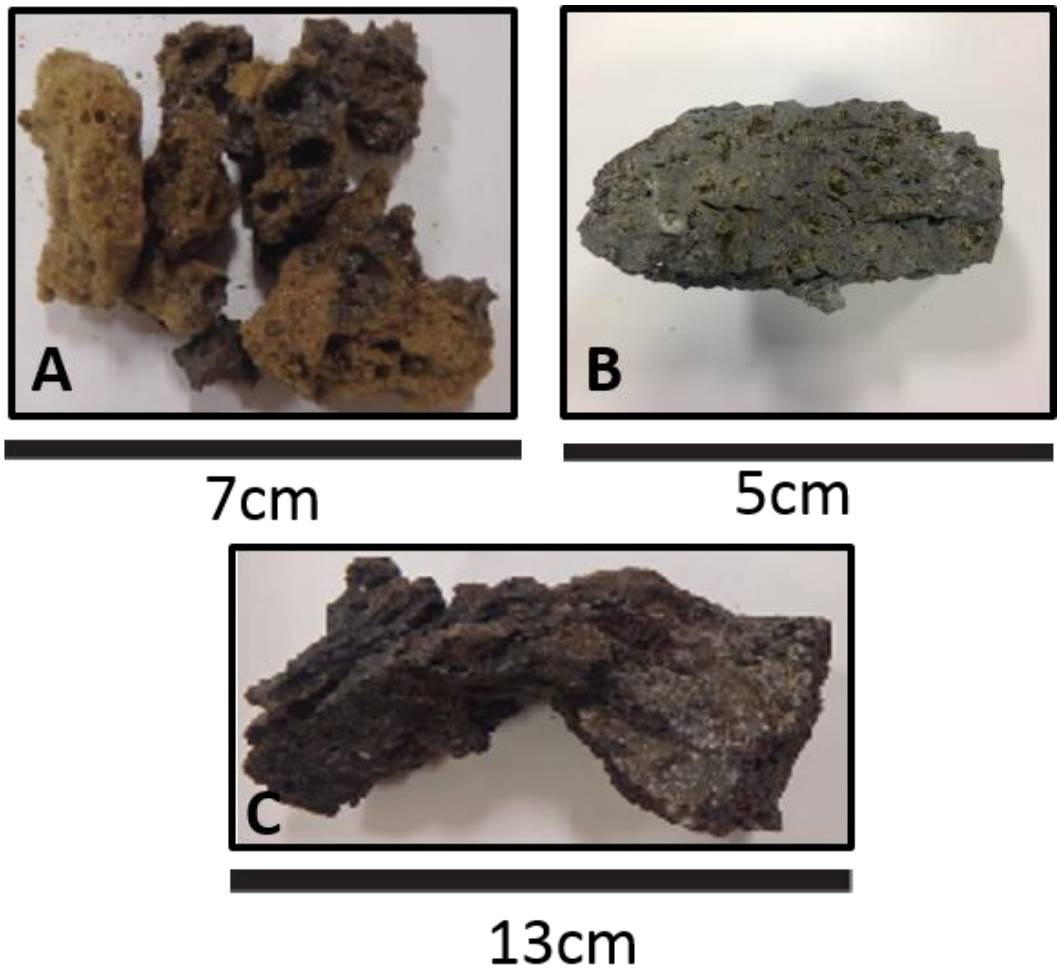

Figure 5.2: Examples of A) tephra B) lava flow and C) spatter from Mauna Loa, Hawaii

5.2.1. Effects of cooling

The cooling rate of any type of volcanic ejecta is very important for diffusion modelling such that it is a temperature controlled process as discussed in chapter 2 - the longer the material stays hot, the longer the window is for diffusion to occur. Air fall deposits can be rapidly quenched upon eruption and be completely cold at deposition (*Thomas and Sparks, 1992*). This quenching freezes the diffusion

timescale into the crystal. Phreato-magmatic eruptions are also rapidly quenched. A phreato-magmatic eruption occurs when there is interaction between magma (lava flow or tephra) and water (*Heiken, 1972; Dzurisin et al., 1995*). The water acts as the quench for the magmatic material. This can take place in the sea, deep on the ocean floor or as an eruption beneath an ice cap or glacier e.g. Grímsvötn, Iceland, Thordarson and Self (1993).

Lava flows on land, particularly pahoehoe lava flows can remain insulated and hot for longer than airfall deposits such as tephra. The cooling rate in a lava flow can be effected by many parameters such as the formation of boundary layers, convective cooling, changing heat flux rates, eruption temperatures and flow volumes (*Hon et al., 1994; Sakimoto and Zuber, 1998*). Lack of quenching of material upon eruption can lead to re-equilibration of diffusion signals if temperatures remain elevated following eruption, making the timescales less meaningful in terms of interpreting subsurface processes. Lava flows can be sampled and quenched immediately by submerging samples in a bucket to preserve the primary mineral zoning, however this can be tricky in practice depending on access to the flow.

Pyroclastic flow deposits contain reworked material. If the diffusion process is reactivated within the hot flow, there is no certainty that any original magmatic timescale recorded in a crystal will be preserved. Also, each clast may have a different origin and so intra-clast comparison is not possible, hence this type of deposit should be avoided.

It is widely regarded that primary volcanic deposits that have been rapidly quenched, specifically tephra, are most suitable for diffusion studies, locking-in the primary magmatic timescale. However, these deposits can have a lack of context on the mineral assemblage and equilibrium (*Kahl, personal communications*) as there is no textural record of the mineralogy surrounding a zoned olivine when the diffusion was taking place. This may effect some parameters e.g. setting a boundary condition.

5.2.2. Variation of volcanic material and crystal proportions

Ultimately, sample type depends entirely on what is ejected from the volcano during eruption.

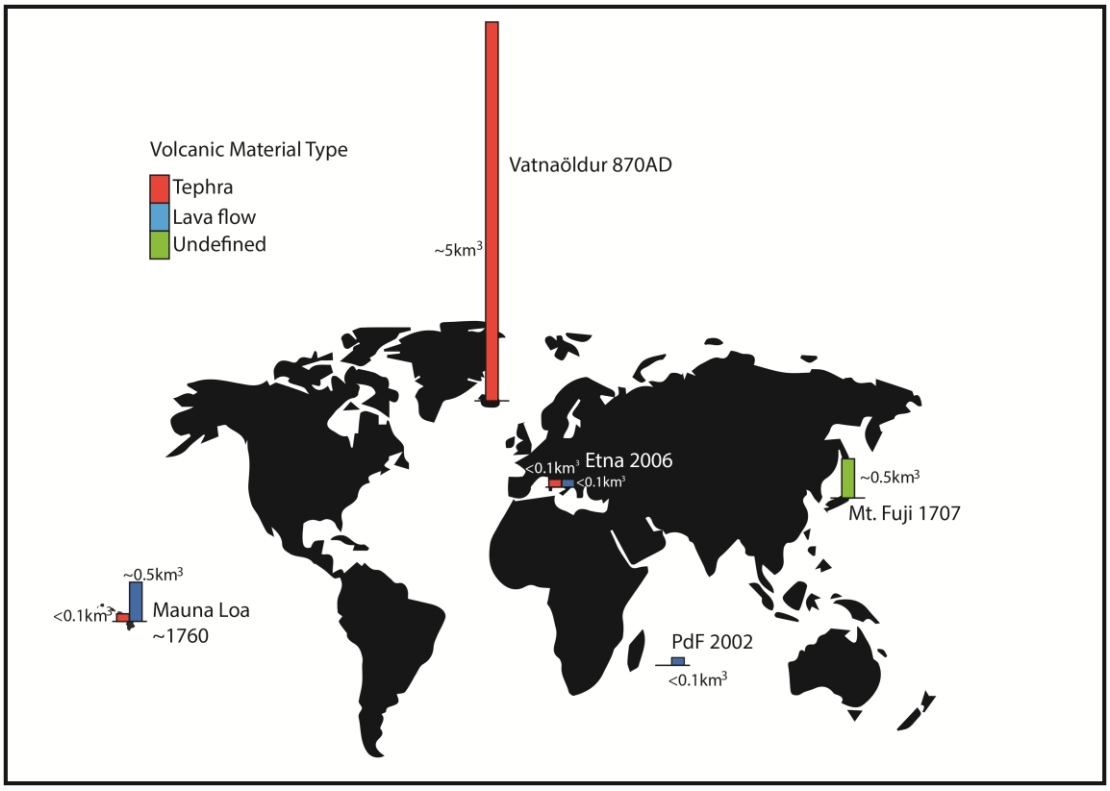

Figure 5.3: schematic world map (not to scale) showing typical volcanic events from global volcanic activity. Where volumes are indicated as <0.1km³, volumes were too small to represent on the chart; Mauna Loa tephra ~0.02km³ (field data), Etna lava flow ~0.043 km³, tephra ~0.001 km³ (italysvolcanoes.com), PdF lava flow ~1.3 x 10⁵ km³ (Vlastelic et al., 2005). Sources for other volumes are; Mauna Loa lava flow (Garcia and Rhodes 2012), Vatnaöldur tephra (Jónsdóttir et al., 2014), Mount Fuji ejecta (Schminkce, 2004). Not corrected to 'dense rock equivalent' (DRE).

Figure 5.3 shows that the type and volume of volcanic ejecta can vary between volcanoes. This is apparent even when only comparing a handful of eruptions from a handful of volcanoes (from intra plate, rift/ridge and stratovolcanoes). Rarely is tephra deposited in such large volumes as from the Vatnaöldur eruption of 870 AD, discussed in chapter 6. This eruption provides a wealth of material for possible diffusion studies. Material type may also vary between eruption cycles of the same volcanoes.

The crystal content of the sample is very important (phyric or aphyric). The more crystals a sample contains, the more likely it may be that some will be zoned, especially if more than one crystal population is present or multiple reservoirs were tapped. The more zoned crystals within a sample, the more traverses can be extracted for modelling and therefore the more robust and reliable the dataset will be. The crystallinity of volcanic deposits can vary between eruption events of the same volcano e.g. the Hapaimamo eruption of Mauna Loa produced an abnormally large deposit of reticulite containing a large modal proportion of olivine crystals, together with picritic lava flows however the 1984 eruption contained only ~3% modal abundance of olivine, few of which were suitably zoned (*Lipman et al., 1985*).

5.3. Sample preparation

Sample preparation is entirely dependent on sample type, as described in the next section. Commonly, samples are prepared as thin sections and polished blocks, or for low crystallinity, soft or highly fragmented samples, they are prepared as grain mounts. Examples of all three are shown in figure 5.4.

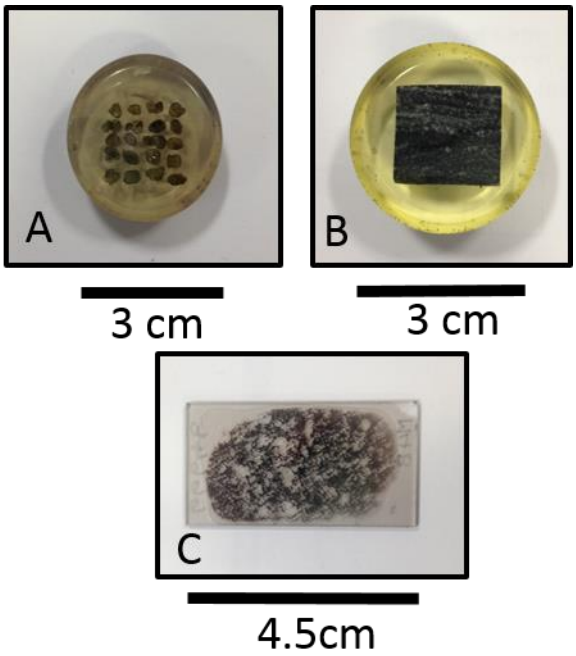

Figure 5.4: Example of A) a grain mount B) a polished block and C) a thin section as defined and used within this chapter

The best type of material for a streamlined workflow will be one that crystals can be retrieved from in the shortest amount of time and the material mounted and polished quickly ready for analysis.

5.3.1. Initial preparation

Lava flow samples require cutting a rock chip from the main sample, mounting and polishing. It can be unclear what the modal abundance of crystals in the cut section will be until the cut has been made. If there was a need to cut more than one rock chip from a sample to increase the number of crystals that can be analysed the efficiency of the new workflow would decrease.

Spatter and scoria require crushing, either by hand or mechanically, depending on its cohesiveness, although mechanically crushing can significantly damage crystals. The resulting crushed material is sieved by size fraction before crystals are picked to be placed in a grain mount. Alternatively, grains can be cut out of the scoria or spatter. This is time consuming and sometimes difficult, but affords a higher chance of maintaining the structural integrity of the crystal. Crushing of spatter as part of this study (spatter from the ramparts along the eruptive fissure of the 1887 eruption, Mauna Loa, Hawaii), resulted in mainly only fragmented crystals being retrieved with few crystal faces from which to take compositional traverses and input into the diffusion model. This rendered them useless. Tephra, was considered to be amongst the easiest to prepare. Either the glassy volcanic material encasing the crystals is very soft and vesiculated and easy to crush by hand, enabling a 'crude pick' of crystals without the use of sieving (this method was employed for the Hapaimamo tephra deposit). Or, the deposit may have been fragmented during phreato-magmatic eruption (seen with the Vatnöldur deposit in chapter 6). Multiple layers of tephra each representing a separation in eruption cycle classically form such a deposit, containing a fragmented mix of material – crystals, glass and crystals encased in glass. Each layer can be sieved separately to avoid contamination to separate grains by size fraction before picking.

5.3.2. Mounting and polishing

Due to the size of the material being mounted, thin sections are often the most time consuming to prepare. Rock chips need to be 'stuck' to the glass slide, impregnated with resin and left to harden to ensure there is no movement between the rock chip and the glass slide during the rest of the preparation. The surface area of the mounted rock chip is large, the standard thin section size is 4-6 cm^2. This makes thin sections more difficult and time consuming to prepare to a completely flat surface

by the end of the final polishing process. The thickness of a thin section (typically 30-60 μm thick) needs to be as even as possible so as not to affect the compositional analysis.

Polished blocks are prepared in a similar way to thin sections but are often smaller in size (25-30 mm in diameter typically). Thickness variations are less important so these are slightly quicker to grind and polish. These must be impregnated with a larger amount of resin and so take longer to harden ready for the grinding and polishing process. Grain mounts are often the quickest and easiest to prepare. Once crystals have been picked, they are separated by size and mounted in a grid-like pattern within a plastic circular container (up to 30 mm in diameter). This makes them easier to grind and polish but also for analytical targeting. They are covered in resin several cm's thick until the grains are completely covered and left to harden for several hours. Grinding and polishing then ensues.

Table 5.1 below summarises the average preparation time for each preparation method.

	Thin section	Polished block	Grain mount
Time to prepare	~8 hours	~4 hours	~4 hours

Table 5.1: Average preparation times for thin sections, polished blocks and grain mounts

Despite grain mounts being the quickest to prepare, further improvements can be made, as discussed in the next section.

5.3.3. Improvements for the streamlined workflow

Individual or crystal agglomerates picked from tephra or crushed spatter or scoria deposits are the ideal starting material of choice (should this be the material that is erupted) due to its considerably quicker and efficient preparation time.

Adaptations to the current preparation time have been made to further improve on this. Once the grains are picked, instead of arranging them in a grid pattern for easy location for repeat analysis on different machines (e.g. EPMA for compositional analysis then EBSD analysis on the SEM), grains can simply be placed onto the centre of a glass slide (the same used for thin section making) at random. Only a couple of

drops of resin are needed to cover the grains, with a couple of drops in each of the four corners so a flat even surface is maintained throughout polishing. This can then be left to harden for only 1 hour, considerably shorter than the traditional grain mount. The coarser grinding stage can be skipped and the slide immediately 'hand lapped', then polished, as there is only a very small surface area. I will refer to this new grain mount as a 'grain-slide' throughout the rest of the thesis. One grain-slide can be completed for a sample in a couple of hours, the shortest preparation time by far.

Table 5.2 below shows comparison of the grain-slide preparation time with the previously used grain mount and figure 5.5 below shows an example of a grain slide compared to a grain mount.

	Grain mount	Grain slide
Time to prepare	~4 hours	~2 hours

Table 5.2. Grain mount preparation time compared to the grain slide preparation time.

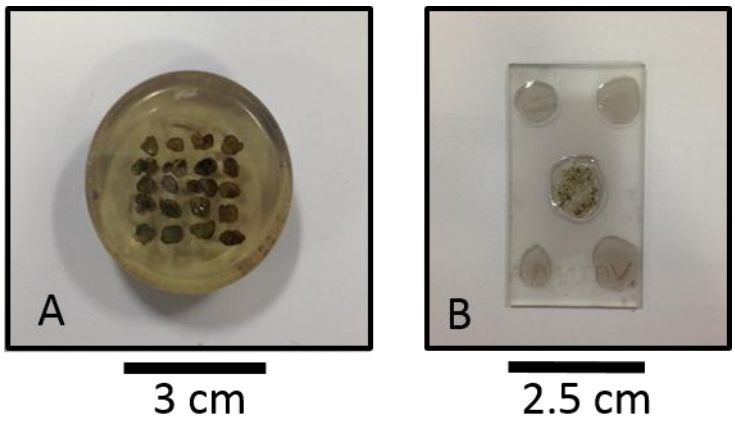

Figure 5.5: Example of A) a grain mount and B) a grain slide

5.4. Grain selection and compositional analysis

Once samples have been prepared and zoned crystals identified, it is important to be somewhat selective about which crystal faces to target for compositional analysis. This in itself makes the workflow much more efficient. Shea et al. (2015a) have done considerable work proposing selection rules when choosing crystals to apply diffusion modelling to and applying and comparing 1D, 2D and 3D models. The selection rules were tested with a synthetic dataset and an idealised olivine

crystal shape. Even in the absence of clear rules, most people will make informed choices and preference selections, even if not consciously, as evidenced in the relatively restricted range of the U-stage data in section 5.7.1.

Crystal selection in the new workflow will occur in real-time on the SEM directly before compositional analysis. It is important to be able to make informed decisions on crystal faces to be analysed quickly, then implement the compositional analysis accurately and efficiently and move on to the next traverse to acquire as much data as possible in the shortest possible time frame.

5.4.1. Selection rules

It was correctly identified by Shea et al. (2015a), that there are several sources of uncertainty relating directly to crystal selection and the application of 1D models. They state these sources as follows; (1) diffusion occurs across a complex volume in three dimensions, not just the 1 dimension that is commonly modelled (e.g. *Costa et al., 2003, 2008*), (2) diffusion within an olivine grain is anisotropic, which implies that a 1D traverse may be sampled along a fast (c-axis) or slow (a or b axis) direction or any direction (a proportion of any three of these axes) in between (*Chakraborty, 1997*), (3) slices taken through the crystal intersect randomly, meaning that the concentration gradient (diffusion zone) geometry is dependent on the orientation of the section taken and its distance from the crystal core (*Pearce et al., 1984; Wallace and Bergantz, 2004).*

Shea et al. (2015a) concluded with a number of simple selection rules that can be applied (if numerous crystals are available within a dataset). This is assuming that basic steps have been taken to separate crystal populations with different crystallisation/diffusion histories e.g. populations with different zoning styles, normal versus reverse versus complex zoning (*Costa and Chakraborty, 2004; Kahl et al., 2011, 2013*).

They are as follows; (1) it is best to select larger crystals and to avoid the smaller ones. They state that smaller crystals have a larger probability of being off centre, therefore not recording the true initial condition for the modelling. They may also represent a smaller crystal population, not the dominant population that will reveal the dominant/true timescale (*Saltikov, 1967*). This is relative to the scale of the

profile as a proportion of the size of the grain. (2) Traverses should be obtained away from crystal corners and obvious locations of concentration gradient convolution caused by merging diffusion fronts from adjacent crystal faces, as depicted in figure 2.6 in chapter 2. Certain morphologies should be avoided e.g. skeletal grains due their numerous corners. Polyhedral grains are preferable unless 2D or 3D models are being employed (3) Olivine slices that are highly off centre or oblique cuts should be discarded. These can be identified by a dipping concentration plateau not a clear flat one. Traverses that would exhibit a dipping plateau compared to a clear plateau are shown in figure 5.6. These also will not identify the true timescale. (4) Sections that display a lack of any concentration gradient symmetry across the different measurable faces of the crystal (different diffusion widths) should be avoided. They have identified such cuts as oblique. (5) At least two suitable traverses should be measured in different crystallographic directions from two different crystal faces of the same crystal. This can help to confirm that diffusion was indeed anisotropic and not diffusion with growth occurring at the same time (*Costa et al., 2008*) testing the variability of timescales within a single olivine.

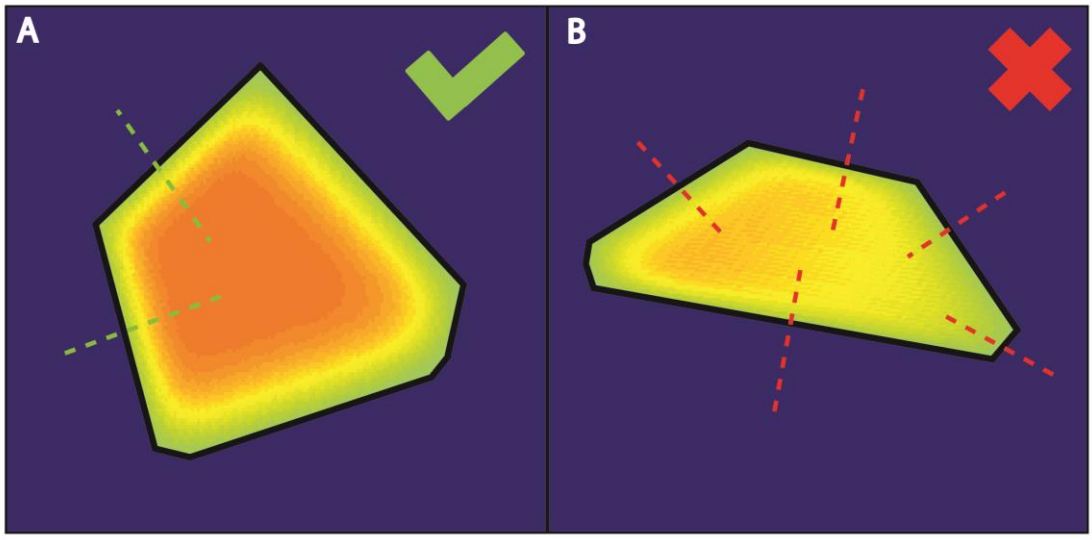

Figure 5.6: *(A) a slice through a zoned olivine shape showing examples of suitable traverses (green dashed line) for diffusion modelling. (B) a slice through a zoned olivine shape showing examples of unsuitable traverses due to core loss and a dipping plateau as outlined above (selection rule 3). Adapted from Shea et al. (2015a).*

Whilst these selection rules need to be considered and have gone some way to greatly simplifying crystal selection for those that are not experts in diffusion modelling, there is a limitation to solely relying on these rules and they should be

considered advisory and preferable where good and plentiful data make them easy to employ – not always the case in nature!

During processing of the three case studies outlined in chapters 3 and 4 and considering the types of volcanic material that are typically worked with in the previous section, it has become clear that these guidelines are not always possible to implement. Within lava flow samples (specifically the Moinui lava flow samples), most of the olivine grains in the thin section are pervasively cracked just inside the perimeter of the crystal and beyond, making it very difficult and in some places impossible, to extract a full profile from rim to core to capture the full magmatic signature without plotting the points manually. This cracking is shown in figure 5.7. This would hinder a new streamlined workflow.

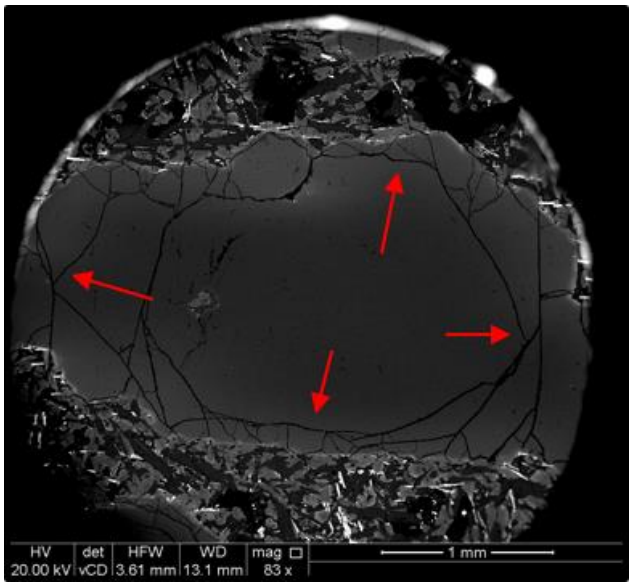

Figure 5.7. A large olivine crystal surrounded by finer grained groundmass. Red arrows highlight pervasive cracking near the edges making it difficult to retrieve a full diffusion profile.

These defects are likely due to the consistent pressure applied during the thin making process and the fragility of the samples, perhaps due to their vesicularity. Alternatively, as the flow cools and hardens, pressure may be exerted on the crystals. Similarly, crystals from spatter samples from the 1887 Mauna Loa lava flow were damaged during the crushing and cutting process. Crystals that were picked and mounted turned out to be crystal shards or fragments with only one crystal face to measure a traverse from or having no measureable crystal face at all. This sample set were not analysed for this reason.

Shea et al. (2015a) used synthetic olivine slices from an idealised theoretical olivine grain. The problem of crystals being fragmented or cracked during sample preparation or due to an explosive eruption was not considered. However, my datasets have shown this problem to be extensive in some natural cases (Moinui). This makes it difficult to measure more than one traverse in two different crystallographic directions as outlined in selection rule (5).

Regardless, this rule is too simplistic, testing only for anisotropy. As shown within the PdF dataset, even when multiple traverses are analysed within a crystal and corrected for anisotropy there is still scatter amongst the timescales, as described in chapter 3. Hypotheses for the cause of this scatter are that it is a product of shallow sectioning, out of plane diffusion, growth/changing boundary condition effects and/or the presence of a narrow continuum of timescales within a single population rather than the timescales correcting to a single unique value. The effects of shallow sectioning and growth/changing boundary conditions on the dominant magmatic timescale will be evaluated later in this chapter using the PdF dataset, to evaluate if the presence of a narrow continuum of timescales still persists.

Rule 4 states that crystals with a lack of concentration gradient symmetry across a slice (different diffusion widths on different faces) should be avoided. This can either be attributed to shallow sectioning or diffusion directly aligned with the crystallographic c-axis (faster diffusion, creating a wider diffusion zone) or diffusion directly aligned with the a-or-b axis (slower diffusion, creating a narrower diffusion zone) (*Shea et al., 2015a*). These potential problems will be evaluated and quantified at a crystal population level later in this chapter. Employing a rejection process too early in the workflow when using population level statistics may induce bias on to the dataset.

To summarise, the Shea et al. (2015a) selection rules are useful, but in reality for a rapid processing workflow it is important to be able to work as well as possible with any crystal slices. The following sections in this chapter will address how much of this will be possible. Shea et al. (2015a) also proposes the statistics needed from one crystal population to unravel the true magmatic timescale in that dataset. They argue that due to crystal shape uncertainties and sectioning effects, the precision of the mean timescales vary by ~5-25% between 1D and true 3D diffusion models

(with or without the anisotropy correction). They suggest ~20 traverses need to be processed using 1D models as a minimum to achieve this accuracy.

This chapter focuses on applying anisotropy corrections to the whole crystal population, with the aim of stating how many crystals and traverses need to be analysed to distinguish how many crystal populations are present and to reveal the dominant true timescale from a natural dataset. Knowing how many crystal populations are present is important because they can hold information of the chemical history of the magma and its journey through the plumbing system. These statistics can then be compared to theoretical statistics from Shea et al. (2015) to provide more robust data collection targets.

5.4.2. Compositional analysis

Composition of the olivine is a key input parameter into the diffusion model. Forsterite content at the core and rim (to set the initial and boundary conditions) is calculated using the following equation (=(Mg/(Mg+Fe+Mn+Ni)). Zoned crystals are usually identified on the SEM or the EPMA, mapped and target boundaries are selected ready for compositional analysis on the EPMA.

The EPMA has excellent beam stability and analytical precision (often with detection limits of a few hundred ppm). Totals of 100% $\pm$ 0.1 (for Fo ~ 1 mol. %) are often achieved. Traverses are plotted during the course of a day and analysis is run overnight. Count times per analysis spot can be 3-4 minutes in order to retrieve accurate and precise data (depending on the number of elements to be measured) and traverses may contain from 10-30 points to achieve good spatial resolution along the complete width of a diffused crystal edge. A large number of traverses are required to create a robust dataset (Shea et al., (2015a) estimate at least 20), for which the analysis time can often run into a couple of days – not ideal for a near-real time monitoring technique despite the quality of data that is acquired.

Tests were performed to acquire this compositional data on the SEM with an Energy Dispersive Spectrometer (EDS) detector rather than the Wave Dispersive Spectrometers (WDS) within the EPMA. This allows compositional data to be acquired much faster (a matter of hours) whilst not compromising the quality of the data, if set up correctly. The SEM is also often cheaper and more widely available.

The SEM is not often currently used for composition analysis for diffusion modelling as it is more imprecise at analysing for composition than the EPMA. The SEM prioritises its imaging facilities over the X-ray spectrometers and optical microscope (*Reed, 1997*). Conditions within the chamber can also be less stable for compositional analysis e.g. due to drift in beam current (*Reed, 1996*). The SEM is quite precise at measuring element ratios using EDS. A method has been tested achieving totals of 96-105%. EDS compositions were calibrated with EPMA compositions for the same traverses and in doing so decided to accept totals within the range of 100 +/- 5%. This calibration is discussed later in the section.

The two main parameters that influence SEM data quality are the stage height and the beam stability, so the geometry of the sample and the detector are important. The more X-rays that get absorbed, the higher the count rate and the better quality the data, although a low dead time must also be maintained. If X-rays arrive too frequently, both signals are lost resulting in a high dead time. The stage height must remain the same throughout the analytical process but the focus can be improved by manually adjusting the stage by small increments. For this study, a recommended 12 mm working distance was set. The beam is optimised using cobalt. This can be performed before each traverse, or recalibration can be done at varying intervals when the traverse totals have started to drift. There is little that can be done to maintain beam stability other than controlling the ambient conditions and keeping the chamber conditions as consistent as possible i.e. venting the chamber as little as possible, and so having the cobalt in the SEM at the same time as the sample. It is also advisable to polish the cobalt to as near the same thickness as the sample as possible (or vice versa), so that the stage height needs to little altered if at all, and another source or error is not introduced. If a top referenced sample holder is available, there will be no height issues between the sample and the cobalt.

Spot analyses using EDS in the SEM can retrieve good results when set for just 1 minute. This is only a quarter of the time necessary for an EPMA spot analysis, further streamlining this part of the new method. Several traverses from the PdF dataset (that were initially analysed with the EPMA), were re-analysed by EDS to measure its effectiveness at retrieving an accurate composition. Figure 5.8 shows an example of a false colour SEM image (placed into the “3-3-2 RGB” lookup table

colours which highlights gradients) of a crystal face where a traverse was re-analysed.

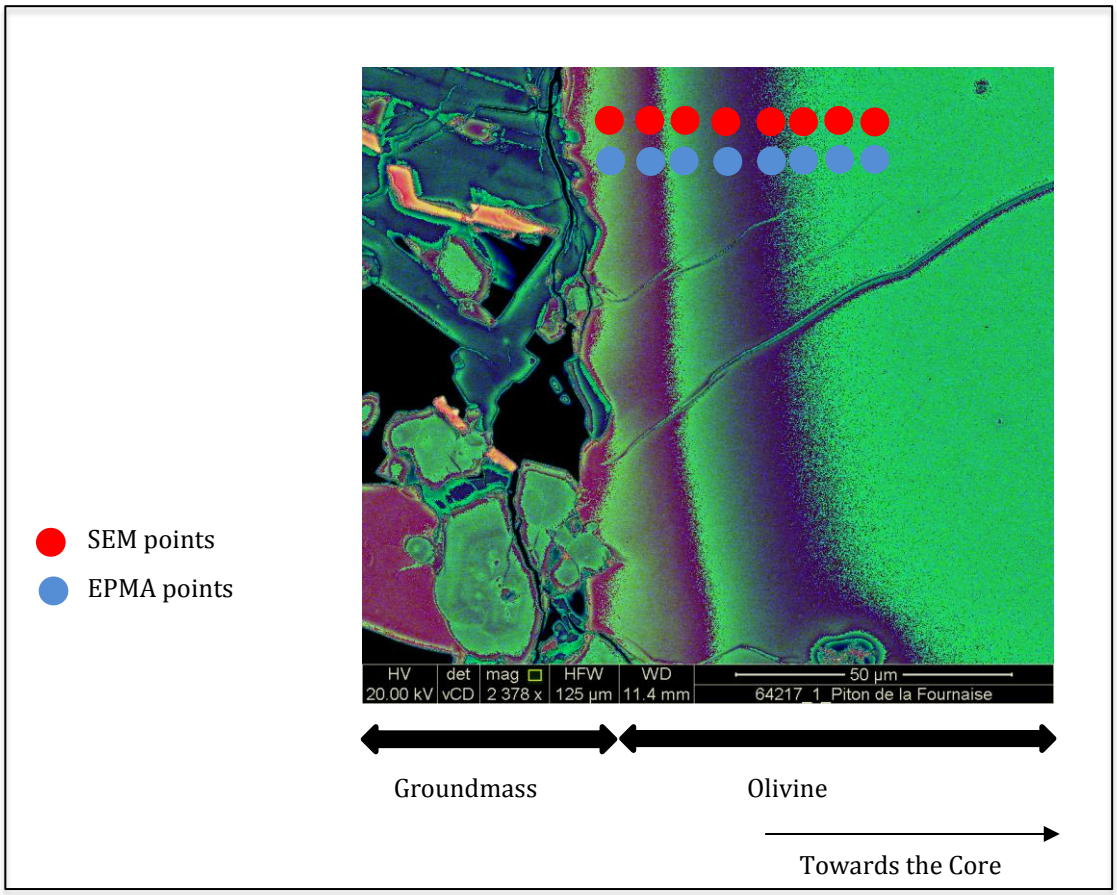

Figure 5.8: *Example of one of the zoned olivine crystal faces analysed for composition on the EPMA and SEM. Traverses measured are shown by the red and blue points.*

The data retrieved from these traverses are shown in figure 5.9. Absolute measurements can fluctuate whereas Fo ratios are very stable. If totals are low due to a lower than average beam current, magnesium measurements will be low and iron measurements will be low, but proportionally by the same amount. If the totals are high, the vice versa is the case. Therefore the ratios are reproducible for the EDS analysis.

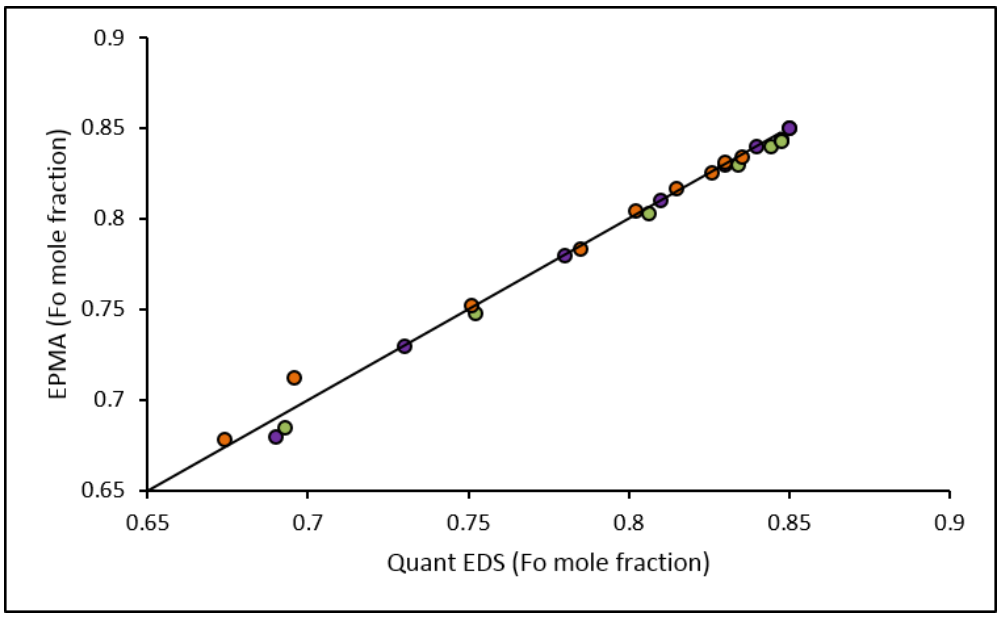

Figure 5.9: Forsterite values for spot analyses taken along three traverses (denoted by the different colours) from two crystals. The same spot was measured with the EPMA and then with Quant EDS on the SEM for comparison.

It is very clear from these results that both methods give nearly the same compositional values for each spot analysis giving confidence in the EDS method to produce accurate data. There is some variation (1 mol %) towards the rim of the profile for one of the traverses. This may be due to inconsistencies in how close to the crystal rim each analysis was taken. Importantly, this method is many hours faster than a similar method on the EPMA due to its lower count times for each spot analysis and crucially the integrity of the data, for major elements, has not been compromised.

5.5. Thermometry and Oxygen fugacity (fO_2)

Thermometry and fO_2 are two of the main controls on diffusion timescales, particularly thermometry, as discussed in chapter 2.

Oxygen fugacity is often difficult to calculate without experimental data (*Fudali, 1964)* or thermometry using the presence of two oxides (*Ghiorso and Sack, 1991*). For the new streamlined workflow, using published values for similar datasets/locations may provide the best estimates for oxygen fugacity. Temperature estimates are only as good as the thermometers from which they are

calculated. Most thermometers carry an uncertainty of $\pm$ 10-30°C (*Putirka, 2008*), as discussed in chapter 2.

Volcanic glass (commonly used for thermometry inputs) is a notoriously difficult material to analyse due to mobility of some Group 1 elements, notably Na (*Morgan and London, 1996*). Its concentration can be underestimated if count times are too long or the beam too strong. The beam is weakened in the EPMA by defocusing to lessen this Na mobility, in the SEM, the beam is simply not as strong. Totals of 97 or 98 for glass are considered acceptable totals in the research community when measured using the SEM, similar to when using the EPMA as discussed in chapter 4 (*Richard Walshaw, personal communications*). To measure glass composition by EDS for this new method, assuming tephra is the material of choice, a glass slide containing glass fragments large enough for analysis can be inserted (preferably with the olivines it harboured). Alternatively, individual grains are often encased in a light coating of glass when picked, exposing a thin layer of glass around the rim of a crystal slice when the grain-slide is polished. This thin rim can often be analysed.

Before compositional data is retrieved, a background beam measurement is taken away from the sample (either on the surface of the metal sample holder or within a faraday cup). This is to ensure the beam current is not too high and will not destabilise the glass as explained above, which would lead to poor compositional measurement. A beam current value is of 0.6-0.8 nA was commonly used. Beam defocusing is important during glass analysis and whilst it is not possible to do in an SEM machine, it can be imitated. Instead of spot analysis, circular or rectangular areas were defined for mapping. These were drawn to any size, but ~5-10 μm is advisory. The beam then scans the defined area pixel-by-pixel to create a small compositional map for the area – this is not dissimilar to beam defocus, as the beam doesn't dwell at any point and therefore migration has little opportunity to occur. Count times are much lower when measuring volcanic glass due to the mobility of some of the elements e.g. Na, as stated above. As little time as possible is preferable to get the best analysis. One minute, thirty seconds and ten seconds were all tested to see how the totals may vary. There was very little variation between the totals which came out at 97-98%. Thirty seconds has been chosen as an optimal count time and totals near 100% were achieved with careful setup.

5.6. Compositional data processing

Two methods have been tested to enable the optimum diffusion profile shape to be extracted that will aid with the speed of processing. Both the SEM image and the EDS compositional data are used.

To acquire the EDS data, full traverses from core to rim with 8 or 9 spot analyses were taken or spot analyses at the core and rim only were taken. Clearly, the first method is much slower to acquire, as it contains more points. Both sets of EDS data were calibrated with the greyscale values extracted from the same traverse on the SEM image using '*Image J*' image processing software (*Schneider et al., 2012*) and were found to calibrate with a good fit and similar profile shape. The two spot analysis method (one at the rim and one at the core) was deemed most appropriate, as the shape of the diffusion curve picked out using only these results in similar results as when more point analyses are used as shown in figure 5.10. When the EDS points are calibrated with the SEM image the full compositional profile can be retrieved.

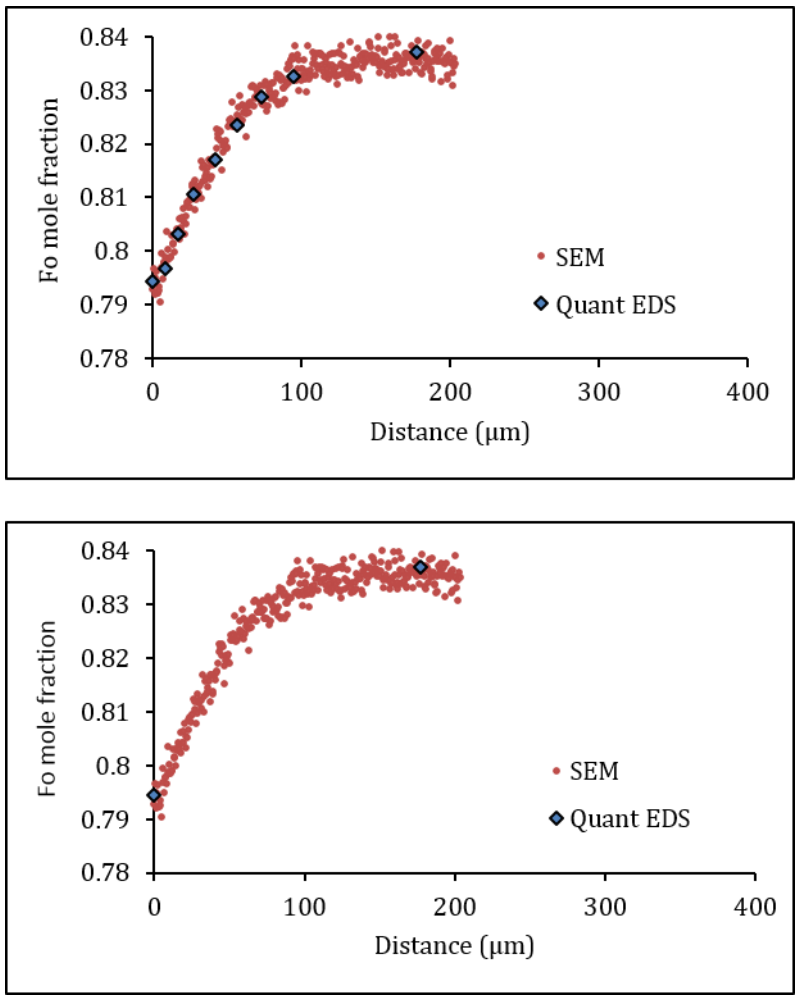

Figure 5.10: A compositional profile firstly measured with many Quant EDS points and secondly measured with Quant EDS points only at the crystal core and rim (blue). The SEM profile (red) also clearly defines the diffusion curve well providing a good match to the Quant EDS points. .

To calibrate the SEM image (and therefore the traverse) for composition, the forsterite value for each group of pixels in the image in the location of the traverse is calculated. This requires only the maximum and minimum grey scale values of the group of pixels, the maximum and minimum forsterite values of the traverse, the pixel values throughout the traverse and the distance between them as inputs. This can be coded simply into a excel spreadsheet to be calculated automatically as soon these values have been input, producing the distance between the pixels in µms and their forsterite value.

The automation of the data processing in this way maintains the streamlined workflow to this point. Time can be spent online extracting the traverse from the SEM image and calculating the forsterite values as the compositional data is output

from the SEM, something that could not be previously done when operating the EPMA – this part of the processing is occurring in almost real time.

It is important to note here that care needs to be taken when acquiring an image from the SEM for this kind of calibration. There are many variables to consider especially when using the image for quantitative analysis, such as aperture, spot size, brightness/contrast/magnification, working distance and voltage. These are defined in detail in chapter 2, section 2.2.5.2. Problems arose with the SEM imaging during data collection for the Hapaimamo tephra olivine illustrated in the figure below.

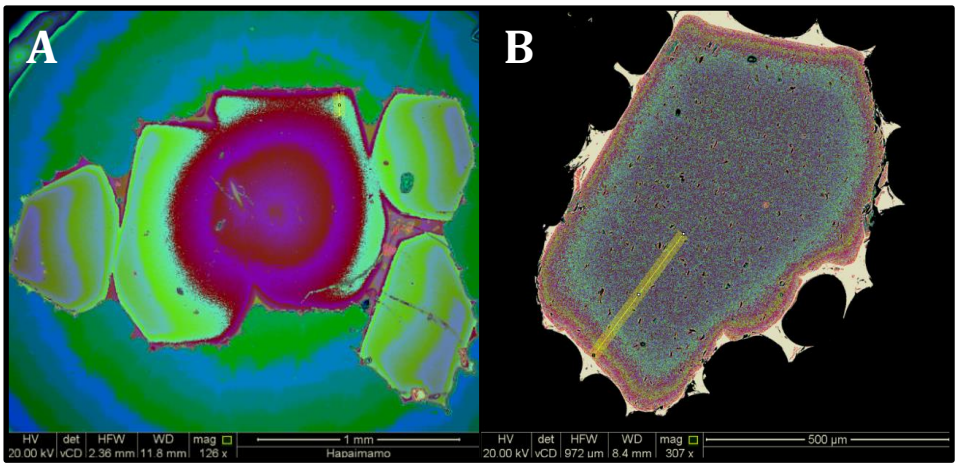

Figure 5.11: *SEM images converted from grey scale to RGB (A) a 'bullseye' pattern on the crystal surface rendering diffusion effects unclear (B) a crystal surface absent of the 'bullseye' pattern showing edge diffusion*

Curious 'zoning' patterns (figure 5.11A) began to emerge in images in this data set. It became important to define whether these patterns are real and therefore compositional or whether it is an artefact due to inappropriate SEM settings. If it is an artefact, the profile shape that is extracted for modelling could be incorrect as will the timescale calculated from it.

Investigation of this phenomenon showed that imaging larger grains (mms in size) from a low magnification (less than x300), a large aperture (aperture 1) and short working distance (10 mm) appears to cause these 'bullseye' patterns. This may be due to the large field of view creating a large angular range for the beam (*Richard Walshaw, personal communications*). However, a wide aperture and short working distance can be useful for taking images for diffusion modelling purposes as these conditions allow more energy to hit the sample. In turn, it becomes easier to pick

out very subtly zoned crystals with the naked eye (as was the case with the Hapaimamo tephra dataset). To truly check if this bullseye pattern was due to the settings above and not compositional, a piece of homogeneous lead glass was imaged, while applying gradated changes to aperture, magnification and brightness/contrast. The tests confirm that a wide aperture, and low magnification create the bullseye pattern and so it is indeed an artefact, as shown below.

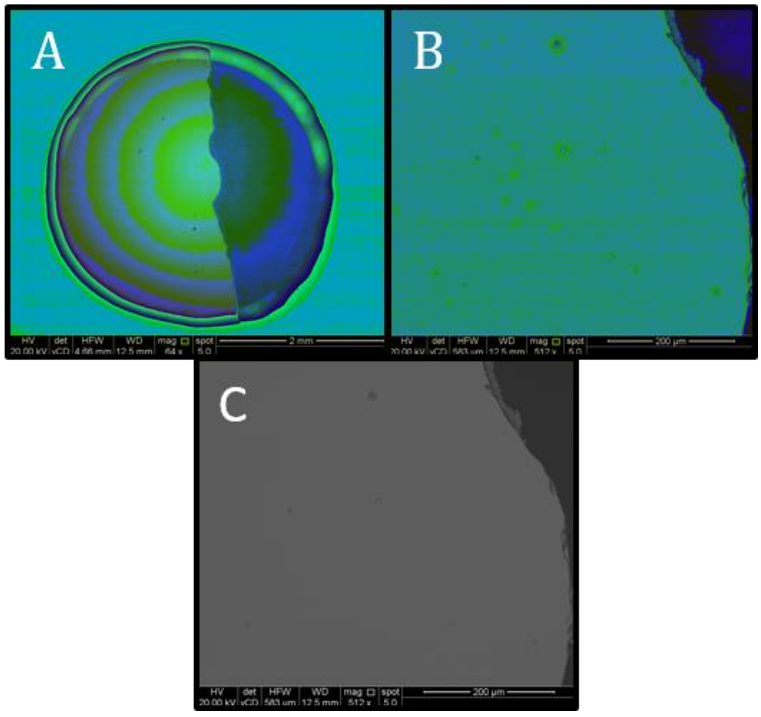

Figure 5.12: SEM images of *homogeneous lead glass (A) a low magnification, wide aperture image showing the bullseye pattern in RGB (B) a higher magnitude, narrower aperture image showing the glass is homogeneous in composition in RGB (C) a grey scale image confirming the homogeneity of the lead glass.*

Whilst it is better to control these settings so as not to have artefacts throughout the images you want to quantify, it may be possible to apply a correction post-processing to enable retrieval of the true profile shape to model for diffusion. Nonetheless, no bullseye images were used for the processing of the PdF or Hawaii datasets nor should they be used as part of a streamlined diffusion modelling method.

It is important to be able to understand what is being processed and how data is acquired for the new streamlined method to be fully successful in the absence of the EPMA. The compositional data discussed is input in to the diffusion model. Other uncertainties and corrections are now considered.

5.7. Quantifying uncertainty and improving geometrical corrections

Necessary corrections that are applied to diffusion datasets are those for anisotropy (crystallographic orientation of the traverse), shallow sectioning, growth and/or changing boundary conditions and crystal shape uncertainties as discussed throughout previous chapters. It is hypothesised that if each of these corrections are applied to or considered for the PdF olivines, the true, dominant, fully corrected timescale with little (if any) scatter should result. In this instance, the uncertainties will be limited to those only incurred by the quality of the measurements themselves (e.g. analytical errors from the EPMA, thermometry errors as discussed in chapter 2), rather than due to some of the corrections not being applied or considered.

The effects of these corrections on the PdF crystal population are evaluated in this section at crystal population level - shallow sectioning and growth/changing boundary condition effects are calculated for individual traverses and then their effects evaluated for the whole crystal population. Anisotropy corrections are applied at population level to both the PdF and Hawaii crystals, and population trends will be unpicked and evaluated. Applying or considering corrections at a population level rather than for individual traverses will increase the speed of processing for the new streamlined method.

5.7.1. Shallow sectioning angle – Universal-stage (U-stage) corrections

Shallow sectioning is a common problem across diffusion datasets due to the arbitrary and random method with which thin sections or grain mounts are made, and the olivine crystals that they contain are cut. There is little control for this during the sample preparation stage (particularly for thin sections) unless time and money has been invested in an XMT scan of the rock (which is rare). The use of XMT would characterise the 3D orientation and exact position of each crystal within the scanned rock, presenting a much better control on the angle and location of the cut through the crystal. This is no easy or cheap task and so this control is not often implemented.

AUTODIFF has the correction for sectioning effects built in to the coding as discussed in chapter 2, if U-stage measurements are input. To fully understand these effects on a crystal population (in this case, the PdF population), the sectioning

angles are evaluated independently with the use of a U-stage in this section as described in chapter 2 however, it is important to remember the possible true diffusion vector is not included in the calculation.

5.7.1.1. Applications to the dataset

The PdF olivines are used to quantify by how much the timescales have been over estimated (if at all) due to shallow sectioning. The antecrystic olivines that have been modelled to form the timescale dataset are very large, up to several millimetres in size. It is expected that there will be a mix of shallowly and less shallowly sectioned olivines within the sample set.

Pearce (1984) calculated the probability of getting an ideal section from random sectioning e.g. when crystals are randomly sectioned for thin section making. He found the probability of a section to be cut across the centre region of a crystal and also be within 10 degrees of perpendicular to any one of the three major faces (not shallowly sectioned), would be around 20%. Therefore around 80% of crystals (most of the dataset) may not be perpendicular and therefore be effected in some way by shallow sectioning. This hypothesis is tested with our measurements of the PdF crystals.

For each of the crystal traverses measured and modelled for diffusive timescales (105 traverses), the angle was measured from the crystal boundary to vertical with the U-stage. Rarely are shallow sectioning corrections incorporated into diffusion datasets e.g. Martin et al., (2008). The measurements from the PdF timescales will give an idea as to how a random population of slices may be affected by shallow sectioning and their effects can then be considered as part of the new streamlined methods. To perform the measurements during an eruption would be too time consuming (it can take a couple of hours per thin section) and so it is not an appropriate methodology for determining shallow sections as part of the rapid workflow. However, consideration of how a population may be affected by shallow sectioning would be very useful for more accurate timescale retrieval. When measuring these angles it was important to note the dip direction of the boundary when tilting the stage for input into AUTODIFF (as discussed in chapter 2). However, for this manual correction the dip direction is less important, as the diffusivity value was not updated.

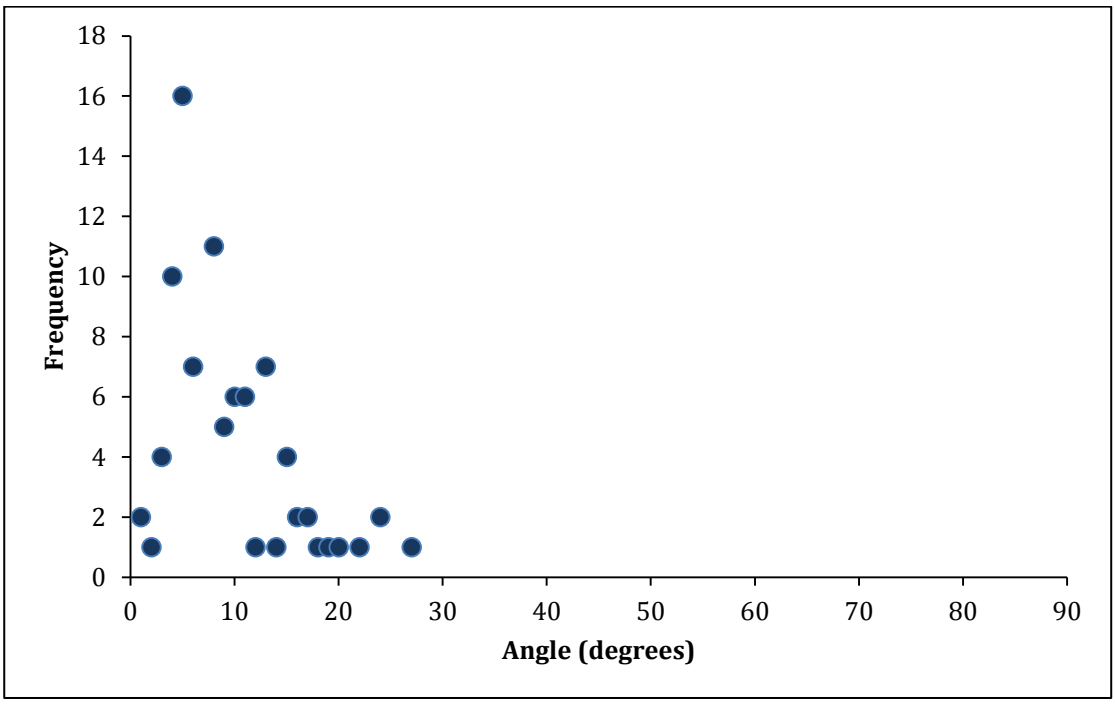

Figure 5.13: Frequency of angles measured between the crystal boundary and vertical with a U-stage for profiles modelled for diffusion timescales from PdF. These angles are used to identify shallow sectioning effects and therefore calculate over estimations of diffusion timescales.

Contrary to what was hypothesised, figure 5.13 shows a large frequency of non-shallow angles (0-10°) and a smaller frequency of the very shallow angles (<30°). These shallower angles can have a very significant effect on timescale. A preliminary summary here would be to assume shallow sectioning has not had a large effect on this dataset. These measurements have been made with the naked eye, and so some measurements were repeated to assess uncertainty. Much of the dataset was re-measured independently and the measurements were reproducible within *5*°.

Angles measured with the U-stage range from 1 to 27° for the 105 traverses. For a full list of angles measured for each traverse see Appendix H. The stretch factor, stretched timescales and timescale shift to be applied to timescales modelled by diffusion (calculated with no correction for sectioning angles), have been calculated and displayed in table 5.3 for a range of angles.

Angle measured with U-stage (°)	Angle measured with U-stage (radians)	Cos Θ	Stretch factor	Stretched timescale	Time shift from original timescale (%)
0	0	1	1	1	0
3	0.05	0.998	1.001	1.002	0.27
6	0.10	0.994	1.005	1.011	1.10
9	0.16	0.987	1.012	1.025	2.50
12	0.21	0.978	1.022	1.045	4.51
15	0.26	0.965	1.035	1.071	7.17
18	0.31	0.951	1.051	1.105	10.55
21	0.37	0.933	1.071	1.147	14.73
24	0.42	0.913	1.094	1.198	19.82
27	0.47	0.891	1.122	1.259	25.96
30	0.52	0.866	1.154	1.333	33.33

Table 5.3: The *percentage time shift that needs to be applied to calculated timescales to account for sectioning effects increases with the size of the angle measured with the U-stage.*

The average angle measured for the PdF crystals is 8.9°. This would require a shift of ~2.5% be applied to the timescale dataset which is negligible and within error of the other parameters that go into the diffusion model. In log units, this percentage shift is 0.011 log units. The uncertainties on the timescales due to temperature, activation energy and D_0 are 0.34-0.38 log units. So comparatively, a 2.5% shift in timescale will not have as large an effect on the timescales, but it would push timescales consistently longer. The largest angle measured (shallowest sectioning angle) is 27°. This would require a shift of ~26% be applied, which is somewhat more significant. Without a shallow sectioning correction, these PdF measurements show that a small amount of scatter is unavoidable across the dataset and there will

likely several timescales affected by very shallow sectioning angles. Figure 5.15 shows a summary of how the population of timescales may be affected.

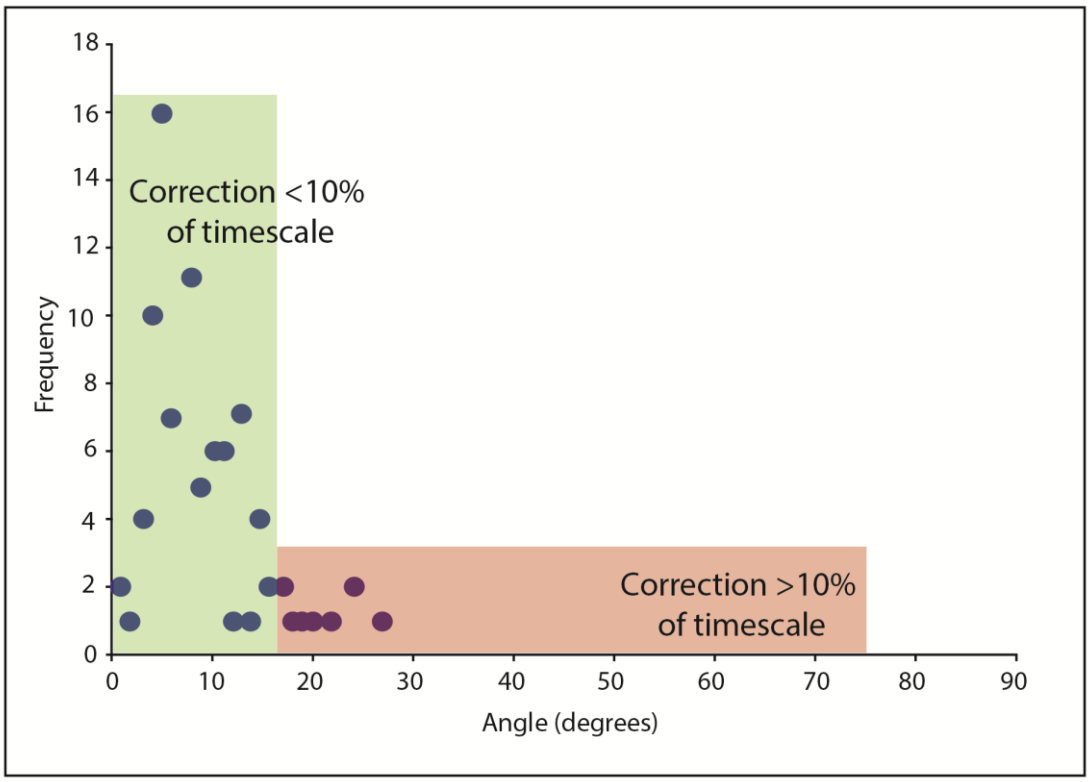

Figure 5.14: The *frequency of angles measured with the U-stage and how the timescale population is affected. Each data point is a measurement of a crystal boundary.*

Figure 5.14 demonstrates that only a handful of timescales would require a correction of greater than a 10% shift in timescale, and the majority of the dataset would require a correction of less than a 10% shift in timescale. When considering the crystal population as a whole (for crystals of this size), the effects of shallow sectioning are not significant. Whilst some scatter would be removed from the PdF population by applying this correction (table 5.4), scatter still exists in the dataset due to either growth and/or changing boundary conditions or the presence of a narrow continuous population of timescales, as hypothesised in chapter 3.

This manual correction need not be applied directly to the timescales as it is has now been incorporated into AUTODIFF (table 5.4). However, the scale of these timescale shifts are worth bearing in mind when processing timescales and making decisions for risk mitigation during an eruption, if not using AUTODIFF for modelling the timescales.

Crystal traverse	**Timescale (days)** (uncorrected for shallow sectioning)	**Timescale (days)** (corrected for shallow sectioning)
64217-1-A (1, 2, 3)	20, 24, 44	17, 22, 42
64217-1-B (1, 4)	11, 13	11, 12
64217-1-D (2,3)	7, 35	4, 24
64217-1-E (2)	18	17
64217-1-F (1, 2, 3)	19, 17, 45	18, 12, 36
64217-1-G (1, 2, 3, 4)	31, 15, 12, 20	30, 15, 12, 20
64217-1-H (5, 6)	16, 12	15, 8
64217-1-I (1, 2, 3)	7, 19, 12	6, 17, 12
64217-1-J (1)	18	15
64217-1-K (1, 2)	104 , 75	78, 54
64217-2-A (1,2, 3, 4)	15, 20, 15, 14	15, 20, 15, 14
64217-2-B (1, 2, 3, 4)	17, 14, 18, 12	16, 11, 16, 11
64217-2-C (1, 2, 3, 4)	11, 13, 17, 15	11, 10, 17, 13
64217-2-D (1, 2, 3, 4)	36, 21, 18, 18	35, 17, 16, 16
64217-2-E (1, 2, 3, 4)	12, 18, 18, 21	11, 16, 17, 21
64217-2-F (1, 2, 3)	25, 13, 12	25, 12, 12
64217-2-G (1, 2, 3, 4, 5, 6)	16, 27, 12, 17, 30, 14	16, 27, 12, 16, 29, 14
64217-2-H (1, 2, 3, 4)	10, 28, 16, 38	9, 25, 15, 38
64217-2-I (1, 2, 3, 4)	31, 17, 11, 15	28, 17, 10, 14
64217-2-J (1, 2, 3, 4, 5)	22, 10, 8, 83, 22	18, 8, 5, 77, 18
64217-3-A (1, 2, 3, 4)	14, 23, 24, 18	13, 21, 23, 18
64217-3-B (1, 2, 3, 4)	16, 13, 19, 12	16, 13, 19, 12
64217-3-C (1, 2, 3, 4)	22, 14, 21, 17	22, 14, 20, 17
64217-3-D (1, 2, 3, 4)	13, 18, 26, 39	11, 17, 25, 39
64217-3-E (1, 2, 3, 4, 5)	14, 12, 10, 13, 11	13, 12, 9, 13, 10
64217-3-F (1, 2, 3, 5)	16, 16, 27, 13	16, 16, 27, 13
64217-3-G (1, 2, 4)	14, 18, 11	13, 17, 11
64217-3-H (1, 2, 3)	62, 13, 19	58, 12, 19
64217-3-I (1, 2, 3, 4)	17, 17, 22, 11	14, 13, 20, 8
64217-3-J (1, 2, 3, 4, 5)	14, 18, 10, 12, 14	12, 13, 9, 10, 12

Table 5.4: Timescales from the PdF dataset uncorrected for shallow sectioning effects compared against timescales corrected for shallow sectioning effects. Those highlighted in red are identified as having scatter within the crystal possibly due to shallow sectioning effects.

Overall the recurrence of smaller shallow sectioning effects within this dataset rather than large ones, is likely due to the subconscious selection of crystal faces analysed. Even when trying not to be biased when selecting crystal slices to work with, thoroughly unworkable crystal slices do not make the initial selection (these ones are the ones likely to be affected by large shallow sectioning effects). As mentioned, this correction is now incorporated in to the AUTODIFF diffusion models, but this manual calculation of the data in isolation provides clarity on how populations of timescales can be affected. Measurements need not be repeated as

part of the new streamlined workflow but shallow sectioning can now be considered more quantitatively, particularly for timescales from crystals of a similar size. Datasets should typically reduce somewhat in scatter and timescales will become shorter.

5.7.2. Growth and changing boundary conditions

Unpicking growth and diffusion when occurring simultaneously is one of the greatest challenges still facing diffusion modellers. Many studies have been carried out to identify these affects using minor element profiles or zoning patterns (*Donaldson, 1975; Pearce, 1987; Watson and Liang, 1995; McCaig et al., 2007; Costa et al., 2008; Watson and Muller, 2009; Shea et al., 2015b*) or isotopes (*Oeser et al., 2015*). The effects of growth and/or changing boundary conditions on timescales are often ignored and not incorporated in diffusion models or affected traverses are discarded altogether and not used.

In an eruption scenario, although selection rules as stated by Shea et al. (2015a) are very helpful, having to continuously discard profiles that appear to have been affected in some way by growth and/or changing boundary conditions is a time consuming and inefficient process. The new streamlined method aims to be able to cope with a range of profile types with oddities accounted for. Here, the effect of growth and/or changing boundary conditions on a population of timescales are discussed and evaluated to determine if affected profiles can still be incorporated into the dataset. The implications these have about the magmatic system are also discussed.

5.7.2.1. Modelling growth and changing boundary conditions

The PdF dataset was used to evaluate and quantify the effects of simultaneous growth and/or changing boundary conditions and diffusion. In chapter 3 it was highlighted that a mismatch in profile both near the rim and nearer the core (where diffusion is most prevalent) was present when comparing the compositional traverses from the crystal to the diffusion model.

These features have been illustrated schematically below;

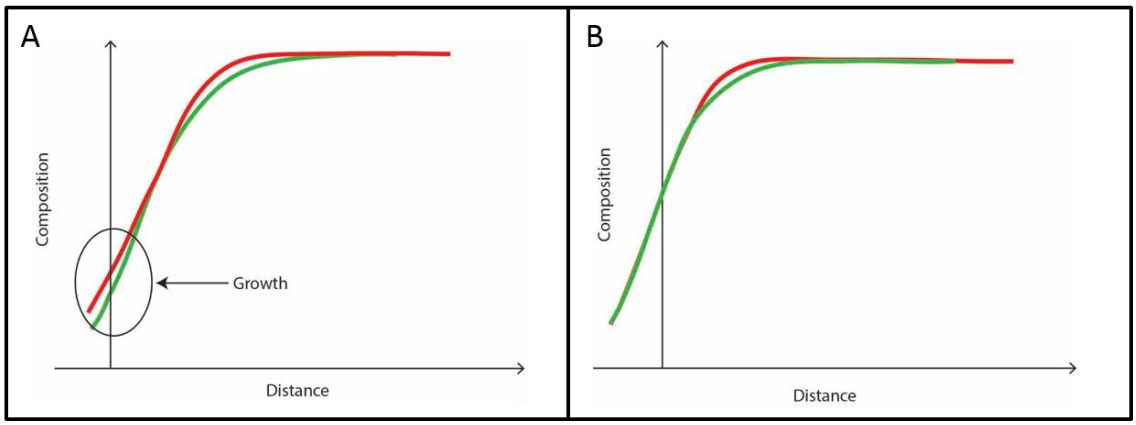

Figure 5.15: Two schematics showing A) effects of growth (towards the crystal rim) and changing boundary conditions (within the curvature of the profile nearer the core) B) effects of changing boundary conditions only, on a diffusion profile. Green shows the compositional change with distance from the crystal rim to the crystal core. Red shows a best fit diffusion model.

Figure 5.15 shows the lack of fit in both schematics between the compositional data (green) and best fit diffusion model (red). As a melt decompresses, it has a changing stability and equilibrium composition (*Hort, 1998; Hammer and Rutherford, 2002*). If the melt is olivine saturated this can lead to crystal growth (*Hort, 1998*). Figure 5.16A shows the profile near the rim can produce a 'flick'. This part of the profile will be remodelled to determine if this is due to crystal growth being faster than diffusion. Shown in both schematics (figure 5.15A and B), the curved part of each compositional profile (green) also does not fit with the model (red). As diffusion occurs, the boundary condition is dropping creating this mismatch. The cause and effects of changing boundary conditions are discussed in more detail in chapter 3. This change in boundary condition can be crudely replicated in AUTODIFF by manually changing the composition of the crystal at its rim until a much better fit with the model is achieved. This simulates the effect of a changing boundary condition.

Both crystal growth and changing boundary conditions are modelled more accurately, in a software called FINDIF (*Morgan, 2017, in prep*) to evaluate the impact on a population of diffusion timescales. The results are considered as part of the new rapid processing workflow.

5.7.2.2. FINDIF methodology for modelling growth and changing boundary conditions

A detailed description of FINDIF's methodologies can be found in chapter 2, but a description of how it can be used for modelling growth and changing boundary conditions is described below. The methodology is slightly different between the two different processes.

For modelling changing boundary conditions, the input image is as standard (as described in chapter 2), but numerous conditions files are setup with decreasing minimum forsterite values assigned to each, to simulate changing conditions at the crystal rim. These are manually set for varying time periods on a trial and error basis depending on the shape of the profile extracted from the crystal. Simulating growth and diffusion is more complicated. This setup is shown in the schematic below.

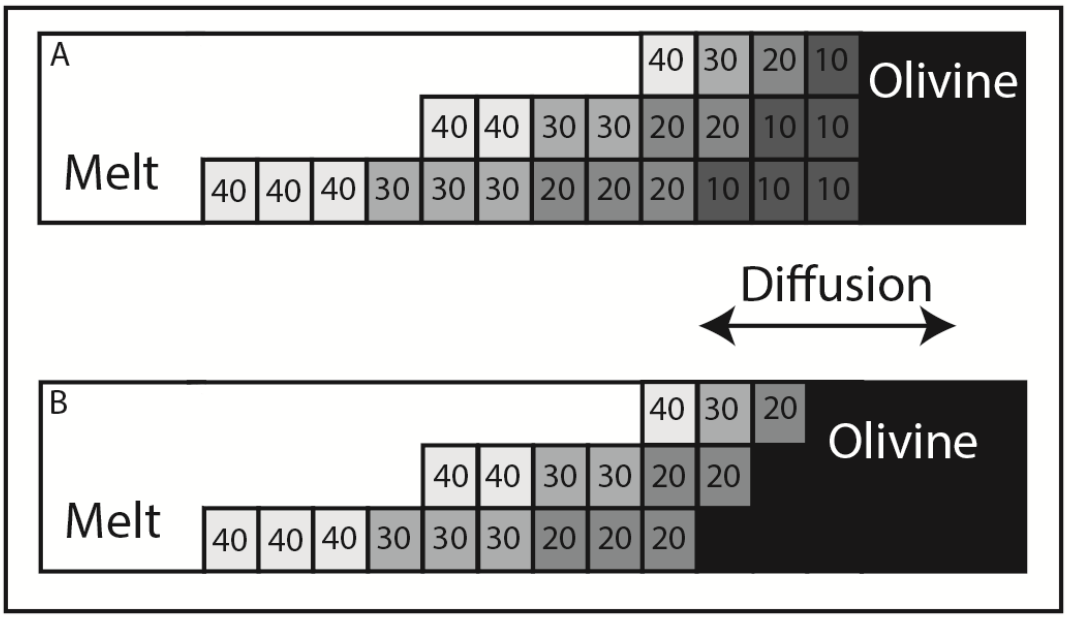

Figure 5.16: (A) an example input file for growth for three profiles. Each growth increment is assigned a different greyscale value. Each growth increment varies in width between the profiles. (B) The input file after the first growth step. The first grey scale value (10) is assigned as olivine and growth of the olivine continues until the last growth step (40).

As the input file for memory size for FINDIF is 512x512 grid, only a finite series of growth conditions can be modelled. It is optimal to setup ~3 different growth stages for this dataset but a maximum of 500 can potentially be reached with this grid size (512 rows of pixels). Each growth stage is assigned a different grey scale colour (buffer value or fixed external composition). Diffusion is set to only occur

horizontally. Each horizontal row of pixels is 1 profile (each profile contains incrementally greater proportions of growth). The growth stages (buffer values) are controlled in the conditions file. The number of conditions files is dictated by how often the boundary condition changes in the simulation and how late stage the crystal growth is. Each condition contains a different buffer value and time period over which this growth condition is applied in the model. This controls the shape of the curve that is output at the end of the simulation. The first growth increment has a buffer value of 10 at one pixel thick (small amount of growth incorporated). The buffer then changes, to 20, 30, 40 etc. (a new growth step) for different time periods as the simulation progresses across the profile. The previous buffer value reverts to olivine, allowing the crystal to 'grow' once the maximum time for each condition is reached. Each subsequent profile (line of pixels) incorporates incrementally larger amounts of growth, buffer values become 2, 3, 4, 5, 6 etc. pixels wide and so on until the last growth profile has been simulated. The amount of growth incorporated depends on how much growth has affected the crystal traverse.

FINDIF can model both growth and changing boundary conditions simultaneously. For this dataset, profiles were modelled first with changing boundary conditions. If this did not produce a good fit between the profile and the model, growth was also incorporated until a better fit was achieved.

5.7.2.3. FINDIF results

After initial 1D-modelling, 60 profiles were identified from the PdF dataset as being affected by either growth and/or changing boundary conditions (whilst diffusion was ongoing). This is a significant proportion of the 105 traverses modelled and so it is important for these effects to be quantified, so they can be considered at population level as part of the new rapid processing workflow. Of the 60 profiles that have been identified as affected by crystal growth and/or changing boundary conditions, 24 were re-modelled in FINDIF. The conditions files were setup with buffer values to start at Fo_{84} (core composition). The buffer value was decreased in each subsequent condition file incrementally by ~0.4-0.5 mol. % until the rim composition for each profile was reached (~Fo_{63-70}).

Figure 5.17 shows a crystal traverse modelled with AUTODIFF (A) compared to the same traverse modelled in FINDIF (B) with only changing boundary conditions applied.

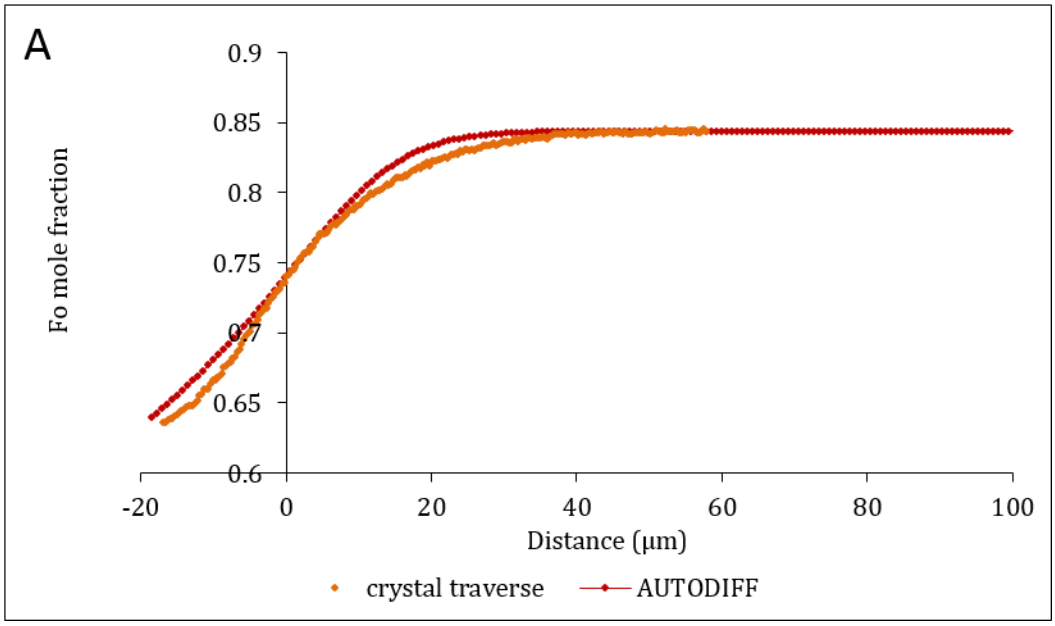

Figure 5.17.A: a crystal traverse (64217-3_F1) modelled using AUTODIFF with a fixed boundary condition. A timescales of 15 days is produced.

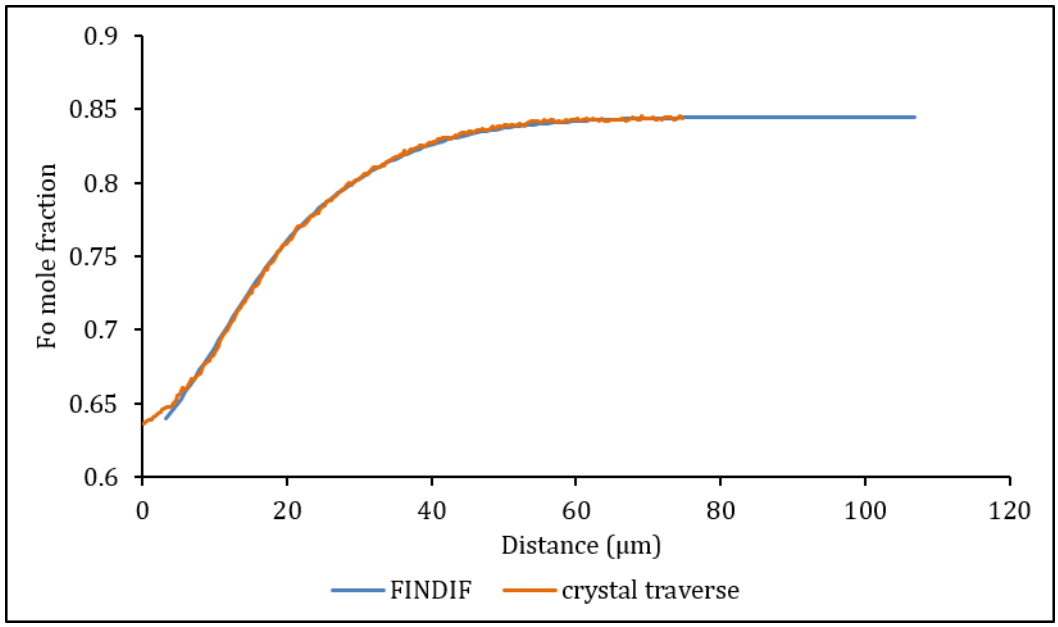

Figure 5.17.B: the same crystal traverse (64217-3_F1) modelled using FINDIF with a changing boundary condition.

Figure 5.17A and B clearly shows a much better model fit to the crystal traverse is achieved with a changing boundary condition (at the same time of diffusion). To achieve this fit, once the model has been calculated (at a given model time) and output from FINDIF, it must be stretched to fit with the profile of the crystal traverse.

That stretch factor is squared and multiplied by the total model time to calculate the true diffusion timescale with changing boundary conditions accounted for.

The changing boundary condition is not the only condition affecting the shape of this profile indicated by the lack of fit between the edge of the traverse profile and the model (near the rim of the crystal) due to the distinctive 'flick'. When growth increments are added into the model, the resultant fit is much better, shown in figure 5.17.C.

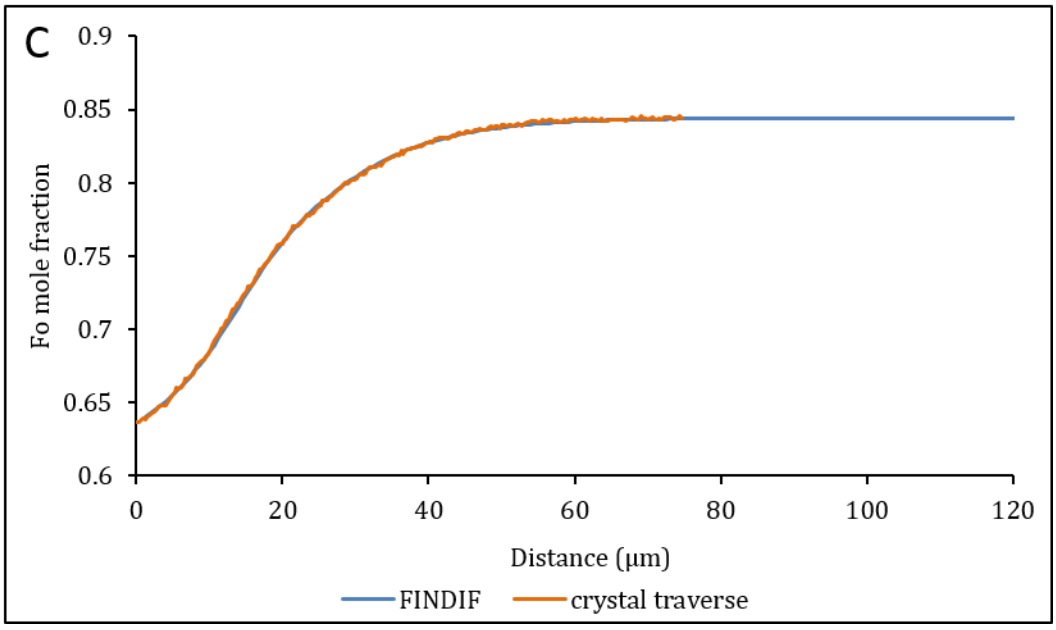

Figure 5.17.C: the same crystal traverse from figures 5.18a and b (64217-3_F1) modelled in FINDIF applying changing boundary conditions and crystal growth simultaneously. A timescale of 4 days is produced – significantly faster than the timescale calculated using AUTODIFF.

Incorporating both changing boundary conditions and growth in to the model drastically improves the fit, and reduces the timescale considerably (from 15 to 4 days). Of the 24 profiles that were remodelled, all of them were affected by changing boundary conditions but only 9 of these were also affected by simultaneous crystal growth. This growth is late stage, only incorporated into the last condition file (applied at the edge of the profile near the rim of the crystal, hence the small 'flick'). Therefore, changing boundary conditions have the biggest influence on diffusion profile shape and effect on the timescales calculated.

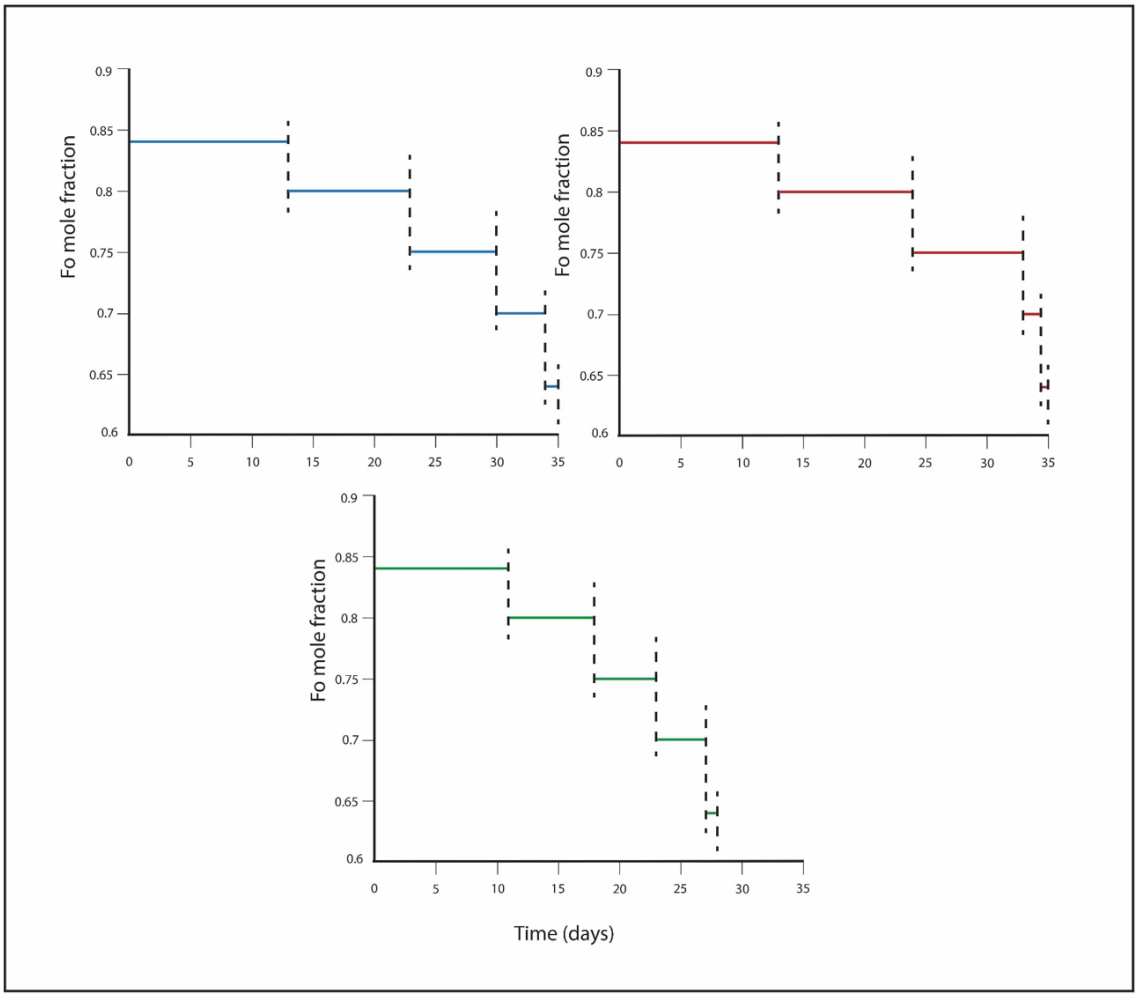

Figure 5.18: The variation of changing boundary condition models in FINDIF used to fit the PdF dataset A) has a model time of 35 days with a linear composition change B) has a model time of 35 days with core compositions held for longer C) has a model time of 28 days with a linear composition change.

All 24 of the profiles were remodelled with a linear composition change (Fo 84-0.8-0.75-0.7-~0.65 forsterite mol. %) at the crystal boundary using 28-35 days total model time. However, not all profiles were modelled with a linear time change with each drop in boundary condition, giving the difference in slope seen in figure 5.19. The composition change reflects changes in the thermal history, which can be modelled in MELTS.

Most of the profiles (18 of the 24 profiles), undergo a linear time change where time decreases by 3 days with each boundary condition change from 13 days down to 1 day (figure 5.19A). For 3 of the 24 profiles, compositions closer to the core were held for longer within the 35 day total model time (for 33 days compared to 30 days). This gives a slightly broader diffusion curve (figure 5.19B). For a further 3 of the 24 profiles, compositions close to the core were not held for as long as in the previous

models (probably cooled faster) with a shorter model time of 28 days giving a narrower diffusion curve (figure 5.19C). There are some slight differences in final rim compositions amongst the traverses. This could be due to chemical differences or a lack of consistency in positioning the traverses when extracting the composition data on the EPMA.

None of the 24 profiles were subjected to a temperature change during modelling – temperatures remained constant. Each condition gets shorter in time towards the rim compositions of the traverse indicating that the amount of diffusion is less. This is likely thermally controlled and could be modelled with MELTS software to determine what is controlling the major element composition of the olivine over time and therefore the changing boundary condition. As the time near the rim is getting shorter it is likely getting colder (lower temperature), but this needs to be confirmed with MELTS modelling as part of the further work.

Quite a significant proportion of traverses have been identified as being affected by changing boundary conditions and to a lesser degree crystal growth, so it is important to know for the new streamlined workflow how this affects the timescales at a population level and therefore the accuracy and reliability of the timescale population. Figure 5.19 shows FINDIF timescales plotted against the AUTODIFF timescales.

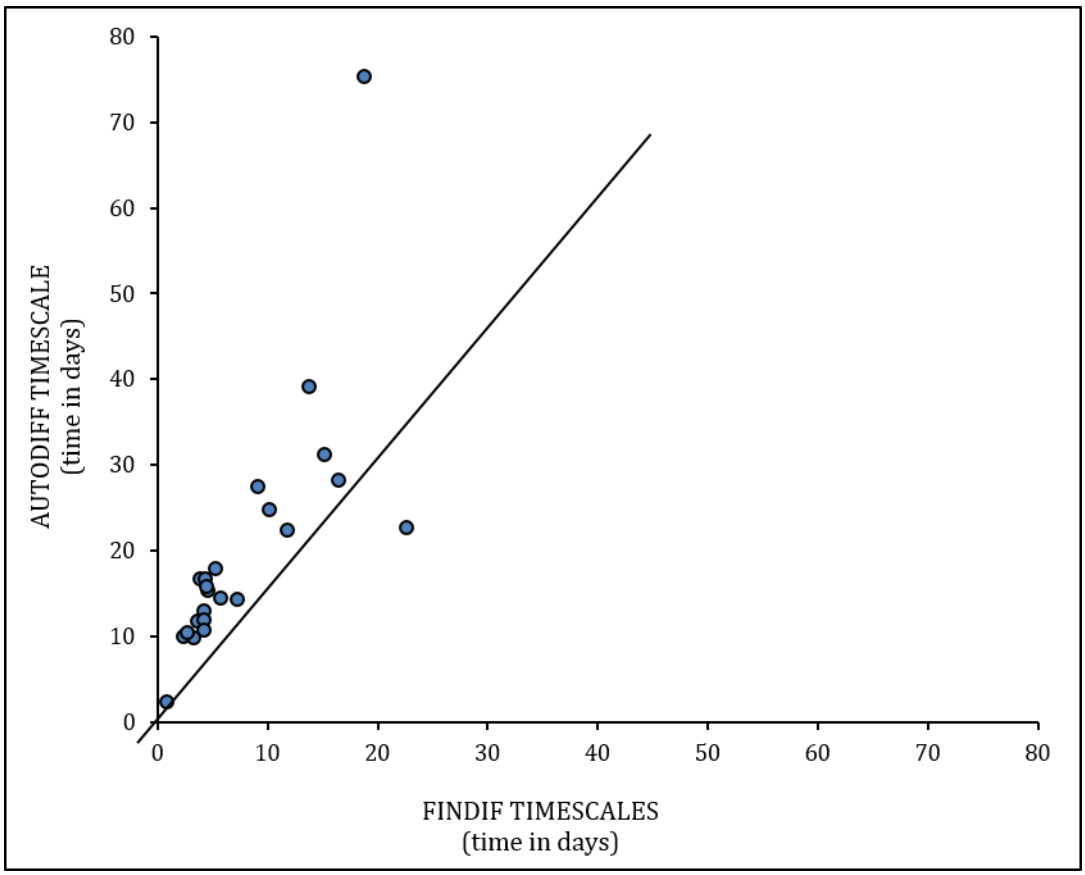

Figure 5.19: FINDIF timescales (incorporating changing boundary conditions and crystal growth parameters) plotted against AUTODIFF timescales (no changing boundary conditions or crystal growth parameters applied).

The trend from figure 5.19 shows that most of the timescales get shorter when remodelled in FINDIF with more realistic parameters for simultaneous crystal growth and changing boundary conditions. A closer inspection of the dataset shows that 23 of the 24 timescales that were remodelled by 33-50%, which is a significant shift. Therefore, the effects of changing boundary conditions and/or crystal growth over a whole timescale population could be significant, and need to be considered a part of the new streamlined processing workflow.

There is less scatter amongst the FINDIF intra-crystal timescales than those modelled using AUTODIFF. The scatter amongst individual crystals has decreased significantly, however, where there is still discord of timescales within crystals. These correlate for the most part with differing sectioning angles (as measured on the U-stage, described in the previous section). For others there is no obvious geometric, textural or mineralogical explanation. Growth effects may explain why

the timescale population does not collapse to a single value, as growth rates are not the same in each direction of the crystal (*Donaldson, 1976*).

5.7.3. Crystallographic Orientation/Anisotropy corrections

Mg-Fe diffusion in olivine is anisotropic, in that diffusion speeds are 6 times faster aligned with the c-axis than the a- or b-axis (*Dohmen and Chakraborty, 2007a and b*). Therefore any crystal face cutting more than one axis e.g. (021) or (101) will be affected by some diffusion component from multiple axes. Timescales can be grossly underestimated or overestimated if the orientation of the traverse with respect to the crystallographic orientation is not known. Traditionally EBSD is used to determine the crystallographic orientation of the crystal slice from which the traverse is taken. Methods are described in chapter 2. This information is incorporated into the diffusion model and timescales are correctly calculated.

For the purposes of a new streamlined diffusion work flow, performing orientation corrections using EBSD is very time consuming. Firstly, it is analytically difficult as few SEMs have EBSD attachments or the expertise to use them viably on geological materials is not available. Also, the sample must have an extra polish in a suspended silica solution for at least 20 minutes per sample (*Lloyd et al., 1987*). This requires specialist equipment and knowledge. Time must be taken to set up the SEM precisely for EBSD analysis, retrieving at least one map per grain. For multiple grains per thin section this can take a couple of hours, depending on the number of grains being analysed. This data must then be further processed using Aztec Channel 5 software and some additional geometric calculations performed to retrieve the azimuth and plunge of the crystallographic axis, together with the angle of the traverse, to be input in to the diffusion model. In an eruption scenario, these extra hours of work are needless if alternative, quicker methods can be developed.

A potential method is detailed in this section which involves modelling the crystal population using a one-directional diffusion coefficient only and then performing a population-level correction based on sectioning statistics.

5.7.3.1. One-directional diffusion coefficient

By measuring the whole crystal population with a single diffusivity rather than correcting each individual traverse separately, some timescales will be calculated correctly, others will be overestimated and others underestimated. However, with enough statistics the dominant timescale should be recoverable. This dominant timescale is likely the timescale of interest, in the event of an eruption. The 'step' initial condition shown in figure 5.21 is biased towards an overestimate of the timescale as illustrated.

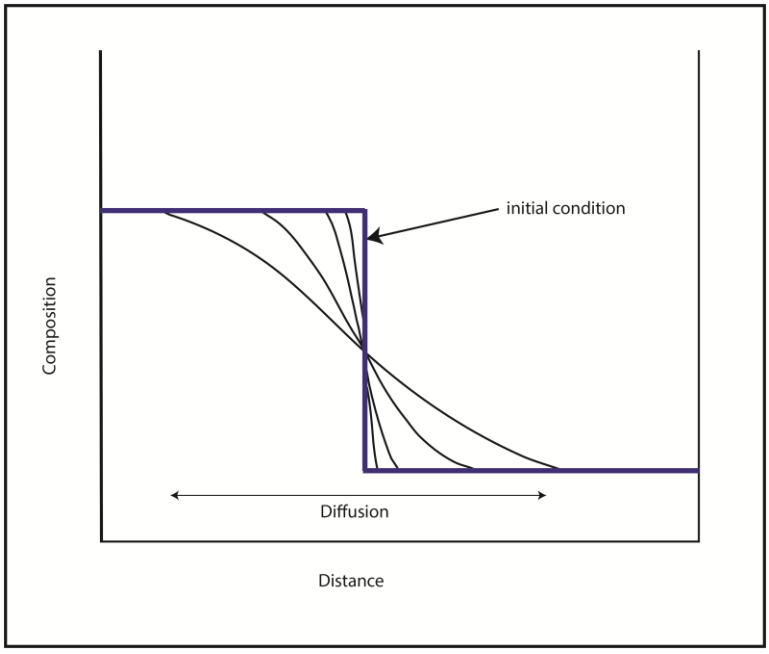

Figure 5.20: a *schematic showing an initial (step) condition (blue) defined by compositional variation from the core to the rim of a crystal and a gradually relaxing curve representing the onset of diffusion (black)*

Figure 5.20 shows the time difference between an initial step function and any diffused profile is a maximum – the time cannot be longer. Gradually the curve relaxes as diffusion progresses. This 'step' shaped initial condition is inherently biased toward an overestimate of the timescale (*Buening and Buseck, 1973; Crank, 1975; Lasaga, 1983; Costa et al., 2008; Costa and Morgan, 2010; Chakraborty, 2010*). It is hypothesised that using a single diffusivity would produce a distribution as shown in the schematic below;

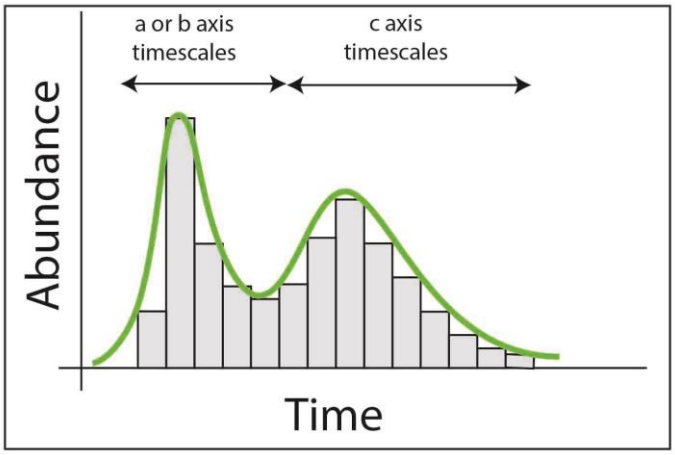

Figure 5.21: schematic of a *hypothesised distribution of timescales using only a single diffusivity - in this case the a-axis diffusion coefficient. The first peak is the dominant peak and perhaps the most useful for eruption monitoring*

The diffusivity being considered for this study is that for the a- or b-crystallographic direction (the 'slow' diffusion coefficient), due to the absence of c-faces on the PdF olivines. In figure 5.21, the first peak corresponds to the a- or b-axis timescales with scatter and the second peak corresponds to the c-axis timescales with scatter as indicated. Any tail would correspond to shallow sections, timescales affected by crystal growth and/or changing boundary conditions or anomalous timescales if they are not corrected accordingly.

The new methodology introduced uses the a-axis coefficient only. This is preferable in an eruption scenario as it can give a better constraint on the timescale, as illustrated in figure 5.22.

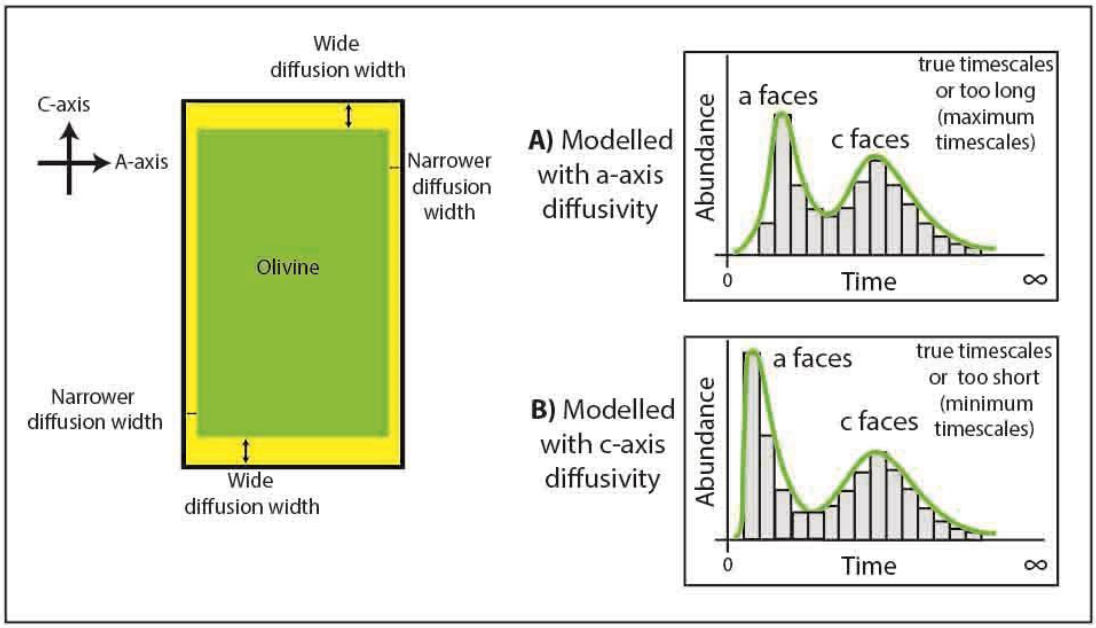

Figure 5.22: *a simplified example of a diffused olivine grain (green and yellow). Diffusion widths vary with crystallographic orientation due to varying diffusion speeds (anisotropy). Timescales modelled with the a-axis diffusion coefficient are superior to using the c-axis diffusion coefficient for this study as it provides a better constraint on the timescales – a maximum timescale.*

Using the a-axis diffusivity, the timescales will always be a maximum - either be correct or overestimated, providing an upper limit for the timescales. The opposite is the case for timescales modelled with the c-axis diffusivity only. They would give a timescale dataset that is less-well constrained – timescales would either be correct or too short providing a minimum timescales with no upper limit. This constraint on the timescales together with the bias towards overestimate of the timescales defined by using a step function as the initial condition (figure 5.20), justifies the choice of using only the a-axis diffusivity for the new orientation methods (rather than the c-axis diffusivity).

The 'binning' method shown in the schematic histograms was found to not be the best way to represent this type of timescale data. It is unclear and arbitrary as to how to define the bin widths depending on the timescales range within a dataset. A new method has been developed using rank order plots.

Rank order plots

To get meaningful timescales this section focuses on creating an orientation correction that can be applied to a crystal population that has been modelled with a single diffusivity, without using EBSD. To develop this method, EBSD-corrected timescale datasets are used, referred to as 'corrected' data. These have been presented in earlier chapters and are used as reference datasets (PdF, Hapaimamo and Moinui). The same timescale datasets with no-EBSD correction are used but modelled with the a-axis diffusion coefficient only (a single diffusivity). These are referred to as 'uncorrected' data.

To formulate a correction, the PdF timescales are initially used. This dataset has been established as belonging to a single, continuous crystal population. This will form an empirical correction. A more theoretical correction from an equally simple dataset was also formulated from the synthetic crystal population created by Shea et al. (2015a). Due to problems established with using binning methods, the orientation corrects were formulated using rank order plots. A rank order plot is a statistical tool often applied to scientific dataset. It is a non-parametric method whereby only the relative positions of data points is meaningful and arithmetic operations are not applicable (*Swan and Sandilands, 1995*). Each data value is replaced by a number giving its place in the sequence from highest to lowest or vice versa. Each timescale is ranked from shortest to longest and each timescale is assigned a rank e.g. PdF 1-105, Hapaimamo 1-91, Moinui 1-71. Each individual data point (rank) is plotted against its timescale. The calculations are based on the ranks, whereby the ranks contain all of the meaningful data (*Swan and Sandilands, 1995*).

The hypothesis is that a perfectly corrected dataset associated with a single diffusion timescale belonging to 1 single crystal population would plot as a horizontal, straight line (with some gradient if it is a continuous population) on a rank order plot. Therefore any deviation from this type of distribution after correction, would indicate that multiple crystal populations are present. Large numbers of data points are important for defining these dominant distributions. Each of the reference datasets contains sufficient numbers (70+ timescales).

Demonstrating crystal population distributions using synthetic datasets

To test how a dataset should distribute depending on the associated crystal population complexity and which crystal faces are selected, synthetic timescales were created. Olivine crystals can vary in morphology (*Faure et al., 2003; Welsch et al., 2010; Shea et al., 2015a and b*) as shown in the PdF XMT results in chapter 3 and the Moinui dataset in chapter 4. Whilst the (100), (010) and (001) faces (a b and c) are perpendicular to the crystallographic orientations, the (021) face is not and has components of c-axis and the a-axis and/or b-axis.

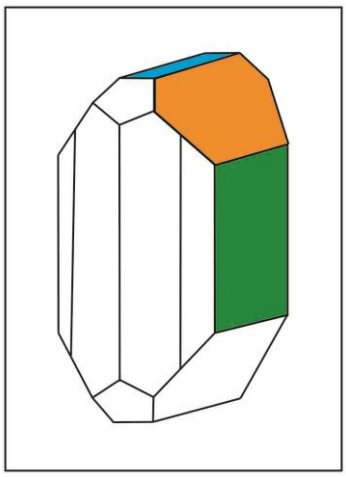

Figure 5.23: Schematic of an olivine crystal. It shows an example of a face normal to the c-axis (blue), a face with a component of the c-axis (orange) and a face parallel with the a-axis (green). The ratio of diffusion profiles from each face is an important control on the orientation correction.

The diffusion of Mg-Fe in olivine is a factor of 6 faster (*Dohmen and Chakraborty, 2007a and b*) down the c-axis and so incorporating the correct proportion of faces within the synthetics is important. Three types of faces were incorporated into the synthetics that represent diffusion with slow and fast diffusion speeds and somewhere in between – the (100), (001) and (021) faces were used.

A synthetic population(s) was created that can vary in size (1-∞ timescales), proportion of crystal faces measured and size of sectioning angle. This creates a synthetic dataset as realistic as possible. Arbitrary ranges in timescales were assigned to create a population of timescales based on those extracted from the PdF crystal population.

Random sectioning angles to a maximum of 30° were also used, based on the values measured with the U-stage from the PdF olivines, and a high proportion of a or b

faces and lower proportion of (021) or c faces were used which is consistent with the faces present on the XMT dataset from chapter 3. The synthetics test what distribution a single crystal population (e.g. PdF) has on a rank order plot, compared to a more complex crystal populations (e.g. Hapaimamo or Moinui). The synthetics are uncorrected for anisotropy and so can only be compared to the uncorrected natural timescale datasets.

Figure 5.24 shows the synthetic timescale distribution for a single, continuous crystal population created based on the timescale range and sectioning angles of the PdF olivines.

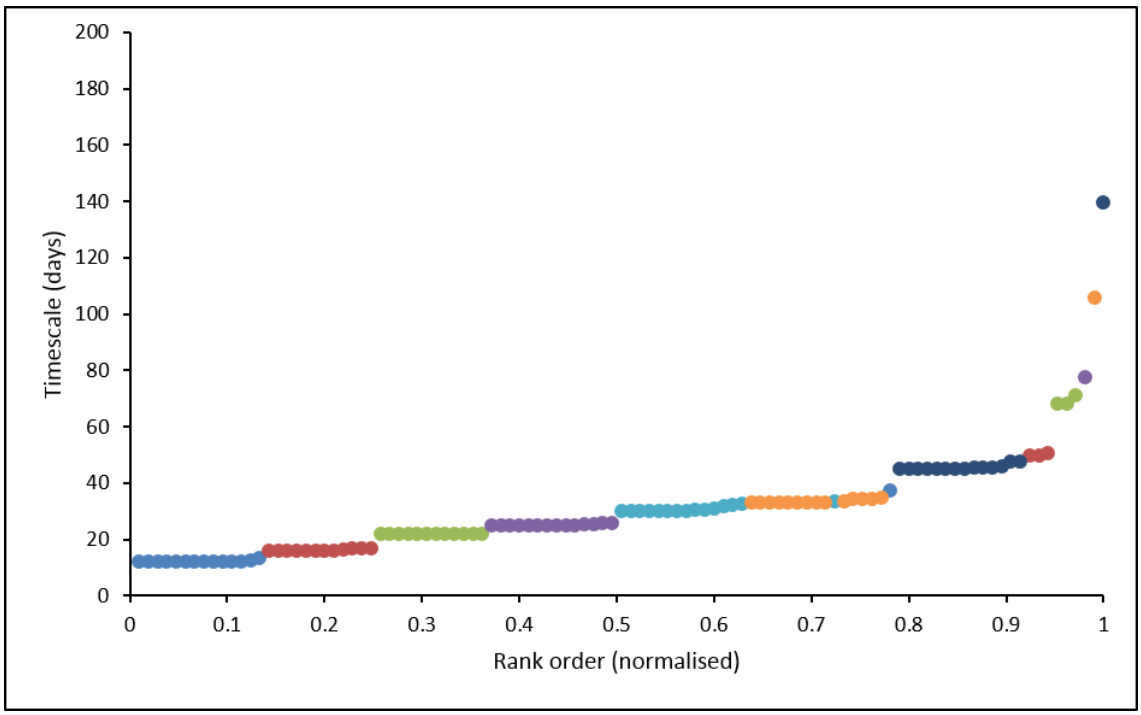

Figure 5.24: Distribution of a synthetic timescale population calculated based on parameters from the PdF dataset (e.g. timescale range and sectioning angles measured). These timescales are uncorrected for anisotropy. Each colour represents a smaller range of timescales within the full timescale range. The cumulative effect of this results in a continuous range of timescales as reflected in the PdF dataset.

This distribution is created with the inclusion of a proportion of (100) faces (90% modal abundance), some (021) faces (10% modal abundance) and no (001) faces (0%) and the formulation of a continuous narrow timescale range. The changing colours represent the continuous nature of the timescales around a central timescale. The 'tail' (defined by points where there has been a sharper change in gradient) is created by the presence of the (021) faces and the gradient of the line is produced by the spread in initial timescales. The XMT and SEM images confirm the

presence of an (021) face and the absence of a (001) face. The longest timescales in the synthetic distribution are due to genuinely longer timescales (within the continuous range), due to the timescale being extracted from an (021) face or a timescale extracted from an (021) face combined with a large sectioning angle. A large sectioning angle applied to a timescale across an (100) face does not lead to a longer timescale positioned in the 'tail' section of the distribution. Although there is a small 'tail' present, the overall distribution is a horizontal line with a shallow gradient for a single, continuous crystal population.

Increasing the complexity of the timescale range and the proportion of faces measured changes the shape of the distribution considerably (figure 5.25).

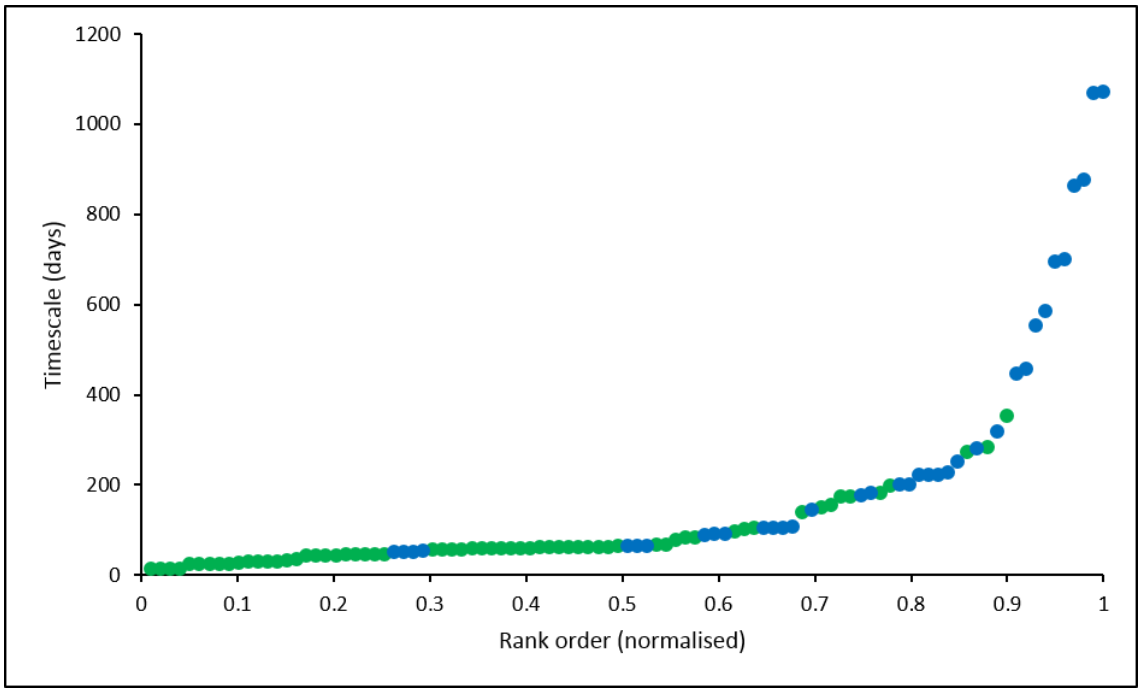

Figure 5.25: Distribution of a synthetic timescale population calculated based on parameters from the PdF (sectioning angle) and Hapaimamo (timescale range) datasets. These timescales are uncorrected for anisotropy. The green data points are a larger, younger population. The blue data points are a second, smaller, older population.

This distribution is very different to that produced for a single continuous population of timescales. It is a result of the summation of two synthetic crystal populations – one larger and younger (green) and a second, smaller and older (blue). A much larger proportion of (001) and (021) faces (15% of each) were included in these populations and therefore a smaller proportion of a-axis faces (70%). It is the proportion of (001) and (021) faces together with the wider range in timescales that controls the 'tail' and therefore the gradient of the younger plateaued region. It can

be seen that whilst there is overlap between the two populations, the majority of the second population of timescales is positioned within the 'tail' after the change in gradient from the shallowly increasing plateau into the 'tail' region. This type of distribution of synthetic timescales (much longer 'tail', change in gradient and wide spread of timescales) is clearly indicative of the presence of two crystal populations. Two crystal populations were established in the Hapaimamo and Moinui timescale datasets.

Single and more complex rank order distributions (with continuous timescales) have been built from synthetic data. These data are not corrected for anisotropy. The shapes produced are characteristic to the number of crystal populations present (one or more). Interpreting different aspects of the curves quickly, understanding how different proportions of crystal faces (a faces vs c faces) affect the shape of the distribution and how the correction is built forms the focus of the new orientation correction.

Using natural crystal populations to create a new orientation correction

Each of the natural timescale datasets, PdF, Hapaimamo and Moinui have been EBSD corrected and plotted as a rank order plot (figure 5.26.A, B and C) to compare to their true, natural (uncorrected) distributions (figure 5.27 A, B and C). PdF lava contain a simple crystal population and Hapaimamo and Moinui lavas contain the more complex crystal populations as deduced from the geochemical and textural data in chapters 3 and 4.

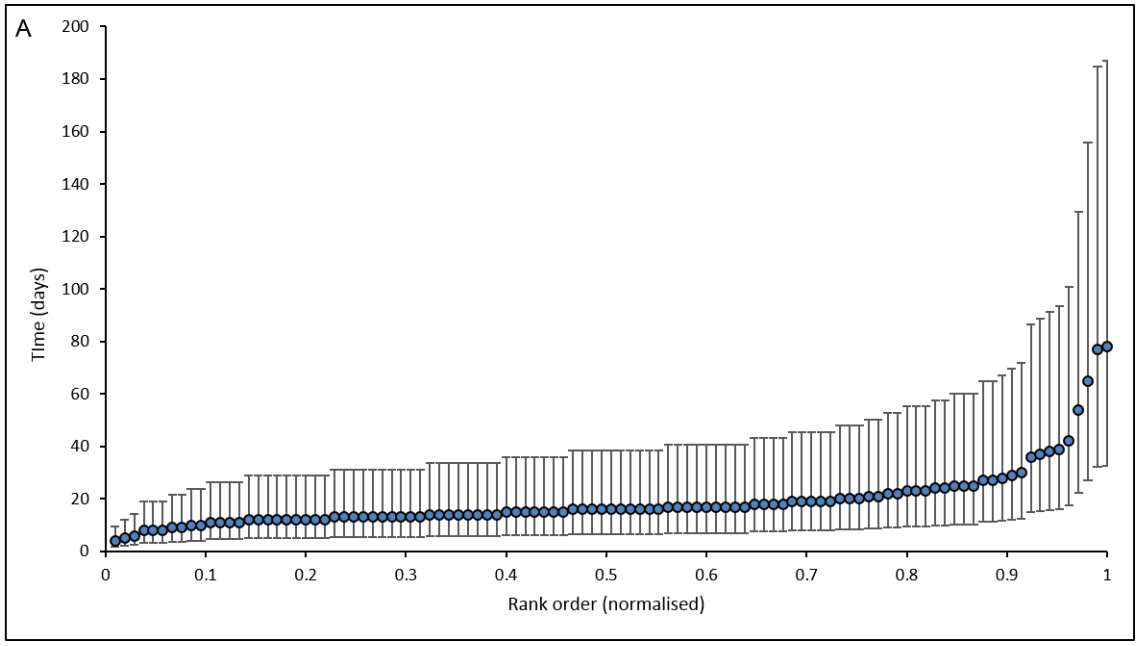
A
Time (days)
Rank order (normalised)

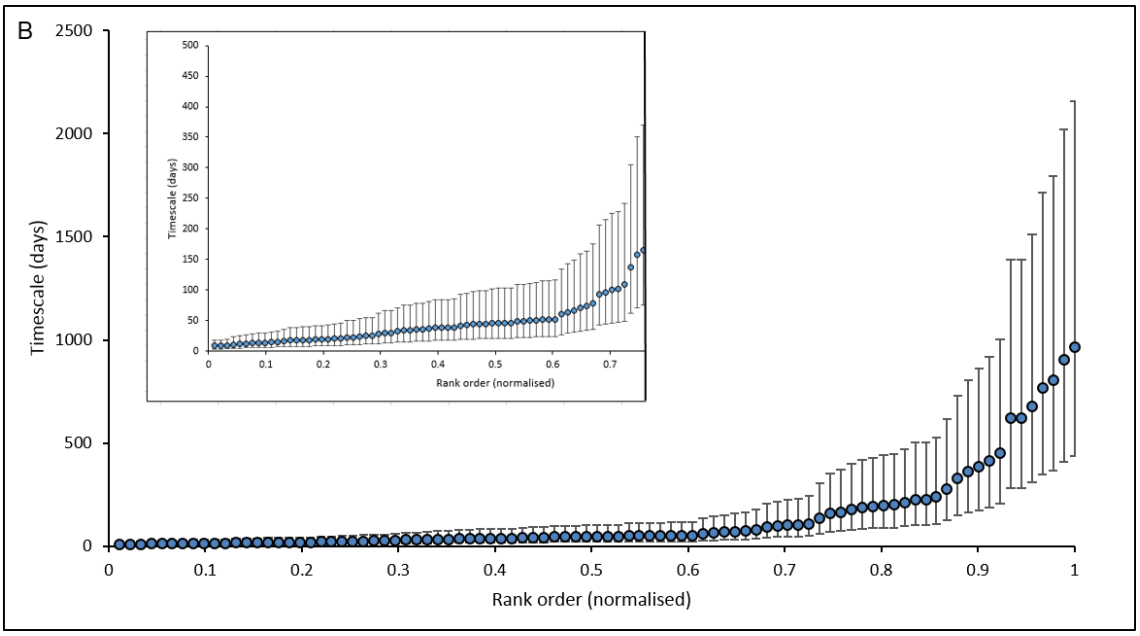
B
Timescale (days)
Rank order (normalised)
Timescale (days)
Rank order (normalised)

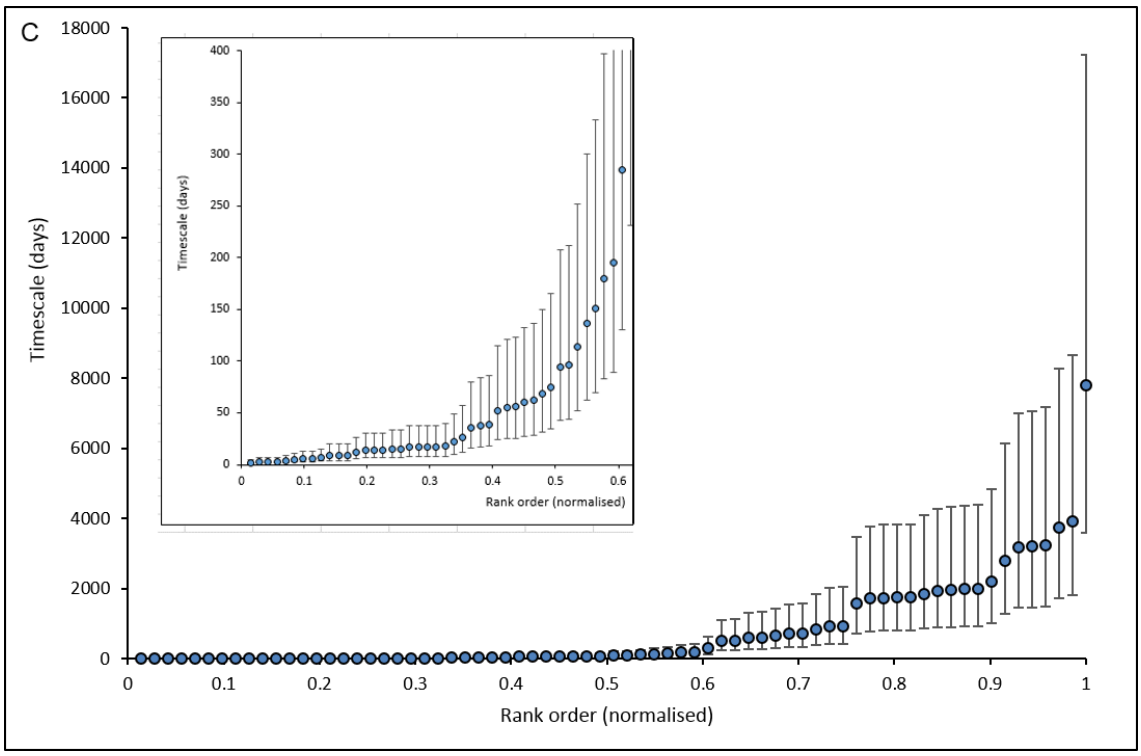

Figure 5.26: rank order plots for EBSD-corrected timescale data (blue) from each case study A) PdF (n = 105) B) Hapaimamo (n = 91) C) Moinui (n = 71)

Figure 5.26A shows a nominally flat, horizontal distribution with a slight gradient, and a small curve ('tail') incorporating the longer timescales. This population has been EBSD corrected and corrected for sectioning effects by incorporating measurements from the Universal Stage (U-Stage) into the diffusion model. The 'tail' within the PdF data is not due to shallow sectioning effects but due to simultaneous growth and/or changing boundary conditions whilst diffusion was ongoing or out of plane diffusion. This EBSD corrected data also shows a slight gradient implying that the data doesn't represent a single timescale. This population likely formed over a period of time, not instantaneously, hence the scatter in timescales and so it is not possible to correct these timescales to a single value, even with fully constrained 3D diffusion models. Theoretically we would expect the timescales to correct to a single value (fully flat horizontal distribution with little gradient) if fully corrected, which shows natural systems are more complicated than an idealised theory.

Due to vagaries of eruption and cooling times, natural data are likely to give distributions, not single, quantifiable timescales. Therefore PdF is a good model for

a basaltic system. It is clear that a single, simple population of timescales (with EBSD and shallow sectioning corrections applied) is projected as a near-straight line with a smooth change in gradient in the tail on a rank order plot. Figures 5.26B and 5.26C show distinctly different distributions of timescales.

Both the Hapaimamo and Moinui EBSD-corrected datasets (figures 5.26B and 5.26C) display a straight distribution of timescales with a slight gradient amongst the younger, dominant timescales and a significant, abrupt change in gradient before the tail section rather than the smooth curve shown in figure 5.26A. This is not due to greater sampling – both the Hapaimamo and Moinui datasets contain less timescales than the PdF dataset. 'Tail' timescales are mostly due to the presence of (001) and (021) timescales and/or an inferred 'second' crystal population, associated with the change in gradient at the base of the tail. This is consistent with what is seen within the synthetic dataset of mixed populations (figure 5.25). This being said, the data within the tails should not be over-interpreted, especially as part of the rapid processing method. The distinct distributions created by single and complex populations are clear from both the synthetic (uncorrected) and natural (corrected) datasets. Each display data arrays on a rank order plot that are analogous to each type of population – a shallow, smooth curve for a single population and a curve with gradient changes for more complex populations. It is clear that the new orientation correction method needs to be able to be applied across various datasets.

The rank order plots and polynomials will be used to construct the new orientation correction method. For this the uncorrected timescales (modelled with the a-axis diffusion coefficient only) are ranked, and plotted for comparison with the EBSD corrected timescales for each dataset (figures 5.27A, B, and C).

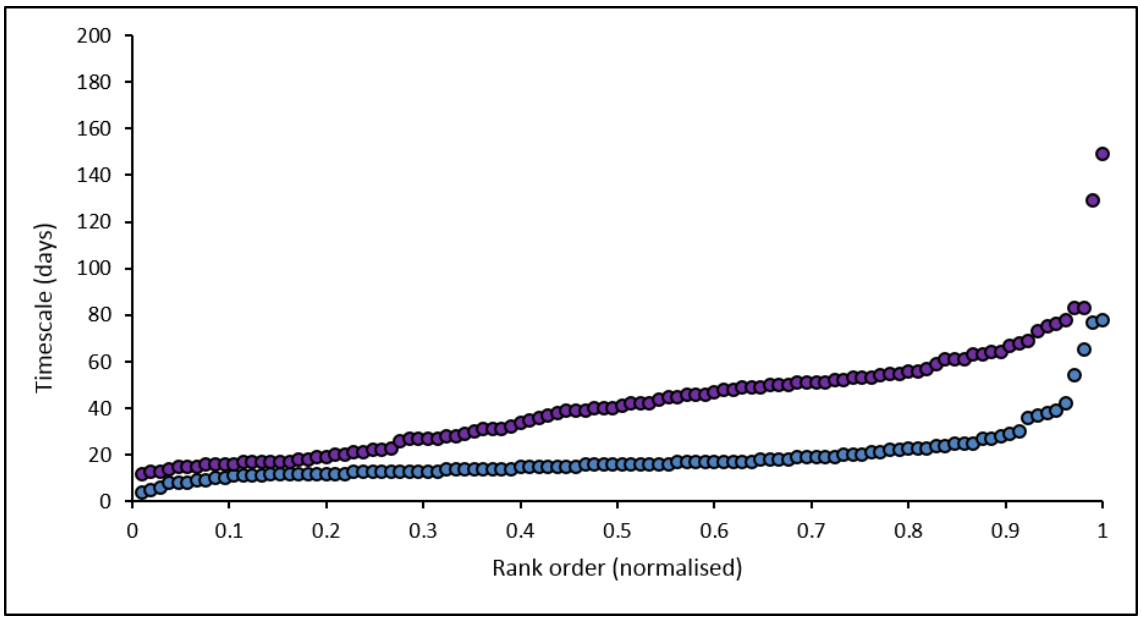
200
180
160
140
120
100
80
60
40
20
0
Timescale (days)
0
0.1
0.2
0.3
0.4
0.5
0.6
0.7
0.8
0.9
1
Rank order (normalised)

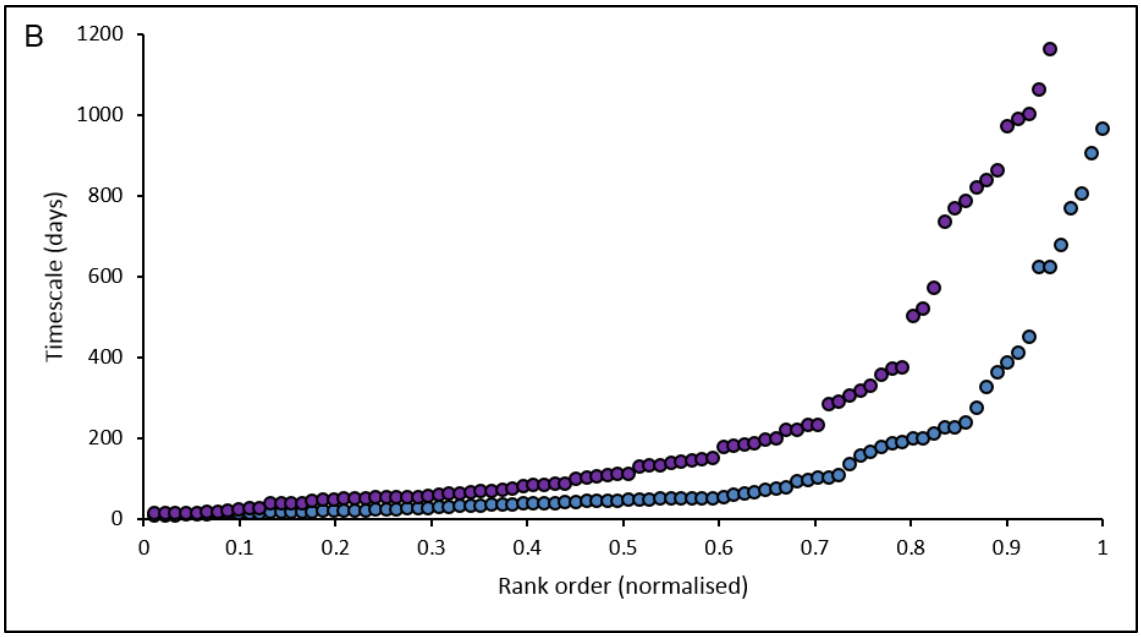
B
1200
1000
800
600
400
200
0
Timescale (days)
0
0.1
0.2
0.3
0.4
0.5
0.6
0.7
0.8
0.9
1
Rank order (normalised)

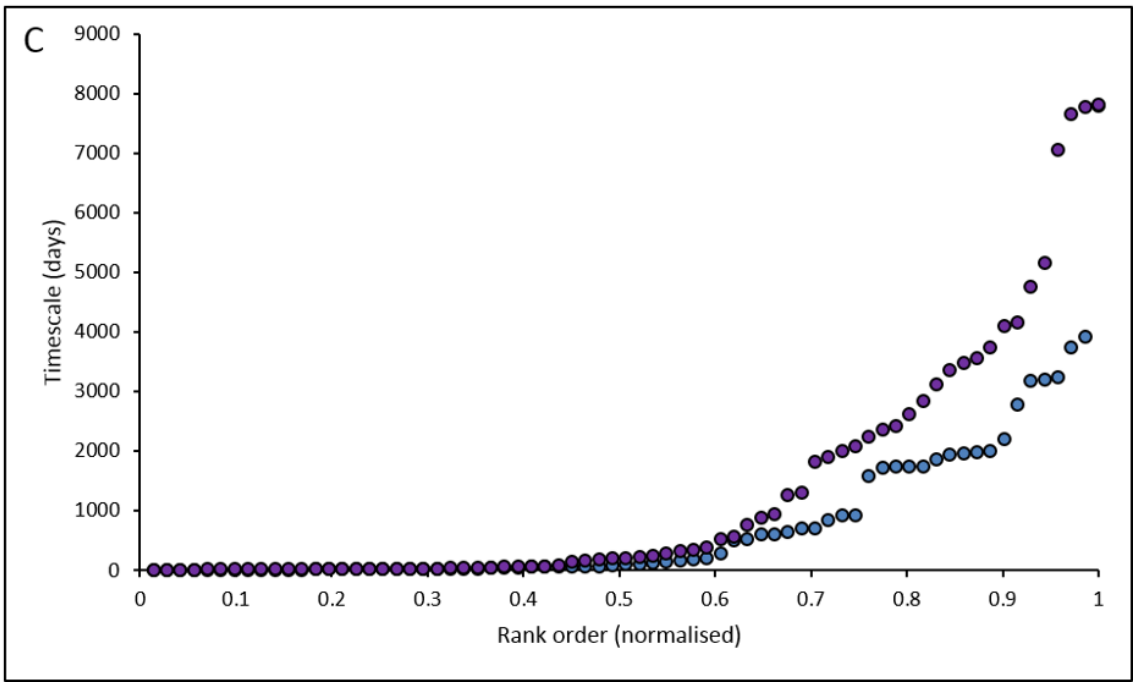

Figure 5.27: rank order distributions for timescales with no orientation correction (modelled with the a-axis diffusion speed only) (purple) in comparison with the same timescale distributions with an EBSD-correction (blue) for each case study A) PdF (n = 105). The average uncertainty on each calculated timescale is 0.38 log units (1σ) B) Hapaimamo (n = 91). The average uncertainty on each calculated timescale is 0.35 log units (1σ) C) Moinui (n = 71). The average uncertainty on each calculated timescale is 0.34 log units (1σ).

A method has been developed that maps the uncorrected dataset (purple on figure 5.27A-C) on to the EBSD corrected dataset (blue on figure 5.27A-C) using a polynomial regression. This is a method of fitting a curve to a dataset (*Swan and Sandilands, 1995*). It is appropriate if the scatter of the data shows certain types of curvature that are more complex in nature such as parabolic (*Swan and Sandilands, 1995*). To fit the uncorrected data on to the EBSD corrected data, the ratio of the uncorrected to corrected timescales is calculated as a function of rank order position and fit with a polynomial. This is only done once for the simple crystal population (PdF). The resulting polynomial is then applied to the other datasets. This correction is portable because a population behaviour should be reproducible with sufficient statistics. Polynomial equations are defined by terms for x, x^2, x^3 etc. (*Swan and Sandiland, 1995*). Each power of x is associated with a coefficient and as such the regression must be solved for all of the coefficients (*Swan and Sandiland, 1995*). Increasing the number of terms in the polynomial, increases the sense of curvature i.e. the inflection points (*Swan and Sandiland, 1995*). Increasing the number of terms in a polynomial from a linear regression, gives a quadratic, cubic, quartic equation

and so on until the polynomial curve fits the data set in question (*Swan and Sandiland, 1995*). A quadratic curve has no inflection points, a cubic curve allows one inflection point, quartic curves allow two inflections and so on (*Swan and Sandiland, 1995*).

The polynomial that provides the best fit for the correction factor for the simple crystal population (the PdF dataset) contains 6 terms. And can be defined with the following expression;

$$-69.66(x^5) + 203.31(x^4) - 227.47(x^3) + 114.06(x^2) - 21.542(x) + 2.7982$$

Each x term within the polynomial is assigned the rank order value (x value) of each uncorrected data point. The correction (defined by the polynomial curvature and rank order value) is applied to each uncorrected timescale and its associated rank value and maps them onto the distribution defined by the EBSD corrected dataset.

This correction can be applied to any dataset that has not already had an orientation correction using EBSD applied. As this is the simplest correction for the simplest crystal population, it will try to force the data points onto a simple distribution with a very shallow gradient (timescales are continuous and do not correct to a single value in natural datasets). When applied to datasets that contain more than one crystal population it will not be possible to force all of the points on to the straight line distribution, and a change in gradient will be inflicted on to the distribution. This shape is seen in the uncorrected synthetics in figure 5.25. This change in gradient is set by the y-values of the distribution - the wider range in timescales calculated using a one-directional diffusion coefficient (a-axis) in turn defined by the varying crystal core and rim values. I will refer to this new method of performing the orientation correction as the “pseudo-correction” or “pseudo-corrected” for the remainder of the thesis. Below shows the pseudocorrection (created using the PdF dataset only) as applied to the uncorrected data for all the datasets (figures 5.28A, B and C) to demonstrate how well the correction performs compared to each EBSD corrected dataset.

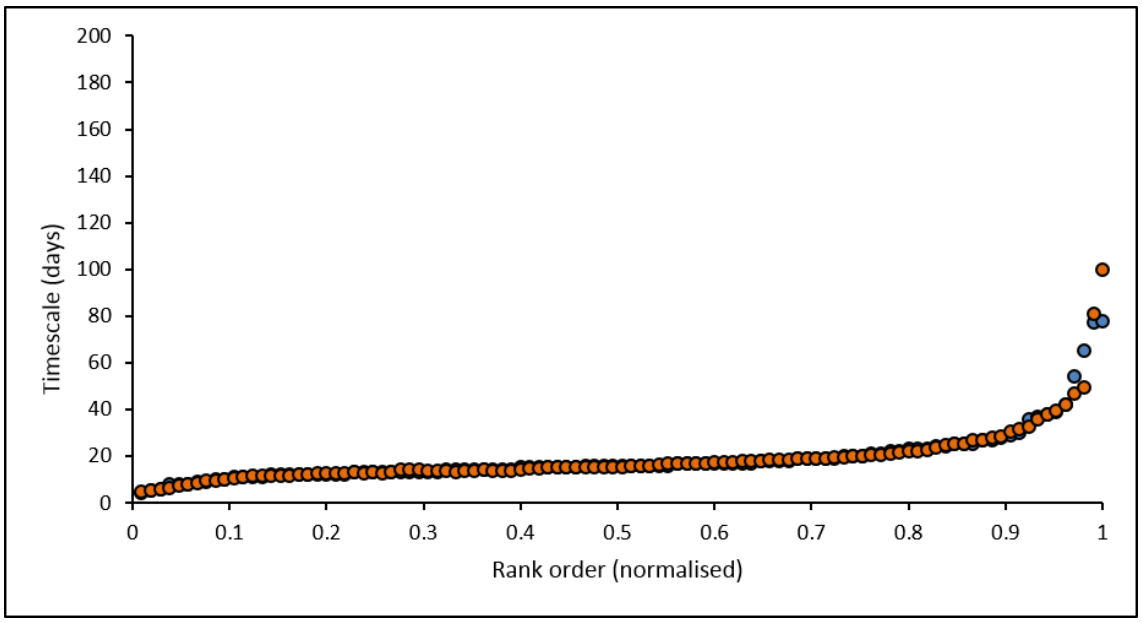
200
180
160
140
120
100
80
60
40
20
0
Timescale (days)
0
0.1
0.2
0.3
0.4
0.5
0.6
0.7
0.8
0.9
1
Rank order (normalised)

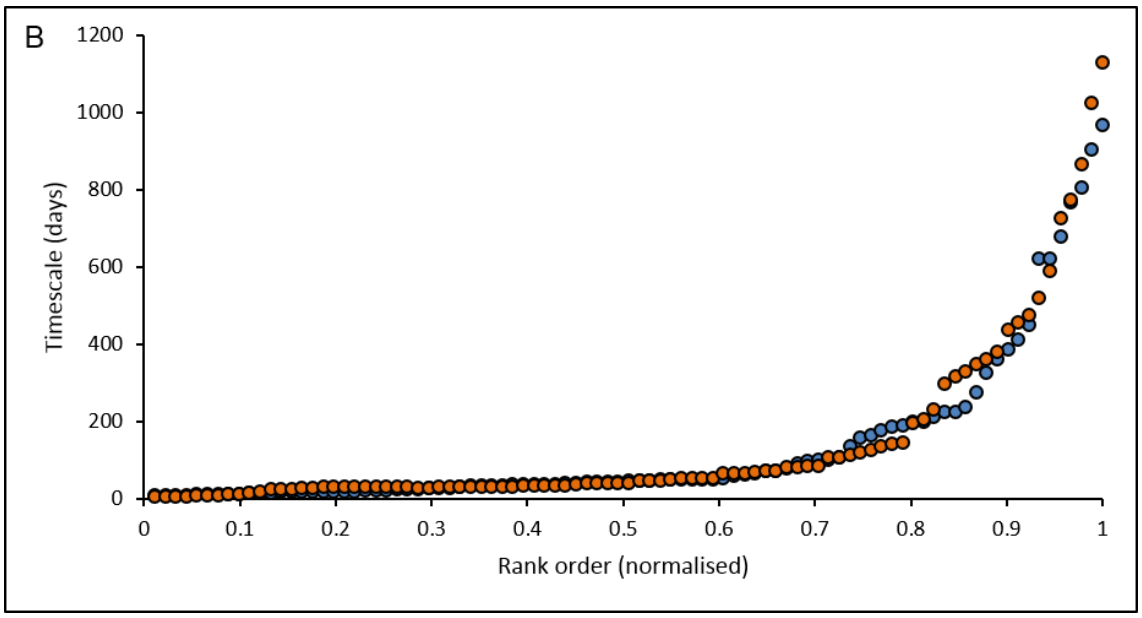
B
1200
1000
800
600
400
200
0
Timescale (days)
0
0.1
0.2
0.3
0.4
0.5
0.6
0.7
0.8
0.9
1
Rank order (normalised)

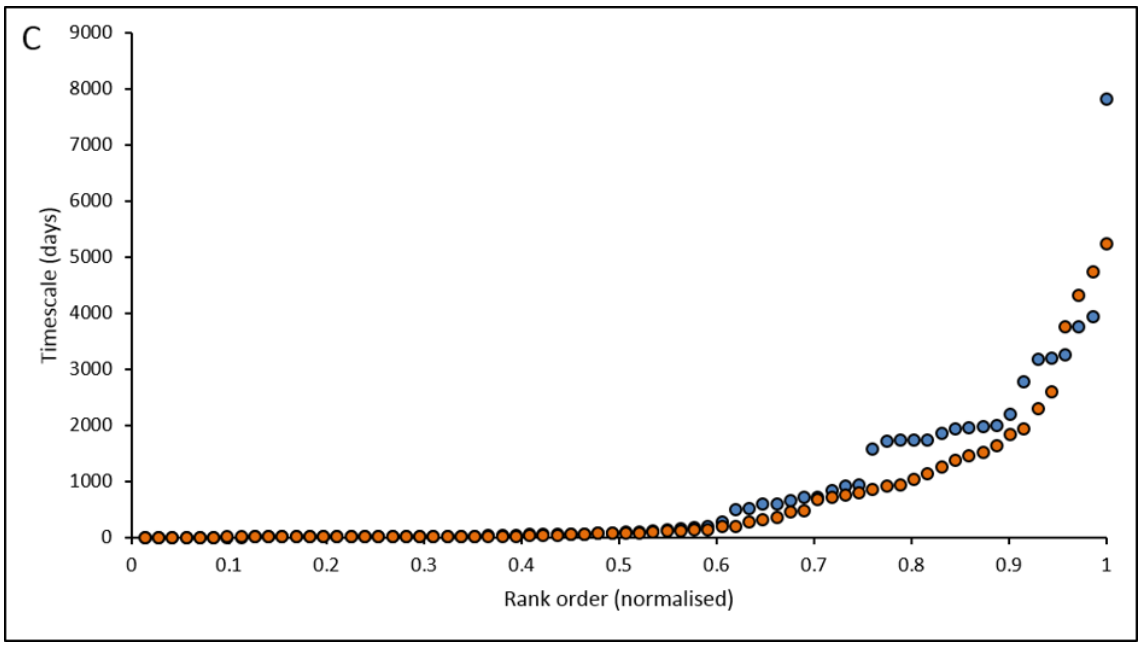

Figure 5.28: rank order distributions for timescales with the "pseudo-correction" applied (modelled with the a-axis diffusion speed only) (orange) in comparison with the same timescale distributions with an EBSD-correction (blue) for each case study A) PdF (n = 105). The average uncertainty on each calculated timescale is 0.38 log units (1σ). B) Hapaimamo (n = 91). The average uncertainty on each calculated timescale is 0.35 log units (1σ). C) Moinui (n = 71). The average uncertainty on each calculated timescale is 0.34 log units (1σ).

Figures 5.28A, B and C show each of our natural datasets with the pseudo-correction based on the simple PdF crystal population compared to its EBSD corrected dataset. The dominant crystal population of each dataset – the most relevant information for near-real time eruption monitoring – is flattened to the straight line part of the distribution consistent with the EBSD data for each sample. The crystal populations for Hapaimamo and Moinui show a distinct change in gradient in the tail of the distribution that is consistent with the presence of more complex crystal populations, (also consistent with the EBSD data for these samples).

To test the success of the PdF-type correction, a second correction was formulated from a synthetic dataset published by Shea et al. (2015a). Their study created a theoretical olivine shape with (001), (111), (010), (021), and (101) faces. This shape was randomly rotated and sliced to create a population of crystal slices. The olivine shape was diffused for Mg-Fe inter-diffusion with initial and boundary conditions of Fo_{70} at the crystal rim and Fo_{90} within the crystal core using a 1D and 3D diffusion model, creating a population of 200 timescales. The timescales were modelled using only the c-axis diffusion coefficient and form two datasets, corrected for anisotropy and uncorrected for anisotropy. Their population of timescales corrects to a single

timescale of 144 days with the 3D diffusion model. With the 1D model, there is scatter in the data around the 144 day peak. This is in contrast to the fully corrected PdF dataset, which corrects to a narrow range of timescales. The PdF dataset set is fully corrected for shallow sectioning in contrast to the Shea et al. (2015a) dataset.

The polynomial (using the same methodology as the empirical correction) that forms the Shea-type correction factor based on the Shea et al. (2015a) dataset can described as follows;

$$-1.4711(x^5) - 27.848(x^4) + 44.41(x^3) - 11.703(x^2) - 1.0464(x) + 1.3338$$

The Shea-type correction factor has been converted to account for a-axis diffusion speeds so that it can be directly comparable with the empirical PdF correction factor. Both correction factors are applied to the uncorrected PdF dataset, resulting in pseudo-corrected datasets that can be compared with each other and to the fully EBSD corrected dataset (figure 5.29).

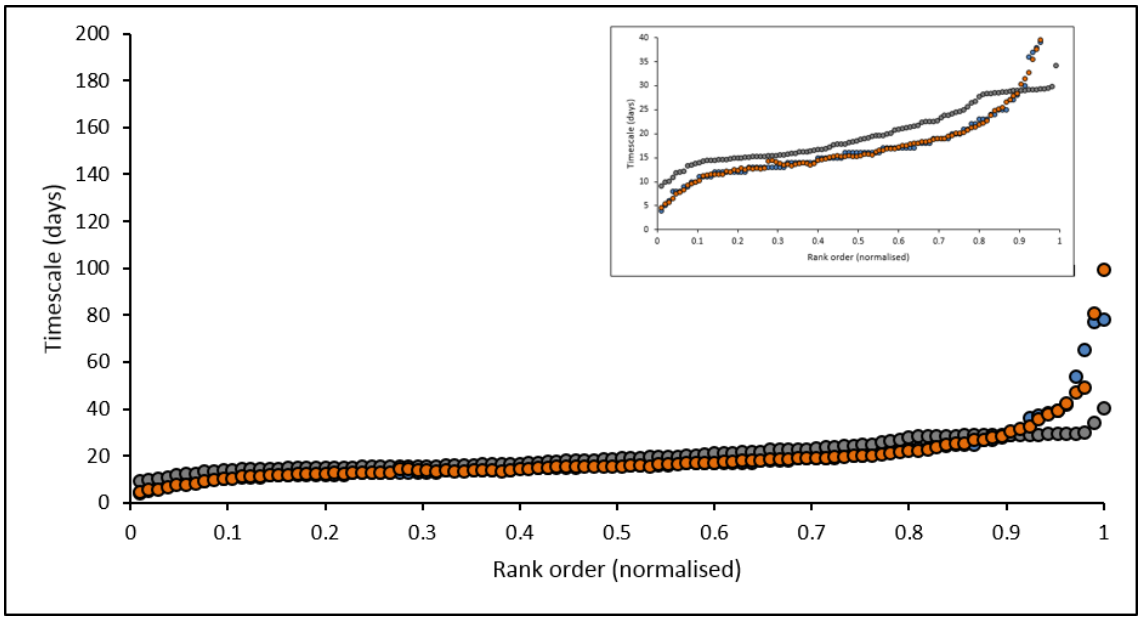

Figure 5.29: rank order distribution for timescales from PdF with the PdF-type "pseudo-correction" applied (modelled with the a-axis diffusion speed only) (orange). The timescales have also been modelled with the Shea-type "pseudo-correction" applied (grey). The EBSD-corrected timescales (blue) are plotted for comparison. Inset shows the same plot at a smaller scale showing a much better correlation for the PdF-type correction with the EBSD-corrected dataset, although the Shea-type correction follows the same gradient.

Figure 5.29 shows both pseudo-corrected PdF datasets plotted with the EBSD corrected dataset. Both types of correction provide a good fit to the EBSD dataset attesting to the success of the population-level pseudo-correction. There are similarities and differences between how the two methods are performing the corrections. Both the PdF-type and Shea-type corrections correct to a straight line with a slight gradient implying scatter amongst the timescales. For the PdF dataset, this is due to natural subtleties in the dataset e.g. the diffusion clocks starting over a period of time calculated with a 2-and-a-half-D diffusion model. However, for the synthetic dataset this is due to the data being calculated with a 1D model. These models are comparable as all traverses have been extracted from crystal faces away from crystal corners and their merging diffusion fronts. The pseudo-corrected datasets exhibit stark differences towards the 'tail' end of the dataset. The PdF-type correction gives a very good fit to the EBSD corrected dataset in this section, but the Shea-type correction doesn't. It appears flattened with the longer timescales becoming suppressed. This part of the dataset is overcorrected.

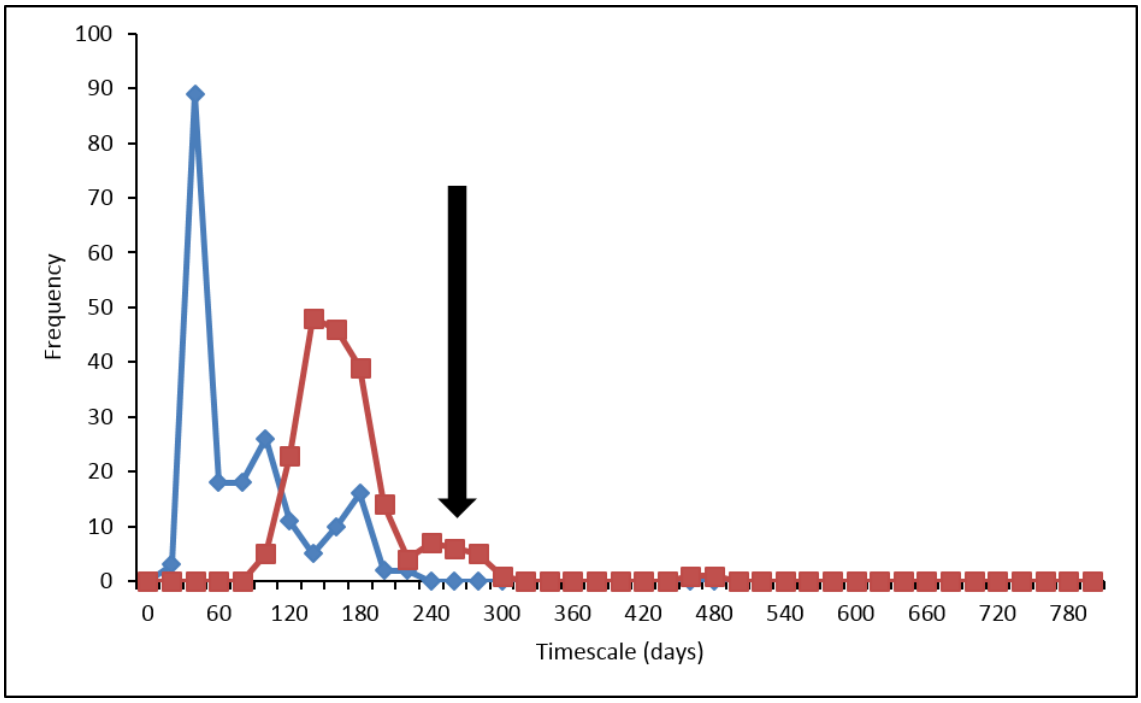

Figure 5.30: Timescale data retrieved from the Shea et al. (2015) dataset (n = 200). Anisotropy corrected data (red) is plotted with non-anisotropy corrected data (blue). Timescales are calculated using c-axis diffusion speeds using a 1D model. A second peak in the anisotropy corrected data is highlighted (black arrow) representing timescales affected by sectioning effects.

The synthetic dataset is not corrected for shallow sectioning effects, shown by the longer timescales in the second smaller peak in the timescale distribution (highlighted with the black arrow). This leads to part of the dataset becoming 'hyper-corrected' - the data points forming the 'tail' section are over-corrected. This can be problematic, if the data within the 'tail' is to be used to indicate of the presence of a further crystal population. The presence of these populations can flag the potential of a sample to unravel the complexities of the full history of the crystal cargo. Beyond the immediate eruption concern, these can be re-modelled with traditional methods and so having ambiguities at the high-time end may lead to over-interpretation or misinterpretation.

Both pseudo-corrections provide realistic shape distributions when applied to a simple crystal population particularly at the short timescale end, but they need to be applicable to more complex crystal populations which are more common in eruption products. The PdF and Shea-type corrections derived from simple populations are applied to more complex crystal populations from Hapaimamo and Moinui (figure 5.31A and 5.31B).

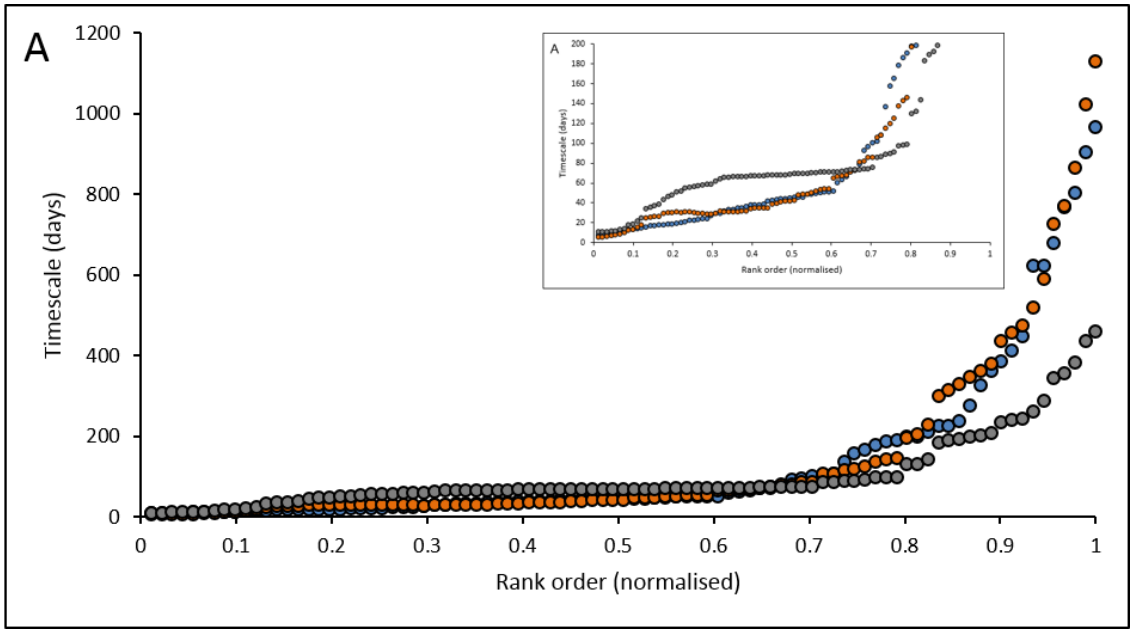

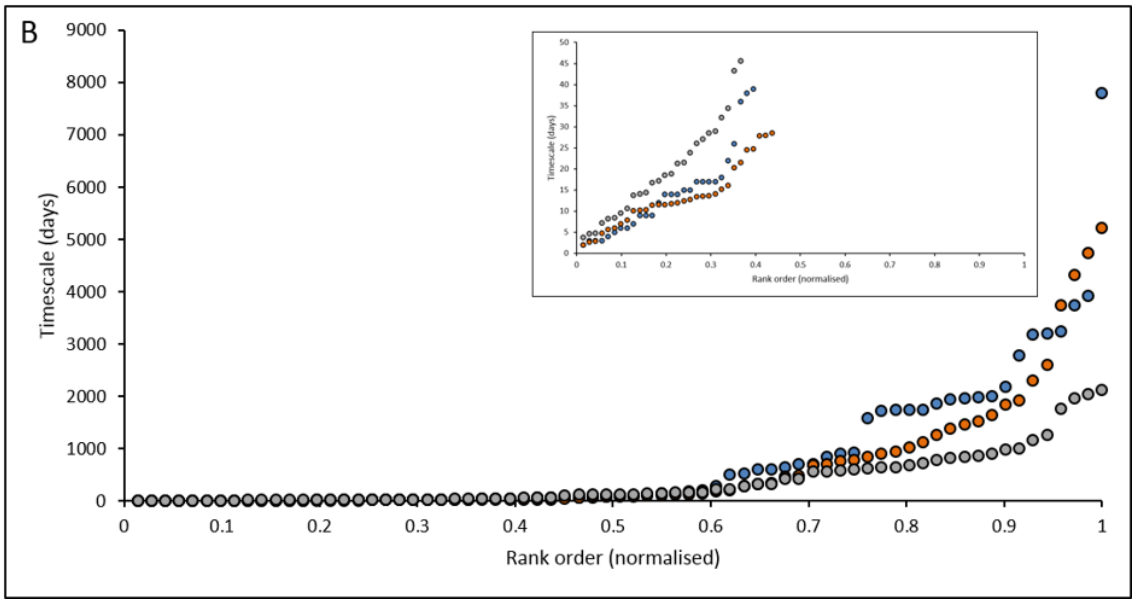

Figure 5.31: rank order distributions for timescales from A) Hapaimamo and B) Moinui. The Piton-type "pseudo-corrected" timescales (modelled with the a-axis diffusion speed only) are shown in orange. The Shea-type "pseudo-corrected" timescales are shown in grey. The EBSD-corrected timescales for each dataset (blue) are plotted for comparison. Inset shows the same plot at a smaller scale showing a much better correlation for the Piton-type correction with the EBSD-corrected dataset.

Figure 5.31 shows that each pseudo-correction provides a good match to the EBSD dataset, both picking out the change in gradient that is indicative of at least two crystal populations. Again the Shea-type correction overcorrects the data in the tail section.

Whilst the Shea-type correction calculates the correct change in gradient of the line, a large portion of the timescales are mismatched with the EBSD data, particularly amongst the younger timescales, which are the most important to consider for eruption monitoring. These Shea-type corrected timescales are longer, due to the use of a different diffusivity or different theoretical crystal shape/faces compared to the PdF-type correction. The olivine shape used by Shea et al. (2015a) had (001) faces. A large proportion of these incorporated in to his dataset may be what is affecting the shape of the polynomial. Crystal shape is an important control on how the rank order distributions behave shown by the synthetic distributions in figures 5.24 and 5.25.

Plotted against each other, the PdF-type and Shea-type correction are shown to rarely be the same – they do not plot with a linear 1:1 relationship (figure 5.32A). A careful choice is necessary to justify which is the best pseudo-correction to take

forward and implement within the streamlined diffusion processing methods used during an eruption event.

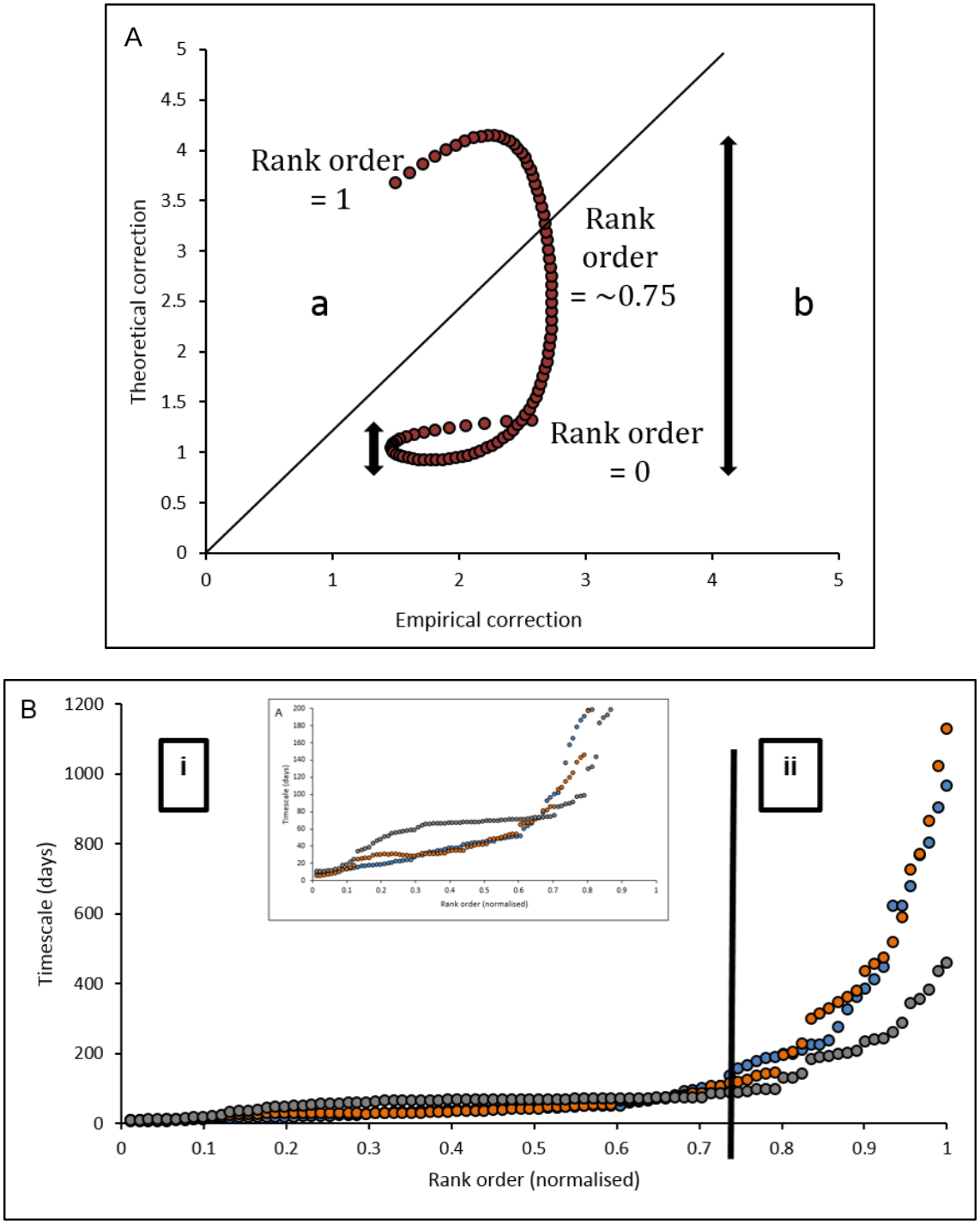

Figure 5.32: A) the theoretical correction factor plotted against the empirical correction factor showing little correlation between the two B) Same as figure 5.31a i) the PdF-type correction is stronger ii) the Shea-type correction is stronger

Figure 5.32A clearly shows that there is little correlation between the two correction types. The regions marked by arrows show where the corrections are almost the same but elsewhere one is stronger than the other. Above the 1:1 line, (a) the Shea-

type correction is stronger. Below the 1:1 line, (b) the PdF-type correction is stronger. Relating this to figure 5.33B, the Pdf-type correction is stronger within region (i) and the Shea-type correction is stronger within region (ii).

With this in mind, although both correction types can correct the timescale data to the same gradient as the EBSD corrected data and also pick out the break in slope that indicates the presence of potentially multiple crystal populations, the PdF-type correction is seemingly more appropriate when applied to natural data. Therefore this correction type will be taken forward as the orientation method of choice as part of the rapid processing workflow methods.

5.8. Conclusions

Each part of the traditional processing workflow has been evaluated and a more streamlined approach considered to reduce the processing time of the whole workflow. From sample preparation to crystallographic orientation corrections, processing steps have been tweaked to create thoroughly streamlined new methods. The new workflow consists of the same number of processing steps but different methods have been composed to make them faster to carry out.

Geometric corrections such as shallow sectioning, effects of simultaneous crystal growth and/or changing boundary conditions and anisotropy have been considered and where possible quantified and applied at a crystal population level rather than to individual crystal traverses. Whilst shallow sectioning effects have shown not to have a large effect on a population of timescales (~10% in timescales on average) from larger crystals (1-2 mm in size), other corrections such as those for crystal growth and/or changing boundary conditions can affect a population of timescales considerably. Both of these corrections need to be considered at a population level on any new dataset, particularly if having trouble fitting compositional data to diffusion profiles.

A simpler, efficient method for performing an anisotropy correction has been devised using a single crystal population from the PdF dataset and calculating a correction that can be applied to any dataset. This correction is applicable to all datasets if there is some constraint on which crystal faces are present. This information can usually be garnered from SEM images. If the type and proportion of

crystal faces present can be quickly constrained, the user will have a better understanding of how the PdF-type correction is being applied to their dataset. Nonetheless, this new orientation correction can provide an accurate and reliable estimate of the youngest, dominant diffusion timescales and also infer when more than one crystal population is present in the dataset.

To truly test how efficient these new methods are, they need to be performed as a single workflow as though an eruption were occurring. The time taken for each processing step can be noted and at the end of the processing workflow the time taken for its implementation can be compared with the traditional workflow. To do this a stress test is needed. The next methods are tested in this way in the next chapter on a new dataset.

CHAPTER 6

A stress test using a case study from Vatnaöldur, Iceland

6.1 Introduction

The diffusion modelling methods have been adjusted from traditional methods (as discussed in chapter 2 and implemented in chapters 3 and 4) to more streamlined methods, by isolating each step in the workflow to evaluate how they can be made more efficient (as discussed in chapter 5). Sample preparation and analytical methodologies have been streamlined and the geometric corrections that are usually applied to individual crystal traverses e.g. anisotropy corrections, are now applied to the crystal population as a whole. By developing these methods using the PdF, Hapaimamo and Moinui timescale datasets, complexities between different populations can be deciphered. The new streamlined diffusion modelling methods have been established to appraise data during a volcanic crisis that can be used to aid hazard mitigation and risk analysis.

The new rapid processing methods have the following stages;

1) The eruption begins

2) Collect the rock sample

3) Depending on sample type, samples are cut, crushed, and sieved to pick the mineral grains

4) Mount mineral grains or rock chip to a glass slide to create a grain slide or thin section

5) Retrieve compositional traverses from any zoned crystals (from any crystal face available) and glass compositions from the surrounding matrix using Quantitative EDS on the SEM

6) Input the compositional data into the diffusion model together with appropriate pressure, temperature and oxygen fugacity values with a-axis crystallographic orientation data applied to each traverse to calculate a timescale for each profile

7) Apply an empirical, polynomial-based orientation correction to the calculated timescales that are ranked in order from the shortest to the longest timescales

8) Consider the peak timescale immediately before eruption and any gradient changes in the tail of the rank order plot which may be indicative of more than one crystal population. The style of zoning (normal, reverse or complex), the peak timescale, and gradient changes can be indicative of timescales and the magmatic processes responsible.

To fully evaluate the efficiency of the new methods, they were implemented from start to finish to determine how quickly and efficiently the full workflow can be executed. To simulate eruption conditions, a complete sequence of tephra layers was used (oldest at the base, youngest at the top) containing all of the deposits from the start to the end of an eruption. Deposits from each layer were processed as they would have be in the event of a real eruption scenario to 'stress test' the new methods i.e. in near-real time. The method performance was evaluated to check for robustness and any improvements that may need to be made.

6.2. Geological background

The tephra sequence that was analysed is from Iceland. This is one of the most volcanically-active countries in the world due to its position on the Mid-Atlantic Spreading Ridge and the existence of the mantle plume (*Saemundsson, 1979*). The surface expression of the spreading ridge is the zone of active volcanism (the Neovolcanic zone) composed of three main parts; the Eastern Volcanic Zone (EVZ), the Western Volcanic Zone (WVZ), and the Northern Volcanic Zone (NVZ). These are connected across the centre of Iceland by the Mid-Icelandic Belt (MIB) (figure 6.1) (*Gudmundsson, 2000; Thordarson and Larsen, 2007*). These zones are composed of ~30 volcanic systems (*Gudmundsson, 2000; Thordarson and Larsen, 2007*). These systems are typically ~40-150 km long and ~5-20 km wide and develop a central volcano e.g. Katla, Hekla, Krafla and Askja (*Thorarinsson and Sigvaldason, 1972; Brandsdottir and Einarsson, 1979; Einarsson and Bransdottir, 1980; Sparks et al., 1981; Gudmundsson, 2000; Thordarson and Hoskuldsson, 2002; Oladottir et al., 2008; Thomson and Maclennan, 2013*). Intermediate and silicic products are often

produced but basaltic volcanism dominates (*Gudmundsson, 2000; Thordarson and Larsen, 2007*).

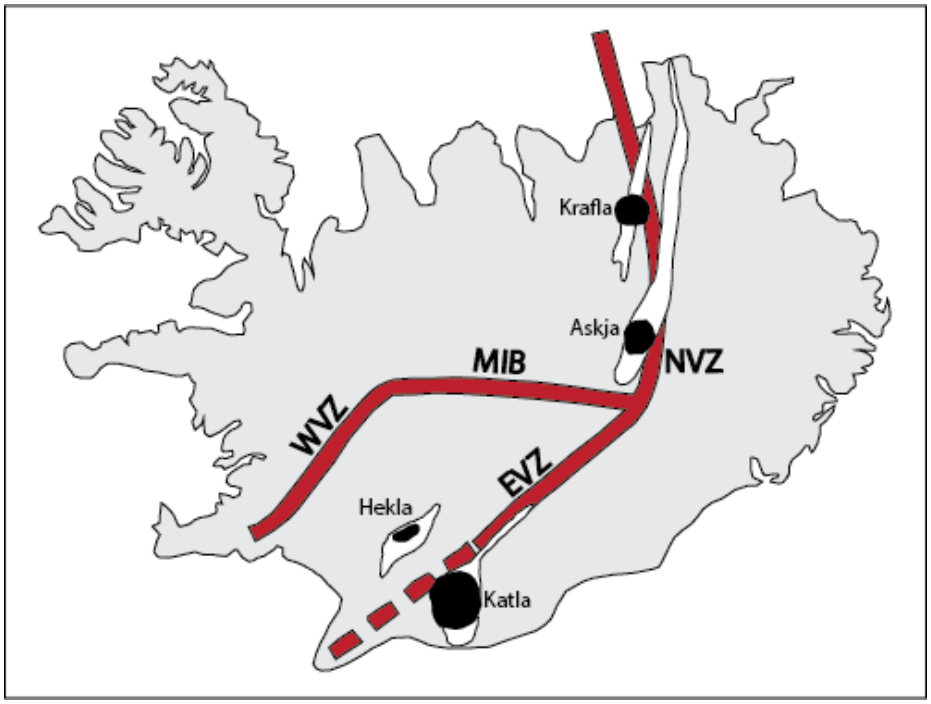

Figure 6.1: Map of Iceland showing the position of the volcanic zones (red) and the position of Krafla, Askja, Hekla and Katla central volcanoes (black circles) and their associated fissure system (elongate white shapes). Adapted from Thordarson and Larsen (2007).

The magma supply for many of the volcanic systems comes from a double magma chamber – shallow chambers supplied by a deep-seated reservoir (*Gudmundsson, 2000*). The central volcano is supplied by a shallow reservoir as are some crater rows, other crater rows are supplied with magma from deeper sources (*Sigmarsson et al., 1991; Gudmundsson, 2000*). Shallow chambers are generated above source regions where magma has accumulated due to traps in the crust such as stress barriers (*Gudmundsson, 1990; Gudmundsson, 2000*). Here the compressive horizontal stresses are larger than the vertical stress, trapping propagating dikes and deflecting the magma into sills (*Gudmundsson, 1990; Gudmundsson, 2000*). These accumulations of magma need not be always under the centre of a rift zone (*Gudmundsson, 2000)*. Icelandic magmas have been highlighted by many previous studies as having a complex history and/or journey through the magma plumbing system, transported through a complicated network of dikes and sills (*Neave et al., 2013, 2014; Passmore et al., 2012; Hartley et al., 2016*). Pankhurst et al. (2017, in review) proposed the tapping of multiple magma reservoirs before the eruption of

Eyjallafjökull in 2010. Multiple crystal populations that are chemically distinct with varying zoning patterns (normal, reverse and/or complex) are often found within an erupted magma (*Guilbaud et al., 2007; Thomson and Maclennan, 2013*).

Tephra was identified as the ideal volcanic material with which to work for diffusion studies in chapter 5, due to the rapid quench and often easier non-destructive extraction of the crystals from the surrounding glass. Since Iceland was settled in the 9th century AD, there have been around 200 known eruptions of which over 75% ejected a tephra layer, so this type of volcanic material is readily available to sample (*Thorarinsson, 1981; Larsen and Eriksson, 2007; Thordarson and Larsen, 2007; Larsen, 2008*). Explosive eruptions characterised Icelandic volcanism through much of the Holocene, specifically explosive phreato-magmatic eruptions - many of Iceland's volcanoes are underneath glaciers and the groundwater table is high in many volcanically active areas (*Thorarinsson, 1981; Gudmundsson et al., 1997; Larsen, 2008*). The interaction of rock and ice during phreatomagmatic eruptions often leads to fragmentation of the magma, leading to a rapid quench. The tephra falls and deposits as a series of horizontal layers, the oldest tephra at the base and the youngest at the top. This sequence provides a time-series deposit ready for exploitation by diffusion chronometry. The fragmentation of the magma leads to less cohesive material being deposited and therefore it is much easier and quicker to pick crystals from the depositional layers.

Vatnaöldur

Vatnaöldur, part of the Veidivötn fissure system (*Larsen, 1984),* was identified as a target for the stress test (figure 6.2.A). This volcanic system is located in the central-eastern volcanic zone. Three large eruptions took place in this area in ~1480AD, ~870 AD and 150 AD (*Larsen, 1984)*. The eruption in ~870 AD is the focus of this study and is, according to Thordarson and Hoskuldsson, (2002), the second largest Icelandic tephra eruption of historical times. Basaltic tephra fallout covered half of the island (figure 6.2.B) (*Thordarson and Hoskuldsson, 2002; Jonsdottir et al., 2014; Larsen, 1984*). The tephra layer is also known as the settlement layer, as it predates the first settlers in Iceland by a few years (*Thordarson and Hoskuldsson, 2002)*. The system is composed of a cone and crater row ~42km long, with its basin submerged

in water (*Larsen, 1984*)(figure 6.2.C). The probable centre is thought to originate underneath Bardabunga volcano (*Saemundsson*, 1979; *Larsen, 1984*).

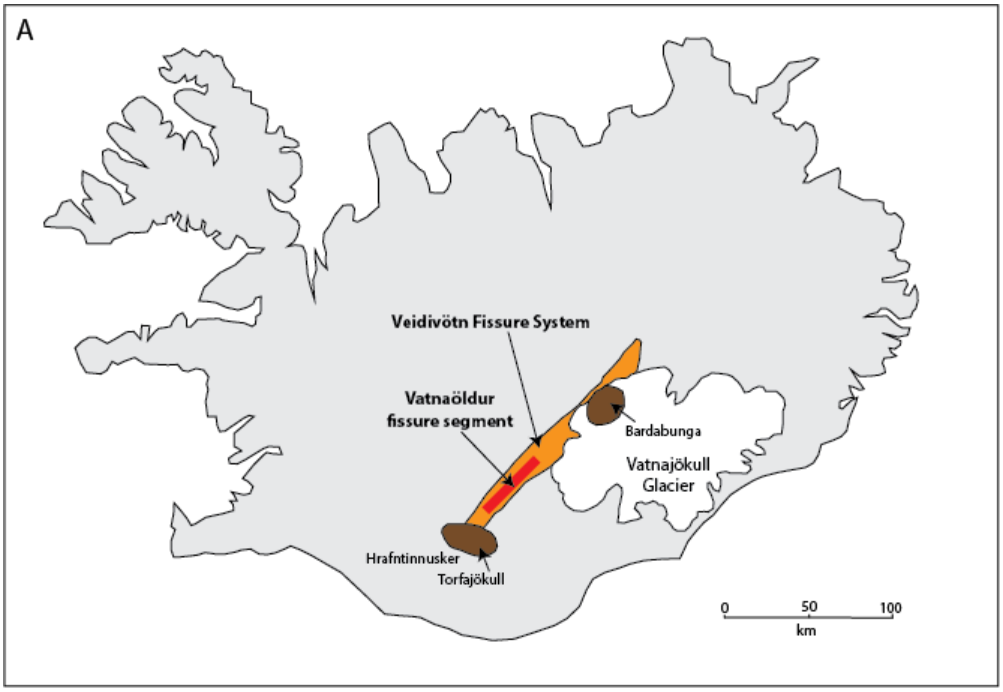

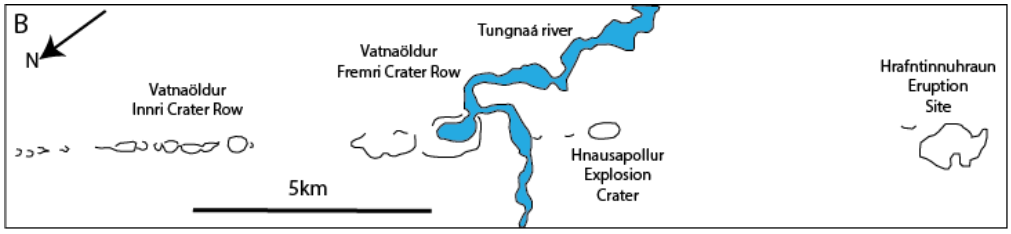

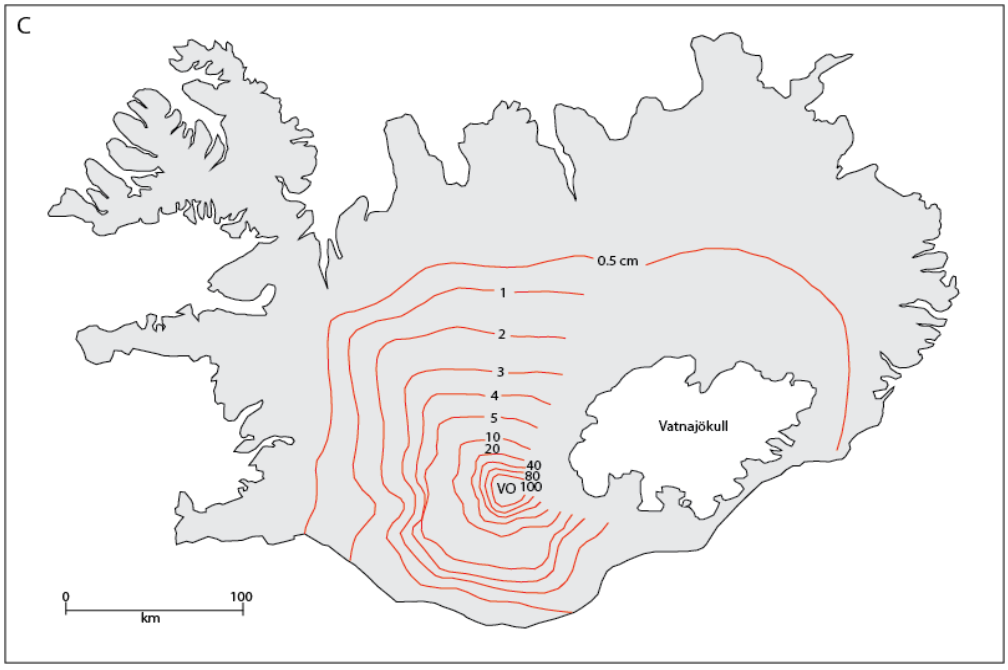

Figure 6.2: A) Schematic map of Iceland showing the Veidivötn fissure adapted from Larsen (1984). The Vatnaöldur segment of the fissure system is defined in red. B) The crater row of the Vatnaöldur fissure system. Adapted from Larsen (1984). C) A simplified isopach map of the basaltic part of the Vatnaöldur 870 AD eruption. Adapted from Larsen (1984).

The eruption in 870 AD was almost entirely explosive (*Thordarson and Hoskuldsson, 2002*). Magma erupted from new fissures, and interacted explosively with water (phreato-magmatic). The craters in the Veidivötn area have been described as tephra rings with maar-type explosions, thought to be synonymous with hydro-magmatic activity (*Larsen, 1984*). All fissures are thought to have been active simultaneously during the early part of the eruption, producing more silicic tephra towards the SW and more basaltic tephra towards the NW, although the bulk of material produced was basaltic (*Larsen, 1984*). The eruptive events are hypothesised to be initiated by rifting episodes within the Veidivötn system (*Larsen, 1984*). The feeder dike for the 870 AD eruption cut through the Torfajökull central volcano (*Larsen, 1984*; *Thordarson and Hoskuldsson, 2002*) and thus initiated an eruption adjacent to Hrafntinnusker, which produced a rhyolite tephra and an obsidian lava flow (figure 6.2.A) (*Thordarson and Hoskuldsson, 2002*). The eruption frequency for the Veidivötn fissure system is estimated to be roughly one large eruption every 600-800 years, with periods of quiescence between larger eruption events (*Larsen, 1984*).

The Vatnaöldur basaltic tephra deposit contains both olivine and plagioclase crystals with some clinopyroxene – they vary in size, and modal proportions within each tephra layer as described in the next section. The bulk volume is calculated as ~1 km^3 (DRE) in the literature (*Larsen, 1984*). Only the olivines will be modelled for magmatic timescales. The total eruption time has been estimated at ~ 5 days by extrapolation of soil thickening rates in several soil sections between dated tephra layers below and above the Vatnaöldur tephra (*Larsen, 1984*). Field evidence and diffusion timescales from this study will be evaluated to see if our results are in agreement with this estimation of eruption length.

6.3. Field description and sample summary

6.3.1. Field description

Sampling was carried out in August 2015 ~9-11 km west of the eruptive vent (GR N 64 10.458, W 19 07.437 (Icelandic Grid System)) at an altitude of ~1500 ft. Five vertical tephra sequences were dug out, orientated downslope (the youngest material found upslope and the oldest material found downslope). Cumulatively these tephra layers reveal the full eruption sequence. Nineteen tephra layers were identified in total. Together they provide a data time-series from the first tephra layer erupted to the last tephra later erupted, which is ideal for a stress test of this kind (figure 6.3).

It is very important to locate the first sample of the eruption (found at the base of the deposit), as this contains the first crystals to be erupted. The initial interpretation of magmatic processes occurring in the subsurface can be extracted from the first crystals to be erupted. These may reveal information regarding the eruption trigger and how long before eruption it occurred. For the purposes of the stress test, it is also important to correctly identify the last layer to be erupted. Analysis of this layer and layers from the middle of the eruption gives information on how the eruption evolved over time. This is useful information when considering future eruptions. Each of the tephra layers represents some change during the eruption e.g. composition, crystal content or thickness. The volume of material ejected or explosivity may have varied from layer to layer and composition and/or crystal content may vary over time. Initial field observations provide a starting point for initial interpretations of subsurface and eruptive. The tephra layers that were analysed as part of the stress test are described in more detail in section 6.3.2.

As this is a pre-historic eruption before the first settlers were on the island, it is difficult to know how much time elapsed between each tephra layer. In a real life scenario, there may be very little time between each eruptive layer, so it is important for the methods to be quick and simple enough to cope with rapid continuity between layers. For the purposes of this stress test, each tephra layer will be processed as quickly as possible to simulate data gathering during an ongoing eruption scenario. Processing time is controlled by the thickness of the tephra layer

and crystal content and size i.e. a thicker tephra layer with few crystals takes longer to process than a thinner tephra layer with plentiful, large crystals.

Figure 6.3 below shows a schematic field log taken through the tephra sequence for the 870 AD eruption. Tephra layers range from 15 cm thick to 1m thick with modal olivine proportions varying from ~3% to > 1%. Collection of these samples in real time would take only minutes as the samples would be fresh and it would not be necessary to dig down and expose each of the layers.

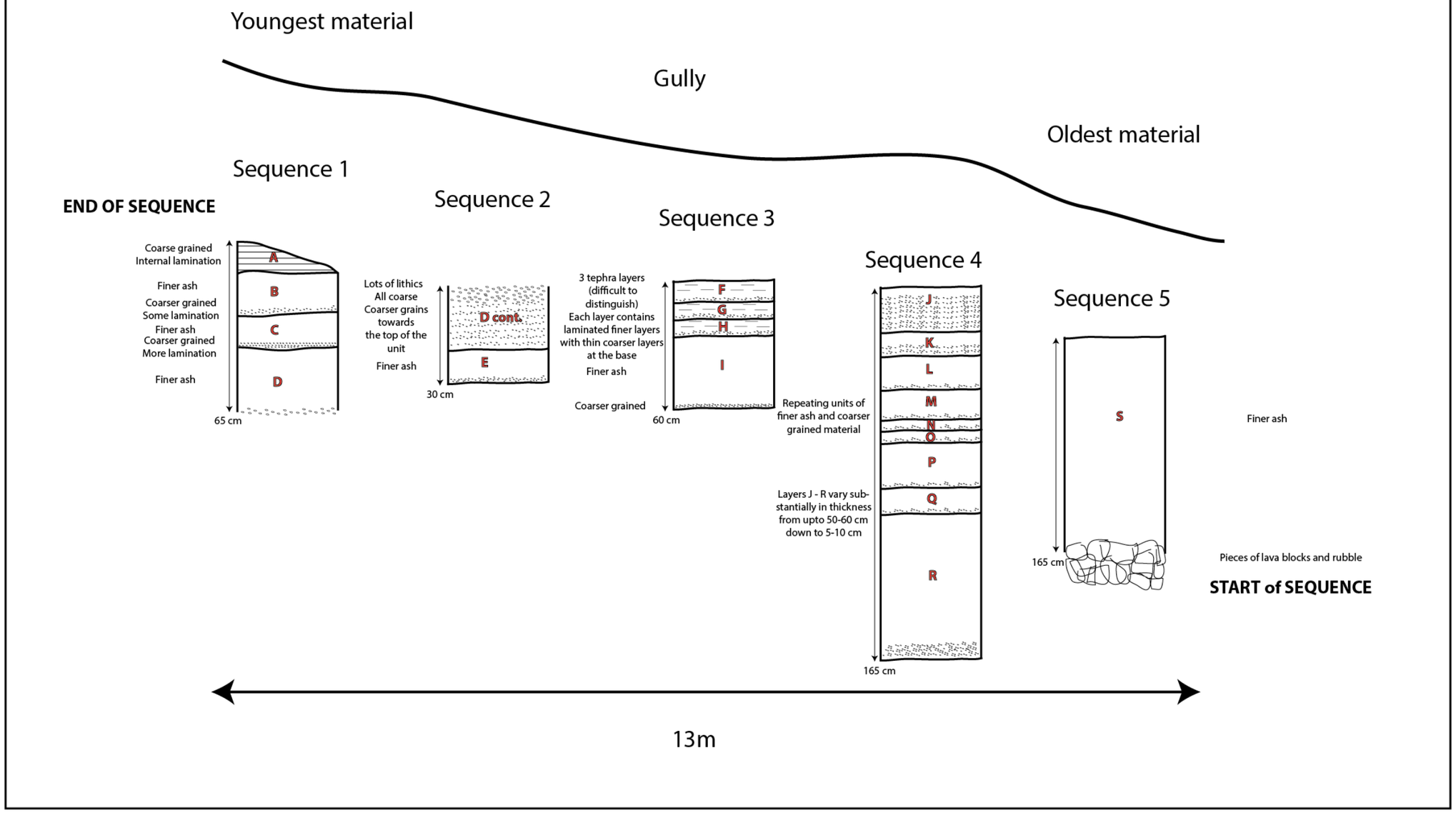

Figure 6.3: A schematic field log through a complete sequence of tephra deposits (A-S) in time order from the 870 AD eruption.

6.3.2. Sample summary

Only crystals from the oldest (first) eruptive layer (S), two middle layers (stratigraphically) (E/F) and the youngest (last) eruptive layer (A) were processed. These three/four layers incorporate material from the start of the eruption through to the end of the eruption providing a time-series of samples deemed appropriate for determining how the eruption evolved from start to finish.

6.3.2.1. Oldest tephra layer 'S'

Large lava blocks and pieces of rubble, up to 10 cm in size marked the base of this tephra deposit. The top or base of a tephra sequence is marked by a change in stratigraphy e.g. lava flow or a change in depositional style such as a surge deposit or flow deposit (*Thorarinsson, 1954*).

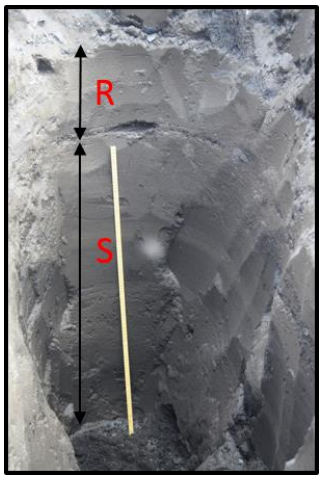

Figure 6.4: Tephra pit showing sequence 5. The tephra layer S was sampled and analysed as part of the stress test

This base layer of the tephra sequence (S) was the first material to be ejected from the volcano upon eruption. It is one of the thickest layers at ~1 m thick composed of varying material from fine ash (< 125 μm) to coarser glass fragments a couple of mms in size with sporadic fragments up to 1cm in size however, most of the material in this layer is fine (<0.5 mm in size). Both olivine and plagioclase crystals are present at around 1-2% and 5% modal abundance respectively. Pyroxene crystals can be found but they are rare. Olivine crystals are often equant but fragmented,

~200 µm to 500 µm in size. If whole crystals are present, they are likely much bigger (up to 1 mm).

6.3.2.2. Middle tephra layer(s) 'E and F'

Tephra layers E and F were deposited whilst the eruption was ongoing. These layers sit roughly in the middle of the whole erupted sequence by unit number, however it is not clear whether these deposits were ejected nearer the start or the end of the eruption. There is little evidence to suggest the time lapse between each of the deposited tephra layers.

Figure 6.5: Tephra pit showing sequence 3. The tephra layers E and F were sampled and analysed as part of the stress test

These layers are some of the thinnest found within the sequence, tephra layer E is ~15 cm thick and tephra layer F is much thinner, ~5 cm thick. Both layers show evidence of some sorting within the layers – the coarsest glass fragments at the base of the layers and the finer fragments towards the top. This may imply these layers are single explosions, grading from the air fall. Like tephra layer S, each layer E and F is composed of fine ash (< 125 µm) to coarser material up to 1 mm in size. Both layers contain an abundance of plagioclase, up to 3-5% however both are also sparse in olivine < 1%. This is the reasoning for sampling two middle layers rather than one – initially only layer E was sieved and picked for olivine crystals but their low abundance justified the addition of olivines from layer F. Olivine crystals are often equant but fragmented as in tephra layer S. They are ~200 µm to 300 µm in size,

where more complete slices have been found suggesting the crystals in this layer were slightly smaller.

6.3.2.3. Youngest tephra layer 'A'

The end of the tephra sequence, (top of layer A), is marked by an erosional contact, from a pyroclastic flow or surge, probably a later event. This layer is ~10 cm at its thickest part and ~3 cm at its thinnest part. It contains the coarsest fragments (up to 1-2 mm) and also the largest abundance of crystals – both plagioclase and olivine (~3-5%).

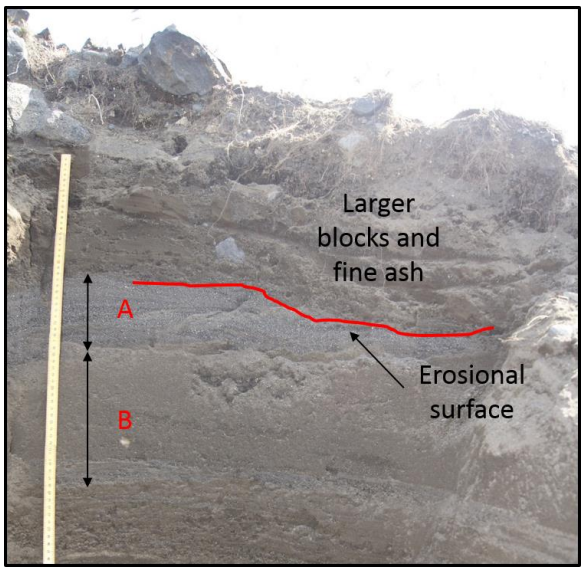

Figure 6.6: Tephra pit showing sequence 1. Tephra layer A, the final layer to be deposited at the end of the eruption was sampled and analysed as part of the stress test

Both the plagioclase and olivine crystals in layer A are easily visibly to the naked eye, up to 1-2 mm in size. The fragmented glass found in all of the tephra layers is a product of the phreato-magmatic nature of the eruption. Crystals are mostly found isolated, or encased in a thin layer of glass.

6.4. Streamlined Processing Workflow

The data sections utilise the following notation for crystal traverses: VA_500_1_A. 'V' refers to the eruption (Vatnaöldur), '500' refers to the maximum sieve size in μm, '1' refers to the crystal and 'A' refers to the profile extracted from the crystal. In terms of field deployment, it is important to quantify how much time each step in

the processing workflow takes for comparison with traditional techniques and for consideration on how they could be improved/further streamlined.

6.4.1 Drying of Samples

All samples were initially dried out in an oven, as they were damp, an unfortunate side effect of the Icelandic weather. This process only took an hour or so for each sample from a tephra layer. This step may not always be necessary depending on if there is rainfall when the material is deposited. This time is not included in the final processing time for this method.

6.4.2 Sieving

All three layers were sieved and separated into size fractions to make grain picking quicker and easier. Very few fragments were found to be over 1 mm in size, even within the coarsest layer. A decision was made to only pick crystals from the size fractions, 250-500 μm and 125-250 μm. Nothing smaller was picked. This is in line with selection rule 1 outlined by Shea et al. (2015a) described in chapter 5. This enabled zoned crystals of sufficient size to be found, whereby the homogeneous core did not appear to have been erased by diffusive re-equilibration thus retaining the full diffusion profile. This enables a fuller understanding of the magmatic process that created that chemical signature measured. It could be argued that less than 250 μm is still a very small crystal in itself, but there was a lack of larger crystals to study within this sample set. These smaller crystals have a maximum recordable timescale.

Time spent processing each sample was influenced by the thickness of the sample – thicker layers required more material to be sieved than thinner layers to ensure a proportionate amount of material was processed. Tephra layer A contained the largest amount of coarse material but also contained the largest crystal fragments and largest abundance of those fragments. Tephra layers E and F contained some of the finest material but also the fewest and smallest crystal fragments whereas tephra layer S contained material that would fall somewhere between these layers by size and abundance.

Sieving times for each layer are as follows;

Tephra layer A – 30 minutes

Tephra layer E – 15 minutes

Tephra layer F – 15 minutes

Tephra layer S – 20 minutes.

I have focused on the first tephra layer (S) to be deposited at the start of the eruption at the end of each subsection. The processing times were tallied as the workflow was executed, to keep track of how long the whole processing workflow takes.

Total streamlined-workflow processing time (S) – 20 minutes.

6.4.3. Grain Picking

Where possible only olivine grains were picked from the glassy tephra fragments from the 500 μm and 250 μm size fractions. Due to similarities in colour and lustre, clinopyroxene and plagioclase were sometimes mistaken for olivine. Tephra layer A has a large amount of crystals > 500 μm (~3-5%) however tephra layer E, F and S had very little (> 1-2%). Several ten's of crystals were picked from each layer where possible, sufficient to make 2 or 3 grain slides of varying crystal size fractions. This was deemed appropriate for the stress test.

Crystal picking times for each layer are as follows;

Tephra layer A – 1 hour 25 minutes

Tephra layer E – 1 hour 15 minutes

Tephra layer F – 3 hours 30 minutes

Tephra layer S – 3 hours 30 minutes.

The fast grain picking durations for both layer A and layer E are due to opposite reasons – layer A contains large (500 μm -1 mm) olivine crystals easy to see with the naked eye amongst a lot of coarse glassy fragments. Layer E contains smaller

olivines (200 µm - 400 µm) that are easier to pick out amongst less surrounding material (thinner layer).

Total streamlined-workflow process time (S) – 3 hours 50 minutes

6.4.4. Sample preparation

Olivine crystals picked from the glassy tephra fragments were mounted on to a glass slide. Two grain slides were prepared for tephra layers A and S due to the larger quantity of crystals picked.

The procedure for preparing grain slides is simple and straight forward. The larger crystals (> 500 µm) were prepared to a thickness of ~350-450 µm. The smaller crystals (250-500 µm) were prepared to a thickness of ~200 µm. It is important to know what thickness the grain slide is within the SEM as manually focusing between the sample and the cobalt is of utmost importance, as described in chapter 5. The less thickness difference there is between the cobalt and the sample, the better, as the working distance from the pole piece to the analysed surface is critical to the X-ray geometry and count rates. Sample preparation involves frosting the glass, placing the grains in the middle of the glass (in any orientation) and covering with a few drops of resin (to fix the crystals to the slide). The resin hardens on a hot plate which is followed by grinding, finer grinding (hand lapping) and polishing (first using a 3 µm, then a 1 µm and a ¼ µm diamond paste). Grinding and polishing is one of the most important steps to ensure a perfectly flat sample. The time for polishing can vary slightly as re-polishing is required if samples have become uneven or appear pitted.

The preparation time for each thin section from mounting to final polishing is as follows for each layer;

Tephra A - 2 hours 30 minutes (when adjusted for 2 thin sections per sample – 3 hours)

Tephra E – 2 hours 30 minutes

Tephra F – 2 hours 30 minutes

Tephra S – 2 hours 30 minutes (when adjusted for 2 thin sections per sample – 3 hours)

The thin sections require carbon coating for SEM analysis, which only adds on ~10 minutes (3 thin sections can be carbon coated at once).

Total streamlined-workflow process time (S) – 6 hours 50 minutes

6.4.5. Compositional Analysis (Quant EDS)

Compositional traverses were retrieved using the Quant EDS analysis within the SEM, as described in chapter 5. Two samples can be placed in the SEM for analysis at the same time, together with the cobalt on which to calibrate the beam. The beam current remained relatively stable throughout the analytical process at ~0.6-0.7 nA and samples were carefully focused before any Quant EDS was performed.

Firstly and importantly, zoned crystals need to be identified. Without zoned crystals this method is not viable. Numerous zoned crystals are also required to truly represent a crystal population, discussed in detail elsewhere within this thesis (chapters 1-5). Once they have been identified, there are two ways of extracting the compositional data. Firstly by measuring complete traverses at ~5 μm spacing, plotted manually utilising the Oxford Instrument's *Aztec* software. Each compositional spot is set to acquire data for 2 minutes and other functions cannot be carried out whilst the composition is being retrieved. When diffusion zones are wide (they can be up to 300 μm in this dataset) this analysis takes some time, and so is not ideal in an eruption scenario when fast processing is needed. Alternatively, two points can be taken – one at the core and one at the rim (three can be taken, one in between the points if the diffused zone is particularly wide) and calibrated with a pixel greyscale profile taken from an SEM image, similar to the calibration described in chapter 2.

Once zoned crystals have been identified, a picture is taken at ~100 μs per pixel, with line integration, and the crystal core and rim points are analysed for their

composition. The analysis time for the core and rim points was reduced to 60 seconds after testing showed that the same results can be achieved as when analysing for 120 seconds. During the initial inspection of the crystals it was interesting to note that many of the crystals were often fragments showing few or no crystal faces. These cannot be analysed as the diffusion profiles have been shortened where the crystal has broken. This is somewhat restrictive of where profiles can be taken from. Figure 6.7 shows an example of the type of crystal slices found within the dataset.

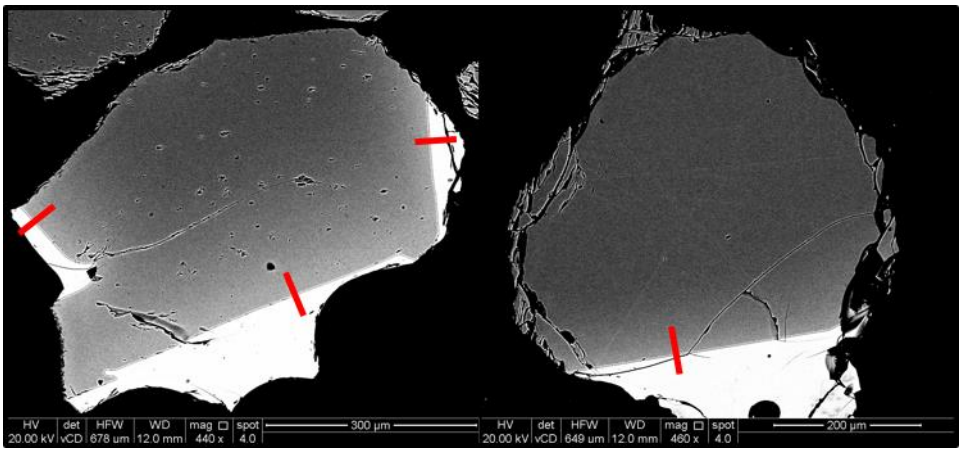

Figure 6.7: An example of two olivine crystal slices imaged using the SEM. To the left, the crystal is less fragmented with 3 possible crystal faces suitable to extract compositional profiles (red). To the right, the crystal is much more fragmented with only a single crystal face where a compositional traverse could be extracted (red). Red markers indicate the possible positions of the traverses only, not the full length of the traverse.

The crystal fragments are the result of the eruption being phreato-magmatic in nature and these types of crystal slices should be anticipated if that is the observed eruption style when collecting the sample.

As many points as time allows (at least ten) should be analysed to retrieve the glass composition for input into the thermometer. A circular area was defined and analysed for 30 seconds to minimise effects on mobile elements such as Na (*Morgan and London, 1996*). Totals of 95 - 104 were achieved for the compositional traverses (most totals fell within 97-103) and totals of 98-101 were achieved for the matrix glass by keeping conditions within the chamber stable and refocusing on the sample before analyses as necessary. A selection of compositional data can be found in Appendix F.

Tephra Layer	Number of traverses through olivine crystals	Number of spot analyses for matrix glass compositions
S	39	12
E/F	9	23
A	38	12

Table 6.1: List of traverse and spot analyses taken per sample.

It was stated by Shea et al. (2015a) that at least 20 timescales should be obtained for a crystal population to reveal the true timescale in addition to selection rules that have been discussed in chapter 5. Where tephra layers contained a larger abundance of olivine (layers A and S), more than 20 timescales can easily be extracted for a population.

Acquisition time for profile retrieval on the SEM for each sample is as follows;

Tephra A – 13 hours

Tephra E and F - 13 hours

Tephra S – 13 hours

Total streamlined-workflow process time (S) – 19 hours 50 minutes

To provide a check on the accuracy of the totals and therefore the compositions retrieved using the Quant EDS method, some profiles were re-analysed using the EPMA.

Core and rim values were re-measured using a focused beam at 20kV and a beam current of 40nA. Peak counting times were as follows; 45s for Ni, 40s for Mn, 30s for Si, Cr, Al, and Mg and 20s for Fe. Most analyses returned totals of 98.5-100.4 wt. %. Repeat analysis of the San Carlos olivine standard were used to estimate the precision of Fo measurements. The Fo content of the San Carlos olivine was determined with a precision of 2σ = 0.099 mol% (n=24). Other assigned standards

and detection limits are reported in Appendix F. The EPMA forsterite compositions were compared with the Quant EDS forsterite compositions for reproducibility. Figure 6.8 shows the comparison.

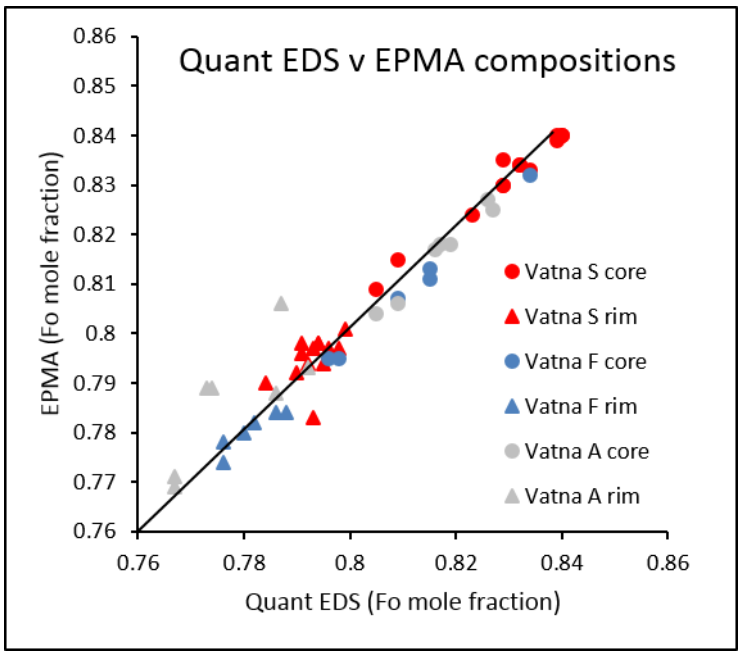

Figure 6.8: Compositions obtained using Quant EDS plotted against compositions obtained using the EPMA.

The near agreement of the Quant EDS data with the EPMA data along the 1:1 line shows the accuracy and reliability of the Quant EDS methods. For each individual point, the difference rarely exceeds more than 1 mol. %. There is some scatter of composition between those extracted using the EPMA and those extracted using Quant EDS (there is a difference in mol. % of up to 0.19%). For the purposes of this exercise, this would lead to a negligible change in timescale on a crystal population scale.

6.4.6 Compositional profile processing

A profile through the diffused zone is extracted from the SEM image using 'ImageJ' image processing software (*Schneider et al., 2012*). This profile gives grey scale value per pixel across the diffused zone. These grey scale values are converted into forsterite values following a similar routine to that described in chapter 2, by calibrating them with the core and rim compositional values obtained using the

Quant EDS methods. As the SEM images are used to define the shape of the diffusion curve within the crystal (as only the composition of the core and rims are extracted using Quant EDS), it is critical that the correct settings are used to acquire the picture to avoid the 'bullseye' effect described in chapter 5. If the images are indeed affected by this phenomenon, a correction may be applied. However, this in turn will lead to more processing time leading to the streamlined processing workflow becoming less efficient.

The times taken for all compositional traverses to be calibrated and input into AUTODIFF for modelling are

Tephra A – 3 hours 30 minutes

Tephra E/F – 1 hour 20 minutes

Tephra S – 4 hours 30 minutes

Total streamlined-workflow process time (S) – 24 hours 20 minutes

6.4.7. Initial Petrological Observations

Initial observations show that crystals are mostly euhedral in shape, when they are less fragmented. However some crystal faces are embayed, particularly those from tephra layer A as shown in figure 6.9.

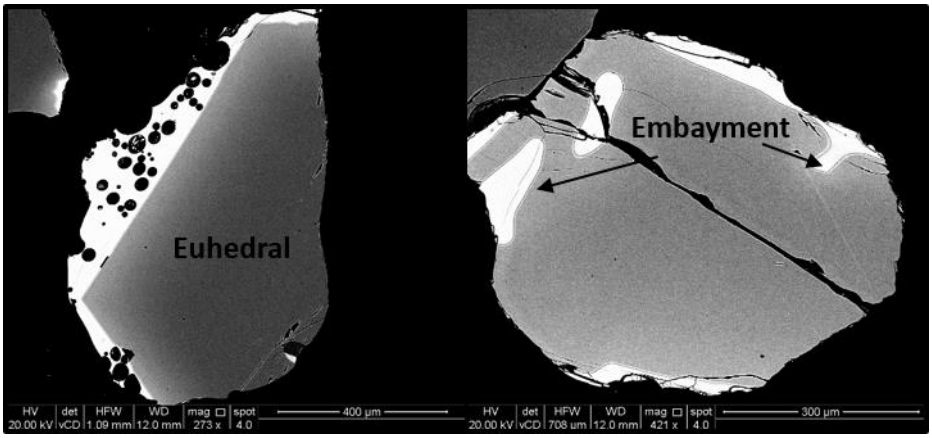

Figure 6.9: Examples of a euhedral olivine fragment on at least three sides and an olivine crystal fragment with obvious embayments

All crystals are normally zoned. In tephra layer S, the olivines have core compositions of Fo_{82-84}, and rim compositions of Fo_{78-80}. In tephra layer E and F, the olivines have core compositions of Fo_{80-84} and rim compositions of Fo_{77-79}. In tephra layer A, the olivines have core compositions of Fo_{81-86} and rim compositions of Fo_{77-80} as shown in figure 6.10.

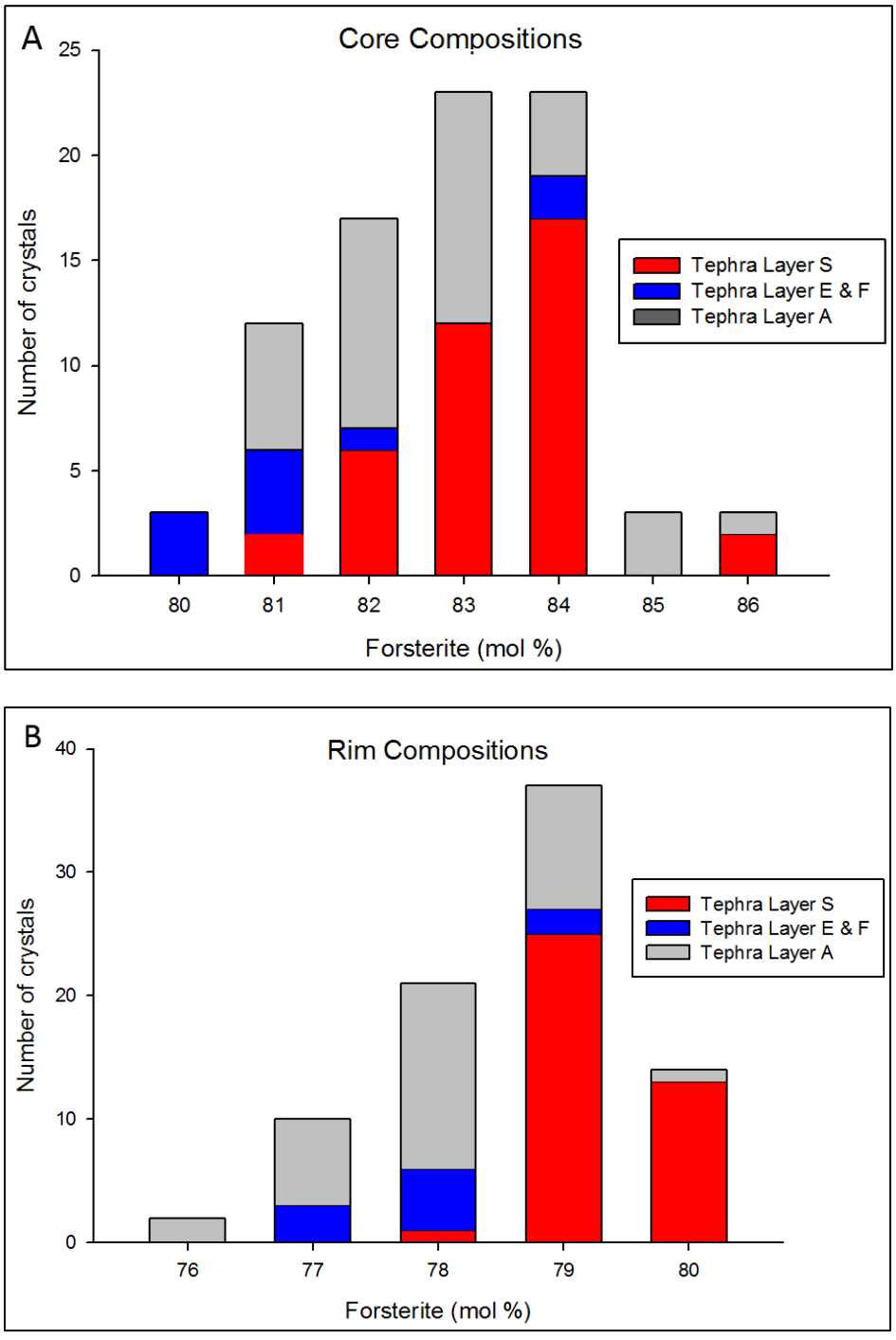

Figure 6.10: A) core compositions from 84 analyses across the three tephra layers - S (red), E and F (blue) and A (grey) B) rim compositions from 84 analyses across the three tephra layers S (red), E and F (blue) and A (grey).

6.4.8. Thermometry and Oxygen Fugacity

Temperature was calculated using compositions from the matrix glass. Few of the olivine crystals contained melt inclusions. Where present, the melt inclusions were not located within the diffused zone and so would not be a good proxy for liquid composition at the time of diffusion, as discussed in chapter 4. Temperatures calculated from the matrix glass will provide a minimum temperature for diffusion related processes. Temperature was calculated using the same method as that for the Hawaiian matrix glass. The thermometer of choice was the Montierth et al. (1995) thermometer, as described in chapter 4.

The matrix glass has an average MgO content of ~6.5 wt. %. The temperature calculated for the Vatnaöldur lavas is 1169 °C (+/- 10°C). This is slightly higher than the temperatures calculated for the Hawaiian lavas (~1160°C), but not unusual for Icelandic lavas (*Neave et al., 2014; Pankhurst et al., 2017, in review*). The oxygen fugacity chosen for this dataset is NNO -0.5 log units. This was felt appropriate for this airfall, near-vent dataset as discussed for the Hapaimamo tephra in chapter 4. This is also consistent with other authors who have carried out diffusion studies on Icelandic tephras (e.g. *Thomson and Maclennan, 2013; Hartley et al., 2016)*. These values were input as parameters into AUTODIFF with the compositional profiles for modelling of the timescales.

6.4.9. Orientation and other corrections

Effects of changing boundary conditions and/or growth, shallow sectioning angle and crystal shape have been discussed in chapters 3 and 5. Crystal shape in particular is an important consideration when applying the 1-directional diffusion coefficient correction for orientation and interpreting the resulting timescales - what crystal faces are present in the population. The effects of the other corrections are negligible for this sample set. The fragmentation of many of the crystals leads to difficulties in defining which crystal faces are present and may lead to difficulties interpreting the timescales after the orientation correction has been applied.

In chapter 5, EBSD was ruled out as an effective technique for obtaining the crystallographic orientation as part of rapid processing methods, due to the

availability of the hardware, and the preparation, acquisition and processing time required. A faster yet reliable method was described using a 1-directional diffusion coefficient. This orientation correction was applied separately to the dataset from each tephra layer.

The orientation of all the compositional profiles were set as parallel with the crystallographic a-axis direction within AUTODIFF. The timescales calculated from each tephra layer were collated and input into a rank order plot. An empirical polynomial correction, calculated from the PdF dataset described in chapter 5, was applied to each dataset. The results and interpretations of magmatic processes that these curves and timescales may relate to are discussed in the next section.

The times taken to collate the timescales and apply the orientation correction are as follows,

Tephra A – 40 minutes

Tephra E and F - 30 minutes

Tephra S – 40 minutes

FINAL total streamlined-workflow process time (S) – 26 hours

Table 6.2 summarises the processing times for each tephra layer (S, E/F and A) compared to the processing time when using current traditional methods.

Processing Step	Streamlined methods **Tephra layer S (hours)**	Streamlined methods **Tephra layer E/F (hours)**	Streamlined methods **Tephra layer A (hours)**	Traditional Methods (hours)
Drying	1	1	1	-
Sieving & Grain picking	3.8	5.25	2	-
Sample prep	3	2.5	3	8
Compositional analysis	13	13	13	60
Compositional processing	4.3	1.3	3.5	48
Parameter input and Orientation correction	0.66	0.5	0.66	72+
Total processing time	**~26**	**~24**	**~23**	**8 days +**

Table 6.2: Table summarising how long each processing step within the streamlined workflow took for each tephra layer compared to how long it could take using traditional methods based on processing time of the previous samples using such methods. Dashes indicate steps where no time improvement can be made. The orientation correction for the traditional methods includes extra preparation, analysis and processing time for EBSD measurements and U-stage measurements.

The final processing time for the rapid processing workflow to enable petrological timescales to be available for eruption monitoring is ~ 26 hours depending on the thickness of the deposit and how easy it is to extract the crystals from the deposit. This is significantly quicker than current traditional methods. This has exciting implications for eruption monitoring and therefore risk management and hazard mitigation but also for processing large amounts of data in less time.

6.5. Magmatic Timescales and their Interpretation

The timescales calculated for each tephra deposit are shown in the figures 6.11A-C. These timescales are corrected for sectioning effects and anisotropy with the correct temperature and fO_2 conditions applied but they are not corrected for changing boundary conditions and/or simultaneous growth effects. This orientation correction also assumes no c-axis faces present as discussed in chapter 5.

The timescale ranges for each tephra are as follows: tephra layer S (the first to be erupted) range from 146 days to ~11 years, tephra layer E/F (from the middle of the eruption) range from 121 days to ~5 years and tephra A (the last to be erupted range from 30 days - ~9 years).

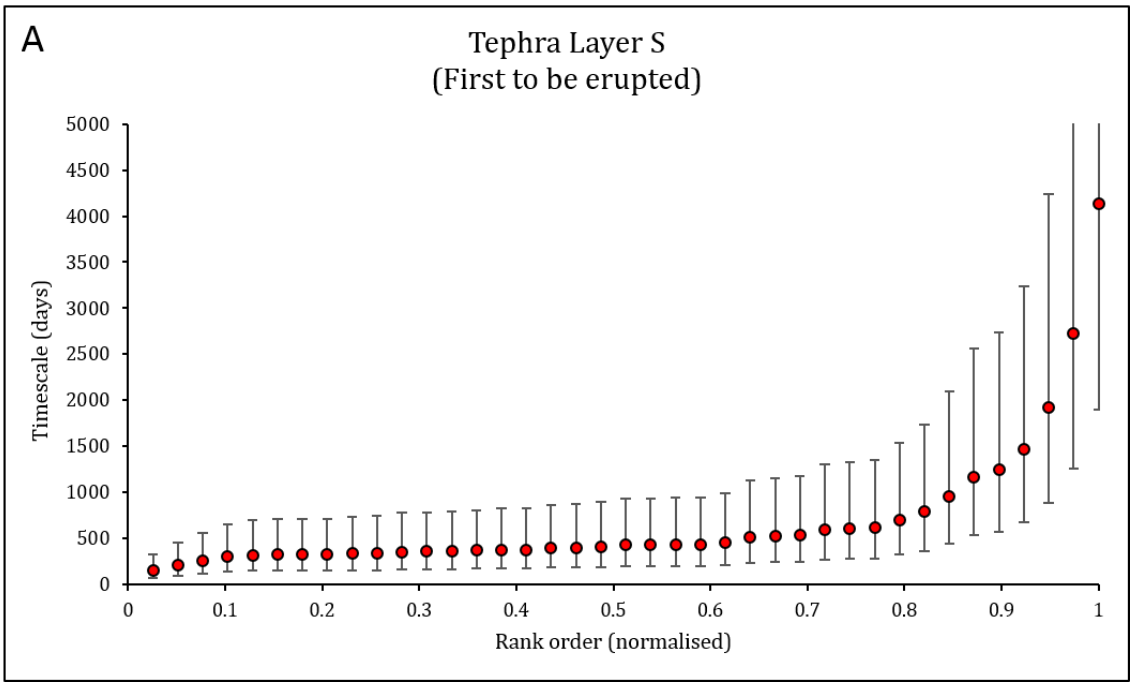

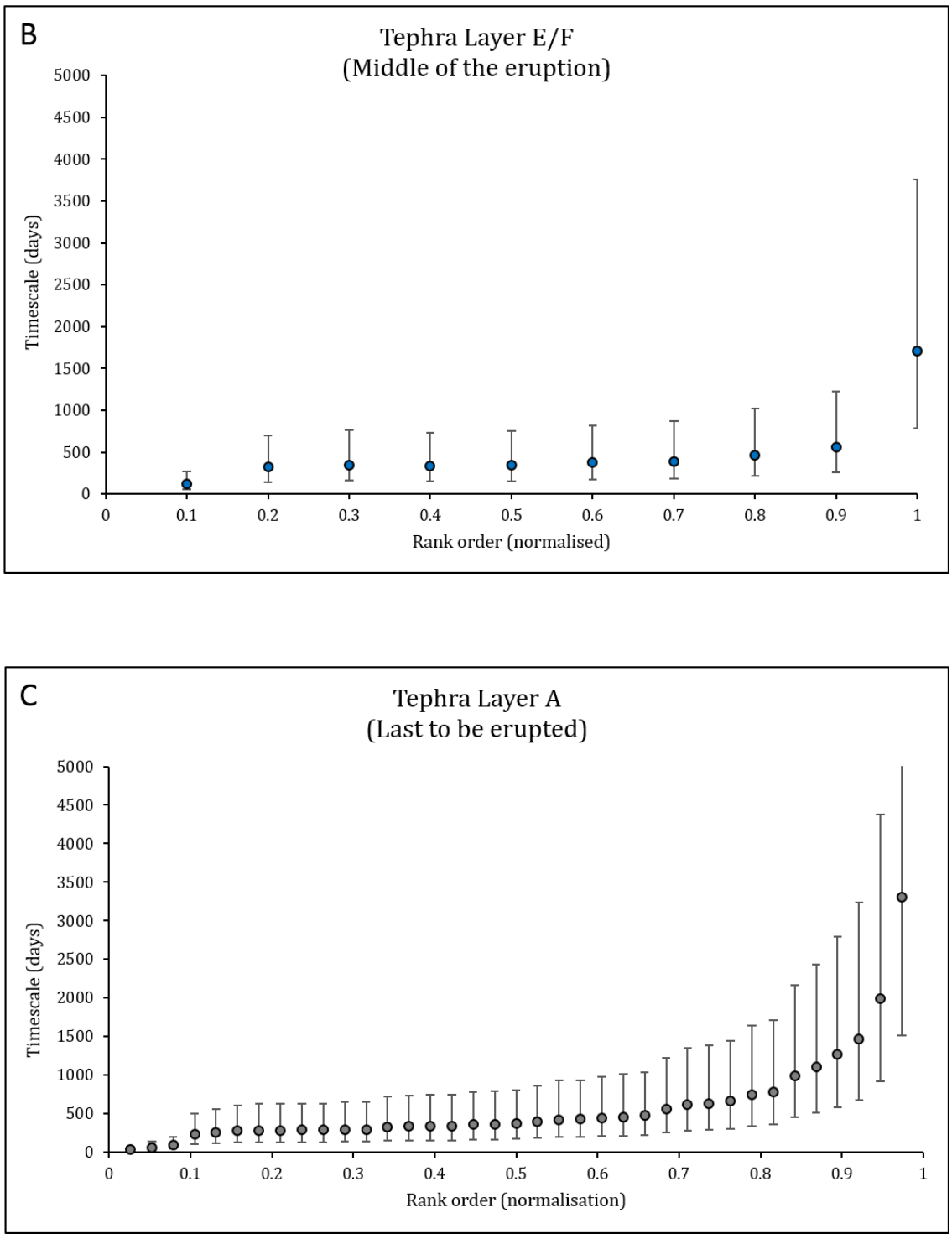

Figure 6.11: Rank order plot of the timescale distributions from olivines from each tephra layer A) tephra layer S, B) tephra layers E/F and C) tephra layer A.

The rank order distributions show simple, continuous curves with a slightly increasing gradient towards the right hand side of the plots with no distinct steep change in gradient at the tail. This is similar to the shapes seen for the single crystal

population within the PdF dataset. This is our first indication that each tephra layer may contain only a single population of olivines. As previously mentioned, the core compositions fall over a narrow range and there is only 1 zoning type, further bolstering this hypothesis. The synthetic examples and the natural case study examples from chapter 5 show that the most important information (the youngest timescales associated with the most recent magmatic process) in an eruption scenario is within the initial, flatter part of the curve, not in the tail. This area is highlighted in the diagram below for tephra layer S.

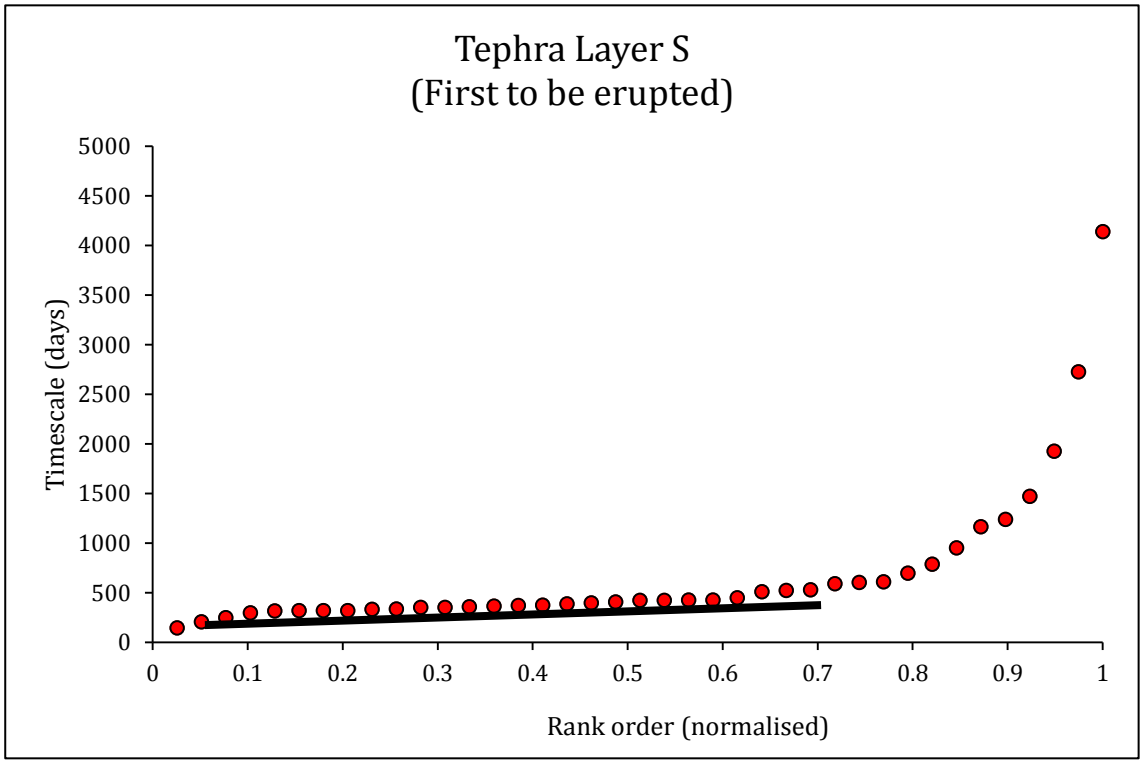

Figure 6.12: Rank order plot of the timescale distribution from tephra layer S. The black line highlights the youngest most important timescales from the start of the eruption.

The youngest timescales within the first erupted tephra layer forming the main linear part of the correction curve range from 146 days – 446 days (~5 months to 1.2 years). This means that something changed in the system ~1 year before eruption until ~5 months before eruption e.g. magma migration (the diffusion clocks first started ~1.2 years before eruption and the last diffusion clocks started ~5 months before eruption). All of the crystals show normal zoning which may be due to decompression as discussed in chapter 4. Therefore these timescales may be representative of when the crystals were emplaced in a shallow storage reservoir

and are indicative of residence time. The youngest timescales of 5 months indicate that no new material was added to the storage reservoir after this time i.e. no new clocks were started. There were no magmatic processes occurring in the subsurface that left behind a diffusion signature in the crystals less than 5 months before eruption. This is significant information to obtain during an ongoing eruption, as it may imply that the shallow storage reservoir is no longer in communication with a magma supply. This is useful information in terms of hazard as it may imply that what has already been emplaced (or some portion of what has already been emplaced) is all that can be ejected from the volcano during the eruption. This kind of time information linked to magmatic process is not currently available in a monitoring situation and is really important in terms of knowing more about what may be the duration of an eruption. In this particular case, were it a modern day eruption, this data could be linked to InSAR data, as deflation should match eruption rate. This data could also be use before an eruption has started. It would be expected that the inflation and holding period highlighted by the diffusion timescales would be seen in InSAR data. The diffusion data suggests there may be an eruption some months later, useful information for a monitoring team.

The youngest timescales within the last erupted layer forming the main linear part of the correction curve range from 295 days - 472 days (~10 months to ~ 1.3 years). There are also three much younger timescales present within the last erupted layer ranging from 30 days – 91 days. The timescale distributions from all the tephra layers can be plotted on the same rank order plot as shown in figure 6.13.

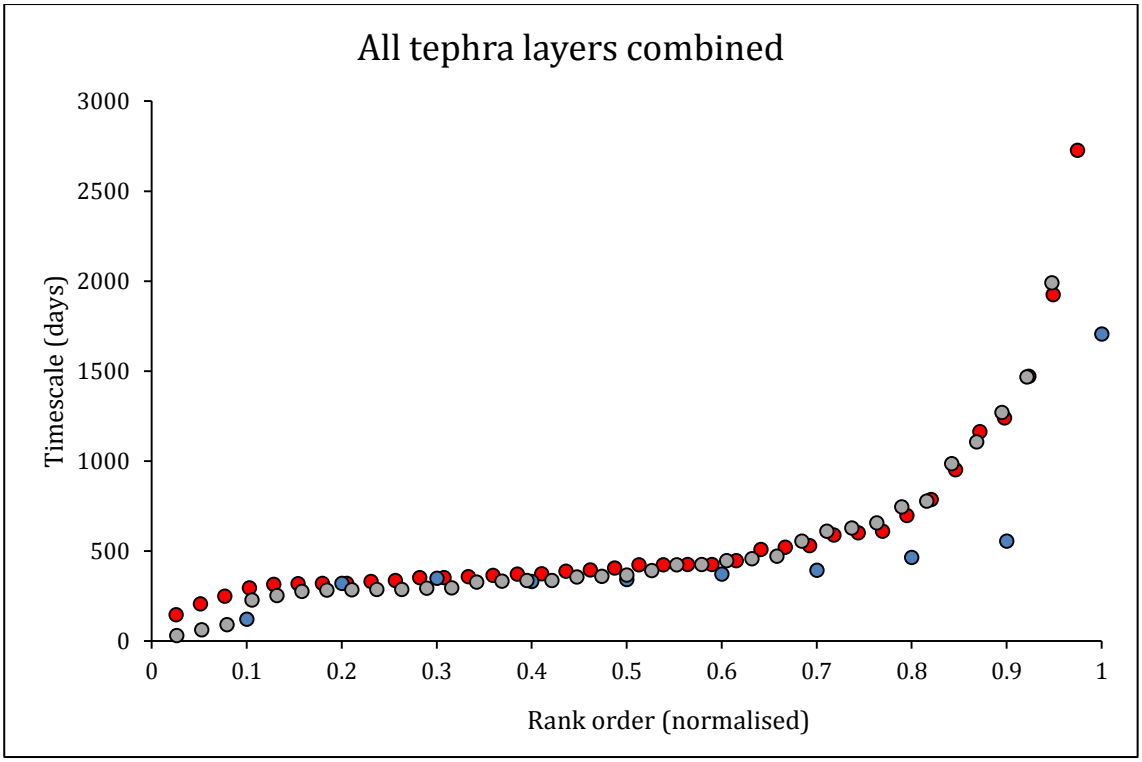

Figure 6.13: Rank order plot showing the timescale distributions from each of the tephra layers plotted together showing good overlap. The first to be erupted are from tephra layer S (red), timescales from tephra layers E and F are from the middle of the eruption (blue) and the last erupted timescales (grey) are from tephra layer A.

Figure 6.13 shows that there are no significant changes in the overall population of timescales being recovered from the start of the eruption to the end of the eruption. This implies that the same source is being tapped as the eruption evolved. This is also further evidence that there is no main dyke supplying the system with new magma. The few significantly younger timescales within the last eruptive layer may be indicative of a small amount of localised mixing or a small amount of recharge occurring near the end of the eruption. They may reflect a connection to depth being re-established towards the end of the eruption as pressure on the shallow system was released. This may have encouraged some magma to ascend from depth.

The timescales from layers E and F do not match well with the timescales from the start and end of the eruption. This may be due to the lack of statistics showing that this technique is only robust when a larger number of timescales are collated. The lack of coherency with the other layers may also be due to the mixed olivines from two different layers.

The indication from the rank order plots implies that there were no significant changes in the magma system between the start and the end of the eruption. This is consistent with the eruption occurring over only a few days. There are no erosional contacts between the tephra layers implying that a continuous ejection of material without a hiatus occurred before any rainfall. This would have enabled the reworking of the deposits. This interpretation is consistent with Larsen, (1984)'s estimate of the eruption occurring over 5 days.

This timescale data gives a lot of information regarding magma migration and storage and the timescales over which it occurred during the 870 AD eruption - the eruption produced the second largest amount of tephra in Iceland, ~5 km^3 (or ~1-2 km^3 DRE) over very short timescales. Knowledge of magma accumulation rates for such a large and explosive eruption is very important for hazard response planning.

There is no information in this dataset regarding what the eruption trigger was. Ultimately, evidence of the eruption trigger may have been retained in the melt inclusions or volatile saturations within the magma but a study of this kind is beyond the scope of this project.

Below is a schematic summary of the processes beneath the volcano pre-eruption as indicated by the diffusion timescales.

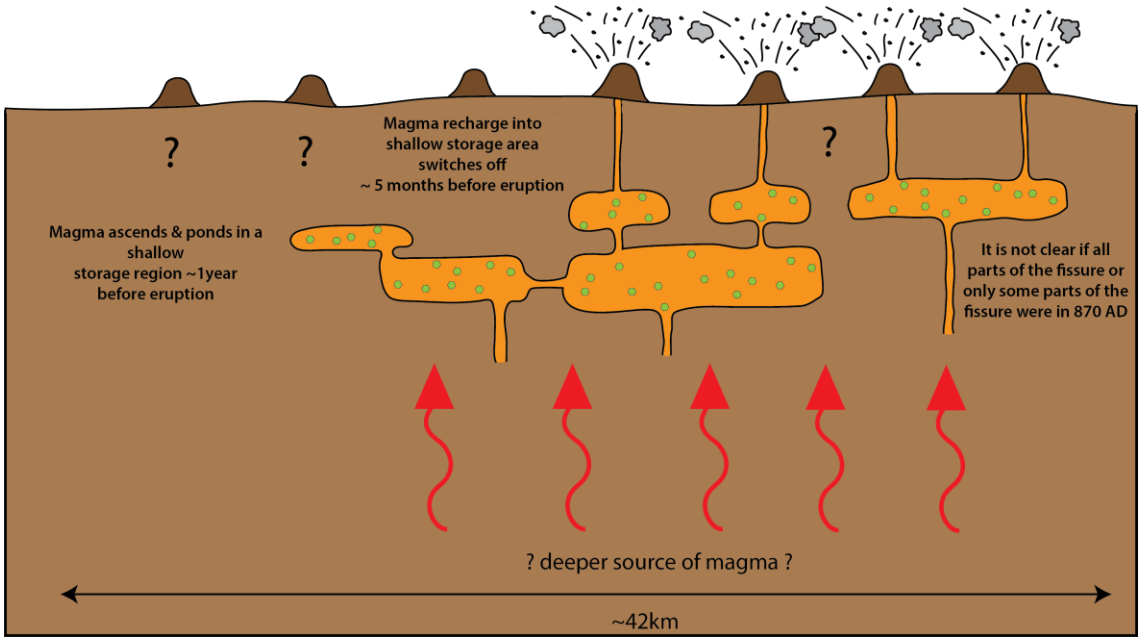

Figure 6.14: Schematic summary of the 870 AD eruption. NOT TO SCALE

6.6. Conclusions

The stress test successfully obtained diffusion timescale data and has demonstrated that the new streamlined methods produce a workflow at least 8 times faster than conventional methods. The largest dataset (39 timescales) took only 26 hours to process from drying the sample out to initial timescale interpretations which by comparison is over an order of magnitude faster than the current traditional methods used. Traditional methods would not have produced data before the end of the eruption if the estimation of eruption duration of 5 days by Larsen (1984) is correct. Even InSAR would have difficulty – it has a 3 day repeat time so there would have only been 2 InSAR frames.

The Vatnaöldur eruption of 870 AD provided deposits of a single olivine crystal population within tephra layers from the start of the eruption to the end of the eruption providing a complete time-series of data through the eruption. The streamlined methods successfully unpicked the timescales and the magmatic processes they represent to document how the eruption evolved in 'near-real' processing time. The data indicates the scope of magma build up and implies that the magma was pre-resident at eruption state, for at least 5 months before it erupted. This could have been correlated to pre-eruption InSAR.

This stress test has shown that diffusion modelling can successfully be implemented as an eruption monitoring tool. This has exciting implications for how eruption monitoring may be developed in the future with this magmatic perspective now recoverable on monitoring timescales. Full integration of this type of dataset with the geophysical methods would make for a more robust monitoring effort providing more information for the local authorities and communities affected by volcanic eruptions than ever before.

CHAPTER 7

Diffusion chronometry: potential and problems as a volcano eruption monitoring tool

7.1 Introduction

Diffusion modelling is a useful tool for retrieving magmatic timescales from zoned crystals, demonstrated throughout this thesis. Whether the methods are being implemented using traditional processing methods (chapters 3 and 4) or by using new streamlined methods (chapter 6), both can pull out usable information. However, it is important to consider the potential and limitations of the new technique (and diffusion modelling as a whole). In a monitoring scenario, it can be used to detect changes in the system which is useful for making evaluatory decisions. For example, during the Eyjafjallajökull eruption in 2010, the olivine diffusion timescales reset to zero halfway through the eruption (*Pankhurst et al., 2017*). This indicated a new dyke intrusion. The volcano was seismically quiet and so this diffusion data would have been very useful for decision making if the data were available in near-real time. However, it does have some problems as a monitoring tool; for example, it is not possible to apply the new methods to all types of volcanic eruptions. It is important to discuss the best implementation of the tool for monitoring in more general terms. Some issues are unresolvable, however others if optimised and carefully considered can still result in useful data being retrieved. These issues will be discussed in this chapter.

7.2. Suitable volcano targets and tephra availability

According to the Global Volcanism Program volcano database, there are 1,211 Holocene (11,000 years ago to present) volcanoes in the world. Of these, 976 are basaltic, andesitic, basaltic-andesite or trachy-basaltic in composition. These compositions all have the potential to be olivine-bearing. This is three quarters of all Holocene volcanoes that the new monitoring tool developed as part of this thesis could be applied to. It is, however, a question of where these volcanic centres are located and the threat that they pose in terms of their proximity to population

centres or human resources (such as water and power sources), and the hazard impact they could have on these. Ultimately this is what would dictate the need for this monitoring tool. Also, these types of compositions, more explicitly basaltic eruptions, are typically not as explosive and hazardous as silicic eruptions e.g. such as those that occurred at Mount St Helens in 1980 and Mount Pinatubo in 1991. More explosive eruptions close to population centres would warrant a greater use for this tool.

Rock type is obviously important because it has to be olivine-bearing to be able to implement the new streamlined diffusion methods – they are olivine specific. But material type is also important, both in terms of the time constraints for sample preparation of different materials as discussed in chapter 5, but also in terms of understanding what the olivines are telling us – are they recording shallow-near surface processes (chapter 4, Moinui lava flow), processes in the lava flow after emplacement at the surface (chapter 3, PdF lava flow) or processes in a deeper storage system (chapter 4, Hapaimamo tephra). Tephra was identified as the ideal material type in chapter 5 both in terms of rapid sample preparation times and the quenching of the material upon eruption, freezing the magmatic timescales of the sub-surface into the crystal. However, the availability and volume of tephra (specifically olivine-bearing tephra) from eruptions can vary on a case by case basis. It may be present in large volumes such as from the Vatnaöldur 870 AD eruption as discussed in chapter 6, or it may be present in small volumes or not at all e.g. Moinui ~17 AD, discussed in chapter 4.

Taking Hawaii and Iceland as two examples, in the past 10,000 years only 1 mappable tephra unit has been identified from Mauna Loa, 12km north of Kilauea (*Wolfe and Morris, 1996*). However, there has been a continuous series of spatter or scoria cones that have formed from lava fountains along fissures (*Wolfe and Morris, 1996*). By contrast Kilauea has produced three mappable tephra units as reported by Wolfe and Morris (1996) including local air-fall deposits of ash and lapilli in 1959 near Kilauea Iki crater and in 1960 near Kapoho Crater, lithic tuff with basaltic lava fragments from explosive eruptions at Puulena Crater in the east rift zone and relatively widespread air-fall and surge deposits that record violent explosions at the summit in 1790. However, this is a relatively small amount of tephra.

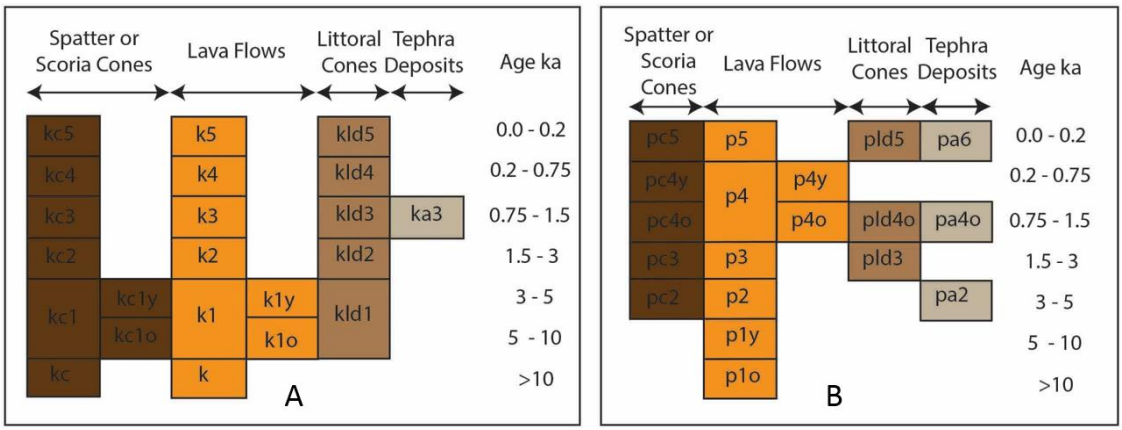

Figure 7.1: Mappable units by material type for A) Mauna Loa (Kau basalt) and B) Kilauea (Puna basalt), Hawaii. Adapted from Wolfe and Morris (1996).

In Iceland, tephra is much more widespread and common from eruptions. Over the last 1,100 years (a much shorter time frame than that reported for Hawaii), 25km^3 DRE of tephra has been produced, 19km^3 of which is basaltic (*Thordarson and Larsen, 2007*). There have been 205 eruptions, 3 of which produced a tephra volume larger than 1km^3 DRE (*Thordarson and Larsen, 2007*). One stratovolcano, Hekla, produced 2.2km^3 DRE of tephra between 1104 AD and 2000 AD from 28 events (*Thordarson and Larsen, 2007*). This is a significant fraction of the erupted volume (*Thordarson and Larsen, 2007*). For individual events, volumes of 0.004-0.6km^3 DRE were erupted shown in table 7.1.

Year of Eruption (AD)	Tephra (km^3)	Tephra DRE (km^3)	Lava (km^3)
2000	0.01	0.0004	0.17
1991	0.02	0.01	0.15
1980-1981	0.06	0.026	0.12
1970	0.07	0.03	0.2
1947-1948	0.18	0.08	0.8
1845	0.23	0.1	0.63
1766-1768	0.4	0.18	1.3
1693	0.3	0.13	0.9
1636	0.18	0.08	0.5
1597	0.29	0.13	0.9
1510	0.32	0.14	1.0
1389	0.15	0.07	0.5
1341	0.18	0.08	0.5
1300	0.5	0.22	1.5
1222	0.04	0.02	0.1
1206	0.4	0.18	1.2
1158	0.33	0.1	0.1
1104	2	0.61	
Total	5.6	2.2	10.8

Table 7.1: Historical eruptions from Hekla central volcano, Iceland. Data from Thordarson and Larsen (2006) and references therein.

Over roughly the same period (~900 AD – 1999), ~21 eruptions at Katla ejected ~6-7km^3 DRE of tephra (*Thordarson and Larsen, 2007*). Variable amounts are ejected per eruption, similar to what is seen at Hekla. At Katla, 10 eruptions produced a maximum of 0.1km^3 (likely less), 5 eruptions produced 0.1-5km^3 and 6 eruptions produced over 0.5km^3 (*Thordarson and Larsen, 2007*).

Looking at the two case studies of Hawaii and Iceland, the volume of tephra ejected over time is highly variable. And whilst there may be relatively large volumes of tephra being ejected from some volcanoes e.g. Katla, its' lavas contain rare phenocrysts of olivines (*Thordarson and Larsen, 2007*). This fluctuating availability of tephra at all, especially tephra that hosts olivine crystals decreases the viability of the new diffusion tool somewhat.

7.3. Lava flow

Whilst tephra has been identified as the ideal material type to work with for diffusion studies, lava flows are not redundant. It is, however important to interpret

the meaning of the timescales correctly. Olivine crystals from lava flows may have undergone a longer and potentially more complex set of processes than olivine crystals from tephra and the original diffusion signature could be overprinted or erased (*Costa et al., 2008*).

Diffusion timescales from olivines in lava flows can give information about lava flow cooling rates as seen in the PdF dataset in chapter 3, but they can also retain timescales regarding subsurface processes. This is very evident in the Moinui crystal population in chapter 4. Here, two crystal populations very texturally distinct from one another (euhedral/subhedral cumulates vs. bladed olivines) record very different processes. The cumulate olivines record deep magma transfer and storage information, which due to their very large size is retained and not overprinted, whereas the bladed olivines record shallower crystal storage and emplacement processes once the magma has been erupted. Lava flows have two end member types; pahoehoe and a'a. The Moinui (chapter 4) flow is a pahoehoe flow and therefore better insulated which may partially explain why there are much longer timescales in the cumulate Moinui olivines than the cumulate olivines in the a'a Hapaimamo flow (chapter 4). A'a will cool more quickly but will be more prone to oxidation evidenced by the lack of recoverable material in the clinker deposits.

Timescales were recovered from olivines within the top pahoehoe crust and centre lobe of the Moinui. This was possible due to these olivines being taken from a lobe at the very top of the flow. Olivines can be widely effected by oxidation in a pahoehoe flow particularly if they reside in the bottom crust. As a fresh lobe rolls over a previously laid down lobe that contains air, olivines can become oxidised (*Blondes et al., 2012*). Oxidised zones need to be carefully avoided.

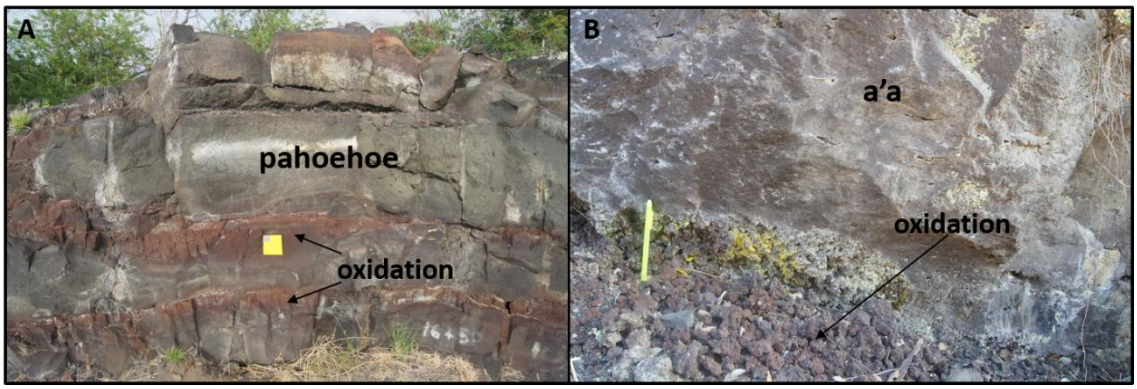

Figure 7.2: Extensive oxidation is present in parts of both the Hawaii lava flows A) the pahoehoe lava flow of the Moinui B) the a'a lava flow of the Hapaimamo.

The two types of olivines within the Moinui pahoehoe flow were easily distinguishable due to their different textures and it was much easier to decipher what processes each population had recorded. However, these textures were not distinctive of a pahoehoe type flow, but a function of magma transport processes. Rapid ascent to the surface and supersaturation enabled the rapid growth of the bladed olivines and quenched rim around the edge of the cumulates (*Donaldson, 1976; Walker et al., 1976; Bianco and Taylor, 1977*). The Hapaimamo lava flow olivines did not show any textural distinction between the two olivine populations but they did show longer timescales on a rank order plot when compared with the timescales from the tephra (chapter 4, figure 4.24). If no tephra has been produced from an eruption, for the lava flow olivines to be usable for interpreting subsurface processes, some thermal calculation or correction may need to be required. This is likely the case with most lava flow olivines, unless a manual quench in a bucket of water was possible during sampling.

Crystals from both types of lava flow have been interrogated using diffusion methods as part of this project. It has been found that neither are preferable for study. Both can be suitable for diffusion studies if the textures and timescale lengths are understood and oxidised parts of flows (an issue that affects both types of flow) are avoided. In the absence of any tephra deposit, the new diffusion tool can be implemented on lava flow samples more quickly to unpick subsurface processes recorded in the crystals, if the textural and chemical distinctions between populations are clear and olivine zoning does not appear to be overprinted or erased i.e. the crystals are very large. If any of this evidence is lacking, interpretation may take more time.

7.4. Availability of crystals and crystal boundaries

Material type is a strong control on the availability of crystals and how many crystal boundaries are exposed. As discussed in chapter 5, ejected material can be variable, from tephra to spatter to lava flow. But even the type of tephra can be variable. The Hapaimamo tephra is composed of reticulite which can be crushed by hand to maintain the integrity of the olivine crystals (chapter 4). When sliced, it is likely 2, 3, 4 or more crystal faces will be exposed. Reticulite is associated with explosive eruptions, hence its high vesicularity, yet very few if any crystals appeared to be

fragmented. This is in contrast to more fragmented tephras such as those ejected during a phreato-magmatic eruption. The explosivity of the eruption leaves few, if any, crystals intact and sometimes only 1 crystal face exposed when sectioned (chapter 6). Both of these material types associated with more violent eruptions, enable quicker crushing and/or picking of crystals but the integrity of the crystal in the latter case is compromised. More competent air-fall ejecta such as scoria or spatter requires mechanical crushing or careful cutting. Even when crystals are carefully cut from the matrix, a time consuming process, this doesn't guarantee the integrity of the crystal, as seen with 1887 samples. These have been omitted from this study for this reason.

There are problems associated with all material types and some lead to more fragmented crystals than others. In the case that there are only fragmented crystals to work with, the new methods perform well. Using the more traditional methods, two profiles from each crystal are preferable for consistency (due to the anisotropy) and there may not be two crystal faces to measure. The new diffusion methods deal with this better as only one timescale is needed from each crystal slice to fit to the shape of the rank order curve. This results in a lower confidence level in the timescales yet they are still appropriate for initial interpretation of magmatic processes in a monitoring scenario.

7.5. Controls on the Piton-type orientation correction

The new orientation correction has shown to give consistent results and can be used on any type of volcanic material as shown in chapter 5. Use of this correction compared to more traditional methods using EBSD is at least 8 times faster, as discussed in chapter 6. Both the Moinui lava flow and the Hapaimamo tephra texturally and/or chemically show at least two crystal populations are present (chapter 4). They have very similar distributions on the rank order plot, distinctive from the single, continuous PdF population (chapter 3) – they have longer tail sections and there is a distinct change in gradient between the more dominant population defined by a continuous shallow gradient in the rank order plot and the tail.

To demonstrate the robustness of the correction and to highlight the controlling factors, the timescales of the Moinui lava flow were separated into their two

populations based on their distinctive textures (equant and bladed) and core compositions. Each timescale distribution was plotted on a rank order plot shown in figure 7.3.

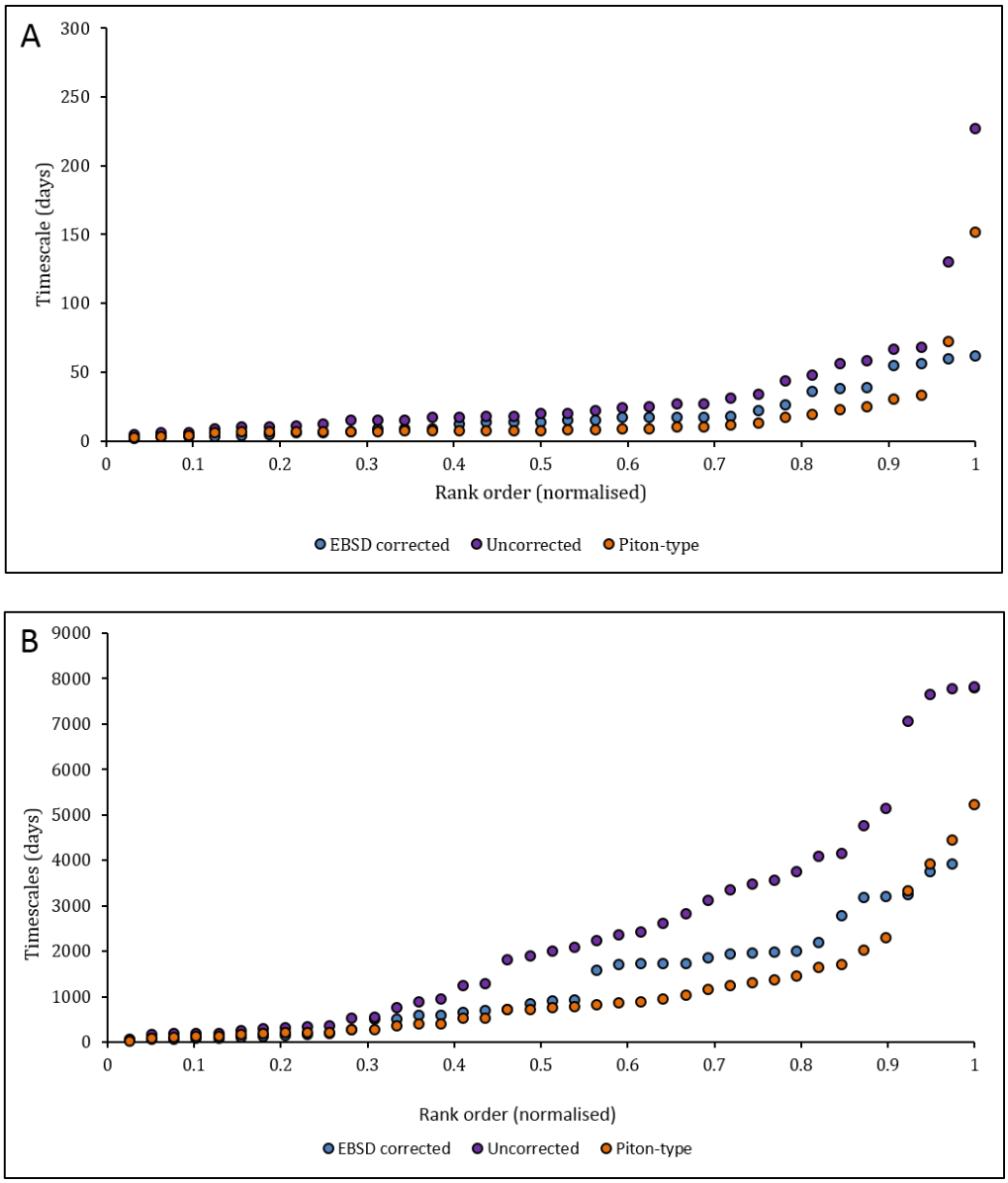

Figure 7.3: Rank order plots showing EBSD corrected (blue), uncorrected (purple) and pseudo-corrected (Piton-type) (orange) timescales from Moinui A) bladed olivines only B) cumulate olivines only. Timescales modelled with a single diffusivity (a-axis diffusivity).

Figure 7.3 shows that for neither the pseudo-corrected (Piton-type) bladed population nor the pseudo-corrected (Piton-type) equant population are a good fit to the EBSD corrected data for the whole extent of the curve. The shapes are accurate but the pseudo-corrected data is overcorrected in the tail section in both cases, although the very youngest timescales give a good fit. Although, these youngest timescales would be the most important in an eruption scenario (particularly of the

cumulate population). In the case of the bladed population, the overcorrection is due to the crystal faces that have been measured. A couple of rare profiles from (001) faces have been extracted and modelled from this population (the 2 anomalous points in the tail section of the uncorrected data). The PdF population (from which the correction was created) does not contain any c-faces as discussed in chapters 3 and 5, but it does contain (021) faces. All profiles measured from the bladed population are mostly a-faces, and so when the PdF-type correction is applied composed of a mixture of a-faces and (021) faces, the timescales are over corrected. This is likely a similar scenario for the cumulate population.

The shape of the crystal population is one of the main controls on the shape of the curve and so this needs to be carefully considered. Currently the orientation correction is only for one population of shapes. There needs to be adaptations to this to make the new diffusion tool more widely functionable. However, the initial part of the pseudo-corrected rank order distribution gives a tight fight across the board and this is the most important timescale information in the event of an eruption.

7.6. Counting statistics required

At the onset of a volcanic eruption, gathering data on the processes occurring beneath the volcano as efficiently as possible is paramount. Having some idea of how many profiles are needed to reveal the true timescales of a crystal population would be very valuable. Previous studies by Shea et al. (2015a) and Costa et al. (2008) have suggested ~20 timescales is optimum.

Synthetic datasets of a crystal population of varying size was created to decipher if the new methods required more or less timescales than suggested in previous studies as shown in figure 7.4A-C.

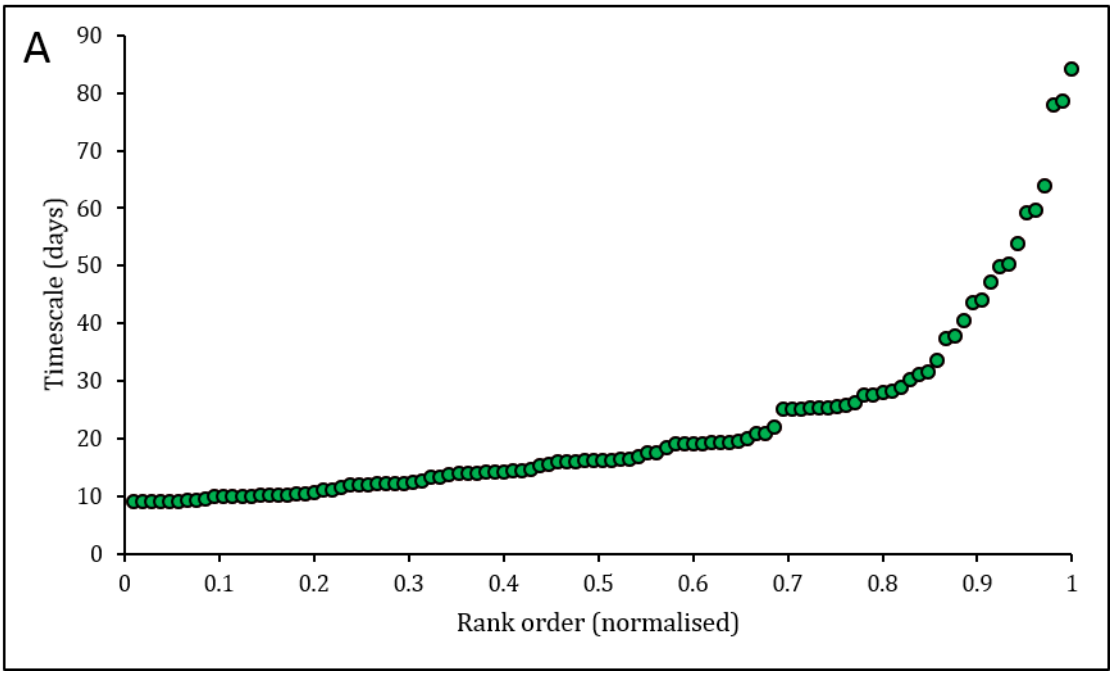

Figure 7.4.A: Rank order distribution of synthetic timescales of a single population (n = 105).

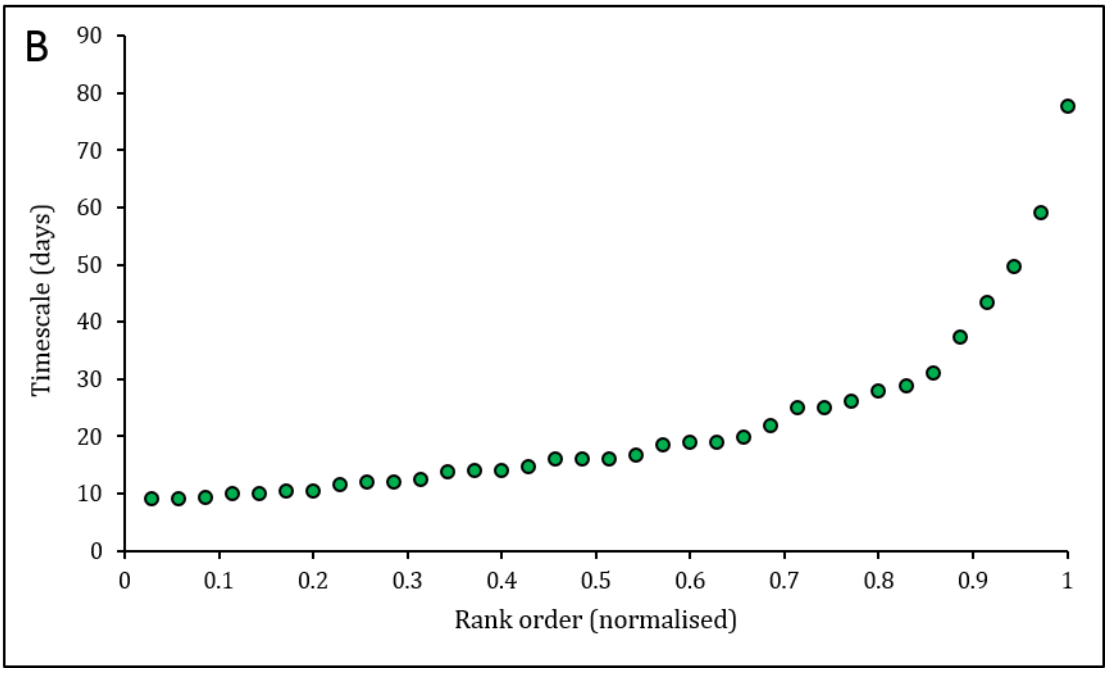

Figure 7.4.B: Rank order distribution of synthetic timescales of a single population (n = 30).

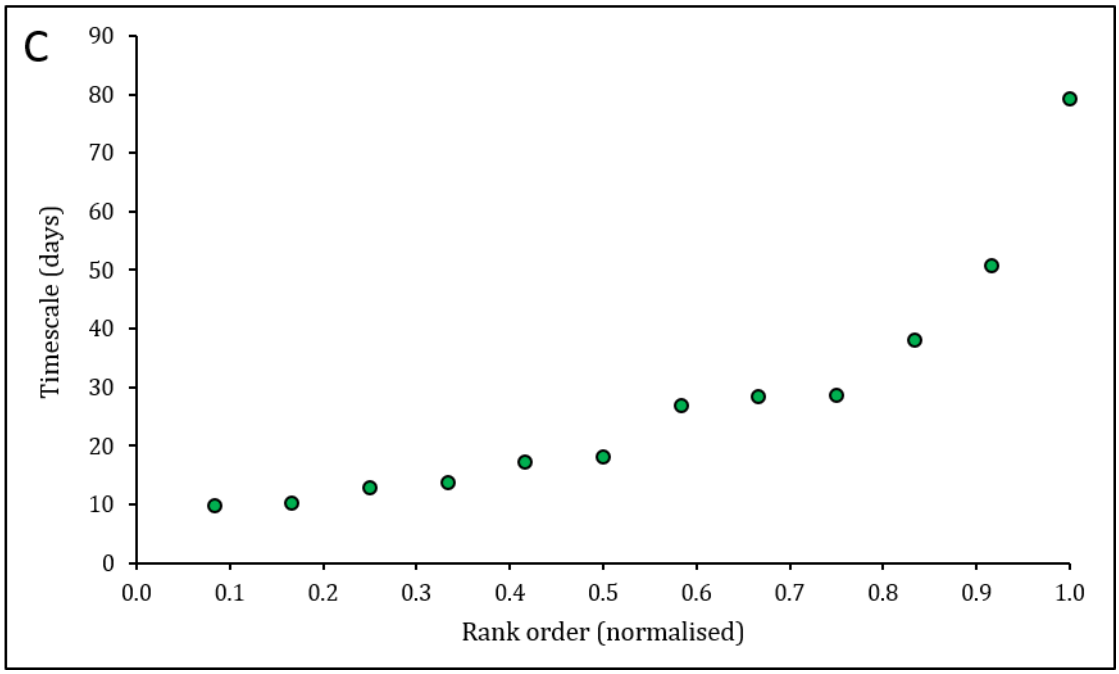

Figure 7.4.C: Rank order distribution of synthetic timescales of a single population (n = 12).

The shape of the rank order distribution for this type of orientation correction is critically important to correctly interpret the true timescales for monitoring purposes and the number of crystal populations present in the magma, to identify a cause for further study. There is a minimum number of data points required to accurately do this but there is also an ideal ratio of crystal faces present in the population that help define that shape (a-faces:c-faces:021 faces). To ensure that a range of faces are chosen, a larger number of crystal faces needs to be measured. Figure 7.4.C crudely shows that few timescales, in this case 12, leads to a lack of definition in the curve and therefore inaccurate timescale retrieval. Figure 7.4.A. shows a larger number of crystal faces, in this case 105, is overkill and the shape of the curve can be correctly defined with fewer data points. These synthetic datasets have been developed using a ratio of crystal faces of 90:0:10. Figure 7.4.B. shows that ~30 timescales are optimum in an eruption scenario to accurately define the true timescale and shape of the curve. This is in-line with the number of timescales identified in other studies (*Costa et al., 2008; Shea et al., 2015a*).

7.7. Further work and conclusions

The problems and potential associated with diffusion modelling methods for monitoring purposes has been discussed to identify how they might be improved and how effective they can be in an eruption scenario. The new methods have been rigorously tested (chapters 5 and 6) and considered (chapter 7) throughout the thesis and have shown they can be a useful additional tool for a monitoring team where a hazardous mafic eruption has occurred. However, considering the work across all previous chapters (including this one) it is clear that further work is needed to make this tool as robust as possible but also make it adaptable for various types of eruption.

First and foremost, although mafic eruptions containing olivine occur globally and can often have the potential to be hazardous to human life, it is the more explosive, silicic eruptions that monitoring teams and communities are often more concerned with. Therefore it would be useful to develop several tools that can incorporate a fast workflow for other minerals found in more silicic eruptions such as for feldspars, pyroxenes or oxides, when diffusion in these minerals is better experimentally constrained (*Cherniak and Dimanov, 2010; Cherniak, 2010; Van Orman and Crispin, 2010*). More quantitative corrections at a population level may be required for sectioning effects and crystal growth/changing boundary condition effects, incorporating different crystal growth rates, various changing boundary conditions and effects of different crystal sizes. Each volcanic system is unique and one type of correction may not fit all crystal populations.

Whilst the new orientation correction performs well for the sample sets discussed, there are improvements that can be made. Different orientation corrections could be developed for different crystal populations with different crystal shapes or proportions of crystal faces. Synthetics could be used to develop these. The XMT dataset could also be utilised to analyse how differing degrees of crystal euhedrality in 3D, crystal sizes and the nature of crystal agglomerates affect diffusion timescales. This would provide a better constraint on crystal shape uncertainties. Alternatively, a completely new method could be developed such as re-orientating a 2D section to 3D with the use of the XMT dataset. This could be used as standalone method or as a proof of concept of the single diffusivity orientation correction already developed and discussed in this thesis.

CHAPTER 8

Conclusions

8.1. Conclusions

The main aims of volcanology is to understand the subsurface magmatic processes beneath volcanoes and unravel the timescales over which these occur. They can occur over months or years before the onset of an eruption, or even days or hours. Having this type of information is critical to formulating effective hazard planning procedures and mitigating risk. Geophysical monitoring methods can detect and locate magma movement and storage via seismology and deformation of the edifice. But they cannot detect changes in ambient conditions such as pressure, temperature, melt composition, and volatile contents due to specific magma processes at depth, nor can they resolve the timescales over which this occurs. The crystal cargo can record these changes as it is transported through and stored within the plumbing system and the timescales can be retrieved using diffusion modelling. This wealth of information provides a deeper insight into the complex processes occurring in the build up to and during an eruption, but it is not currently available as part of monitoring techniques due to the complexity of the modelling.

This thesis has successfully presented new streamlined diffusion modelling methods that can be implemented on monitoring timescales. These new methods can be used to calculate and interpret magmatic timescales for processes such as magma mixing, magma mobilisation, and magma residence time in near-real time after the onset of an eruption, providing a new magmatic perspective to complement current monitoring techniques. Various cases studies have been analysed and evaluated and many modelling parameters and geometrical corrections have been considered to formulate the new streamlined methods.

1) The timescales for antecrystic olivines were modelled from a 2002 lava flow sample from Piton de la Fournaise. The timescales range from 7-45 days and when combined with textural findings are interpreted to be indicative of late-stage diffusion. The olivines were found to form a monodisperse single

crystal population evidenced by the narrow timescale range, consistent core compositions and CSD data. Rather than correcting to a single timescale, this population is composed of a narrow continuum of timescales, due to the diffusion clocks starting at different times within the natural system. This dataset formed the baseline dataset from which to compose the new methods, to then be tested on something more complex.

2) Field, petrological and textural studies of olivines within the Hapaimamo tephra and Moinui lava flow reveal complex transport and storage processes beneath Mauna Loa, Hawaii. These deposits have not previously been studied in great detail. Although both occurring from the SWRZ, each event (separated by over 1,000 years) resulted in different eruption products, due to differences within the magma transport and storage system. Both deposits have shown to be composed of at least two olivine populations. The Moinui lava flow is characterised by distinct olivine morphologies (equant vs. bladed) due to a combination of shallow and deeper processes. The Hapaimamo tephra is characterised by olivine with subtle chemical differences characteristic of their contrasting transport and storage mechanisms. Both of the Hapaimamo and Moinui deposits provided more complex case studies on which the new streamlined methodologies could be tested for robustness and adaptability.
3) With three suitable case studies identified, the current diffusion modelling methodologies were picked apart (including sample preparation, composition retrieval, and geometrical considerations) and each of the stages in the workflow was evaluated to produce streamlined methods. Where possible, corrections were applied at population level rather than to each individual traverse. It was found that due to unconscious bias when selecting appropriate crystal slices to analyse, traverses may not be significantly effected by shallow sectioning effects – a population of timescales may only be effected by ~2.5% shift in timescale. It was also found that changing boundary conditions whilst diffusion is ongoing can have a significant effect on timescales (by as much as 33-50% shift in timescale). These changing boundary condition effects should be considered when applying a temperature to diffusion models, as temperature is often applied as a single value.

4) A new method has been developed to apply an orientation correction at a population level rather than to each individual traverse. Using a single diffusivity, the dominant timescale and information on crystal populations present can be retrieved using rank order plots and polynomial fittings when correctly applied. This method is significantly faster than the current EBSD methodology.
5) From sample preparation to magmatic timescale interpretation, the new streamlined workflow was stress tested and completed within 26 hours. This is significantly faster than current methodologies (that can take at least 8 days), providing magmatic timescale information in near-real time. These methods are user-friendly and easy to deploy in a monitoring scenario. When applied to Vatnaöldur, they showed that magma accumulated ~ 1 year before eruption and the magma supply was switched off ~ 5 months before eruption. Whilst this does not reveal any insight in to the eruption trigger, knowing whether the shallow storage is connected to its source during an eruption is invaluable information for the local authorities and would otherwise not be available on a monitoring timescale without this new methodology.

New processing methodologies for implementation on a monitoring timescale have successfully been formulated using various case studies and analysis and evaluation of existing techniques. These will provide more detailed information for correlation with existing geophysical monitoring methods and the timescales produced can be incorporated into hazard planning and risk mitigation by local authorities in the event of an eruption.

List of References

AKI, K. & FERRAZZINI, V. 2000. Seismic monitoring and modelling of an active volcano for prediction. Journal of Geophysical Research, 105, 16617-16640

ALBAREDE, F., LUIS, B., FITTON, G., SEMET, M., KAMINSKI, E., UPTON, B., BACHELERY, P. & CHEMINEE, J. 1997. The geochemical regimes of Piton de la Fournaise volcano (Reunion) during the last 530,000 years. Journal of Petrology, 38, 171-201

ALLAN, A., MORGAN, D., WILSON, C. & MILLET, M.-A. 2013. From mush to eruption in centuries: assembly of the super-sized Oranui magma body. Contributions to Mineralogy and Petrology, 166, 143-164

ARGANDA-CARRERAS, I., KAYNIG, V., RUEDEN, C., ELICEIRI, K. W., SCHINDELIN, J., CARDONA, A. & SEUNG, H. S. 2017. Trainable weka segmentation: a machine learning tool for microscopy pixel classification. Bioinformatics, Oxford University Press

AUBELE, J., CRUMPLER, L. & ELSTON, W. 1988. Vesicle zonation and vertical structure of basalt flows. Journal of Volcanology and Geothermal Research, 35, 349-374

BACHMANN, O. & BERGANTZ, G. 2008. The magma reservoirs that feed super-eruptions. Elements, 4, 17-21

BAGNARDI, M., POLAND, M. P., CARBONE, D., BAKER, S., BATTAGLIA, M. & AMELUNG, F. 2014. Gravity changes and deformation at Kilauea volcano, Hawaii, associated with summit eruptive activity, 2009-2012, Journal of Geophysical Research: Solid Earth, 119, 7288-7305

BARNARD, W. 1995. Mauna Loa Volcano: Historical Eruptions, Exploration, and Observations (1779-1910). Mauna Loa Revealed: Structure, Composition, History and Hazards, Geophysical Monograph 1992

BEATTIE, P. 1993. Olivine-melt and orthopyroxene-melt equilibria. Contributions to Mineralogy and Petrology, 115, 103-111

BERGANTZ, G., SCHLEICHER, J. & BURGISSER, A. 2015. Open-system dynamics and mixing in magma mushes. Nature Geoscience, 8, 792-796

BEST, M. G. 2002. Igneous and metamorphic petrology. Second Edition, Blackwell Publishing.

BIANCO A. & TAYLOR, L. 1976. Applications of dynamic crystallisation studies: lunar olivine normative basalts. Proceddings of the 8th Lunar Scientific Conference 1593-1610

BLONDES, M. S., BRANDON, M. T., REINERS, P. W., ZEB PAGE, F. and KITA, N. K. 2012. Generation of forsteritic olivine ($Fo_{99.8}$) by subsolidus oxidation in basaltic flows. Journal of Petrology, 53, 971-984

BLUNDY, J., CASHMAN, K. & HUMPHREYS, M. 2006. Magma heating by decompression –driven crystallisation beneath andesitic volcanoes. Nature, 443, 76-80

BOIVIN, P. & BACHELERY, P. 2009. Petrology of 1977 to 1998 eruptions of Piton de La Fournaise, La Reunion Island. Journal of Volcanology and Geothermal Research, 184, 109-125

BOYD, F.R. & MERTZMAN, S.A. 1987. Composition and structure of the Kaapvaal lithosphere, southern Africa. In: Mysen, B.O. (Ed.), Magmatic Processes – Physiochemical Principles. In: Geochemical Society Special Publications, 1, 13-24.

BRADY, J. & CHERNIAK, D. 2010. Diffusion in minerals: an overview of published experimental diffusion data. Reviews in Mineralogy and Geochemistry, 72, 899-920

BRANSDOTTIR, B. & EINARSSON, P. 1979. Seismic activity associated with the September 1977 deflation of the Krafla central volcano in north eastern Iceland. Journal of Volcanology and Geothermal Research, 6, 197-212

BREIMAN, L. 2001.Random forests. Machine Learning, 45, 5-32

BRYAN, C. J. & SHERBURN, S. 1999. Seismicity associated with the 1995-1996 eruptions of Ruapehu volcano, New Zealand: narrative and insights into physical processes. Journal of Volcanology and Geothermal Research, 90, 1-18

BUENING, D. & BUSECK, P. 1973. Fe-Mg lattice diffusion in olivine. Journal of Geophysical Research, 78, 6852-6862

BUREAU, H., PINEAU, F., METRICH, N., SEMET, M. & JAVOY, M. 1998. A melt and fluid inclusion study of the gas phase at Piton de la Fournaise Volcano (Reunion Island). Chemical Geology, 147, 115-130

BURGISSER, A. & BERGANTZ, G. 2011. A rapid mechanism to remobilise and homogenise highly crystalline magma bodies. Nature, 471, 212-215

CARSLAW, H. & JAEGER, C. 1959. Conduction of heat in solids (2nd edition): Oxford, UK, Clarendon Press

CASHMAN, K. 1993. Relationship between plagioclase crystallization and cooling rate in basaltic melts. Contributions to Mineralogy and Petrology, 113, 126-142

CASHMAN, K. & MARSH, B. 1988. Crystal size distribution (CSD) in rocks and the kinetics and dynamics of crystallization II: Makaopuhi lava lake. Contributions to Mineralogy and Petrology, 99, 292-305

CASHMAN, K., THORNBER, C. & KAUAHIKAUA, J. 1999. Cooling and crystallisation of lava in open channels, and the transition of Pahoehoe lava to A'a. Bulletin of Volcanology, 61, 306-323

CHAKRABORTY, S. & GANGULY, J. 1990. Compositional zoning and cation diffusion in garnets. In Diffusion, Atomic Ordering, and Mass Transport: Selected Topics in Geochemistry, edited by J. Ganguly, 120. New York: Springer-Verlag

CHAKRABORTY, S. & GANGULY, J. 1991. Compositional zoning and cation diffusion in garnets. Advances In Physical Geochemistry, 8, 120-175

CHAKRABORTY, S., FARVER, J., YUND, R. & RUBIE, D. 1994. Mg tracer diffusion in synthetic fosterite and san carlos olivine as a function of P, T and fO_2. Physics and Chemistry of Minerals, 21, 489-500

CHAKRABORTY, S. 1997. Rates and mechanisms of Mg-Fe inter-diffusion in olivine at 980-1300°C. Journal of Geophysical Research, 102, 12317-12331

CHAKRABORTY, S. 2008. Diffusion in solid silicates: a tool to track timescales of processes comes of age. Annual Review of Earth and Planetary Sciences, 36, 153-190

CHAKRABORTY, S. 2010. Diffusion coefficients in olivine, wadsleyite and ringwoodite. Reviews in Mineralogy and Geochemistry, 72, 603-635

CHARLIER, B. L. A., MORGAN, D., WILSON, C. J. N., WOODEN, J. L., ALLAN, A. S. R. & BAKER, J. A. 2012. Lithium concentration gradients in feldspar and quartz record the final minutes of magma ascent in an explosive supereruption. Earth and Planetary Science Letters, 319-320, 218-227

CHEN, C-Y. 1993. High-magnesium primary magmas from Haleakala volcano, east Maui, Hawaii: petrography, nickel, and major-element constraints. Journal of Volcanology and Geothermal Research, 55, 143-153

CHERNIAK, D.J. 2003. REE diffusion in feldspar, Chemical Geology, 193, 25-41

CHERNIAK, D.J. 2010. Cation diffusion in feldspars. Reviews in Mineralogy and Geochemistry, 72, 691-723

CHERNIAK, D. J. and DIMANOV, A. 2010. Diffusion in pyroxene, mica and amphibole. Reviews in Mineralogy and Geochemistry, 72, 641-685

CHERNIAK, D.J., HERVIG, R., KOEPKE, J., ZHANG, Y. & ZHAO, D. 2010. Analytical methods in diffusion studies. Reviews in Mineralogy & Geochemistry. 72, 107-170

CHRISTOPHER, T., EDMONDS, M., TAISNE, B., ODBERT, H., COSTA, A., HARDS, V. & WADGE, G. 2015. Periodic sulphur dioxide degassing from the Soufriére Hills Volcano related to deep magma supply. The Role of Volatiles in the Genesis, Evolution and Eruption of Arc Magmas, Geological Society, London, Special Publications, 410, 123-141

CLAGUE, D. & DENLIGUER, R. 1994. Role of olivine cumulates in destabilizing the flanks of Hawaiian volcanoes. Bulletin of Volcanology, 54, 425-434

COOGAN, L., HAIN, A., STAHL, S. & CHAKRABORTY, S. 2005. Experimental determination of the diffusion coefficient for calcium in olivine between 900°C and 1500°C. Geochimica et Cosmochimica Acta, 69, 3683-3694

COOGAN, L., JENKIN, G. & WILSON, R. 2007. Contrasting cooling rates in the lower oceanic crust at fast- and slow-spreading ridges revealed by geospeedometry. Journal of Petrology, 1-22

COOMBS, M. & GARDNER, J. 2004. Reaction rim growth on olivine in silicic melts: Implications for magma mixing. American Mineralogist, 89, 748-759

COSTA, F. & CHAKRABORTY, S. 2004. Decadal time gaps between mafic intrusion and silicic eruption obtained from chemical zoning patterns in olivine. Earth and Planetary Science Letters, 227, 517-530

COSTA, F., CHAKRABORTY, S. & DOHMEN, R. 2003. Diffusion coupling between trace and major elements and a model for calculation of magma residence times using plagioclase. Geochimica et Cosmochimica Acta, 67, 2189-2200

COSTA, F. & DUNGAN, M. 2005. Short time scales of magmatic assimilation from diffusion modelling of multiple elements in olivine. Geology, 33, 837-840

COSTA, F., DOHMEN, R. & CHAKRABORTY, S. 2008. Time scales of magmatic processes from modelling the zoning patterns of crystals. Reviews in Mineralogy and Geochemistry, 69, 545-594

COSTA F. & MORGAN, D. 2010. Time constraints from chemical equilibration in magmatic crystals. Timescales of magmatic processes: From Core to Atmosphere, Blackwell Publishing

CNUDDE, V. & BOONE, M. N. 2013. High-resolution X-ray computed tomography in geosciences: a review of the current technology and applications. Earth Science Reviews

CRANK, J. 1975. The mathematics of diffusion. Oxford Science Publications

DEER, W., HOWIE, R. & ZUSSMAN, J. 1997. Rock forming minerals: Orthosilicates, Volume 1A. The Geological Society

DODSON, M. H. 1986. Closure profiles in cooling systems. Material Science Forum, 7, 145-154

DOHMEN, R., & CHAKRABORTY, S. 2007a. Fe-Mg diffusion in olivine I: experimental determination between 700 and 1200°C as a function of composition, crystal orientation and oxygen fugacity. Physical Chemistry of Minerals, 34, 389-407

DOHMEN, R., & CHAKRABORTY, S. 2007b. Fe-Mg diffusion in olivine II: point defect chemistry, change of diffusion mechanisms and a model for calculation of diffusion coefficients in natural olivine. Physical Chemistry of Minerals, 34, 409-430

DONALDSON, C. H. 1975. Calculated diffusion coefficients and the growth rate of olivine in a basalt magma. Lithos, 205

DONALDSON, C. H. 1976. An experimental investigation of olivine morphology. Contributions to Mineralogy and Petrology, 57, 187-213

DONALDSON, C. H. 1985. The rates of dissolution of olivine, plagioclase and quartz in a basalt melt. Mineralogical magazine, 49, 683-693

DZURISIN, D., LOCKWOOD, J. P., CASADEVALL, T. J. & RUBIN, M. 1995. The Uwekahuna Ash Member of the Puna Basalt: product of violent phreatomagmatic eruptions at Kilauea volcano, Hawaii, between 2800 and 2100 ^{14}C years ago. Journal of Volcanology and Geothermal Research, 66, 163-184

DZURISIN, D. 2003. A comprehensive approach to monitoring volcano deformation as a window on the eruption cycle. Reviews of Geophysics, 41,

ERDMANN, S., SCAILLET, B. & KELLET, D. 2012. Textures of peritectic crystals as guides to reactive minerals in magmatic systems: New insights from melting experiments. Journal of Petrology, 53 (11), 2231-2258

EINARSSON, P. & BRANSDOTTIR, B. 1980. Seismological evidence for lateral magma intrusion during the July 1978 deflation of the Krafla volcano in NE-Iceland. Journal of Geophysics, 47, 160-165

EVANS, B. & TROMMSDORFF, V. 1974. On elongate olivine of metamorphic origin. Geology, 2, 131-132

FAAK, K., CHAKRABORTY, S. & COOGAN, L. 2013. Mg in plagioclase: Experimental calibration of a new geothermometer and diffusion coefficients. Geochimica et al Cosmochimica Acta 123, 195-217

FAMIN, V., WELSCH, B., OKUMURA, S., BACHELERY, P. & NAKASHIMA, S. 2009. Three differentiation stages of a single magma at Piton de la Fournaise (Reunion hotspot). Geochemistry Geophysics Geosystems, 10

FAURE, F., TROLLIARD, G., NICOLLET, C. & MONTEL, J-M. 2003. A developmental model of olivine morphology as a function of the cooling rate and the degree of undercooling. Contributions to Mineralogy and Petrology, 145, 251-263

FAURE, F. & SCHIANO, P. 2005. Experimental investigation of equilibration conditions during forsterite growth and melt inclusion formation. Earth and Planetary Science Letters, 236, 882-898

FAURE, F., SCHIANO, P., TROLLIARD, G., NICOLLET, C. & SOULESTIN, B. 2007. Textural evolution of polyhedral olivine experiencing rapid cooling rates. Contributions to Mineralogy and Petrology, 153, 405-416

FAURE, F. & TISSANDIER, L. 2014. Contrasted liquid lines of descent revealed by olivine-hosted melt inclusions and the external magma. Journal of Petrology, 55, 1779-1798

FINK, J. 1998. Morphology, eruption rates and rheology of lava domes: insights from laboratory models. Journal of Geophysical Research, 103, 527-545

FISHER, R. 1979. Models for pyroclastic surges and pyroclastic flows. Journal of Volcanology and Geothermal Research, 6, 305-318

FLYNN C.P. 1972. Point Defects and Diffusion. Clarendon Press, Oxford

FRIEDMAN, I. & LONG, W. 1984. Volcanic glasses, their origins and alteration processes. Journal of Non-Crystalline Solids, 67, 127-133

FUDALI, R. F. 1965. Oxygen fugacities of basaltic and andesitic magmas. Geochimica et Cosochimica, 29, 1063-1075

GAETANI, G. & WATSON, E. 2002. Modelling the major element evolution of olivine-hosted melt inclusions. Chemical Geology 183, 25-41

GAFFNEY, A. 2002. Environments of crystallisation and compositional diversity of Mauna Loa xenoliths. Journal of Petrology, 43, 963-981

GARCIA, M., HULSEBOCH, T. & RHODES, J. 1995. Olivine-rich submarine basalts from the southwest rift zone of Mauna Loa Volcano: implications for magmatic processes and geochemical evolution. In: Rhodes, J., and Lockwood, J., (eds) Mauna Loa Revealed: Structure, Composition, History and Hazards, American Geophysical Union, 219-239

GARCIA, M. & RHODES, M. 2012. South West Mauna Loa, AGU Chapman Conference Fieldtrip Field Guide

GARRETT, I. & MAHONEY, J. 2005. Flow and melting of a heterogeneous mantle: 1. Method and importance to the geochemistry of ocean island and mid-ocean ridge basalts. Earth and Planetary Science Letters, 230, 29-46

GERLACH, D. & GROVE, T. 1982. Petrology of medicine lake high volcanics: characterisation of end members. Contributions of Mineralogy and Petrology, 80, 147-59

GHIORSO, M. S. & SACK, R. 1991. Fe-Ti oxide geothermometry: thermodynamic formulation and the estimation of intensive variables in silicic magmas. Contributions to Mineralogy and Petrology, 108, 485-510

GIGGENBACH, W. F. 1996. Chemical composition of volcanic gases. Monitoring and Mitigation of Volcano Hazards, 221-256

GIRONA, T. & COSTA, F. 2013. DIPRA: A user-friendly program to model multi-element diffusion in olivine with applications to timescales of magmatic processes. Geochemistry, Geophysics and Geosystems, 14, 422-431

GONZÁLEZ, P. J., BAGNARDI, M., HOOPER, A. J., Larsen, Y., Marinkovic, P., Samsonov, S. & Wright, T. J. 2015. The 2014-2015 eruption of Fogo volcano: geodetic modelling of Sentinel-1 TOPS interferometry. Geophysical Research Letters, 42, 9239-9246

GRIFFITHS, R. W. 2000. The dynamics of lava flows. Annual Review of Fluid Mechanics, 32, 477-518.

GUDMUNDSSON, J. 1990. Emplacement of dikes, sills and crustal magma chambers at divergent plate boundaries. Tectonophysics, 176, 257-275

GUDMUNDSSON, M., SIGMUNDSSON, F. & BJORNSSON, H. 1997. Ice-volcano interaction of the 1996 Gjalp subglacial eruption, Vatnajökull, Iceland. Nature, 389, 954-957

GUDMUNDSSON, A. 2000. Dynamics of volcanic systems in Iceland: Example of tectonism and volcanism at juxtaposed hot spot and mid-ocean ridge systems. Annual Review of Earth and Planetary Science, 28, 107-40

GUILBAUD, M., BLAKE, S., THORDARSON, T. & SELF, S. 2007. Role of syn-eruptive cooling and degassing on textures of lavas from the AD 1783-1784 Laki eruption, south Iceland. Journal of Petrology, 48, 1265-1294

HAMMER, J. & RUTHERFORD, M. 2002. An experimental study of the kinetics of decompression-induced crystallisation in silicic melt. Journal of Geophysical Research, 107

HARTLEY, M., MORGAN, D., MACLENNAN, J., EDMONDS, M. & THORDARSON, T. 2016. Tracking timescales of short-term precursors to large basaltic fissure eruptions through Fe-Mg diffusion in olivine. Earth and Planetary Science Letters, 439, 58-70

HARVEY, J., YOSHIKAWA, M., HAMMOND S. & BURTON, K. 2012. Deciphering the trace element characteristics in Kilbourne hole peridotite xenoliths: Melt-rock interaction and metasomatism beneath the Rio Grande Rift, SW USA. Journal of Petrology, 53, 1709-1742.

HASTIE, T., TIBSHIRANI, R. & FRIEDMAN, J. 2008. The elements of statistical learning. Springer Series in Statistics

HEIKEN, G. 1972. Morphology and petrography of volcanic ashes. Geological Society of America Bulletin, 83, 1961-1988

HELZ, R. T. & THORNBER, C. 1987. Geothermometry of Kilauea Iki lava lake, Hawaii. Bulletin of Volcanology, 49, 651-668

HELZ, R. T., HELIKER, C. C., MANGAN, M. T., HON, K., NEAL, C. A. & SIMMONS, L. 1991. Thermal history of current Kilauean Eas Rift eruption. Eos, 72, 557-558

HERZBERG, C. & O'HARA, M. J. 1998. Phase equilibrium constraints on the origin of basalts, picrites and komatiites. Earth Science Reviews, 44, 39-79

HERZBERG, C., ASIMOW, P., IONOV, D., VIDITO, C., JACKSON, M. & GEIST, D. 2013. Nickel and helium evidence for melt above the core-mantle boundary. Nature, 493, 393-397

HIGGINS, M. 1994. Determination of crystal morphology and size from bulk measurements on thin sections: numerical modelling. American Mineralogist, 79, 113-119

HIGGINS, M. 2000. Measurement of crystal size distributions. American Mineralogist. 85, 1105-1116

HILDRETH, W. & WILSON, C. 2007. Compositional zoning of the Bishop Tuff. Journal of Petrology, 48, 951-999

HON, K., KAUAHIKAUA, J., DENLINGER, R. & MACKAY, K. 1994. Emplacement and inflation of pahoehoe sheet flows: Observations and measurements of active lava flows on Kilauea Volcano, Hawaii. Geological Society of America Bulletin, 106, 351-370

HORT, M. 1998. Abrupt change in magma liquidus temperature because of volatile loss or magma mixing: effects on nucleation, crystal growth and thermal history of the magma. Journal of Petrology, 39, 1063-1076

HOZAPFEL, C., CHAKRABORTY, S., RUBIE, D. & FROST, D. 2007. Effect of pressure on Fe-Mg, Ni and Mn diffusion in $(Fe_xMg_{1-x})_2SiO_4$ olivine. Physics of the Earth and Planetary Interiors, 162, 186

HUEBNER, J. & SATO, M. 1970. Oxygen-fugacity temperature relationships of manganese oxide and nickel oxide buffers. American Mineralogist, 55, 934-952

HUMLER, E. & WHITECHURCH, H. 1988. Petrology of basalts from the Central Indian Ridge (lat. 25°23'S, long. 70°04'E): estimates of frequencies and fractional volumes of magma injections in a two-layered reservoir. Earth and Planetary Science Letters, 88, 161-181

HUMPHREYS, M., BLUNDY, J. & SPARKS, R. S. J. 2008. Shallow-level decompression crystallisation and deep magma supply at Shiveluch Volcano. Contributions to Mineralogy and Petrology, 155, 45-61

ILYINSKAYA, E., AIUPPA, A., BERGSSON, B., DI NAPOLI, R., FRIDRIKSSON, T., ÓLADÓTTIR, A. A., ÓSKARSSON, F., GRASSA, F., PFEFFER, M., LECHNER, K., YEO, R. & GIUDICE, G. 2015. Degassing regime of Hekla volcano 2012-2013. Geochimica et Cosmochimica Acta, 159, 80-99

INGHAM, M. R., BIBBY, H. M., HEISE, W., JONES, K. A., CAIRNS, P., DRAVITZKI, S., BENNIE, S. L., CALDWELL, T. G. AND OGAWA, Y. 2009. A magnetolluric study of Mount Ruapehu volcano, New Zealand. Geophysical Journal International, 179, 887-904

JAROSWECH, E. 2002. Smithsonian Microbeam Standards. Journal of Research of the National Institute of Standards and Technology, 107, 681-685

JONSDOTTIR, T., LARSEN, G. & GUDMUNDSSON, M. 2014. Grain size distribution and characteristics of the tephra from the Vatnaöldur AD 871 +/- 2 eruption, Iceland. Geophysical Research Abstracts, EGU General Assembly 2014

KAHL, M., CHAKRABORTY, S., COSTA, F. & POMPILIO, M. 2011. Dynamic plumbing system beneath volcanoes revealed by kinetic modelling, and the connection to monitoring data: An example from Mt. Etna. Earth and Planetary Science Letters, 308, 11-22

KAHL, M., CHAKRABORTY, S., COSTA, F., POMPILIO, M., LIUZZO, M. & VICCARO, M. 2013. Compositionally zoned crystals and real-time degassing data reveal changes in magma transfer dynamics during the 2006 summit eruptive episodes of Mt. Etna. Bulletin of Volcanology, 75

KAHL, M., CHAKRABORTY, S., POMPILIO, M. & COSTA, F. 2015. Constraints on the nature and evolution of the magma plumbing system of Mt. Etna volcano (1991-2008) from a combined thermodynamic and kinetic modelling of the compositional record of minerals. Journal of Petrology, 56, 2025-2068

KILE, D. E. 2009. The universal stage: the past, present and future of a mineralogical research instrument, Geochemical News, 140, Geochemical Society

KOHN, S. C., HENDERSON, C. M. B. & Mason, R. A. 1989. Element zoning trends in olivine phenocrysts from a supposed primary high-magnesian andesite: an electron- and ion-microprobe study. Contributions to Mineralogy and Petrology, 103, 242-252

KRESS, V. & GHIORSO, M. 2004. Thermodynamic modelling of post-entrapment crystallisation in igneous phases. Journal of Volcanology and Geothermal Research, 137, 247-260

LACROIX. A. 1923. Océanites. Minéralogie de Madagascar, III, 49-50

LARSEN, G. 1984. Recent volcanic history of the Veidivötn fissure swarm, Southern Iceland – an approach to volcanic risk assessment. Journal of Volcanology and Geothermal Research, 22, 33-58

LARSEN, G. & EIRIKSSON, J. 2008. Late quaternary terrestrial tephrochronology of Iceland – frequency of explosive eruptions, type and volume of tephra deposits. Journal of Quaternary Science, 23, 109-120

LASAGA, A. 1983. Geospeedometry: An extension of Geothermometry. In Kinetics and Equilibrium in Mineral Reactions, Edited by Saxena, S.

LASAGA, A. 1998. Kinetic Theory in the Earth Sciences. Princeton series in Geochemistry

LEE, C-T., LUFFI, P., PLANK, T., DALTON, H. & LEEMAN, W. 2009. Constraints on the depths and temperatures of basaltic magma generation on Earth and other terrestrial planets using new thermobarometers for mafic magmas. Earth and Planetary Science Letters, 279, 20-33

LENAT, J., BACHELERY, P. & MERLE, O. 2012. Anatomy of Piton de la Fournaise volcano (La Reunion, Indian Ocean). Bulletin of Volcanology, 74, 1945-1961

LIPMAN, P., BANKS, N. & RHODES, J. 1985. Degassing-induced crystallisation of basaltic magma and effects on lava rheology. Nature, 317, 604-607

LLOYD, G. E. 1987. Atomic number and crystallographic contrast images with the SEM: a review of backscattered electron techniques. Mineralogical Magazine, 51,3-19

LOCKWOOD, J. 1995. Mauna Loa eruptive history – The preliminary radio carbon record. Mauna Loa revealed: Structure, Composition, History, and Hazards, Geophysical Monograph 92

LOCKWOOD, J. & LIPMAN, P. 1985. Holocene eruptive history of Mauna Loa Volcano. Chapter 18, Volcanism in Hawaii, US Geological Survey Professional Paper 1350

LOFGREN, G., DONALDSON, C., WILLIAMS, R., MULLINS, O. & USSELMAN, T. 1974. Experimentally reproduced textures and mineral chemistry of Apollo 15 quartz normative basalts. Proceedings of the 5th Lunar Science Conference, Geochimica et Coschimica Acta Supplement, 1, 549-567

LOFGREN, G. 1980. Experimental studies on the dynamic crystallisation of silicate melts. Physics of Magmatic Processes, Princeton University Press

LONGPRE, M-A., STAUDACHER, T. & STIX, J. 2007. The November 2002 eruption at Piton de la Fournaise volcano, La Réunion Island: ground deformation, seismicity, and pit crater collapse. Bulletin of Volcanology, 69, 511-525

MAALOE, S. 1985. Principles of Igneous Petrology. Springer.

MACDONALD G. A. 1972. Volcanoes. Prentice Hall Inc. Englewood Cliffs, New Jersey, p. 501

MACQUEEN, J. 1967. Some methods for classification and analysis of multivariate observations. Proceedings of the Fifth Symposium on Math, Statistics, and Probability, 281-297

MAITLAND, T. & SITZMAN, S. 2007. Electron Backscatter Diffraction (EBSD) technique and materials characterization examples. Scanning Microscopy for Nanotechnology Techniques and Applications, Springer, p. 399

MARSH, B. & CASHMAN, K. 1988. Crystal size distribution (CSD) in rocks and the kinetics of crystallization II: Makaopuhi lava lake. Contributions to Mineralogy and Petrology, 99, 292-305

MARTIN, V. M., MORGAN, D., JERRAM, D., CADDICK, M., PRIOR, D. & DAVIDSON, J. P. 2008. Bang! Month-scale eruption triggering at Santorini volcano. Science, 321, 1178

MCBIRNEY, A. 1995. Mechanisms of differentiation in the Skaergaard Intrusion. Journal of the Geological Society, London, 153, 421-435

MCCAIG, A., COVEY-CRUMP, S., ISMAIL, W. & LLOYD, G. 2007. Fast diffusion along mobile grain boundaries in calcite. Contributions to mineralogy and petrology, 153, 159-175

MCNUTT, S. 2005. Volcanic seismology. Annual Review of Earth and Environmental Sciences, 32, 461-491

MISENER, D. 1974. Cationic diffusion in olivine to 1400°C and 35 kbar. Geochemical Tranport and Kinetics, Carnegie Institute of Washington, 117-129

MOCK, A. & JERRAM, D. 2005. Crystal size distributions (CSD) in three dimensions: insights from the 3D reconstruction of a highly porphyritic rhyolite. Journal of Petrology, 46, 1525-1541.

MONTIERTH, C., JOHNSTON, D. & CASHMAN, K. 1995. An empirical glass-composition-based geothermometer for Mauna Loa lavas. Mauna Loa Revealed: Structure, Composition, History and Hazards, Geophysical Monograph 92

MORGAN, D., BLAKE, S., ROGERS, N., DEVIVO, B., ROLANDI, G., MACDONALD, R. & HAWKESWORTH, C. 2004. Time scales of crystal residence and magma chamber volume from modelling of diffusion profiles in phenocrysts: Vesuvius 1944. Earth and Planetary Science Letters, 222, 933-946

MORGAN, D. & BLAKE, S. 2006. Magmatic residence times of zoned phenocrysts: introduction and application of the binary element diffusion modelling (BEDM) technique. Contributions to Mineralogy and Petrology, 151, 58-70

MORGAN, G. & LONDON, D. 1996. Optimizing the electron microprobe analysis of hydrous alkali aluminosilicate glasses. American Mineralogist, 81, 1176-1185

MORGAN, D. & JERRAM, D. 2006. On estimating crystal shape for crystal size distribution analysis, Journal of Volcanology and Geothermal Research, 154, 1-7

MULLER, A. 2005. The Hapaimamo flow: a youn pre-historic picritic lava flow on Mauna Loa's southwest rift zone. MSc thesis. University of Massachussetts, Amherst.

NAKAMURA, M. 1995. Continuous mixing of crystal mush and replenished magma in the ongoing Unzen eruption. Geology, 23, 807-810

NAKAMURA, A. & SCHMALZRIED, H. 1983. On the non-stoichiometry and point defects of olivine. Physics and Chemistry of Minerals, 10, 27-37

NEAVE, D, PASSMORE, E., MACLENNAN, J., FITTON, G. & THORDARSON, T. 2013. Crystal-melt relationships and the record of deep mixing and crystallisation in the AD 1783 Laki eruption, Iceland. Journal of Petrology, 54, 1661-1690

NEAVE, D., MACLENNAN, J., HARTLEY, M., EDMONDS, M. & THORDARSON, T. 2014. Crystal storage and transfer in basaltic systems: the Skuggafjöll eruption, Iceland. Journal of Petrology, 55, 2311-2346

NICHOLS, R. 1936. Flow units in basalts. The Journal of Geology, 44, 617-630

NORMAN, M. & GARCIA, M. 1999. Primitive magmas and source characteristics of the Hawaiian plume: petrology and geochemistry of shield picrites. Earth and Planetary Science Letters, 168, 27-44

ODBERT, H., RYAN, G., MATTIOLI, G., HAUTMANN, S., GOTTSMANN, J., FOURNIER, N. & HERD, R. 2014. Volcano geodesy at the Soufriére Hills volcano, Montserrat: a review. From the Eruption of Soufriére Hills Volcano, Montserrat from 2000 to 2010, Geological Society, London, Memoirs, 39, 195-217

OESER, M., DOHMEN, R., HORN, I., SCHUTH, S. & WEYER, S. 2015. Processes and time scales of magmatic evolution as revealed by Fe-Mg chemical and isotopic zoning in natural olivines. Geochimica et Cosmochimica Acta, 154, 130-150

OLADOTTIR, B., SIGMARSSON, O., LARSEN, G. & THORDARSON, T. 2008. Katla volcano, Iceland: magma composition, dynamics and eruption frequency as recorded by Holocene tephra layers. Bulletin of Volcanology, 70, 475-493

PANKHURST, M. J., DOBSON, K. J., MORGAN, D. J. LOUGHLIN, S. C., THORDARSON, T., LEE, P. D. & COURTOIS, L. 2014. Monitoring the magmas fuelling volcanic eruptions in Near-real-time using X-ray Micro-computed Tomography. Journal of Petrology, 55, 671-684

PANKHURST, M.J., Morgan, D. J., Thordarson, T. & LOUGHLIN, S. C. 2017. Retracing magma: patterns in crystal histories explain pre-eruptive volcanic unrest. Nature Communications, *in review*

PASSMORE, E., MACLENNAN, J., FITTON, G. & THORDARSON, T. 2012. Mush disaggregation in basaltic magma chambers: evidence from the AD 1783 Laki eruption. Journal of Petrology, 53, 2593-2623

PEARCE, T. 1984. The analysis of zoning in magmatic crystals with emphasis on olivine. Contributions to Mineralogy of Petrology, 86, 149-154

PEARCE, T. H. 1987. The theory of zoning patterns in magmatic minerals using olivine as an example. Contributions to Mineralogy and Petrology, 97, 451-459

PERRING, C., BARNES, S., VERRALL, M. & HILL, R. 2004. Using automated digital image analysis to provide quantitative petrographic data on olivine-phyric basalts. Computers and Geosciences, 30, 183-195

PELTIER, A., BACHÈLERY, & P. STAUDACHER, T. 2009. Magma transport and storage at Piton de La Fournaise (La Réunion) between 1972 and 2007: A review of geophysical and geochemical data. Journal of Volcanology and Geothermal Research, 184, 93-108

PETERS, B. J., DAY, J. M. D. & TAYLOR, L. A. 2016. Early mantle heterogeneities in the Réunion hotspot source inferred from highly siderophile elements in cumulate xenoliths. Earth and Planetary Science Letters, 448, 150-160

PETERSON, D. & TILLING, R. 1980. Transition of basaltic lava from pahoehoe to a'a, Kilauea volcano, Hawaii: field observations and key factors. Journal of Volcanology and Geothermal Research, 7, 271-293

PETRY, C., CHAKRABORTY, S. & PALME, H. 2004. Experimental determination of Ni diffusion coefficients in olivine and their dependence on temperature, composition, oxygen fugacity and crystallographic orientation. Geochimica et Cosmochimica Acta, 68, 4179-4188

PHILIBERT, J. 1991, Atom Movements, Diffusion and Mass Transport in Solids. Les editions de Physique, Les Ulis, France, 577

PRATA, A. & BERNARDO, C. 2007. Retrieval of volcanic SO_2 column abundance from atmospheric infrared sounder data. Journal of Geophysical Research, 112,

PUTIRKA, K., PERFIT, M., RYERSON, F.J. & JACKSON, M.G. 2007. Ambient and excess mantle temperatures, olivine thermometry, and active vs. passive upwelling. Chemical Geology, 241, 177-206

PUTIRKA, K. 2008. Thermometers and barometers for volcanic systems. Reviews in Mineralogy and Petrology, 69, 61-120

PUTNIS, A. 1992. An Introduction to Mineral Sciences. Cambridge University Press

RAE, A. S. P., EDMONDS, M., MACLENNAN, J., MORGAN, D., HOUGHTON, B., HARTLEY, M. & SIDES, I. 2016. Timescales of magma transport and mixing at Kilauea volcano, Hawaii. Geology, 44, 463-466

REED, S. J. B. 1996. Electron microprobe analysis and scanning electron microscopy in geology. Cambridge University Press

REED, S.J.B. 1997. Electron microprobe analysis. Second Edition. Cambridge University Press

RHODES, J. 1988. Geochemistry of the 1984 Mauna Loa eruption: implications for magma storage and supply. Journal of Geophysical Research, 93, 4453-4466

RHODES, J. 1995. The 1852 and 1868 Mauna Loa picrite eruptions: Clues to parental magma compositions and the magmatic plumbing system. Mauna Loa revealed: Structure, Composition, History, and Hazards, Geophysical Monograph 92

RHODES, J. & VOLLINGER, M. 2005. Ferric/ferrous ratios in 1984 Mauna Loa lavas: a contribution to understanding the oxidation state of Hawaiian magmas. Contributions to Mineralogy and Petrology, 149, 666-674

ROEDER, P. & EMSLIE, R. 1970. Olivine-liquid equilibrium. Contributions to Mineralogy and Petrology, 29, 275-289

ROWLAND, S. & WALKER, G. 1987. Toothpaste lava: Characteristics and origin of a lava structural type transitional between pahoehoe and a'a. Bulletin of Volcanology, 49, 631-641

ROWLAND, S. & WALKER, G. 1988. Mafic-crystal distributions, viscosities, and lava structures of some Hawaiian lava flows. Journal of Volcanology and Geothermal Research, 35, 55-66

ROWLAND, S. & WALKER, G. 1990. Pahoehoe and A'a in Hawaii: volumetric flow rate controls the lava structure. Bulletin of Volcanology, 52, 615-628

RUBIN, A. 1995. Propagation of magma filled cracks. Annual Review of Earth and Planetary Sciences, 23, 287-336

RUPRECHT, P. & PLANK, T. 2013. Feeding andesitic eruptions with a high-speed connection from the mantle. Nature, 500, 68-72

RYMER, H. & WILLIAMS-JONES, G. 2000. Volcanic eruption prediction: Magma chamber physics from gravity and deformation measurements. Geophysical Research Letters, 27, 2389-2392

SAKIMOTO, S. E. H. & ZUBER, M. T. 1998. Flow and convective cooling in lava tubes. Journal of Geophysical Research, 103, 27465-27487

SAEMUNDSSON, K. 1979. Outline of the geology of Iceland. Jökull, 29, 7-28

SALTIKOV, S. 1967. The determination of the size distribution of particles in an opaque material from a measurement of the size distribution of their sections. Stereology, 163-173

SAUNDERS, K., BLUNDY, J., DOHMEN, R. & CASHMAN, K. 2012. Linking petrology and seismology at an active volcano. Science, 336, 1023-1027

SCHINDELIN, J., RUEDEN, C. T. & HINER, C. et al. 2015. The ImageJ ecosystem: An open platform for biomedical image analysis. Molecular Reproduction and Development.

SCHMINKCE, H.-U. 2004. Volcanism. Springer.

SCHNEIDER, C. A., RASBAND, W. S. & ELICEIRI, K. W. 2012. NIH Image to Image J: 25 years of image analysis. Nature methods, 9, 671-675

SCHWINDINGER, K. 1999. Particle dynamics and aggregation of crystals in a magma chamber with application to Kilauea Iki olivine. Journal of Volcanology and Geothermal Research, 88, 209-238

SCHWINDINGER, K. & ANDERSON, A. 1989. Synneusis of Kilauea Iki olivines. Contributions to Mineralogy and Petrology, 103, 187-198

SELF. S., KESZTHELYI, L. & THORDARSON, T. 1998. The importance of pahoehoe. Annual Review or Earth and Planetary Sciences, 26, 81-110

SERVADIO, Z., VILLENEUVE, N. & BACHELERY, P. 2013. Automatic mapping of the lava flows at Piton de la Fournaise Volcano, by combining thermal data in near and visible infrared. Remote Sensing – Applications.

SHEA, T., COSTA, F., KRIMER, D. & HAMMER, J. 2015a. Accuracy of timescales retrieved from diffusion modelling in olivine: A 3D perspective. American Mineralogist, 100, 2026-2042

SHEA, T., LYNN, K. & GARCIA, M. 2015b. Cracking the olivine zoning code: Distinguishing between crystal growth and diffusion. Geology, 43, 935-938

SIGMARSSON, O., CONDOMINES, M., GRONVOLD, K. & THORDARSON, T. 1991. Extreme magma homogeneity in the 1783-84 Lakagigar eruption – origin of a large volume of evolved basalt in Iceland. Geophysical Research Letters, 18, 2229-22232

SISSON, T. & LAYNE, G. 1993. H_2O in basalt and basaltic andesite glass inclusions from four subduction-relate volcanoes. Earth and Planetary Science Letters, 117, 619-635

SOILLE, P. & VINCENT, M. 1990. Determining watersheds in digital pictures via flooding simulations. Proc SPIE, 1360, 240-250

SPARKS, R. S. J. 2003. Forecasting volcanic eruptions. Earth and Planetary Science Letters, 210, 1-15

SPARKS, R. S. J. & WALKER, G. P. L. 1973. Products of ignimbrite eruptions. Geology, 115-118

SPARKS, S., WILSON, L. & SIGURDSSON, H. 1981. The pyroclastic deposits of the 1875 eruption of Askja, Iceland. Philosophical Transactions of the Royal Society, 299, 241-273

SWAN, A. R. H. & SANDILANDS, M. 1995. Introduction to geological data analysis. Blackwell Science Ltd

SWANSON, D. 1973. Pahoehoe flows from the 1969-1971 Mauna Ulu eruption, Kilauea volcano, Hawaii. Geological Society of America Bulletin, 84, 615-626

THOMAS, R. M. E. & SPARKS, R. S. J. 1992. Cooling of tephra during fallout from eruption columns. Bulletin of Volcanology, 54, 542-553

THOMSON, A. & MACLENNAN, J. 2013. The distribution of olivine compositions in Icelandic basalts and picrites. Journal of Petrology, 54, 745-768

THORARINSSON, S. 1954. The eruption of Hekla 1947-48. The tephra-fall from Hekla on March 29, 1947, part 2, chapter 3, Soc. Sci. Islandica, Reykjavik,1-68

THORARINSSON, S. & SIGVALDASON, G. 1972. The Hekla eruption of 1970. Bulletin of Volcanology, 36, 269-288

THORARINSSON, S. 1981. The application of tephrochronology in Iceland. Tephra Studies, NATO Advanced Study Institutes Series, 75, 109-134

THORDARSON, T. & HOSKULDSSON, A. 2002. Iceland (Classic geology in Europe). Dunedin academic press

THORDARSON, T. & LARSEN, G. 2007. Volcanism in Iceland in historical time: Volcano types, eruption styles and eruptive history. Journal of Geodynamics, 43, 118-152

THORDARSON, T. & SELF, S. 1993. The Laki (Skaftár Fires) and Grímsvötn eruptions in 1783-1785. Bulletin of Volcanology, 55, 233-263

THORDARSON, T. & SELF, S. 1998. The Rosa Member, Columbia River Basalt Group: A gigantic pahoehoe lava flow field formed by endogenous processes? Journal of Geophysical Research, 103, 27411-27445

THORDARSON, T., SELF, S. & ÓSKARSSON, N. 1996. Sulfur, chlorine, and fluorine degassing and atmospheric loading by the 1783-1784 AD Laki (Skáftar Fires) eruption in Iceland. Bulletin of Volcanology, 58, 205-225

TSAI, T.-L. & DIECKMANN, R. 2002. Variation of the oxygen content and point defects in olivines, $(Fe_x\ Mg_{1-x})_2SiO_4$, $0.2 < x < 1$. Physics and Chemistry of Minerals, 29, 680-694

TSANG, C., DAVIDSON, C. & TRUSDELL, F. 2008. Do secondary magma chambers exist in Mauna Loa's Southwest Rift zone? A petrological and geochemical analysis of xenoliths, Masters Thesis, Carleton College, USA

VAN ORMAN, J. & CRISPIN, K. 2010. Diffusion in oxides. Reviews in Mineralogy and Geochemistry, 72, 757-810

VANCE, J. 1969. On synneusis. Contributions to Mineralogy and Petrology, 24, 7-29

VILLEMANT, B., SALAÜN, A. & STAUDACHER, T. 2009. Evidence for a homogenous primary magma at Piton de la Fournaise (La Réunion): A geochemical study of matrix glass, melt inclusions and Pélé's hairs of the 1998-2008 eruptive activity. Journal of Volcanology and Geothermal Research, 184, 79-92

VINET, N. & HIGGINS, M. 2010. Magma solidification processes beneath Kilauea Volcano, Hawaii: a quantitative textural and geochemical study of the 1969-1974 Mauna Ulu lavas. Journal of Petrology, 51, 1297-1332

VLASTELIC, I., STAUDACHER, T & SEMET M. 2005. Rapid change of lava composition from 1998 to 2002 at Piton de la Fournaise (Réunion) inferred from Pb isotopes and trace elements: Evidence for variable crustal contamination. Journal of Petrology, 46, 79-107

WAGSTAFF, K., CARDIE, C., ROGERS, S. & SCHROEDL, S. 2001. Constrained K-means clustering with background knowledge. Proceedings of the Eighteenth International Conference on Machine Learning, 577-584

WALKER, G. 1971. Compound and simple lava flows and flood basalts. Bulletin of Volcanology, 35, 579-590

WALKER, D., KIRKPATRICK, R., LONGHI, J. & HAYS, J. 1976. Crystallisation history of lunar picrate basalt sample 12002: phase equilibria and cooling-rate studies. Geological Society of America Bulletin, 87, 646-656

WALLACE, G. & BERGANTZ, G. 2004. Constraints on mingling of crystal populations from off-centre zoning profiles: A statistical approach. American Mineralogist, 89

WATSON, E. B. 1994. Diffusion in volatile-bearing magmas. Reviews in Mineralogy and Geochemistry, 30, 371-411

WATSON, E. B. & LIANG, Y. 1995. A simple model for sector zoning in slowly grown crystals: Implications for growth rate and lattice diffusion, with emphasis on accessory minerals in crustal rocks. American Mineralogist, 80, 1179-1187

WATSON, E. B. & MÜLLER, T. 2009. Non-equilibrium isotopic and elemental fractionation during diffusion-controlled crystal growth under static and dynamic conditions. Chemical Geology, 267, 111-124

WELSCH, B., FAURE, F., FAMIN, V., BARONNET, A. & BACHÉLERY, P. 2012. Dendritic crystallization: A single process for all the textures of olivine in basalts? Journal of Petrology, 1-36

WOLFE, E. & MORRIS, J. 1996. Geological Map of the Island of Hawaii, USGS Data Series 144

ZELLMER, G., SAKAMOTO, N., MATSUDA, N., MOEBIS, A., IIZUKA, Y., MOEBIS, A. & YURIMOTO, H. 2015. On progress and rate of the peritectic reaction Fo + SiO_2 ⟶

En in natural andesitic arc magmas. Geochimica et Cosmochimica Acta, 185, 383-393

ZHANG, Y. 2010. Diffusion in minerals and melts: theoretical background. Reviews in Mineralogy and Petrology, 72, 5-59

APPENDICES

Appendix A

Thermometry

This appendix presents the thermometry data used for the PdF, Hapaimamo, Moinui and Vatnaöldur diffusion datasets.

Piton de la Fournaise Quantitative Maps (MgO wt % and Total wt %) (EPMA)

Map 1

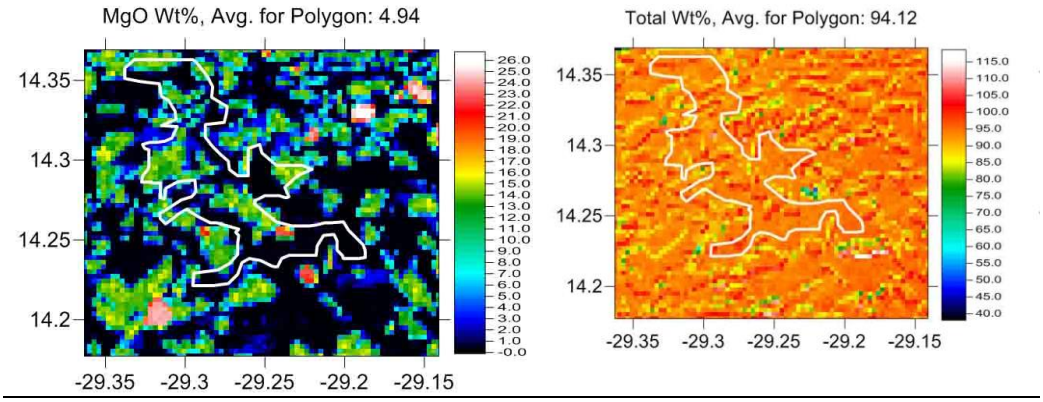

Map 2

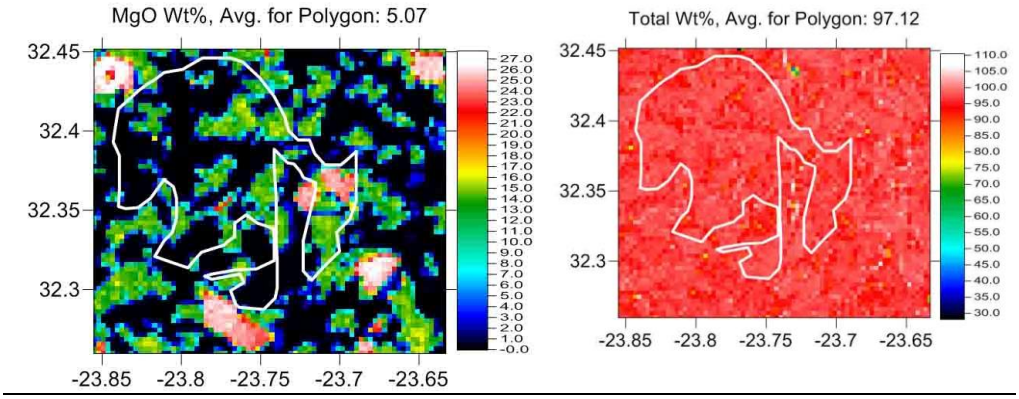

Map 3

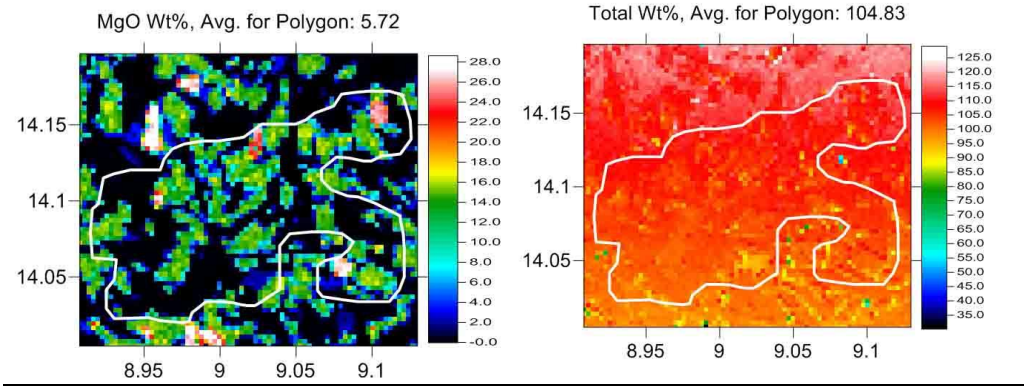

Selection of Hapaimamo Melt inclusion glass and adjacent olivine major oxide compositions (EPMA)

	Oxide wt %													
SAMPLE	SiO_2	TiO_2	Al_2O_3	Cr_2O_3	FeO	NiO	MnO	MgO	CaO	Na_2O	K_2O	P_2O_5	O	TOTAL
Melt Inclusions														
Block 2_Ba_MI1_1	53.86	1.73	13.45	0.03	10.18	0.01	0.13	6.72	10.48	2.19	0.26	0.23	0.00	99.28
Block 2_Ba_MI1_1	53.78	1.69	13.38	0.06	10.14	-0.02	0.16	6.68	10.39	2.16	0.26	0.21	0.00	98.91
Block 2_Ba_MI1_1	54.11	1.75	13.31	0.05	10.24	0.01	0.19	6.74	10.43	2.19	0.26	0.19	0.00	99.48
Block 2_Bb_MI2	53.81	1.90	13.58	0.04	10.13	0.03	0.16	6.76	10.49	2.18	0.39	0.30	0.00	99.76
Block 2_Bb_MI2	53.28	1.90	13.78	0.02	9.99	0.01	0.14	6.72	10.43	2.26	0.40	0.29	0.00	99.23
Block 2_Bb_MI2	53.46	1.92	13.66	0.04	10.17	0.01	0.18	6.78	10.53	2.21	0.40	0.27	0.00	99.63
Block 2_D_MI3	55.14	1.85	14.49	0.04	6.87	0.01	0.11	6.89	10.62	2.36	0.35	0.20	0.00	98.94
Block 2_D_MI3	55.34	1.86	14.47	0.06	6.83	0.01	0.12	6.83	10.75	2.43	0.35	0.20	0.00	99.26
Block 2_E_MI4	52.62	1.74	14.34	0.06	8.42	0.03	0.11	7.28	11.74	2.03	0.33	0.18	0.00	98.88
Block 2_E_MI4	52.74	1.75	14.33	0.05	8.41	0.04	0.13	7.35	11.65	1.89	0.31	0.18	0.00	98.84
Block 2_F_MI5	55.49	1.84	14.42	0.24	7.49	0.03	0.14	6.64	10.55	2.16	0.35	0.23	0.00	99.58
Block 2_G_MI6	52.50	1.97	13.99	0.04	9.35	0.01	0.15	6.83	10.67	2.37	0.33	0.21	0.00	98.43
Block 2_G_MI6	53.02	1.98	14.02	0.07	9.14	0.01	0.14	6.91	10.75	2.20	0.31	0.21	0.00	98.76
Block 2_Ib_MI7	54.53	1.89	14.32	0.07	7.07	0.04	0.10	6.97	10.63	2.32	0.43	0.27	0.00	98.63
Block 2_Ib_MI7	54.35	1.89	14.31	0.05	7.09	0.04	0.13	6.92	10.68	2.35	0.42	0.28	0.00	98.51
Block 2_L_MI9	53.79	1.94	14.06	0.10	7.41	0.03	0.11	6.90	10.59	2.36	0.36	0.23	0.00	97.89
Block 2_N_MI10	52.17	1.99	13.75	0.03	9.87	0.01	0.19	6.72	10.58	2.31	0.41	0.26	0.00	98.27
Block 2_N_MI10	52.73	1.98	14.18	0.07	9.64	0.01	0.16	6.59	10.55	2.46	0.40	0.24	0.00	99.03
Block 2_N_MI10	52.49	2.01	14.27	0.03	9.66	0.01	0.14	6.68	10.63	2.54	0.42	0.21	0.00	99.11
Block 2_O_MI11	54.73	1.92	13.32	0.03	8.80	0.01	0.16	6.86	10.11	2.08	0.48	0.25	0.00	98.75
Block 2_O_MI11	54.19	1.95	13.10	0.03	8.82	0.01	0.14	6.85	10.14	1.97	0.45	0.27	0.00	97.92
Block 2_Q_MI12	52.59	1.74	14.17	0.06	8.45	0.02	0.14	7.19	11.78	2.04	0.35	0.24	0.00	98.76
Block 2_S_MI13	51.88	2.04	13.46	0.04	10.56	0.01	0.17	6.77	10.38	2.36	0.40	0.20	0.00	98.27
Block 3_B_MI14	51.79	1.99	13.76	0.04	10.78	-0.01	0.16	6.56	10.49	2.29	0.37	0.24	0.00	98.44
Block 3_B_MI14	51.22	1.99	13.78	0.04	10.53	0.00	0.17	6.47	10.53	2.25	0.41	0.23	0.00	97.61
Block 3_Cb_MI15	54.42	1.87	14.69	0.04	6.73	0.03	0.12	6.80	10.77	2.29	0.44	0.34	0.00	98.54
Block 3_F_MI16	52.32	1.83	13.67	0.05	9.83	0.03	0.16	6.34	10.46	2.48	0.41	0.20	0.00	97.76
Block 3_J_MI17	53.35	2.01	13.99	0.04	7.79	0.02	0.15	6.95	10.57	2.09	0.46	0.31	0.00	97.75
Block 3_J_MI17	52.94	2.02	13.82	0.05	7.73	-0.01	0.10	6.83	10.63	2.07	0.47	0.24	0.00	96.90

Block 3_J_MI18	53.64	2.01	13.91	0.02	7.65	0.05	0.12	6.95	10.69	2.07	0.44	0.26	0.00	97.80
Block 3_J_MI18	53.56	2.04	13.90	0.04	7.66	0.03	0.13	7.02	10.68	2.20	0.44	0.29	0.00	98.00
Olivine														
Block 2_MI1_Ol1	39.54	0.00	0.02	0.05	15.44	0.30	0.19	44.43	0.21	-0.02	0.02	0.01	0.00	100.19
Block 2_MI1_Ol2	40.31	0.01	0.01	0.06	15.43	0.31	0.21	44.82	0.20	0.00	-0.01	0.02	0.00	101.38
Block 2_MI1_Ol3	39.50	0.01	0.05	0.07	15.99	0.29	0.24	44.33	0.21	0.01	0.00	0.02	0.00	100.73
Block 2_MI2_Ol1	39.79	0.01	0.01	0.07	15.15	0.27	0.21	44.75	0.20	-0.02	0.00	0.02	0.00	100.46
Block 2_MI2_Ol1	39.56	0.01	-0.01	0.07	15.38	0.27	0.20	45.13	0.19	-0.04	0.00	0.01	0.00	100.79
Block 2_MI2_Ol1	39.54	0.00	0.01	0.09	15.26	0.29	0.20	44.84	0.19	0.01	-0.01	0.01	0.00	100.42
Block 2_MI2_Ol2	39.67	0.00	0.01	0.08	15.23	0.30	0.20	44.71	0.21	0.00	-0.01	0.00	0.00	100.41
Block 2_MI2_Ol2	39.89	0.00	0.04	0.06	15.35	0.29	0.22	44.60	0.20	0.01	-0.01	0.02	0.00	100.67
Block 2_MI2_Ol2	39.57	0.00	0.02	0.09	15.18	0.29	0.20	44.77	0.20	-0.02	0.00	0.01	0.00	100.30
Block 2_MI2_Ol3	39.14	0.02	0.04	0.06	15.61	0.28	0.20	44.24	0.20	0.00	0.00	0.01	0.00	99.79
Block 2_MI2_Ol3	39.24	0.01	-0.02	0.06	15.91	0.29	0.20	44.13	0.20	0.01	0.00	0.00	0.00	100.03
Block 2_MI2_Ol3	39.53	0.00	0.01	0.08	15.63	0.26	0.18	44.48	0.21	-0.01	0.00	0.01	0.00	100.40
Block 2_MI3_Ol1	40.41	0.01	0.00	0.06	12.31	0.32	0.13	47.37	0.19	0.02	0.00	0.01	0.00	100.83
Block 2_MI3_Ol1	40.27	0.01	0.07	0.06	12.09	0.34	0.18	46.91	0.21	0.00	0.00	0.01	0.00	100.15
Block 2_MI3_Ol1	40.12	0.01	0.01	0.09	12.28	0.32	0.15	47.20	0.20	-0.02	0.01	0.02	0.00	100.38
Block 2_MI3_Ol2	40.30	0.02	0.04	0.05	11.40	0.35	0.19	48.09	0.18	0.00	0.00	0.01	0.00	100.63
Block 2_MI3_Ol2	40.47	0.00	0.03	0.05	11.39	0.34	0.15	47.94	0.20	0.00	0.01	0.00	0.00	100.56
Block 2_MI3_Ol2	40.43	0.03	0.05	0.08	11.21	0.30	0.16	47.92	0.21	0.03	0.00	0.00	0.00	100.44
Block 2_MI4_Ol1	40.47	0.01	0.04	0.06	11.93	0.36	0.15	47.36	0.22	-0.01	0.00	-0.01	0.00	100.59
Block 2_MI4_Ol1	40.25	0.00	0.13	0.08	12.13	0.38	0.17	47.24	0.24	0.03	-0.01	-0.01	0.00	100.64
Block 2_MI4_Ol1	40.11	0.00	0.04	0.07	12.09	0.38	0.16	47.21	0.25	0.00	0.00	0.01	0.00	100.31
Block 2_MI4_Ol2	40.31	0.01	0.00	0.07	12.17	0.33	0.18	47.13	0.25	0.02	0.00	0.02	0.00	100.48
Block 2_MI4_Ol2	40.43	0.00	0.02	0.05	12.03	0.38	0.17	47.42	0.26	-0.04	0.00	0.01	0.00	100.75
Block 2_MI4_Ol2	40.45	0.00	0.05	0.04	12.05	0.36	0.17	47.19	0.23	-0.03	0.00	0.01	0.00	100.51
Block 2_MI5_Ol1	39.65	-0.01	0.03	0.08	12.28	0.34	0.16	46.47	0.18	-0.23	0.00	0.02	0.00	98.97
Block 2_MI5_Ol1	39.89	0.01	0.03	0.11	12.43	0.33	0.17	46.71	0.18	0.01	-0.01	0.02	0.00	99.86
Block 2_MI5_Ol1	40.05	0.00	0.02	0.10	12.50	0.34	0.16	46.85	0.20	0.02	0.00	0.02	0.00	100.26
Block 2_MI5_Ol2	40.16	0.01	0.02	0.11	12.44	0.33	0.16	46.88	0.19	-0.02	0.00	0.02	0.00	100.29
Block 2_MI5_Ol2	40.45	0.00	0.01	0.11	12.46	0.33	0.14	47.18	0.19	0.00	-0.01	0.00	0.00	100.85
Block 2_MI5_Ol2	39.95	0.00	0.05	0.08	12.44	0.28	0.16	46.74	0.21	-0.02	0.00	0.03	0.00	99.92
Block 2_MI6_Ol1	40.09	0.00	0.04	0.04	14.63	0.22	0.19	45.47	0.19	-0.02	0.01	0.00	0.00	100.87

Block 2_MI6_Ol1	39.98	0.00	0.01	0.06	14.51	0.25	0.18	45.06	0.22	0.01	-0.01	0.00	0.00	100.30
Block 2_MI6_Ol1	40.38	0.00	0.03	0.08	14.62	0.24	0.22	45.08	0.23	0.00	0.00	-0.01	0.00	100.87
Block 2_MI6_Ol2	39.86	0.00	0.04	0.06	14.59	0.26	0.21	45.13	0.22	-0.05	-0.01	0.00	0.00	100.32
Block 2_MI6_Ol2	40.07	0.00	0.03	0.05	14.55	0.28	0.20	44.86	0.21	0.03	0.00	0.02	0.00	100.30
Block 2_MI6_Ol2	39.73	0.01	0.03	0.06	14.63	0.28	0.21	45.20	0.21	-0.01	0.00	0.01	0.00	100.35
Block 2_MI7_Ol1	40.46	0.01	0.06	0.08	11.78	0.38	0.16	47.04	0.19	0.01	0.01	0.01	0.00	100.19
Block 2_MI7_Ol1	40.14	0.00	0.01	0.09	11.83	0.37	0.16	47.28	0.20	-0.01	0.00	0.01	0.00	100.07
Block 2_MI7_Ol1	41.28	0.02	0.02	0.08	11.72	0.37	0.17	47.52	0.21	0.00	-0.01	0.03	0.00	101.41
Block 2_MI7_Ol2	40.86	0.01	0.01	0.07	11.93	0.40	0.15	47.30	0.19	0.01	0.00	0.04	0.00	100.97
Block 2_MI7_Ol2	41.10	0.00	-0.03	0.08	12.02	0.37	0.16	47.20	0.20	0.00	0.00	0.03	0.00	101.12
Block 2_MI7_Ol2	40.60	0.00	0.03	0.09	11.93	0.37	0.16	47.01	0.19	-0.01	-0.01	0.02	0.00	100.37
Block 2_MI8_Ol1	40.61	0.00	0.01	0.07	12.95	0.34	0.18	46.53	0.23	-0.02	0.00	0.03	0.00	100.93
Block 2_MI8_Ol1	40.94	0.01	0.03	0.06	13.07	0.36	0.18	46.25	0.25	0.02	-0.01	0.03	0.00	101.19
Block 2_MI8_Ol1	40.84	0.01	0.04	0.06	13.17	0.32	0.21	46.56	0.21	0.01	-0.01	0.04	0.00	101.46
Block 2_MI8_Ol1	40.77	0.01	0.03	0.08	13.10	0.35	0.16	46.59	0.23	-0.08	0.01	0.03	0.00	101.29
Block 2_MI9_Ol1	40.81	0.00	0.03	0.10	11.89	0.31	0.18	47.78	0.19	-0.04	0.00	0.04	0.00	101.30
Block 2_MI9_Ol1	40.78	0.00	0.05	0.11	11.96	0.32	0.14	47.61	0.21	0.01	0.00	0.01	0.00	101.20
Block 2_MI9_Ol1	40.76	0.00	0.02	0.07	11.94	0.31	0.16	47.49	0.18	-0.02	0.01	0.01	0.00	100.94
Block 2_MI9_Ol1	40.42	0.01	0.04	0.09	11.96	0.32	0.18	47.39	0.22	0.01	-0.01	0.01	0.00	100.65
Block 2_MI10_Ol1	41.29	0.01	0.02	0.09	10.86	0.34	0.15	48.35	0.19	0.00	0.00	0.01	0.00	101.31
Block 2_MI10_Ol1	40.61	0.00	0.01	0.07	10.91	0.37	0.14	48.25	0.18	-0.01	0.01	0.00	0.00	100.54
Block 2_MI10_Ol1	40.61	0.01	0.04	0.10	10.89	0.40	0.11	48.48	0.19	-0.01	0.00	0.04	0.00	100.86
Block 2_MI10_Ol2	41.13	0.00	0.07	0.10	10.96	0.40	0.15	48.22	0.20	0.02	0.01	0.01	0.00	101.29
Block 2_MI10_Ol2	40.74	0.01	0.03	0.11	11.06	0.37	0.16	48.51	0.20	0.03	0.00	-0.01	0.00	101.21
Block 2_MI10_Ol2	40.70	0.01	0.01	0.12	10.88	0.36	0.14	48.14	0.22	0.01	0.01	0.02	0.00	100.60
Block 2_MI10_Ol3	40.85	0.00	0.04	0.10	10.94	0.37	0.17	48.27	0.19	0.00	0.01	0.02	0.00	100.95
Block 2_MI10_Ol3	40.98	-0.01	0.02	0.10	10.88	0.42	0.14	48.68	0.18	0.01	0.02	0.01	0.00	101.43
Block 2_MI10_Ol3	40.52	0.00	0.04	0.11	10.84	0.37	0.15	48.54	0.19	-0.03	0.00	0.02	0.00	100.76
Block 2_MI11_Ol1	40.67	0.00	0.00	0.09	13.06	0.34	0.17	46.42	0.20	0.01	0.01	0.01	0.00	100.99
Block 2_MI11_Ol1	40.62	0.00	0.01	0.05	13.07	0.36	0.19	46.44	0.18	0.03	0.00	0.04	0.00	100.99
Block 2_MI11_Ol1	40.52	0.01	0.05	0.05	13.03	0.35	0.18	46.33	0.20	-0.02	-0.01	0.01	0.00	100.72
Block 2_MI11_Ol2	40.28	0.01	0.06	0.11	13.08	0.36	0.19	46.35	0.19	-0.03	0.01	0.04	0.00	100.64
Block 2_MI11_Ol2	40.22	0.01	0.06	0.07	13.09	0.34	0.18	46.11	0.16	0.00	0.00	0.02	0.00	100.28
Block 2_MI11_Ol2	40.37	0.01	0.02	0.11	13.07	0.37	0.18	46.12	0.17	0.00	0.00	-0.01	0.00	100.41

Block 2_MI12_Ol1	40.34	0.01	0.02	0.06	12.48	0.34	0.18	46.88	0.25	0.00	0.01	0.03	0.00	100.60
Block 2_MI12_Ol1	40.36	0.02	0.04	0.07	12.30	0.33	0.18	46.97	0.23	-0.02	0.00	0.02	0.00	100.50
Block 2_MI12_Ol1	40.64	0.01	0.03	0.05	12.34	0.33	0.18	46.88	0.25	0.02	0.00	0.02	0.00	100.73
Block 2_MI12_Ol1	40.76	0.00	0.02	0.04	12.55	0.34	0.18	47.45	0.23	0.00	0.00	0.01	0.00	101.60
Block 2_MI13_Ol1	39.43	0.00	0.06	0.07	15.75	0.26	0.19	45.00	0.24	-0.03	-0.01	0.02	0.00	100.98
Block 2_MI13_Ol1	39.94	-0.01	-0.01	0.05	14.07	0.31	0.20	45.48	0.24	-0.01	0.01	0.03	0.00	100.29
Block 2_MI13_Ol1	41.17	0.01	0.01	0.09	13.63	0.34	0.18	46.51	0.23	0.03	0.00	0.03	0.00	102.23
Block 2_MI13_Ol1	40.33	0.02	0.02	0.04	13.52	0.31	0.17	46.08	0.23	0.00	-0.01	-0.01	0.00	100.71
Block 2_MI14_Ol1	40.19	0.01	0.06	0.08	13.30	0.35	0.18	46.10	0.18	0.03	0.00	0.02	0.00	100.49
Block 2_MI14_Ol1	39.89	0.02	0.03	0.08	13.93	0.30	0.18	45.27	0.20	-0.03	0.00	0.01	0.00	99.88
Block 2_MI14_Ol1	40.56	0.01	0.04	0.10	14.00	0.30	0.19	45.50	0.19	0.02	0.01	-0.01	0.00	100.92
Block 2_MI14_Ol2	40.15	0.01	0.03	0.10	12.96	0.39	0.17	46.78	0.19	0.01	0.00	0.05	0.00	100.83
Block 2_MI14_Ol2	40.44	0.01	0.04	0.12	13.01	0.35	0.17	46.05	0.20	0.02	0.00	0.01	0.00	100.42
Block 2_MI14_Ol2	40.73	0.00	0.08	0.13	13.45	0.38	0.17	45.79	0.20	0.01	0.00	0.03	0.00	100.94
Block 2_MI15_Ol1	40.25	0.01	0.05	0.09	11.72	0.40	0.15	47.18	0.18	0.00	-0.01	0.01	0.00	100.02
Block 2_MI15_Ol1	40.51	0.01	0.07	0.08	11.89	0.35	0.14	47.16	0.20	0.02	0.00	0.02	0.00	100.45
Block 2_MI15_Ol1	40.43	0.01	0.02	0.07	11.93	0.38	0.16	47.12	0.16	-0.01	0.00	0.01	0.00	100.28
Block 2_MI15_Ol1	40.46	0.01	-0.02	0.09	12.06	0.40	0.16	47.17	0.18	-0.01	0.00	0.02	0.00	100.50
Block 2_MI16_Ol1	39.82	0.01	0.04	0.07	14.27	0.27	0.20	45.48	0.23	0.00	0.00	0.00	0.00	100.39
Block 2_MI16_Ol1	40.01	0.01	0.04	0.05	14.69	0.27	0.23	45.06	0.24	-0.03	-0.01	0.01	0.00	100.56
Block 2_MI16_Ol1	39.76	0.00	0.01	0.06	14.51	0.25	0.21	45.04	0.24	0.01	-0.01	0.01	0.00	100.09
Block 2_MI16_Ol1	40.23	0.00	0.04	0.05	14.26	0.26	0.21	45.77	0.25	0.00	0.00	0.00	0.00	101.07
Block 2_MI17_Ol1	40.55	0.01	0.02	0.07	11.88	0.36	0.18	47.38	0.20	-0.02	0.01	0.01	0.00	100.65
Block 2_MI17_Ol1	40.69	0.01	0.04	0.08	11.87	0.37	0.16	47.36	0.23	0.03	0.01	0.02	0.00	100.87
Block 2_MI17_Ol1	40.24	0.02	0.05	0.09	12.15	0.34	0.17	47.31	0.20	-0.02	0.00	0.01	0.00	100.56
Block 2_MI17_Ol2	40.36	0.02	0.04	0.07	11.88	0.33	0.15	47.15	0.22	0.02	-0.01	0.01	0.00	100.24
Block 2_MI17_Ol2	40.42	0.01	0.04	0.09	12.03	0.37	0.18	47.34	0.19	0.04	-0.01	0.01	0.00	100.71
Block 2_MI17_Ol2	40.14	0.01	0.00	0.06	11.86	0.34	0.18	47.15	0.21	0.00	0.00	0.01	0.00	99.95
Block 2_MI18_Ol1	40.40	0.01	0.02	0.06	11.82	0.35	0.15	47.15	0.20	0.03	0.01	0.00	0.00	100.20
Block 2_MI18_Ol1	39.81	0.00	0.02	0.10	11.74	0.32	0.16	46.77	0.19	-0.01	0.00	0.01	0.00	99.12
Block 2_MI18_Ol1	40.32	0.01	0.01	0.04	11.94	0.37	0.16	47.15	0.20	-0.02	0.01	0.03	0.00	100.21
Block 2_MI18_Ol2	40.65	0.01	0.00	0.07	11.82	0.33	0.17	47.19	0.21	0.02	0.00	0.00	0.00	100.47
Block 2_MI18_Ol2	40.54	0.02	0.02	0.07	11.89	0.39	0.16	47.11	0.22	-0.03	0.00	0.00	0.00	100.39
Block 2_MI18_Ol2	40.44	0.10	0.01	0.08	11.99	0.37	0.18	47.30	0.20	0.00	0.00	0.01	0.00	100.69

Selection of Hapaimamo corrected melt inclusion major oxide compositions (EPMA)

	Oxide wt %													
SAMPLE	SiO_2	TiO_2	Al_2O_3	Cr_2O_3	FeO	NiO	MnO	MgO	CaO	Na_2O	K_2O	P_2O_5	O	TOTAL
Block 2_Ba_MI1_1	52.76	1.60	12.42	0.04	10.59	0.03	0.14	9.62	9.69	2.02	0.24	0.21	0.00	99.35
Block 2_Ba_MI1_1	52.70	1.56	12.31	0.06	10.56	0.01	0.17	9.74	9.58	1.99	0.24	0.19	0.00	99.10
Block 2_Ba_MI1_1	53.13	1.63	12.43	0.05	10.63	0.03	0.19	9.25	9.74	2.05	0.24	0.18	0.00	99.56
Block 2_Bb_MI2	52.67	1.74	12.47	0.04	10.54	0.05	0.16	9.86	9.65	2.00	0.36	0.28	0.00	99.82
Block 2_Bb_MI2	52.23	1.76	12.72	0.02	10.41	0.03	0.15	9.67	9.65	2.08	0.37	0.27	0.00	99.35
Block 2_Bb_MI2	52.34	1.77	12.57	0.04	10.57	0.03	0.18	9.83	9.70	2.03	0.37	0.25	0.00	99.69
Block 2_D_MI3	54.57	1.78	13.93	0.04	7.08	0.02	0.11	8.46	10.22	2.27	0.34	0.19	0.00	99.01
Block 2_D_MI3	54.72	1.78	13.87	0.06	7.05	0.03	0.12	8.49	10.31	2.33	0.33	0.19	0.00	99.29
Block 2_E_MI4	51.45	1.58	12.96	0.06	8.76	0.06	0.12	11.12	10.63	1.83	0.30	0.17	0.00	99.04
Block 2_E_MI4	51.65	1.60	13.09	0.05	8.74	0.07	0.14	10.83	10.66	1.73	0.28	0.16	0.00	98.99
Block 2_F_MI5	54.43	1.71	13.46	0.23	7.81	0.05	0.14	9.31	9.85	2.00	0.33	0.22	0.00	99.54
Block 2_G_MI6	51.63	1.83	13.00	0.04	9.72	0.03	0.16	9.56	9.94	2.20	0.31	0.19	0.00	98.60
Block 2_G_MI6	52.23	1.86	13.17	0.07	9.47	0.03	0.14	9.22	10.11	2.07	0.29	0.19	0.00	98.85
Block 2_Ib_MI7	53.76	1.79	13.54	0.07	7.33	0.06	0.10	9.17	10.06	2.19	0.40	0.25	0.00	98.71
Block 2_Ib_MI7	53.53	1.78	13.48	0.06	7.37	0.06	0.13	9.25	10.08	2.21	0.40	0.26	0.00	98.60
Block 2_K_MI8	52.54	1.68	12.89	0.06	8.98	0.04	0.13	10.21	10.41	1.93	0.29	0.26	0.00	99.43
Block 2_L_MI9	52.88	1.80	13.07	0.10	7.73	0.04	0.11	9.79	9.86	2.19	0.34	0.21	0.00	98.13
Block 2_N_MI10	50.41	1.60	11.46	0.07	9.88	0.08	0.16	14.58	8.56	1.99	0.32	0.20	0.00	99.31
Block 2_N_MI10	50.21	1.62	11.55	0.04	9.90	0.09	0.13	14.70	8.63	2.05	0.34	0.18	0.00	99.45

Block 2_O_MI11	53.46	1.75	12.12	0.04	9.18	0.04	0.16	10.43	9.22	1.90	0.43	0.22	0.00	98.95
Block 2_O_MI11	52.94	1.77	11.90	0.03	9.21	0.04	0.15	10.48	9.23	1.79	0.41	0.25	0.00	98.20
Block 2_Q_MI12	51.57	1.60	12.99	0.06	8.78	0.05	0.14	10.49	10.82	1.87	0.33	0.22	0.00	98.92
Block 3_B_MI14	49.98	1.68	11.62	0.05	11.17	0.05	0.16	12.73	8.88	1.94	0.31	0.20	0.00	98.76
Block 3_B_MI14	49.70	1.72	11.95	0.05	10.99	0.04	0.17	11.65	9.15	1.95	0.35	0.20	0.00	97.91
Block 3_Cb_MI15	53.73	1.78	13.97	0.04	6.98	0.05	0.12	8.78	10.25	2.18	0.42	0.32	0.00	98.62
Block 3_F_MI16	50.95	1.63	12.17	0.05	10.31	0.05	0.16	10.64	9.34	2.21	0.36	0.18	0.00	98.05
Block 3_J_MI17	52.26	1.84	12.80	0.04	8.14	0.05	0.15	10.41	9.68	1.91	0.42	0.29	0.00	98.00
Block 3_J_MI17	51.87	1.85	12.61	0.05	8.10	0.02	0.11	10.38	9.72	1.89	0.43	0.22	0.00	97.25
Block 3_J_MI18	53.05	1.92	13.29	0.02	7.84	0.06	0.13	8.74	10.22	1.98	0.42	0.25	0.00	97.91
Block 3_J_MI18	52.98	1.96	13.32	0.05	7.83	0.04	0.13	8.69	10.24	2.11	0.43	0.28	0.00	98.05

Thermometer and Barometer (Lee et al., 2009)

Pressure (GPa) = $\frac{\ln(Si_4O_8 - 4.019 + 0.0165(Fe_4Si_2O_8) + 0.0005(Ca_4Si_2O_8))^2}{-770T^{-1} + 0.0058T^{\frac{1}{2}} - 0.003(H_{16}O_8)}$

Temperature (°C) = $916.45 + 13.68(Mg_4Si_2O_8) + \frac{4580}{(Si_4O_8)} - 0.509\ (H_{16}O_8)(Mg_4Si_2O_8)$

Selection of Hapaimamo matrix glass major oxide compositions (EPMA)

	Oxide wt %													
SAMPLE	SiO_2	TiO_2	Al_2O_3	Cr_2O_3	FeO	NiO	MnO	MgO	CaO	Na_2O	K_2O	P_2O_5	O	Total
Block 2_K	52.46	1.96	13.89	0.03	10.77	0.03	0.18	6.85	10.67	2.28	0.38	0.21	0.00	99.72
Block 2_K	51.96	1.98	13.92	0.05	10.73	0.03	0.15	6.84	10.69	2.23	0.37	0.22	0.00	99.17
Block 2_K	52.25	1.95	13.61	0.05	10.77	0.01	0.15	6.83	10.58	2.22	0.36	0.23	0.00	99.02
Block 2_K	52.17	1.95	13.77	0.02	10.71	0.02	0.16	6.83	10.66	2.27	0.37	0.22	0.00	99.15
Block 2_K	52.26	1.96	13.82	0.02	10.83	0.00	0.18	6.81	10.65	2.22	0.37	0.24	0.00	99.38
Block 2 K	52.15	1.92	13.90	0.04	10.74	0.00	0.16	6.86	10.54	2.27	0.39	0.22	0.00	99.20
Block 2_K	51.94	1.95	13.73	0.06	10.81	0.02	0.19	6.80	10.55	2.25	0.37	0.24	0.00	98.91
Block 2_K	52.56	1.95	13.75	0.06	10.72	-0.24	0.16	6.87	10.83	2.23	0.38	0.23	0.00	99.51
Block 3_A	52.24	1.98	13.70	0.04	10.66	0.01	0.16	6.76	10.55	2.21	0.40	0.22	0.00	99.22
Block 3_A	52.15	1.98	13.91	0.04	10.66	0.02	0.17	6.68	10.73	2.25	0.40	0.22	0.00	99.61
Block 3_A	52.42	1.95	13.92	0.04	10.84	0.03	0.15	6.79	10.67	2.16	0.38	0.25	0.00	100.35
Block 3_A	52.98	1.97	14.15	0.05	10.80	0.02	0.14	6.81	10.58	2.22	0.38	0.24	0.00	99.54
Block 3_A	52.22	1.97	13.98	0.04	10.86	0.04	0.17	6.68	10.78	2.20	0.39	0.21	0.00	98.83
Block 3_A	52.20	1.95	13.72	0.03	10.57	0.03	0.17	6.67	10.67	2.24	0.35	0.24	0.00	99.02
Block 3_A	52.04	1.96	13.85	0.01	10.74	0.02	0.16	6.64	10.75	2.22	0.38	0.26	0.00	100.12
Block 3_A	52.86	1.96	14.05	0.02	10.76	0.02	0.17	6.67	10.76	2.19	0.40	0.25	0.00	98.90
Block 3_G	53.00	1.97	13.84	0.02	10.17	0.04	-0.15	6.75	10.21	2.39	0.40	0.25	0.00	98.88
Block 3_G	53.44	2.00	14.09	0.01	10.25	-0.01	0.15	6.84	10.21	2.34	0.39	0.24	0.00	99.97
Block 3_G	52.63	1.98	14.02	0.03	10.32	0.01	0.17	6.86	10.37	2.31	0.41	0.25	0.00	99.34
Block 3_G	53.09	1.97	13.91	0.03	10.47	0.01	0.19	6.81	10.36	2.34	0.40	0.23	0.00	99.81
Block 3_G	52.50	1.98	14.09	0.02	10.49	0.00	0.16	6.93	10.43	2.26	0.39	0.24	0.00	99.51
Block 3_G	53.10	2.01	13.62	0.02	10.49	0.00	0.17	6.94	10.44	2.21	0.39	0.23	0.00	99.63
Block 3_G	52.71	1.98	14.00	0.03	10.38	0.04	0.17	6.91	10.43	2.26	0.39	0.23	0.00	99.53
Block 3_G	52.87	2.02	13.79	0.03	10.20	0.03	0.13	6.78	10.28	2.22	0.40	0.26	0.00	99.02
Block 3_J	52.88	1.96	14.06	0.02	10.26	0.01	0.16	6.82	10.49	2.30	0.42	0.20	0.00	99.57
Block 3_J	52.58	1.98	14.09	0.03	10.36	0.03	0.18	6.81	10.46	2.26	0.41	0.22	0.00	99.40
Block 3_J	52.82	1.97	13.79	0.04	10.36	0.02	0.15	6.75	10.37	2.30	0.40	0.24	0.00	99.20
Block 3_J	53.04	1.96	13.87	0.05	10.46	0.02	0.14	6.76	10.43	2.34	0.39	0.24	0.00	99.69
Block 3_J	53.03	1.92	13.92	0.04	10.44	0.00	0.16	6.83	10.56	2.20	0.40	0.22	0.00	99.71

Moinui matrix glass major oxide compositions (EPMA)

	oxide wt %												
	SiO2	TiO2	Al2O3	Cr2O3	FeO	NiO	MnO	MgO	CaO	Na2O	K2O	P2O5	O	TOTAL
M3T2_Glass1	52.65	2.30	13.72	0.05	9.38	0.03	0.15	6.65	10.74	2.36	0.37	0.21	0.00	98.62
M3T2_Glass2	53.49	2.34	13.56	0.04	9.52	0.02	0.15	6.80	10.79	2.34	0.39	0.23	0.00	99.68
M3T2_Glass3	52.52	2.31	13.59	0.06	9.43	0.02	0.14	6.70	10.70	2.46	0.37	0.19	0.00	98.50
M3T2_Glass4	52.88	2.36	13.93	0.03	9.54	0.02	0.17	6.68	10.66	2.49	0.41	0.28	0.00	99.45
M3T2_Glass5	52.59	2.33	13.95	0.03	9.42	0.02	0.15	6.67	10.61	2.54	0.35	0.27	0.00	98.94
M3T2_Glass6	53.07	2.36	13.54	0.03	9.41	0.01	0.13	6.69	10.60	2.53	0.41	0.23	0.00	99.00
M3T2_Glass7	53.20	2.35	13.96	0.05	9.56	0.01	0.14	6.64	10.65	2.42	0.38	0.21	0.00	99.57
M3T2_Glass8	53.22	2.31	13.69	0.06	9.40	0.03	0.16	6.72	10.67	2.47	0.41	0.24	0.00	99.37
M3T2_Glass9	52.91	2.31	13.23	0.06	9.45	0.00	0.14	6.66	10.66	2.39	0.39	0.21	0.00	98.40
M3T2_Glass10	53.20	2.30	13.69	0.02	9.42	0.02	0.17	6.74	10.65	2.39	0.39	0.22	0.00	99.20
M3T2_Glass11	53.12	2.32	13.62	0.05	9.50	0.01	0.16	6.69	10.71	2.45	0.36	0.21	0.00	99.19
M3T2_Glass12	53.06	2.31	13.72	0.05	9.55	-0.02	0.15	6.64	10.63	2.49	0.39	0.26	0.00	99.24
M3T2_Glass13	46.88	2.28	13.58	0.05	9.57	0.03	0.13	6.77	10.58	2.38	0.39	0.23	0.00	92.89
M3T2_Glass14	53.10	2.34	13.57	0.04	9.46	-0.01	0.17	6.57	10.65	2.45	0.36	0.24	0.00	98.95
M3T2_Glass15	53.28	2.34	13.63	0.05	9.47	0.00	0.15	6.73	10.62	2.49	0.38	0.23	0.00	99.37
M3T2_Glass16	52.68	2.31	13.73	0.03	9.46	0.00	0.15	6.67	10.65	2.34	0.41	0.24	0.00	98.67
M3T2_Glass17	52.97	2.33	13.64	0.06	9.63	0.00	0.15	6.77	10.68	2.24	0.39	0.26	0.00	99.12
M3T2_Glass18	53.37	2.26	13.54	0.05	9.47	0.01	0.15	6.77	10.67	2.46	0.40	0.21	0.00	99.36
M3T2_Glass19	53.55	2.34	13.95	0.08	9.40	0.01	0.18	6.67	10.55	2.56	0.40	0.23	0.00	99.92
M3T2_Glass20	53.21	2.30	13.56	0.04	9.47	0.02	0.15	6.66	10.58	2.48	0.40	0.22	0.00	99.09
M3T2_Glass21	53.04	2.25	13.50	0.03	9.52	0.01	0.15	6.64	10.50	2.53	0.37	0.23	0.00	98.77
M3T2_Glass22	53.93	2.30	13.39	0.02	9.50	0.00	0.15	6.73	10.61	2.43	0.38	0.24	0.00	99.66
M3T2_Glass23	53.51	2.31	13.51	0.03	9.56	0.02	0.14	6.70	10.70	2.43	0.38	0.22	0.00	99.50
M3T2_Glass24	53.50	2.34	13.64	0.06	9.49	-0.01	0.14	6.74	10.59	2.45	0.37	0.26	0.00	99.58
M3T2_Glass25	53.06	2.29	13.69	0.05	9.46	0.04	0.14	6.74	10.68	2.45	0.43	0.22	0.00	99.23
M3T2_Glass26	53.38	2.32	13.53	0.04	9.59	0.03	0.14	6.73	10.65	2.47	0.41	0.23	0.00	99.52
M3T2_Glass27	53.67	2.33	13.55	0.04	9.47	0.02	0.15	6.87	10.67	2.42	0.32	0.22	0.00	99.72
M3T2_Glass28	53.46	2.37	13.28	0.07	9.42	0.04	0.13	6.80	10.86	2.49	0.42	0.24	0.00	99.58
M3T2_Glass29	53.79	2.31	13.34	0.03	9.47	0.00	0.14	6.79	10.61	2.42	0.38	0.24	0.00	99.52

Vatnaöldur matrix glass major oxide compositions (Quant EDS only)

SAMPLE		oxide wt % Na_2O	MgO	Al_2O_3	SiO_2	K_2O	CaO	TiO_2	MnO	FeO	O	Total
VS_250_GLASS	Point 1	2.41292	7.044136	13.9823	50.39955	0.265012	11.75328	1.784867	0.269025	12.65916	43.78	100.41
	Point 2	2.41292	7.145248	14.13346	50.33538	0.228874	11.85122	1.918315	0.28485	12.71062	43.95	100.86
	Point 3	2.39944	7.027284	14.13346	50.33538	0.24092	11.75328	1.851591	0.2532	12.87787	43.87	100.71
	Point 4	2.46684	7.094692	14.17125	50.97714	0.228874	11.7113	1.901634	0.363975	12.69776	44.26	101.43
VS_500_GLASS	Point 5	2.2916	6.808208	13.77446	49.07325	0.192736	11.65534	1.901634	0.363975	12.71062	42.88	98.59
	Point 6	2.33204	6.723948	13.56661	49.07325	0.204782	11.58538	1.784867	0.2532	12.67203	42.85	98.34
	Point 7	2.31856	6.707096	13.6044	49.54387	0.192736	11.7113	1.901634	0.205725	12.77495	43.03	98.82
	Point 8	2.359	6.673392	13.75556	49.30856	0.192736	11.61336	1.83491	0.28485	12.95506	43.14	99.11
	Point 9	2.31856	6.808208	13.56661	49.03046	0.204782	11.64134	1.801548	0.28485	12.55624	42.69	98.07
	Point 10	2.30508	6.690244	13.47214	48.83794	0.168644	11.44546	1.868272	0.363975	12.56911	42.48	97.59
	Point 11	2.2242	6.757652	13.50993	49.09464	0.204782	11.62735	1.884953	0.269025	12.865	42.9	98.54
VE_250_GLASS	Point 1	2.359	6.353204	13.16982	48.3887	0.228874	10.77384	1.918315	0	12.55624	41.89	95.92
	Point2	2.37248	6.285796	13.28319	48.02504	0.168644	10.8438	1.985039	0.269025	12.58197	41.78	95.86
	Point 3	2.39944	6.184684	13.07534	47.70416	0.204782	10.75985	1.985039	0.2532	12.74922	41.38	95.17
	Point 4	2.39944	6.302648	13.30208	48.28174	0.192736	10.92775	1.968358	0.22155	12.49192	41.81	95.93
	Point 5	2.31856	6.370056	13.13203	48.21757	0.18069	10.91376	1.934996	0	12.45332	41.78	95.68
	Point 6	2.43988	6.184684	13.37766	48.55984	0.216828	10.74586	1.951677	0.237375	12.74922	41.98	96.34
	Point 7	2.45336	6.134128	13.18871	48.34592	0.204782	10.81582	1.951677	0.2532	12.6463	41.75	95.86
	Point 8	2.4264	6.353204	13.2454	48.17478	0.204782	10.89977	2.018401	0.363975	13.08371	41.93	96.6
	Point 9	2.39944	6.252092	13.20761	48.45288	0.192736	10.85779	1.968358	0.28485	12.76208	42.06	96.51
	Point 10	2.359	6.285796	13.2454	48.55984	0.192736	10.77384	2.035082	0	12.81354	41.94	96.17
	Point 11	2.39944	6.285796	13.16982	48.19618	0.192736	10.8438	2.068444	0.2532	12.99365	42	96.56
	Point 12	2.41292	6.167832	13.01866	47.93947	0.18069	10.81582	2.085125	0.28485	12.98079	41.75	96.03
VA_250_GLASS	Point 1	2.4264	6.521724	13.67998	49.18021	0.252966	11.30554	1.884953	0.269025	12.78781	42.96	98.54
	Point 2	2.43988	6.622836	13.66109	49.28717	0.216828	11.13763	1.934996	0.269025	12.98079	43.03	98.73
	Point 3	2.359	6.57228	13.50993	48.98768	0.228874	11.23558	1.901634	0.300675	12.56911	42.68	97.85
	Point 4	2.38596	6.589132	13.56661	49.22299	0.216828	11.24957	1.951677	0.363975	12.71062	42.93	98.43
	Point 5	2.43988	6.504872	13.6233	49.22299	0.24092	11.26356	2.00172	0.1899	12.89073	43.02	98.68
	Point 6	2.4264	6.48802	13.49103	49.52248	0.24092	11.1936	1.868272	0.300675	12.76208	42.96	98.45

Point 7	2.38596	6.504872	13.52882	49.41552	0.24092	11.24957	1.901634	0.300675	12.69776	42.93	98.39
Point 8	2.41292	6.555428	13.69888	49.43691	0.228874	11.09566	1.951677	0.28485	12.6077	43.05	98.53
Point 9	2.39944	6.555428	13.69888	49.13742	0.265012	11.33352	1.901634	0.34815	12.78781	43	98.67
Point 10	2.38596	6.673392	13.81225	49.50109	0.24092	11.1936	1.884953	0.300675	12.80068	43.23	99.04
Point 11	2.37248	6.555428	13.69888	49.28717	0.204782	11.22158	1.868272	0.300675	12.67203	42.97	98.42
Point 12	2.41292	6.589132	13.6044	49.54387	0.24092	11.12364	1.951677	0.269025	12.72349	43.07	98.65

Primary standards

Hapaimamo melt inclusions

Si – Basaltic glass VG2 298, Ti, Fe – Illmenite 470, Na, Al – Anorthoclase 451, Ni – Ni metal 7317, Cr – Cr2O3 7307, Mn – Rhodonite 7319,

Mg – Springwater olivine 474, Ca – Diopside 7308, K – Kspar 7314, P – Apatite 7303

Hapaimamo matrix glass

Si – Basaltic glass VG2 298, Ti, Fe – Illmenite 470, Na, Al – Anorthoclase 451, Ni – Ni metal 7317, Cr – Cr2O3 7307, Mn – Rhodonite 7319,

Mg – Springwater olivine 474, Ca – Diopside 7308, K – Kspar 7314, P – Apatite 7303

Moinui matrix glass

Si, Al – Basaltic glass VG2 298, Ti, Fe – Almandine 7302, Ni – Ni metal 7317, Cr – Cr2O3 7307, Mn – Rhodonite 7319,

Mg, Ca – Diopside 7308, K – Kspar 7314, P – Apatite 7303, Na – Jadeite 7313

Detection limits

The 99% confidence values (3 sigma) for the minimum concentration detected, are calculated by the Probe for EPMA software using the following equation. As defined in the Probe for EPMA v. 11.8.5 user manual.

$$X_U = \frac{3\sqrt{I_U^B \times t_U^B \times B_U \times C_s}}{t_U^B \times B_U \times I_S^P}$$

I_U^B = the intensity of the background in cps/nA (unknown counts/beam current)

t_U^B = count time used for the unknown background or peak measurement

B_U = the beam current used for the unknown measurement in nA

C_s = the concentration of the element in the standard in wt%

I_S^P = the intensity of the standard in cps/nA (standard intensity/standard beam current)

X_U = unknown concentration in wt%

Average detection limits (ppm) for EPMA analyses of a given phase:

	Si	Ti	Al	Cr	Fe	Ni	Mn	Mg	Ca	Na	K	P
Hapaimamo melt inclusion glass	249	94	202	182	204	237	197	197	115	373	110	84
Hapaimamo olivine adjacent to melt inclusions	276	91	243	177	203	236	196	191	113	361	113	84
Hapaiamamo matrix glass	256	95	207	187	209	238	200	202	116	380	112	85
Moinui matrix glass	326	214	252	261	235	389	226	293	137	347	90	308

Appendix B

Groundmass mineral compositions

Selection of groundmass plagioclase feldspar major oxide compositions from PdF, Moinui and Hapaimamo (EPMA)

		oxide wt %												
	SAMPLE	FeO	SiO_2	MgO	Cr_2O_3	MnO	Na_2O	Al_2O_3	CaO	K_2O	TiO_2	O	TOTAL	An
Moinui	M1C_plag_core_1	0.50	51.47	0.26	0.00	-0.03	3.59	29.81	14.05	0.09	0.06	0.00	99.79	0.68
	M1C_plag_core_1	0.50	51.95	0.24	-0.01	0.03	3.56	29.84	13.82	0.10	0.10	0.00	100.15	0.68
	M1C_plag_rim_1	0.49	51.48	0.23	0.00	0.02	3.50	29.71	13.77	0.11	0.09	0.00	99.39	0.68
	M1C_plag_rim_1	0.54	51.61	0.24	0.01	0.02	3.98	29.96	13.75	0.12	0.08	0.00	100.32	0.65
	M1C_plag_core_2	0.50	51.74	0.25	-0.02	0.03	3.66	29.65	13.88	0.10	0.07	0.00	99.88	0.67
	M1C_plag_core_2	0.47	50.93	0.22	0.00	0.00	3.50	30.13	14.30	0.09	0.06	0.00	99.70	0.69
	M1C_plag_rim_2	0.42	51.52	0.23	0.01	0.00	3.46	29.65	13.96	0.11	0.04	0.00	99.40	0.69
	M1C_plag_core_3	0.47	51.35	0.24	0.00	0.02	3.71	30.13	14.07	0.10	0.07	0.00	100.15	0.67
	M1C_plag_core_3	0.52	51.67	0.22	0.00	0.02	3.57	29.50	13.54	0.10	0.10	0.00	99.23	0.67
	M1C_plag_core_4	0.55	51.73	0.26	0.04	-0.03	3.53	29.36	13.44	0.12	0.08	0.00	99.10	0.67
	M1C_plag_core_4	0.56	51.47	0.27	0.02	-0.03	3.67	29.67	13.84	0.10	0.05	0.00	99.63	0.67
Hapaimamo	H2CL_plag_core_1	0.95	52.14	0.18	-0.03	-0.01	4.00	29.01	13.03	0.14	0.10	0.00	99.51	0.64
	H2CL_plag_core_1	1.16	51.61	0.13	0.03	-0.01	4.07	29.01	13.07	0.15	0.12	0.00	99.33	0.63
	H2CL_plag_rim_1	1.07	52.21	0.18	0.02	0.03	4.07	28.88	12.91	0.13	0.16	0.00	99.65	0.63
	H2CL_plag_core_2	0.83	51.62	0.14	0.00	0.03	3.77	29.47	13.73	0.12	0.10	0.00	99.81	0.66
	H2CL_plag_core_3	0.71	51.37	0.22	0.04	0.03	3.53	29.92	14.15	0.11	0.04	0.00	100.12	0.69
	H2CL_plag_core_3	0.69	50.60	0.22	-0.02	0.03	3.85	29.79	13.79	0.11	0.08	0.00	99.15	0.66
	H2CL_plag_core_4	1.15	51.72	0.16	0.01	0.00	4.24	29.07	13.10	0.12	0.08	0.00	99.67	0.63
PdF	64217-1_plag_core_1	0.87	51.94	0.15	0.01	-0.01	3.93	28.57	12.67	0.26	0.13	0.00	98.51	0.63
	64217-1_plag_core_1	0.78	51.28	0.14	-0.02	0.03	3.71	30.06	13.65	0.22	0.11	0.00	99.96	0.66
	64217-1_plag_core_2	0.99	51.93	0.13	0.01	0.01	4.23	29.64	13.42	0.25	0.13	0.00	100.73	0.63
	64217-1_plag_core_2	1.01	52.12	0.16	0.01	0.01	4.45	28.38	12.43	0.30	0.22	0.00	99.10	0.60
	64217-1_plag_core_3	0.79	51.45	0.17	-0.03	-0.01	3.97	29.47	13.33	0.23	0.18	0.00	99.57	0.64
	64217-1_plag_core_3	1.03	51.69	0.14	0.03	0.03	3.84	29.12	12.87	0.28	0.10	0.00	99.14	0.64
	64217-1_plag_core_4	1.02	52.60	0.18	0.03	0.03	4.38	27.95	11.92	0.37	0.15	0.00	98.64	0.59
	64217-1_plag_core_4	0.94	52.54	0.11	-0.03	0.00	4.38	28.83	12.76	0.26	0.16	0.00	99.96	0.61

Selection of groundmass clinopyroxene major oxide compositions from Pdf, Moinui and Hapaimamo

		oxide wt%													
	SAMPLE	FeO	SiO_2	MgO	Cr_2O_3	MnO	NiO	Na_2O	Al_2O_3	CaO	K_2O	TiO_2	O	TOTAL	Mg#
Moinui	M1C_Pyrx_1_core	6.72	51.38	17.23	0.86	0.17	0.05	0.23	2.71	18.71	0.02	0.85	0.00	98.94	0.82
	M1C_Pyrx_1_core	7.09	51.62	18.06	0.79	0.19	0.05	0.21	2.49	17.47	0.01	0.75	0.00	98.73	0.82
	M1C_Pyrx_1_rim	8.13	51.15	18.20	0.58	0.22	0.04	0.20	2.86	16.02	0.01	0.99	0.00	98.39	0.80
	M1C_Pyrx_2_core	7.45	50.64	16.80	0.37	0.19	0.05	0.20	2.79	19.01	0.01	1.21	0.00	98.72	0.80
	M1C_Pyrx_2_core	7.21	50.44	16.93	0.68	0.18	0.05	0.22	2.96	18.71	0.02	1.22	0.00	98.64	0.81
	M1C_Pyrx_2_rim	7.19	51.58	17.94	0.77	0.18	0.06	0.22	2.48	17.72	0.02	0.86	0.00	99.01	0.82
Hapai	H2CL_Pyrx_1_core	12.96	49.66	13.90	0.01	0.26	0.04	0.29	2.05	17.64	0.01	1.45	0.00	98.27	0.81
	H2CL_Pyrx_1_core	6.72	50.48	16.20	0.97	0.15	0.05	0.25	3.50	19.72	0.02	0.76	0.00	98.82	0.81
	H2CL_Pyrx_1_rim	7.42	50.95	16.74	0.83	0.19	0.04	0.27	2.92	18.56	0.00	0.72	0.00	98.64	0.80
	H2CL_Pyrx_1_rim	10.07	50.71	15.76	0.19	0.23	0.03	0.31	2.26	18.29	0.01	0.93	0.00	98.78	0.74
	H2CL_Pyrx_2_core	14.10	53.29	25.45	0.21	0.28	0.08	0.03	1.56	2.62	0.00	0.38	0.00	98.01	0.76
	H2CL_Pyrx_2_rim	14.53	53.24	25.44	0.11	0.29	0.06	0.03	1.32	2.56	0.01	0.50	0.00	98.09	0.76
	H2CL_Pyrx_3_ol rim	15.42	52.91	24.61	0.10	0.31	0.05	0.04	1.38	2.39	0.00	0.48	0.00	97.70	0.74
	H2CL_Pyrx_3_ol rim	14.93	52.69	23.19	0.11	0.34	0.06	0.06	1.31	5.22	0.01	0.52	0.00	98.42	0.73
PdF	64217-1_Pyrx_1_core	8.12	47.03	14.11	0.37	0.17	0.03	0.34	6.23	19.45	0.02	2.41	0.00	98.29	0.76
	64217-1_Pyrx_1_core	8.38	48.00	13.65	0.52	0.17	0.02	0.37	4.80	20.58	0.03	2.29	0.00	98.82	0.74
	64217-1_Pyrx_1_rim	8.66	49.69	14.89	0.17	0.19	0.02	0.32	3.23	19.67	0.01	1.51	0.00	98.38	0.75
	64217-1_Pyrx_1_rim	8.02	48.28	13.93	0.65	0.17	0.02	0.34	4.69	20.51	0.03	2.16	0.00	98.80	0.76
	64217-1_Pyrx_2_core	7.91	49.66	15.04	0.45	0.18	0.01	-0.12	3.48	20.08	0.01	1.58	0.00	98.28	0.77
	64217-1_Pyrx_2_core	7.36	51.94	16.64	0.53	0.17	0.01	0.21	1.85	19.35	0.01	0.90	0.00	98.97	0.80
	64217-1_Pyrx_2_rim	7.30	49.71	15.32	0.62	0.19	0.02	0.26	3.50	19.96	0.01	1.46	0.00	98.36	0.79
	64217-1_Pyrx_2_rim	9.17	49.35	14.70	0.17	0.20	0.01	0.32	3.41	19.67	0.02	1.73	0.00	98.75	0.74
	64217-1_Pyrx_3_core	7.80	48.60	14.45	0.67	0.16	0.03	0.37	4.90	19.71	0.02	1.85	0.00	98.57	0.77

Selection of groundmass olivine major oxides compositions from PdF

	oxide wt%													
	FeO	SiO_2	MgO	Cr_2O_3	MnO	NiO	Na_2O	Al_2O_3	CaO	K_2O	TiO_2	O	TOTAL	Fo
64217-1_olivine1	30.72	36.95	31.03	0.00	0.46	0.11	0.01	0.02	0.33	0.02	0.04	0.00	99.67	0.64
64217-1_olivine1	31.37	37.26	30.70	0.01	0.47	0.12	0.00	0.02	0.34	0.01	0.04	0.00	100.34	0.63
64217-1_olivine_2_core	34.36	36.46	28.11	-0.01	0.53	0.09	0.02	0.03	0.35	0.01	0.05	0.00	100.00	0.59
64217-1_olivine_2_core	33.55	36.47	28.43	-0.01	0.52	0.10	0.03	0.01	0.35	0.01	0.04	0.00	99.51	0.60
64217-1_olivine_2_rim	34.97	36.06	27.28	0.00	0.58	0.09	0.02	0.02	0.39	0.02	0.08	0.00	99.49	0.58
64217-1_olivine_2_rim	36.27	35.86	26.03	0.00	0.61	0.08	0.01	0.02	0.41	0.02	0.05	0.00	99.35	0.56
64217-1_olivine_3	31.31	37.00	30.54	0.01	0.49	0.11	0.00	0.00	0.38	0.01	0.07	0.00	99.92	0.63
64217-1_olivine_4	28.69	37.21	32.46	0.00	0.42	0.11	0.00	0.03	0.37	0.03	0.05	0.00	99.38	0.66
64217-1_olivine_4	32.20	36.75	29.53	0.01	0.52	0.10	0.03	0.01	0.35	0.02	0.16	0.00	99.67	0.62

Primary standards for groundmass minerals

Plagioclase

K, Al and Si – Kspar 7314, Ti – Rutile 7320, Fe – Almandine 7314, Mg, Ca – Diopside 7308, Cr – Cr2O3 7307, Mn – Rhodonite 7319,

Na – Jadeite 7313.

Clinopyroxene

Ca, Si, Mg – Diopside 7308 K - Kspar 7314, Ti – Rutile 7320, Al – Almandine 7314, Cr – Cr2O3 7307, Mn – Rhodonite 7319,

Na – Jadeite 7313, Ni – Nickel metal 7317

Olivine

Mg and Fe – Springwater olivine 474, Ti – Rutile 7320, Si, Al – Almandine 7314, Ca – Diopside 7308, Cr – Cr2O3 7307, Mn – Rhodonite 7319,

Ni – Nickel metal 7317, Na – Jadeite 7313 K – Kspar 7314

Appendix C

Average EPMA detection limits and primary standards for olivine compositional traverses

Average EPMA Detection Limits

	Detection limits (ppm)									
	SiO2	Al2O3	MgO	FeO	MnO	NiO	CaO	Cr2O3	K2O	Na2O
PdF	151	130	133	132	129	168	64	190	183	234
Hapaimamo	110	128	90	80	90	84		164		
Moinui	150	122	108	124	97	121	37	141		58

Primary Standards for olivine compositional traverses

PdF

Si – Olivine 7318 and 474, Almandine 7302, Al – Kyanite 7315, Almandine 7302, Mg – Diopside 7308, olivine 7308 and 474, Fe – Haematite 7311, Olivine 7318 and 474, Mn – Rhodonite 7319, Ni – Ni metal 7317, Ca – Wollastonite 7323, Diopside 7308, Cr – Cr2O3 7307, K – Kspar 7314, Na – Jadeite 7313

Hapaimamo

Si, Al – Almandine 7302, Mg, Fe – olivine 474, Mn – Rhodonite 7319, Ni – Ni metal 7317 Cr – Cr2O3 7307

Moinui

Si, Al, Fe – Almandine 7302, Mg, Fe – olivine 474, Mg, Ca – Diopside 7308, Mn – Rhodonite 7319, Ni – Ni metal 7317, Cr – Cr2O3 7307, Na – Jadeite 7313

Appendix D

Selected diffusion models

This appendix gives two examples of the inputs and processing of a complete diffusion model such as those presented in chapter 3 (figure 3.8, sample 64217-1_G1) and chapter 4 (figure 4.12, Block 4_Q_2).

64217_1_G1 – EPMA major oxide

	Oxide wt%												
	SiO_2	Al_2O_3	Cr_2O_3	FeO	NiO	MnO	MgO	CaO	Na_2O	K_2O	O	TOTAL	Fo
64217_1_Ol_G_1	37.73	0.03	0.03	24.09	0.29	0.31	36.23	0.27	0.02	0.01	0.00	98.99	0.72
64217_1_Ol_G_1	38.94	0.03	0.04	18.23	0.36	0.26	41.19	0.29	0.03	0.00	0.00	99.36	0.80
64217_1_Ol_G_1	39.67	0.04	0.05	15.38	0.36	0.19	43.56	0.26	0.01	0.01	0.00	99.52	0.83
64217_1_Ol_G_1	39.73	0.03	0.02	14.49	0.38	0.20	44.34	0.25	0.01	0.01	0.00	99.46	0.84
64217_1_Ol_G_1	39.73	0.03	0.05	14.16	0.39	0.22	44.47	0.27	0.00	0.01	0.00	99.32	0.84
64217_1_Ol_G_1	39.85	0.03	0.06	14.21	0.34	0.21	44.50	0.26	0.03	0.03	0.00	99.53	0.84
64217_1_Ol_G_1	39.73	0.02	0.05	14.26	0.34	0.19	44.44	0.28	0.01	0.02	0.00	99.33	0.84
64217_1_Ol_G_1	39.75	0.04	0.07	14.24	0.38	0.21	44.29	0.28	0.04	0.01	0.00	99.31	0.84
64217_1_Ol_G_1	39.72	0.03	0.03	14.15	0.38	0.21	44.38	0.26	0.00	0.02	0.00	99.18	0.84

9 spot analyses at ~9 μm spacing

Method – After profiles have been retrieved from the SEM and EPMA, the SEM profile is calibrated for composition as described in chapter 2 (shown below). These compositions are input in AUTODIFF. AUTODIFF is coded in Microsoft Excel with a variety of IF statements using trigonometry and laws of diffusion as defined in chapter 2. Pressure (estimated using textural relationships), temperature (calculated), oxygen fugacity (estimated from literature values) and c-axis orientation and plunge (calculated from EBSD data), angle of the traverse from the reference point (measured using image J) and sectioning angle (if measured using a U-stage) are also input, together with initial and boundary conditions. Initial conditions are defined as the core composition and boundary condition is define d as the rim composition (at the crystal rim). The boundary condition, oxygen fugacity, pressure and temperature are fixed. The diffusion coefficient is defined as stated in chapter 2. With these values input the timescales are calculated.

SEM-EPMA calibration

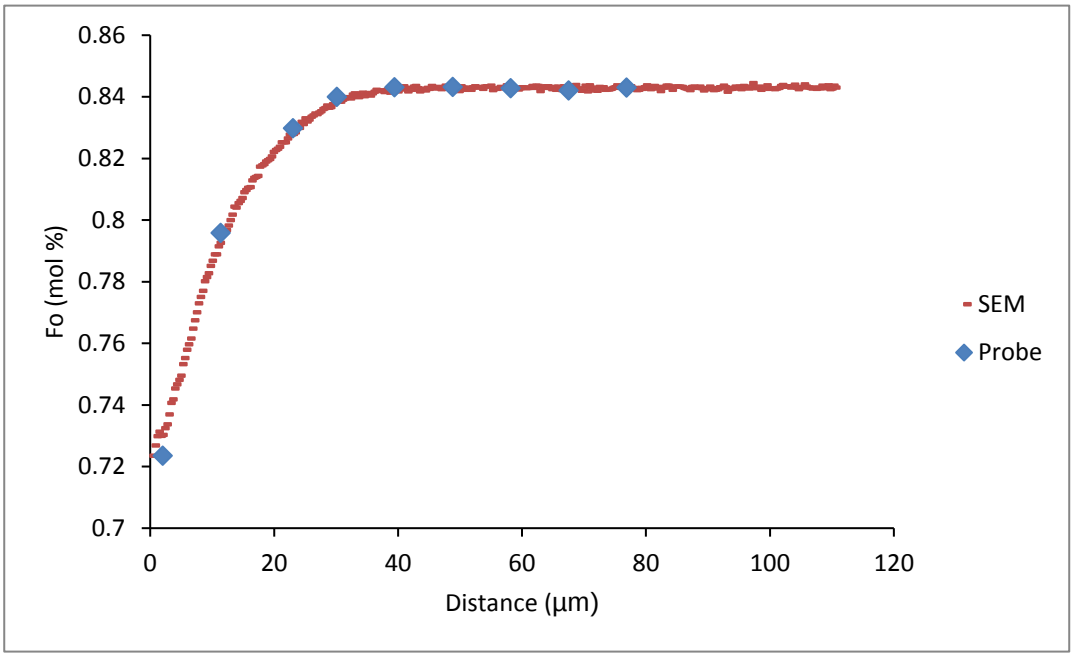

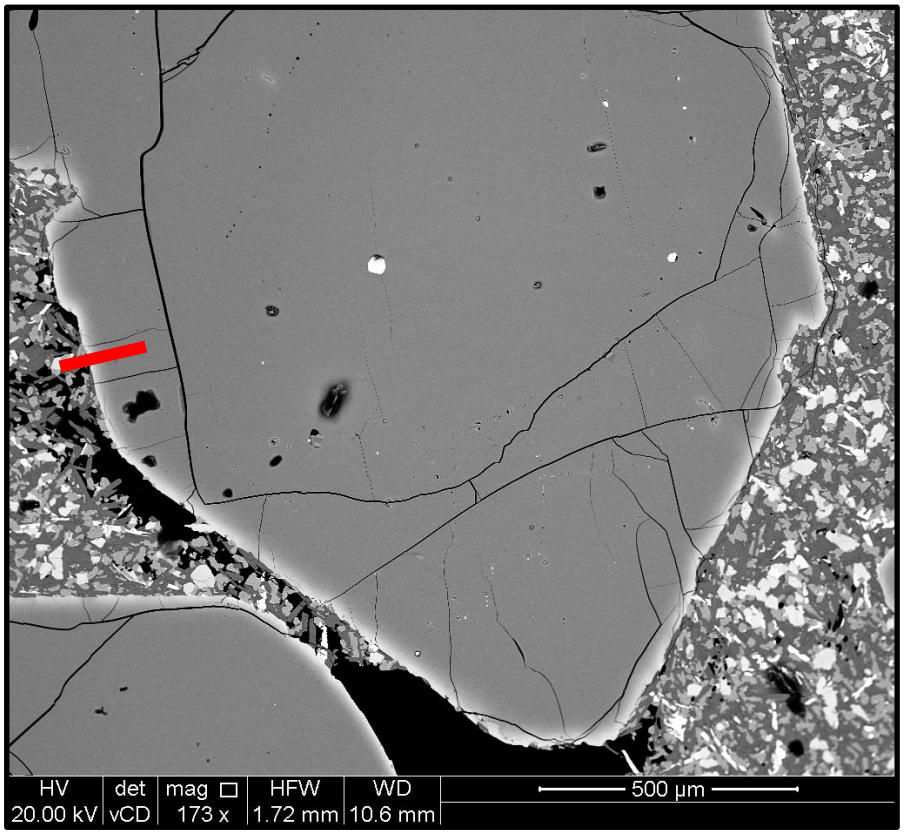

Position of the measured traverse in relation to the shape of the crystal.

Hapaimamo Tephra Block 2_Q_2 – EPMA major oxide compositions

	oxide wt%								
	SiO2	Al2O3	Cr2O3	FeO	NiO	MnO	MgO	O	TOTAL	Fo
Block 4_Ol_Q_2	39.47	0.00	0.06	15.58	0.27	0.21	44.08	0.00	99.68	0.83
Block 4_Ol_Q_2	39.47	0.01	0.07	14.40	0.30	0.20	45.09	0.00	99.53	0.84
Block 4_Ol_Q_2	39.74	0.02	0.06	13.70	0.31	0.18	45.69	0.00	99.71	0.85
Block 4_Ol_Q_2	39.84	0.03	0.06	13.34	0.32	0.19	45.92	0.00	99.70	0.86
Block 4_Ol_Q_2	39.85	0.02	0.08	13.20	0.33	0.18	46.07	0.00	99.74	0.86
Block 4_Ol_Q_2	40.05	0.03	0.03	13.15	0.34	0.18	46.17	0.00	99.95	0.86
Block 4_Ol_Q_2	39.74	0.03	0.07	13.08	0.34	0.18	46.13	0.00	99.56	0.86
Block 4_Ol_Q_2	39.91	0.03	0.06	13.05	0.33	0.18	46.26	0.00	99.81	0.86
Block 4_Ol_Q_2	39.80	0.02	0.06	13.03	0.35	0.18	46.19	0.00	99.63	0.86
Block 4_Ol_Q_2	39.87	0.03	0.06	12.95	0.34	0.16	46.23	0.00	99.64	0.86

10 spot analyses at ~9 µm spacing

Hapaimamo Tephra H1LC C_3 – EPMA major oxide compositions

	oxide wt%									
	SiO2	Al2O3	Cr2O3	FeO	NiO	MnO	MgO	O	TOTAL	Fo
H1LC_Ol_C_3	38.16	0.01	0.02	24.18	0.24	0.31	37.24	0.00	100.17	0.73
H1LC_Ol_C_3	38.67	0.01	0.02	21.22	0.29	0.28	39.63	0.00	100.11	0.76
H1LC_Ol_C_3	39.15	0.00	0.05	18.93	0.30	0.24	41.62	0.00	100.29	0.79
H1LC_Ol_C_3	39.65	0.01	0.04	16.98	0.32	0.22	43.37	0.00	100.59	0.82
H1LC_Ol_C_3	39.79	0.02	0.05	15.57	0.32	0.20	44.51	0.00	100.45	0.83
H1LC_Ol_C_3	39.96	0.02	0.02	14.76	0.33	0.21	45.11	0.00	100.40	0.84
H1LC_Ol_C_3	39.99	0.01	0.03	14.37	0.32	0.19	45.46	0.00	100.39	0.84
H1LC_Ol_C_3	39.99	0.01	0.04	14.23	0.32	0.20	45.63	0.00	100.42	0.85
H1LC_Ol_C_3	39.98	0.02	0.02	14.16	0.33	0.20	45.68	0.00	100.40	0.85
H1LC_Ol_C_3	40.05	0.03	0.04	14.15	0.33	0.20	45.67	0.00	100.47	0.85
H1LC_Ol_C_3	40.00	0.02	0.03	14.11	0.33	0.19	45.65	0.00	100.33	0.85

11 spot analyses at ~9 µm spacing

SEM-EPMA calibration Block 2_Q_2

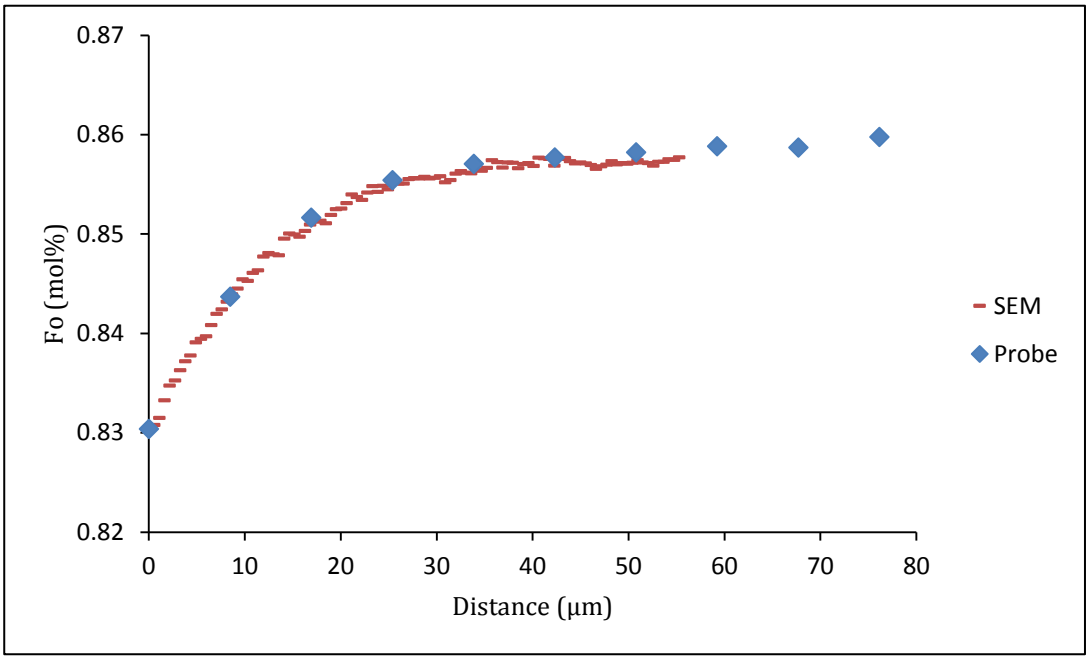

SEM-EPMA calibration H1LC C3

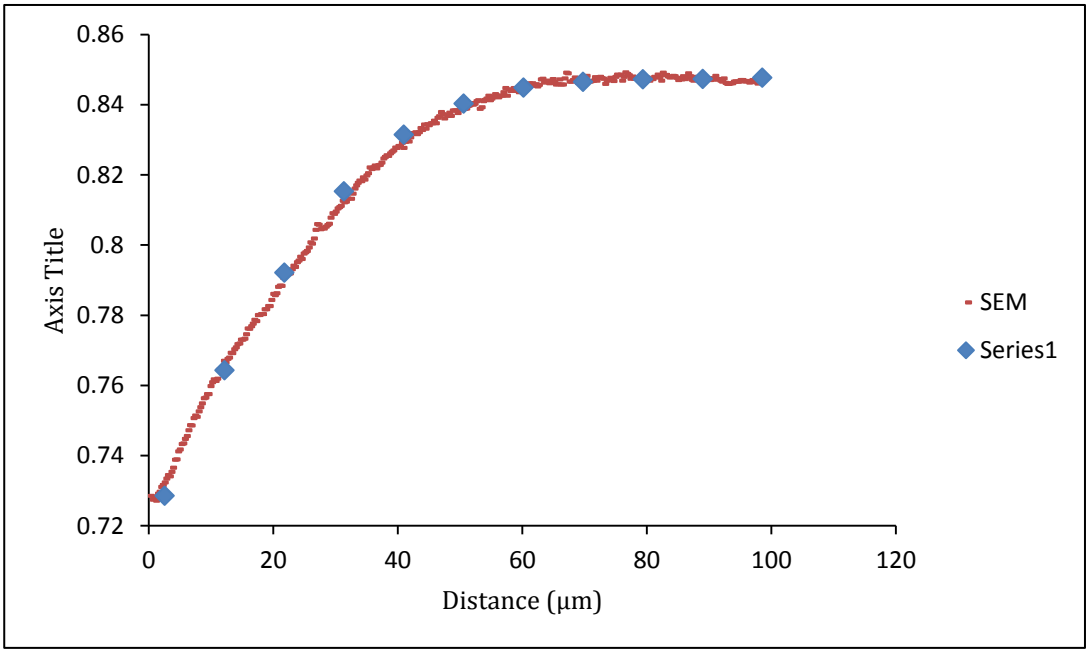

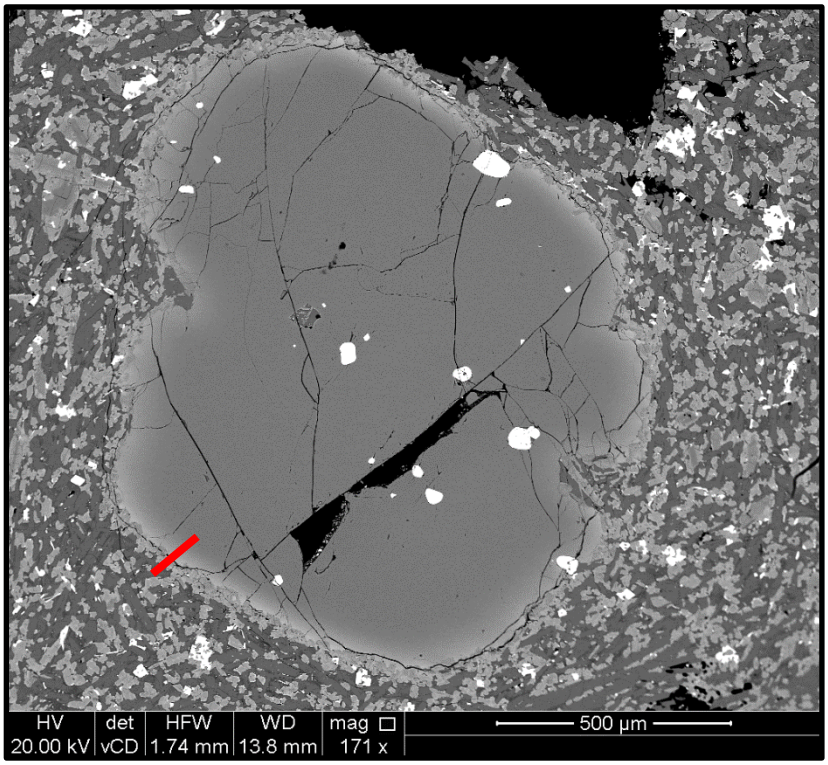

Position of the measured traverse in relation to the shape of the crystal.

H1LC_C3

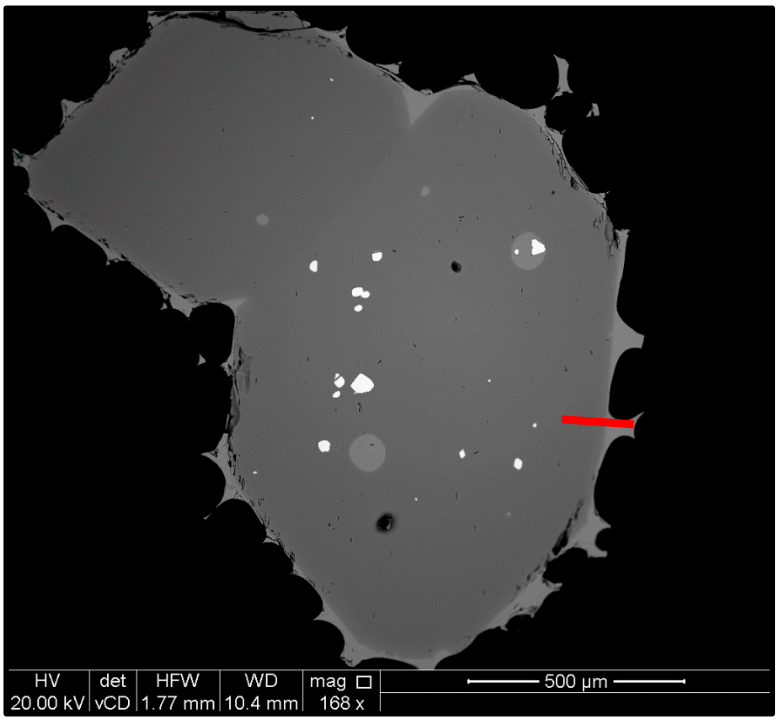

Position of the measured traverse in relation to the shape of the crystal.

Block 4_Q2

Appendix E

XMT Workflow

The workflow was devised with Matthew Pankhurst, a post-doctoral researchera the Universty of Leeds. The raw XMT data contains multiple crystal slices in each image. The following workflow is used to segment a single crystal from a stack of these images using FIJI Image Processing software.

1. Find a target crystal in the raw data stack
2. Scroll through the slices above and below the crystal, note the numbers then copy these slices into a folder for processing
3. Open these slices as an image sequence in FIJI and apply the non-local denoise (NLDN) filter to enhance the edge of the slices
4. Use the rectangular selection tool to define a box that captures the crystal in each slice it is present, crop all slices and save as a cropped image sequence and close
5. Open a single image in the WEKA plugin and load the predefined classifier, apply to all images and save. Images are now segmented. Close FIJI and reload.
6. Import all segmented images, invert the colour scale, save and close
7. Open one of the inverted slices, load the graph cut plugin with limited smoothing and apply to all slices. This separates the image into foreground and background – foreground being the crystal slice in question, background being everything else (e.g. parts of the olivine groundmass that also got segmented). Only the foreground part of the image will be saved.
8. Close all slices and then reopen the image sequence. Apply fill holes, invert then apply erode 3D and dilate 3D.
9. Apply the find connected regions command with the minimum size set to 10000 pixels. This isolates regions of pixels larger than 10000 pixels, resulting in a fully segmented crystal
10. Apply crop 3D. This image sequence is then input in to Aviso image processing software for volume rendering.

Appendix F

Selected Vatnaöldur Quantitative EDS data and a verage EPMA detection limits and standards

Selected Vatnöldur Quantitative EDS data

	Traverse	MgO	SiO	CaO	MnO	FeO	NiO	Total	Distance (μm)	Fo
VS_250_1_A	Point 1	41.74	38.12	0.35	0.35	18.32	0.11	98.27	0	0.798
	Point 2	41.91	38.08	0.32	0.38	18.18	0.13	98.25	5	0.800
	Point 3	41.67	37.89	0.29	0.35	18.08	0.15	97.69	10	0.800
	Point 4	42.10	38.10	0.31	0.36	17.96	0.10	98.19	13	0.803
	Point 5	42.23	38.16	0.31	0.40	17.84	0.15	98.33	17	0.804
	Point 6	42.38	38.12	0.32	0.36	17.52	0.10	98.06	21	0.808
	Point 7	42.70	38.18	0.32	0.36	17.28	0.11	98.22	25	0.811
	Point 8	42.89	38.21	0.32	0.36	17.15	0.13	98.3	31	0.813
	Point 9	43.04	38.42	0.31	0.35	16.84	0.15	98.34	35	0.816
	Point 10	43.09	38.18	0.31	0.28	16.75	0.14	98	39	0.817
	Point 11	43.21	38.31	0.34	0.32	16.63	0.14	98.2	42	0.818
	Point 12	43.36	38.33	0.32	0.41	16.44	0.17	98.26	46	0.820
VS_250_1_B	Point 1	41.39	38.36	0.41	0.38	18.89	0.00	98.67	0	0.793
	Point 2	41.59	38.16	0.35	0.36	18.91	0.09	98.73	4	0.793
	Point 2	41.76	38.03	0.35	0.40	18.74	0.17	98.71	9	0.794
	Point 3	41.81	38.06	0.31	0.40	18.60	0.17	98.59	14	0.795
	Point 4	41.98	38.21	0.32	0.35	18.62	0.14	98.89	20	0.797
	Point 5	41.91	38.10	0.31	0.38	18.45	0.14	98.56	25	0.798
	Point 6	42.15	38.14	0.31	0.38	18.05	0.13	98.4	30	0.802
	Point 7	42.23	38.16	0.31	0.32	18.04	0.17	98.48	36	0.803
	Point 8	42.47	38.25	0.32	0.36	18.06	0.14	98.84	41	0.803

	Point 9	42.37	38.21	0.31	0.35	17.86	0.15	98.48	46	0.804
	Point 10	42.21	37.97	0.36	0.40	17.37	0.17	97.73	51	0.808
VS_250_1_A	Core	44.42	38.23	0.34	0.24	14.69	0.17	97.32	-	0.840
core points	Core	44.52	38.48	0.32	0.28	14.56	0.18	97.58	-	0.841
	Core	44.56	38.53	0.34	0.30	14.72	0.18	97.87	-	0.839
VS_250_7_A	Point 1	42.47	39.23	0.38	0.38	19.62	0.14	101.46	0	0.790
	Point 2	42.82	39.06	0.34	0.38	19.57	0.00	101.42	4	0.793
	Point 3	43.17	39.15	0.31	0.40	19.28	0.14	101.69	10	0.795
	Point 4	43.31	39.32	0.32	0.40	19.16	0.11	101.85	18	0.797
	Point 5	43.33	39.36	0.32	0.36	19.10	0.13	101.85	23	0.798
	Point 6	43.44	39.19	0.34	0.43	18.77	0.15	101.54	31	0.800
	Point 7	43.82	39.34	0.31	0.38	18.45	0.13	101.64	40	0.805
	Point 8	44.05	39.34	0.34	0.36	18.33	0.11	101.77	49	0.807
	Point 9	44.02	39.38	0.35	0.36	18.27	0.13	101.74	57	0.807
	Point 10	44.14	39.47	0.35	0.38	18.05	0.14	101.73	65	0.809
	Point 11	44.29	39.60	0.35	0.32	18.05	0.22	102.06	73	0.810
	Point 12	44.30	39.40	0.34	0.38	17.75	0.15	101.54	83	0.812
VS_250_7	Core	45.50	39.66	0.35	0.36	16.45	0.19	101.72	-	0.827
core points	Core	45.43	39.94	0.34	0.36	16.36	0.19	101.84	-	0.827
	Core	45.69	40.00	0.35	0.33	16.34	0.23	102.15	-	0.828
VS_250_10_A	Point 1	42.25	38.70	0.38	0.38	18.98	0.14	100.06	0	0.794
	Point 2	42.69	38.66	0.31	0.44	18.86	0.10	100.27	8	0.797
	Point 3	43.23	39.02	0.32	0.28	18.45	0.14	100.67	17	0.803
	Point 4	43.87	39.08	0.34	0.36	17.74	0.18	100.8	28	0.811
	Point 5	44.12	39.08	0.32	0.36	17.07	0.18	100.37	42	0.817
	Point 6	44.88	39.49	0.36	0.30	16.69	0.18	101.12	56	0.823
	Point 7	45.25	39.55	0.32	0.35	16.15	0.19	101.02	73	0.829
	Point 8	45.57	39.58	0.34	0.28	15.93	0.14	101.04	95	0.832
VS_250_10_B	Point 1	41.96	38.55	0.32	0.38	19.00	0.15	99.63	0	0.793
	Point 2	42.55	38.85	0.31	0.38	18.60	0.08	100	10	0.799
	Point 3	43.34	39.02	0.29	0.35	17.82	0.10	100.17	22	0.809
	Point 4	44.05	39.23	0.31	0.40	17.28	0.18	100.66	37	0.815
	Point 5	44.57	39.34	0.28	0.33	16.72	0.15	100.64	50	0.822

	Point 6	44.71	39.32	0.38	0.33	16.42	0.11	100.5	62	0.825
	Point 7	45.03	39.43	0.31	0.28	15.98	0.15	100.4	78	0.830
	Point 8	45.45	39.43	0.32	0.35	15.81	0.23	100.78	92	0.832
VS_250_10	core	45.99	39.81	0.31	0.35	15.57	0.15	101.36	-	0.836
core points	core	45.74	39.66	0.35	0.30	15.45	0.18	100.89	-	0.837
	core	45.85	39.77	0.34	0.32	15.55	0.15	101.18	-	0.836
VS_250_15_A	Point 1	42.32	38.46	0.34	0.41	18.46	0.15	99.39	0	0.799
	Point 2	44.71	39.04	0.34	0.36	15.54	0.13	99.34	79	0.833
	Point 3	45.13	38.95	0.34	0.32	14.90	0.19	99.04	237	0.839
VS_500_22_A	Point 1	42.72	39.23	0.34	0.40	18.92	0.00	100.86	0	0.798
	Point 2	45.42	39.53	0.31	0.28	15.68	0.13	100.56	248	0.834
VS_500_24_A	Point 1	42.28	38.85	0.36	0.41	19.71	0.11	100.98	0	0.788
	Point 2	46.04	39.79	0.34	0.32	15.50	0.19	101.37	287	0.837

Average EPMA detection limits

	Detection limits (ppm)						
	SiO2	Al2O3	MgO	FeO	MnO	NiO	Cr2O3
Vatnaöldur	142	138	145	137	127	120	156

Primary Standards

Si, Mg – Olivine 474, Al, Fe – Almandine 7302, Mn – Rhodonite 7319, Ni – Ni metal 7317, Cr – Cr2O3 7307

Appendix G

Hapaimamo and Moinui Whole Rock data (XRF)

		wt %									
		Na2O	MgO	Al2O3	SiO2	P2O5	K2O	CaO	TiO2	MnO	Fe2O3
Hapaimamo	H2TC	2.21	8.45	13.10	51.44	0.244	0.389	10.29	1.98	0.169	11.85
	H2CL	2.22	9.11	13.01	51.72	0.228	0.383	10.23	1.94	0.169	11.89
	H2BC	2.05	10.01	12.62	51.31	0.232	0.358	9.88	1.89	0.168	11.80
Moinui	M1TC	1.89	13.41	11.30	50.00	0.203	0.337	9.26	1.92	0.171	12.14
	M1CL	1.38	22.20	8.17	46.90	0.139	0.229	6.79	1.39	0.177	12.91
	M2BC	1.85	14.67	10.93	49.85	0.19	0.312	8.94	1.85	0.172	12.30

		Sr (ppm)	Ba (ppm)	Zr (ppm)	Cr (ppm)	S (ppm)	LOI	SUM
Hapaimamo	H2TC	309	168	142	409	<20	0	100.1
	H2CL	309	152	134	402	<20	-0.41	100.5
	H2BC	298	133	132	455	<20	-0.03	100.3
Moinui	M1TC	259	145	126	732	71	-0.39	100.2
	M1CL	182	101	89	719	<20	-0.49	99.8
	M2BC	247	137	124	743	<20	-0.47	100.6

Appendix H

U-stage angles measured from PdF thin sections

Angle in degrees (hade)	Frequency
1	2
2	1
3	4
4	10
5	16
6	7
8	11
9	5
10	6
11	6
12	1
13	7
14	1
15	4
16	2
17	2
18	1
19	1
20	1
22	1
24	2
27	1

Supplementary material

The supplementary material contained on the attached CD is listed below;

- Diffusion profiles for each case study
- EBSD data for each profile (pole figures and euler angles)
- Uncertainties on timescales calculations
- Sample SEM images from the PdF dataset
- Examples of csv templates for FINDIF (standard, incorporation of changing boundary conditions only and incorporation of both changing boundary conditions and crystal growth)
- Powerpoint of all PdF olivines segmented from the XMT datasets